CRANFIELD UNIVERSITY

DEFENCE COLLEGE OF MANAGEMENT AND TECHNOLOGY

ENGINEERING SYSTEMS DEPARTMENT

PhD THESIS

Academic Year 2007-2008

Nicholas Whitworth

Mathematical and Numerical Modelling of Shock Initiation in Heterogeneous Solid Explosives

Supervisor   Dr Shaun Forth

February 2008

Abstract

In the field of explosive science, the existence of the 'hot-spot' is generally accepted as essential to any theory on shock initiation. Continuum-based shock initiation models only account for 'hot-spots' implicitly, and the majority of these models use pressure-dependent reaction rates. The development of a simple but physically realistic model to predict desensitisation (double shock) effects within the confines of an existing pressure-based model is described and simulations compared with experimental data with mixed results. The need to invoke a separate desensitisation model for double shocks demonstrates that reaction rates are not substantially dependent on local pressure.

The newly developed continuum, entropy-dependent, CREST model has been implemented and validated in a number of hydrocodes. However, the move to entropy-based reaction rates introduces a number of computational problems not associated with pressure-based models. These problems are described, in particular, an entropy-dependent model over-predicts the rate of energy release in an explosive adjacent an impact surface, and requires a finer mesh than a pressure-dependent model to achieve mesh converged results. The CREST model, fitted only to one-dimensional data of the shock to detonation transition, is shown to be able to accurately simulate two-dimensional detonation propagation data. This gives confidence in the predictive capability of the model.

To account for 'hot-spots' explicitly, a simple model to describe 'hot-spot' initiation has been developed. The simple model is presented where 'hot-spots' are formed as a result of elastic-viscoplastic stresses generated in the solid explosive during pore collapse. Results from the model compare well with corresponding results from direct numerical simulations, and both are consistent with observations and commonly held ideas regarding the shock initiation and sensitivity of heterogeneous solid explosives. The results also indicate that viscoplastic 'hot-spot' models described in the literature are built on an invalid assumption.

Acknowledgements

Contents

List of Tables

List of Figures

Chapter 1

Introductory Chapter

1.1 Introduction

Explosive materials are compact sources of chemical energy that are designed to decompose exceedingly quickly to very hot, high pressure gases. They are able to decompose very rapidly because fuel (*e.g.* carbon or hydrogen) and oxidiser (*e.g.* oxygen or fluorine) are wrapped up together in the chemical structure of the explosive. One example of an explosive compound is HMX (cyclotetramethylene tetranitramine), another is TATB (triamino trinitrobenzene) [1]. Although the explosive compounds such as HMX and TATB can be used in their pure form, the majority of uses for explosives require mechanical properties that the pure materials do not have. In order to change the mechanical properties, the pure explosives are often blended with other (usually) inert materials. The resulting mixtures have good mechanical strength, and the explosives can be easily machined into desired shapes.

Modern day explosives exist in an energetically metastable state, that is an explosive cannot undergo rapid chemical decomposition until sufficient energy has first been added to get the process started. This is usually termed explosive initiation or ignition. For scientists and engineers who use explosives, it is necessary to understand exactly how explosives work. In particular, a very good understanding of how explosives initiate is essential for the development of safer explosives, and to avoid or reduce the chance of inadvertent explosive events which could injure or kill. Various methods for initiation of explosives exist, including heat, electrostatic impulses, friction, shock waves, or any combination of these energy sources. In this work, attention is restricted to the study of the shock initiation mechanism.

The ease with which an explosive can be shock initiated is as known as its sensitivity. To help understand the initiation and sensitivity of explosive materials subjected to shock waves, a variety of experimental tests are routinely conducted. Although the experiments give valuable information on the reaction behaviour and sensitivity of shock initiated explosives, many of the testing methods provide little

insight into the fundamental physical and chemical processes occuring during an initiation event. Coupled with the high costs of experiments and scenarios of interest that may be beyond acceptable costs and safety bounds, this has resulted in increasing demands being placed on the development of computational models of shock initiation to provide both an understanding and predictive capability.

Over the years, a relatively large number of shock initiation models, also known as reactive burn models, have been developed. Numerical models of shock initiation need to be coupled to large computer programs called hydrocodes so that the dynamics of shock wave initiation in explosives can be computed. Hydrocodes are programs that use a number of different solution techniques to solve a wide variety of non-linear problems in solid, fluid, and gas dynamics. Hydrocode calculations usually require a good number of meshes through an explosive's reaction zone for accurate phenomenon resolution. Since reaction zone widths in explosives are very small, typically $\sim$0.1mm for HMX-based explosives, and $\sim$1.0mm for TATB-based explosives, then reactive burn models are very mesh and time intensive. As a result shock initiation models have tended to be relatively simple and this can limit their predictive capability.

Researchers are now making use of recent advances and developments in both hydrocodes and computers. The appearance of powerful Teraflop and Picoflop computers, coupled with modern numerical methods such as adaptive mesh refinement techniques in hydrocodes, gives an opportunity to develop improved shock initiation models for explosives where calculations allow good mesh resolution of the reaction zone. However, any new reactive burn model will only be as good as the quality and quantity of the experimental data against which it has been validated. Therefore, accurate modelling of explosive shock initiation and growth of reaction requires appropriate and accurate experimental data. In developing new reactive burn models, consideration also needs to be given to the requirement that it must be relatively straightforward to implement any model in a hydrocode. In this thesis, a number of aspects of the mathematical and numerical modelling of shock initiation of explosives is considered.

1.2   Background On Explosive Shock Initiation

There has been a significant quantity of experimental research, performed over the past several decades, aimed at understanding the initiation and growth of reaction behaviour in explosive materials subjected to shock waves. When discussing shock initiation of explosives, the process is usually categorised in terms of the physical nature of the explosive as either homogeneous or heterogeneous. The explosive materials themselves are commonly referred to as homogeneous or heterogeneous explosives. Homogeneous explosives are typically liquids or single crystals in which there are a minimal number of physical imperfections (*e.g.* bubbles

or voids). Heterogeneous explosives are generally all other types; heterogeneous means a material that contains any kind of imperfection (*e.g.* void or gas cavities, cracks, solid inclusions *etc*). Homogeneous and heterogeneous explosives exhibit different shock initiation properties, as described in the classic experimental studies of Campbell *et al.* [2] [3]. Homogeneous initiation occurs by a thermal explosion which produces waves that develop into a reactive wave behind the initial shock [2]. Heterogeneous initiation occurs because the shock wave interacts with the material heterogeneities producing so-called 'hot-spots' that start the chemical reaction in the material [3]. In this work, attention is restricted to shock wave initiation of heterogeneous explosives.

The physical structure of a heterogeneous explosive usually consists of pores (void or gas cavities), cracks, and binder material, in addition to the explosive crystals or grains, and distinct boundaries exist between the various constituents. Figure 1.1 is a micrograph showing the physical structure of a typical hetergeneous solid explosive, while Figure 1.2 gives an illustration of a small sample from the micrograph. The irreguarly shaped explosive crystals or grains are clearly visible, and there is mixture of coarse and fine grains to achieve a high packing density. The grains contain imperfections such as cracks. A binder is used to hold the crystals together and to make the explosive safe to handle by stopping the crystals rubbing together. The binder material also helps to improve the mechanical properties of the explosive, meaning that it can be easily manufactured into desired shapes. On the micrograph a number of 'dark holes' are also visible. It is unsure what these are; they could be pores, or a by-product of sample preparation *e.g.* polishing. Note the scale of the explosive grains and imperfections; the largest components of the mix are the grains, and the largest explosive grain size is $\sim$150 μm.

The key to understanding initiation in heterogeneous explosives was first discussed in detail by Bowden and Yoffe [4] whom, to help explain the initiation process, introduced the concept of the 'hot-spot', and who considered that all ignitions were thermal in origin. 'Hot-spots' are small localised regions of elevated temperature that are produced by the interaction of a shock wave with the inhomogeneities in a heterogeneous explosive which create sufficiently high tempertaures to lead to reaction. The necessity of the 'hot-spot' concept arises because, under shock compression, the bulk (homogeneous) temperature is too low to initiate reaction. Local chemical decompostion occurs at the 'hot-spot' sites if sufficient thermal energy is generated and retained there. If sufficient thermal energy is produced, then the 'hot-spots' can burn outwards into the bulk of the (cooler) explosive leading to a possible growth of reaction.

Based on the experimental evidence, the shock initiation process in heterogeneous explosives is usually described as having two separate phases: *(i)* an ignition phase where 'hot-spots' are created due to shock compression, and the subsequent chemical decomposition of the explosive in these localised heated regions, and *(ii)* a growth phase where the build-up of chemical reaction occurs as the 'hot-spots'

grow and coalesce to consume the remainder of the explosive material. Figure 1.3 illustrates the process of 'hot-spot' initiation by a shock wave leading to growth of reaction. The figure shows a snapshot in time when the material behind the leading shock is at various stages of decomposition. Here, growth of reaction from the local dynamically overheated 'hot-spot' regions is shown. However, ignition of 'hot-spots' does not necessarily result in a build-up of reaction. 'Hot-spots' are cooled by the conduction of heat from the 'hot-spots' into the cooler material surrounding them so there is a competition between 'hot-spot' induced reaction and cooling. If the 'hot-spot' is hot enough that the material begins to react before heat conduction cools it too much, the surrounding material can initiate and the reaction can then grow.

When a violent, explosive event occurs we often hear the term detonation mentioned. Detonation is synonymous with shock initiation. If the input shock to a heterogeneous explosive is sufficiently large and sustained, the shock can grow to detonation and this process is usually called a shock-to-detonation transition. In this process the 'hot-spots', created from the interaction of the input shock with the heterogeneities, decompose and add their energy to the flow. This strengthens the leading shock so that when it interacts with additional heterogeneities, higher temperature 'hot-spots' are formed and more of the explosive is decomposed. The shock wave grows stronger and stronger, releasing more and more energy, until it becomes stong enough to produce self-sustaining propagating detonation. A popular means of assessing the shock sensitivity of heterogeneous explosives is by studying the shock-to-detonation transition.

1.3 Shock Initiation Mechanisms and Related Experimental Studies

The importance of 'hot-spots' in describing initiation and growth of reaction in heterogeneous explosives is firmly established. In contrast to the general acceptance of the 'hot-spot' concept, the exact origin of the 'hot-spots' is not well understood. This is due to the very nature of their properties; small dimension, short duration, and high temperature. As a result, it is difficult to obtain direct experimental evidence on the fundamental mechanisms involved in their creation. Bowden and Yoffe [4] attempted to quantify 'hot-spot' temperatures, duration, and sizes. They presented evidence that 'hot-spots' need to have dimensions of typically 0.1 - 10 μm, durations of 10^{-5} - 10^{-3} s, and temperatures greater than 700 K. Despite the fact that little is known or has been directly observed regarding the evolution of 'hot-spots' behind a shock wave, a large number of mechanisms for 'hot-spot' formation have been proposed as summarised by Field [5]. In his paper Field lists ten possible 'hot-spot' mechanisms:

1. Adiabatic compression of trapped gas spaces.

2. Other mechanisms involving cavity collapse such as viscous or plastic heating of the surrounding matrix material or, for very high shock collapse pressures, hydrodynamic shock focusing.

3. Friction between sliding or impacting surfaces, or between explosive crystals and/or grit particles in an explosive.

4. Localised adiabatic shear of the material during mechanical failure.

5. Viscous heating of material rapidly extruded between impacting surfaces.

6. Heating at crack tips.

7. Heating at dislocation pile-ups.

8. Spark discharge.

9. Triboluminescent discharge.

10. Decomposition, followed by Joule heating of metallic filaments.

The proposed 'hot-spot' mechanisms are based on a mixture of experimental observations and numerical modelling work, and there is currently no universal agreement as to the mechanism(s) by which energy localisation occurs to produce 'hot-spots'.

It is well known experimentally that the introduction of pores (voids or gas cavities) in an explosive material causes increased sensitivity to shock initiation. Bowden and Yoffe [4] were among the first researchers to show that the shock sensitivity of explosives could be greatly increased by the presence of gas bubbles, and who attributed the formation of 'hot-spots' to adiabatic compressive heating of the gas. A purely hydrodynamic mechanism to explain 'hot-spot' formation as a result of shock wave interactions with density discontinuities was proposed by Mader [6] [7]. These interactions produce hydrodynamic heating due to void collapse, jetting, and shock collisions. 'Hot-spots' can also be created by the strains invoked in the solid explosive material surrounding the collapsing pores either via inviscid plastic work [8] or viscoplastic work [9]. The modelling studies of Frey [9] showed that heating due to viscoplastic work in the vicinity of collapsing cavities can supply significant heating for ignition to occur within the timescales for shock initiation.

In heterogeneous solid explosives, pores are usually present as part of the manufacturing process, and all heterogeneous explosives have some porosity. Unfortunately, the majority of explosive experiments record only the quantity of pores in terms of an overall percentage extracted by comparing the sample density with the theoretical maximum density (TMD) expected for the particular composition

(TMD is the weighted average of the densities of the constituent parts). Pore size distributions are given only a passing nod by assuming pore size and particle size are related, and the position of the pores is generally ignored. Experimental studies which only record the bulk porosity do, however, show a strong relationship between this porosity and shock sensitivity, with sensitivity increasing for increasing porosity (decreasing density), as observed in the classical studies of Campbell *et al.* [3] and Gittings [10]. More recent work has shown that void content, rather than binder or binder amount, appears to be the dominating factor in shock initiation of pressed granular explosives [11]. For the above reasons, many proposed 'hot-spot' mechanisms are based on shock induced pore collapse.

As well as the pore collapse mechanism, shear banding or adiabatic shear has also been suggested as a possible source of 'hot-spot' formation in shock initiation of heterogeneous solid explosives. Plastic deformation in a solid is an efficient way to convert mechanical energy to thermal energy and, in most crystalline solids, plastic flow occurs inhomogeneously along crystallographic slip planes, called shear bands. Significant localised temperature rises, leading to 'hot-spot' formation, can occur due to this deformation as discussed by Afanasev and Bobolev [12], and Winter and Field [13]. By analysing recovered damaged samples, Howe *et al.* [14] observed shear zones in heavily confined explosive targets subjected to shock impact. Since there was little or no decomposition in their experiments on TNT and Composition-B, it was unclear whether the observed shear damage would have contributed to the initiation process. Using high speed photography and heat sensitive film techniques, Field *et al.* [15] [16] have observed shear driven plastic deformation and associated ignition in PBX's and PETN crystals in drop-weight impact tests. Further experimental evidence on initiation resulting from shear induced plastic flow has recently been provided by Plaksin *et al.* [17] using their high resolution optical probe technique. In addition to the experimental observations, Frey [18] attempted to calculate the temperature rise in shear bands. In TNT explosive, 'hot-spot' temperatures in excess of 1000 K in times $<1\mu$s, and where the shear band (heated region) is $\sim1\mu$m wide were calculated. These conditions are sufficient for ignition to occur in TNT explosive charges.

A dislocation description of localised shear deformation has been developed by Coffey and Armstrong [19] [20] to describe initiation in crystalline explosives by shock or impact. Although they showed that dislocation pile-ups can produce significant localised heating, Field [5] questioned whether such 'hot-spots' reach the critical parameters to cause ignition during the impact or shock loading of explosives. Experiments performed by Mohan *et al.* [21], in which single crystals of RDX and PETN were subjected to particle impact, showed evidence of dislocation pile-up, however, ignition did not take place.

Frictional heating between sliding explosive grains and/or grit particles is another possible source of 'hot-spot' formation as first described by Bowden and co-workers, and whose work is summarised in [4]. To study initiation by friction,

Chaudhri [22] devised an experiment in which a truncated conical striker penetrates a column of the test explosive. The striker picks up a layer of adhering crystals as it enters and drags them along into the compact, causing frictional heating between the adhered particles and the other explosive crystals. In Chaudhri's experiments, it was found that the temperature rise in a compact of lead azotetrazole due to friction during the penetration was sufficient to cause ignition. Chidester *et al.* [23] described experiments to examine the role of frictional work on explosive initiation. In flat plate impact experiments on the HMX-based explosive LX-10, the conditions of impact (0.3 - 1.0 GPa) were less than that required for direct shock initiation but still resulted in violent events. The role of friction in the initiation of explosives has also been dicussed by Frey [18], who formulated a model to describe the temperature rise which can occur at sliding interfaces in an explosive.

The fracture of explosive crystals is also considered as another possible 'hot-spot' mechanism leading to explosive initiation [24]. Using high speed photographic techniques, Chaudhri [22] examined initiation by fracture on single crystals of silver azide, lead azide, and PETN. These studies showed that fast fractures (travelling at several hundred metres per second) were unable to produce the initiation of a fast reaction in the explosive samples. However, an increase in explosive sensitivity to shock loading was observed by Swallowe and Field [25] by the addition of polymers that fail catastrophically by fracture or localised shear.

Direct experimental evidence of 'hot-spots' in shock compressed explosives is very scarce. Eden *et al.* [26] saw some evidence of reacting 'hot-spots' for weak shocks into a heterogeneous explosive. Using high-speed photographic techniques, they observed small areas of local darkening in the explosive material behind a shock of sufficient strength. These areas did not grow (at a sufficient rate) nor multiply in time at a given location in the explosive, but as the pressure increased, more and larger areas were created. These were deduced to be areas of localised reaction in the explosive, or 'hot-spots', which failed to propagate. Bourne and Field [27] have studied the collapse of 'large' gas cavities (> 1 mm in diameter) within a reactive material as the result of the passage of relatively high amplitude (< 3.5 GPa) shocks. They concluded that the two main causes for ignition are hydrodynamic (compressive) heating in the region impacted by the jet, and adiabatic heating of the trapped gas. They estimated that temperatures in excess of 1000 K were achieved in the adiabatically compressed gas. On a similar theme, the experimental study of cavity collapse leading to explosive ignition has been discussed in a number of other papers *e.g.* [28] [29].

Experiments such as those of Bourne and Field [27] provide useful insight into viable mechanisms for 'hot-spot' formation, however the typical size of defects in heterogeneous explosives are much less than 1 mm (usually μm size). Observations of the elementary 'hot-spot' processes occuring around microscopic defects in shocked heterogeneous explosives, within very short (order-μs) timescales, presents obvious great difficulties and is beyond current experimental capabilities. Areas of

uncertainty are therefore: (i) the nature and size of 'hot-spots' formed by shock compression of the explosive material, (ii) the statistical nature of the 'hot-spot' distribution, (iii) cooling effects due to heat conduction, and (iv) the description of the evolution of the reaction front from the 'hot-spot' sites.

Although experimental studies of shock initiation typically have not provided direct information on the mechanisms for 'hot-spot' formation and subsequent chemical energy release, experimental observations have however shown that explosive initiation is strongly dependent on the explosive microstructure (porosity, grain size, crystal orientation *etc*), initial temperature, and the applied shock profile. The experimental studies conducted on shock initiation of heterogeneous solid explosives typically provide data on the macroscopic or bulk response of the explosive.

Early experimental studies were restricted to characterising explosive shock initiation by the distance (or time) required for a sustained input shock to achieve detonation, usually termed the run-distance to detonation. Run-distance to detonation data as a function of input pressure was obtained from Wedge Test experiments using optical techniques [3] [30]. In a Wedge Test the explosive sample is subjected to a sustained planar shock of a prescribed pressure. As the reaction proceeds, the shock velocity in the sample increases until, very late in the run to detonation process, the shock velocity accelerates rapidly to reach detonation velocity. For a given explosive, the tests are performed at various input pressures. The derived shock initiation data is then presented in the form of Pop-Plots [31] which express the relationship between the input shock pressure and the run-distance to detonation as measured from the input boundary. However, such experiments give no information on the growth of reaction in the body of explosive before detonation is attained.

For short duration shock loading, Walker and Wasley [32] introduced the concept of a critical imparted energy, related to the initial shock amplitude and duration, which is constant for a given explosive. If the shock transmitted into the explosive exceeds this critical value, an initiation is triggered which leads to detonation provided there is sufficient explosive present. The boundary between the go and no-go situations corresponds to a point on the initiation threshold curve. Just above the threshold curve, the shock grows to detonation despite the following rarefaction, but the run to detonation is extended compared with a sustained shock of the same initial shock strength. Just below the threshold curve, the shock attenuates and reaction eventually dies out. A similar intiation criterion for short pulses has also been developed by James [33]. The type of initiation threshold experiments described in [32] and [33] also give no information on the reaction history in the shocked material.

More recently, the development of in-material gauging techniques has enabled the shock initiation response of explosives to be characterised in greater detail [34] [35]. Using embedded gauges, simple one-dimensional gas-gun experiments, where projectiles are fired at explosive targets to deliver well defined shocks into the samples, are now routinely performed to provide reaction history data on explosives of

interest. Wackerle *et al.* [34] described the use of embedded manganin pressure gauges to provide information on reaction inside samples of the HMX-based explosive PBX9404. On a similar theme, the electromagnetic gauging technique of Vorthman *et al.* was first described in [35]. Since this time their gauging technique has been used extensively to provide high quality data from inside shocked, reacting explosives from gas-gun experiments [36] [37].

The experimental set-up for a gas-gun shot diagnosed using electromagnetic particle velocity gauges is illustrated in Figure 1.4. When the impactor strikes the explosive sample, a well defined planar shock is generated which starts the initiation process. The particle velocity gauges detail the growth of the bulk reaction as a function of time at different (Lagrangian) particle positions in the explosive sample. Typical of data obtained from the experiments, Figure 1.5 shows the particle velocity gauge data for a 5.2GPa sustained shock into the HMX-based explosive PBX9501 [36]. Here, the gauges are located at approximately 0.5mm intervals in the explosive sample. The first gauge is located on the impact surface, and records the input shock to the target. It can be seen that the wave is flat-topped early on, but after $\sim 0.5\mu$s, the particle velocity at this position begins to gradually decrease, indicating reaction is occuring in the body of the explosive and decelerating the impact surface. The other gauge profiles show a small increase in amplitude at the shock front, and a large following reactive hump that builds with depth. If the impact pressure is high enough, as in this case, then the following reactive hump eventually catches up with the shock front and detonation occurs very shortly thereafter. If the target material was inert, then the sustained input wave would propagate unchanged through the sample. Thus, the build-up in particle velocity is due to reaction inside the explosive, and stronger reaction is produced at greater depths as the wave builds towards detonation. This figure shows an example of the shock to detonation transition in an explosive where, in this case, detonation occurs at a run-distance of ~ 5mm into the explosive sample. These features, a small amount of growth in the shock front and a large amplitude following wave, have been seen in the shock initiation of a range of heterogeneous explosives *e.g.* [38]. This type of data has proved invaluable for: (i) understanding the processes involved in shock initiation of heterogeneous solid explosives, and (ii) calibrating reaction rate models.

Recently, a suite of gas-gun experiments diagnosed with electromagnetic particle velocity gauges have been fired to examine the shock initiation response of the HMX-based explosive EDC37 [38]. The response of the explosive to sustained single shocks, thin pulse shocks, and double shocks was studied. In the case of the double shock compression of EDC37, the initiation and run-distance to detonation was significantly modified by preshocking the explosive. This is commonly termed 'shock desensitisation', where a weak precursor wave renders the explosive less sensitive to a following stronger shock, and has been observed in other HMX-based explosives [39]. On a similar theme, 'dead pressing' has been observed in multiple shock compression of the TATB-based explosive LX-17 [40]. In their experiments,

which were diagnosed using embedded pressure gauges, a weak initial shock, which is below the initiation threshold for the explosive, is reflected from a rigid boundary. The initial shock wave removed the 'hot-spots' sites available to the reflected wave, such that it simply propagated as an inert wave and did not transition to detonation as would have been expected at the pressure of the reflected wave alone.

Many experimental studies have also examined the effects of varying the physical properties of the explosive material, and initial temperature. Factors that have been shown to affect the shock initiation and sensitvity of heterogeneous solid explosives are: initial density (initial porosity), crystal or grain size distribution, crystal orientation, and initial temperature of the explosive. The early experiments of Campbell *et al.* [3] showed that the time required for a given initial shock to reach detonation increased with increasing density. The effects of density on growth to detonation were examined in greater detail for the explosive PETN by Stripe *et al.* [41]. Low density samples were found to be more shock sensitive than high density samples. Gustavsen *et al.* [36] observed significant differences in Pop-Plot data for the HMX-based explosive PBX9501 with initial density. At the same input pressures, the run-distances to detonation decreased with decreasing density (increasing porosity) showing that lower density material is more sensitive to initiation.

Experimental work on crystal or grain size effects in heterogeneous explosives is summarised by Moulard [42] [43] and Chick *et al.* [44]. The general findings are that in terms of the shock to detonation transition (Pop-Plots), small grains inhibit ignition at low pressures while larger particles are better at promoting ignition. At higher pressures, such as in propagating detonation, it is a different story. Here, larger grains are less sensitive than smaller grains. Moulard postulated that at high pressures the ignition phase takes a negligible time, but that growth was easier for fine material due to the larger surface area and 'hot-spot' density. In contrast at lower pressures the ignition takes a significant amount of time but larger 'hot-spots' are more efficient and set the growth going sooner. In summarising detonation experiments on the TATB-based explosive PBX9502, Hill *et al.* [45] concluded that finer grained material was more sensitive; keeping the density constant, a decrease in particle size resulted in an increase in the detonation velocity. There was also a corresponding correlation between grain size and critical diameter. However, in relatively low pressure experiments examining the shock to detonation transition in PBX9502, Gustavsen *et al.* [46] observed that the particle size distribution has a negligible effect on shock initiation behaviour. Since it is generally believed that particle size distribution influences initiation behaviour by determining the size and number density of 'hot-spots', then these findings are surprising.

The shock sensitivity and detonation behaviour of heterogeneous solid explosives is known to vary with temperature, with sensitivity increasing with initial temperature. There are many examples in the literature, see for example [45] and [47]. Studies of initiation in single crystal explosives, such as HMX, RDX and PETN,

has shown that crystal orientation can affect shock sensitivity [48]. Initiation mechanisms in such single crystals are dislocation pile-up and shear heating.

1.4 Continuum-Based Shock Initiation Models

Complementing the experimental developments and observations, a great deal of effort has been expended over many years in developing shock initiation models, also commonly referred to as reactive burn models, to simulate initiation and growth of reaction behaviour in heterogeneous explosives. Here, the review and discussion of shock initiation models concentrates mainly on those models which have been key developments in the field, and those models which are most widely used.

Based on the degree of sophistication of the models, for example the physical and chemical phenomena they attempt to explicitly take account of in the model description, the review is split into two classes of model: (i) continuum-based models, and (ii) physics-based or mesoscale models. Continuum-based shock initiation models give only a generalised description of the underlying physical and chemical processes involved, and their reaction rate equations are simple algebraic relationships, usually in terms of pressure and/or temperature, which model the 'hot-spot' and grain burning contributions implicitly. Physics-based or mesoscale models attempt to explicity take account of the fundamental processes involved in shock initiation, *e.g.* formation and ignition of 'hot-spots', usually by taking one particular 'hot-spot' mechanism and modelling its behaviour in detail. The continuum-based models are described below, while the physics-based or mesoscale models are described in the next section.

Continuum-based reactive burn models first appeared in the late 1970's and early 1980's, and well known models of this era include the Forest-Fire model [6], the Lee and Tarver Ignition and Growth model [49], and the Johnson-Tang-Forest (JTF) model [50]. Due to the computing facilities available at the time, these models had to be relatively simple. Forest Fire [6] is a reaction rate model that predicts the response of explosives subjected to sustained single shocks, where the rate of decomposition is expressed as a simple polynomial in pressure limited by a depletion term. The model is purely phenomenological and relates each explosive's reaction rate to Pop-Plot data and the partially reacted Hugoniot. Model calibration is thus obtained by fitting to Pop-Plot data. The Forest-Fire model assumes that the reaction of the explosive takes place across the shock front which is not in accordance with experimental data. In addition, with the reaction rate being solely dependent on local pressure, the model cannot account for the phenomenon of 'shock desensitisation' [51].

The Lee-Tarver Ignition and Growth model [49] gives a generalised description of the underlying physical and chemical processes involved in shock initiation and, based on the experimental evidence, the reaction rate laws in the model are

divided into an ignition phase where 'hot-spots' are created as a result of the shock compression, and one or more growth phases where the build-up of chemical reaction occurs from the ignitied 'hot-spots'. The original version of model divided the initiation process into an ignition phase and a single growth phase [52], while the model was later modified by the addition of an extra growth term to enable short pulse duration shock initiation experiments to be accurately modelled [53]. Since the model is readily available, it has been embedded in many hydrocodes and has been parameterised for many explosives. Hence, the Lee-Tarver model is the most popular reactive burn model in use today.

The Lee-Tarver model has been successful at predicting run-distance to detonation (Pop-Plot) data [49], in-material manganin pressure gauge measurements examining growth of reaction in shock initiated explosives [52], corner turning data [52], short pulse shock initiation data [53], and detonation propagation and failure [54]. However, for a given explosive, there are numerous examples in the literature of reaction rate parameters being continually re-calibrated to fit an ever increasing range of data covering different phenomena, and/or different sets of parameters being used to model different phenomena. For example, different sets of coefficients for the TATB-based explosive PBX9502 have been used to model the shock to detonation transition [55], and corner turning experiments [56]. In addition, in modelling the shock initiation of the TATB-based explosive LX-17 at temperature extremes, different sets of parameters were required to account for the explosive response to initial temperature [47]. Thus, there are question marks over the ability of the Lee-Tarver model to predict a wide range of phenomena with a single set of parameters, or to predict experiments outside its fitting regime. The main deficiency of the Lee-Tarver model, or any pressure-dependent reaction model, is that there is no mechanism to predict explosive behaviour under double shock loading, in particular the phenomena referred to as 'dead pressing' [40] and 'shock desensitisation' [38] [51].

The JTF model [50] attempts to include an improved description of the 'hot-spot' ignition phase in describing the shock initiation of heterogeneous explosives. The model partitions the explosive into 'hot-spots' and the balance, or remainder, of the explosive. Although the authors declare that the model is an explicit 'hot-spot' model, the 'hot-spots' are defined only in a general way: there are sites within the explosive that are susceptible to mechanical simulation and have a higher local temperature than the bulk material. The ignition phase is based on a thermal explosion where the induction time is a function of temperature. Here, the temperature represents an average 'hot-spot' temperature that is dependent on the pressure of the incident shock wave. The growth phase in the model, describing the burn of the balance of the explosive, is represented by a polynomial in pressure that is very similar to the Forest Fire [6] reaction rate. The main advantage of the JTF model is that the ignition process includes temperature as an explicit parameter. In the model, assuming a double shock process, additional heating of the 'hot-spot' (created by

the first shock) due to the second shock is calculated as isentropic compression. Thus, the model has the potential to describe the phenomenon of desensitisation by preshocking. The model has been shown to match sustained shock initiation data and the essential features of shock desensitisation are reproduced by the model [50].

Following Bowden and Yoffe [4], the general consensus is that reaction rates are largely dependent on temperature and not pressure. To account for this, Partom [57] [58] developed a temperature-dependent reactive burn model based on ignition at 'hot-spots' and propagation of burn surfaces. The reaction rate in the model is dependent on the (bulk) temperature of the unreacted explosive, and the model co-efficients are calibrated to Pop-Plot data. For the TATB-based explosive PBX9502, the model is able to reproduce the Pop-Plot, detonation propagation data, and corner turning data [58]. Although based on temperature, the model is not predictive since the reaction rate had to be modified to account for the phenomenon of 'dead pressing' in insensitive high explosives [59].

The 'classical' models discussed above were developed at a time when experimental data on the shock initiation of heterogeneous explosives came mainly from Wedge Test experiments [3] [30]. These experiments give the run-distance and run-time to detonation from single sustained input shocks, leading to the Pop-Plot [31], but give no information on the reaction history behind the shock before detonation is attained. Since this time, advances in diagnostic techniques, in particular the development and use of robust in-material gauges *e.g.* [35], has revealed new data on the growth of reaction inside shocked decomposing explosives [36]. The newly acquired in-material gauge data has lead to new ideas and hypotheses being put forward regarding the shock initiation of heterogeneous solid explosives [60]. These ideas and hypotheses, coupled with the deficiencies of classical shock initiation models, lead to the development of the CREST reactive burn model [61].

The continuum-based CREST model [61] is based on the conclusions of experimental observations. Analysis of high quailty, in-material, particle velocity gauge records shows that, at least to first order, the reaction rate depends on shock strength and not on the local thermodynamic state (*e.g.* pressure and/or temperature) [60]. The best measure for shock strength for use in hydrocodes is a function of entropy of the shocked, non-reacted explosive, and hence the model has an entropy-dependent reaction rate. CREST needs in-material gauge results in order to calibrate the reaction model coefficients, coupled with both an unreacted and a reaction products equation of state in order to calculate explosive behaviour. At present, the model is giving promising results in simulating a wide range of shock initiation phenomena [61] [62].

The criticisms that can be labelled at continuum-based models are summarised below. Although reaction is said to be temperature-driven, the majority of models use pressure-dependent reaction rates. Although some aspects of shock initiation can be adequately described by pressure-dependent reaction rates *e.g.* the Pop-Plot, such reaction rates have proved problematic in trying to match in-material particle

velocity histories behind behind different shock inputs from gas-gun experiments [63]. In addition, as will be shown in Chapter 2 of this thesis, pressure-based models have no mechanism to describe the phenomenon of shock desensitisation [38] [51].

The reaction rate expressions in continuum-based models depend upon the average or bulk conditions in the reacting explosive mixture. Calculation of temperature, the variable of preference for some reaction rate models due to its presence in Arrhenius theory, requires knowledge of the specific heat capacity which is poorly known for most explosives. In any case, it is known that reaction rates in heterogeneous explosives are not controlled by bulk temperature or pressure, but are instead driven by the local 'hot-spot' temperatures. In addition, the reaction rate models usually contain a relatively large number of fitting constants that have to be calibrated against experimental data, and it has become apparent that parameters fitted to a limited set of experimental results have to be adjusted to fit different data and/or model different phenomena.

The majority of the continuum-level models date back to the 1970's and 1980's. Since this time new experimental data, making use of advances in diagnostic techniques, has been obtained, and new ideas and hypotheses on shock initiation have emerged. Analysis of recently acquired in-material particle velocity gauge data from gas-gun experiments has revealed a number of interesting correlations [60]. These findings lead to the development of CREST which is showing promise as a predictive model, as will be shown in Chapter 3 of this thesis. However, continuum-based models do not address the fundamental processes involved in shock initiation. For example, no attempt is made to explicitly model any of the proposed physical mechanisms leading to 'hot-spot' formation in a heterogeneous explosive. Instead they give only a generalised description of the underlying physical and chemical processes involved, and their reaction rate laws are simple mathematical expressions that approximate the 'hot-spot' mechanisms and subsequent growth of reaction behaviour. This could potentially limit their predictive capability.

For continuum-based reactive burn models, a completely new set of experimentally defined parameters will usually be required if an explosive formulation is varied in any way, for example, if the particle size distribution, porosity, or binder material is changed. Since it employs a porosity-dependent unreacted equation of state, CREST is the only continuum-based model that can take account of the effect of porosity on an explosive's response with one set of parameters [62]. However, to predict differences in explosive behaviour due to particle size effects, the reaction rate coefficients in CREST would have to be re-fitted to match experimental data. To predict the effect of changes in explosive morphology on shock initiation and detonation behaviour so-called physics-based or mesoscale models are required.

1.5   Physics-Based Shock Initiation Models

The shock initiation and detonation behaviour of heterogeneous solid explosives can be affected by a number of properties of the explosive, namely crystal or grain size, pore size and porosity (which may not be wholly independent of grain size), binder material, and ambient temperature. Without advances in the modelling the affect of changes in these initial explosive conditions can only be demonstrated by a battery of experiments. However, with recent advances in computing technology *e.g* Teraflop and Picoflop computers, coupled with modern hydrocodes that exploit modern numerical methods *e.g.* adaptive mesh refinement, the opportunity exists to develop improved models of shock initiation behaviour that can address some of the present shortcomings in the modelling. Below, a number of physics-based models, sometimes also called mesoscale models are reviewed, with emphasis placed on describing models that have been implemented in hydrocodes.

Shock initiation models that are more sophisticated and physically realistic than their continuum-based predecessors have recently been developed *e.g.* AMORC [64], the Cook-Haskins CHARM model [65], and the model of Bennett [66]. These models explicitly describe the dynamical formation of 'hot-spots' in an explosive, and their subsequent evolution with time, based on one particular process, that of the collapse of pores in an explosive material. Pores are prime candidates as potential 'hot-spot' sites as numerous experimental studies have shown that increasing porosity can make an explosive material more sensitive to shock initiation *e.g.* [36]. However, pore collapse leading to the formation of 'hot-spots' in an explosive material is treated differently in these models. In the AMORC model [64], 'hot-spots' are created by viscoplastic flow in the vicinity of collapsing voids. In the Cook and Haskins Model [65], 'hot-spots' are formed as a result of the adiabatic compression of gas-filled bubbles, whereas in the Bennett model [66], pore collapse is modelled with a $P - \alpha$ model [67], where massless voids represent the initial pores. All three models assume spherical pores which collapse symmetrically, and include explicit heat transfer between the 'hot-spots' and cooler portions of the material.

The AMORC model [64] effectively consists to two models, developed and calibrated separately; one devoted to initiation of the reaction by the 'hot-spots' based on viscoplastic pore collapse, and the other to the explosive grain burning which is modelled via a pressure-dependent burning law. It is claimed that the model is based on an explicit description of the microstructure of the explosive and has very few fitting parameters. AMORC has been implemented into a one-dimensional hydrocode, and has been successful at modelling pressure histories from in-material manganin pressure gauges in shock to detonation experiments, the effect of initial temperature on sensitivity, and the influence of microstructure on explosive response in terms of pore and grain size in a number of TATB-based compositions [64]. The model is also able to describe the phenomenon of desensitisation by preshocking in HMX, TATB, and HMX/TATB compositions [68].

The Cook-Haskins model [65] is an ignition and growth model for shock initiation of explosives based on temperature-dependent Arrhenius chemical kinetics. In the model, heterogeneous effects are accounted for via a 'hot-spot' ignition model based on gas-filled pore collapse. To enable simulations on problems of interest to be carried out, CHARM has been implemented as a separate equation of state within the DYNA2D hydrocode [69], and the model successfully applied to fragment impact data [65]. To account for the fact that adiabatic compression of gas bubbles may not be the only important mechanism in describing 'hot-spot' formation, the model was subsequently improved to include a cumulative damage approach for 'hot-spots' [70]. This models straining in the collapsing shell of explosive material, specifically to account for 'hot-spot' phenomena occuring as a result of low velocity impacts *e.g.* shear heating, viscoplastic flow *etc*.

The model of Bennett [66] is based on the Void-Inert-Reactive (VIR) model [71], previously applied to condensed-phase reactions in powder mixtures, but modified to deal with heterogeneous explosives. The model uses the energy deposited from collapsing pores in a heterogeneous explosive as a 'hot-spot' ignition source for the material, where the dynamic pore collapse process is described by a P-α model [67]. The model was built into the DYNA2D hydrocode [69], and was able to match particle velocity gauge data on PBX9501 explosive from a single gas-gun experiment of the shock to detonation transition [66].

There also exists a number of explicit 'hot-spot' models based on viscoplastic pore collapse that have been developed and described in the literature [72]-[73]. All these models use the approach of Carroll and Holt [8] for the study of pore collapse effects in explosive material. These models were principally developed as stand-alone models and were not incorporated into hydrocodes. The model of Khasainov [72] has since been implemented into the Autodyn hydrocode [74], and the two-dimensional Eulerian code EDEN [75]. These viscoplastic 'hot-spot' models are discussed in further detail in Chapter 5.

To date, no theory of hot-spots has attempted to cover all of the different 'hot-spot' phenomena, and most models have isolated the pore collapse mechanism, as described above, and have modelled 'hot-spot' ignition from this perspective. Clearly such an approach disregards the details of the other physically realistic 'hot-spot' mechanisms *e.g.* shear banding, friction between grains *etc*, but this is not to deny the physics of such mechanisms. To allow for the fact that 'hot-spots' may be generated as a result of a number of different mechanisms, a number of so-called statistical 'hot-spot' models have been developed [76] [77].

The statistical 'hot-spot' model of Nicholls [76] has been built into the ALE3D hydrocode [78]. Their approach relies on an assumption of the size and number density of 'hot-spots' in shocked compressed material as the starting point for the calculations. Such information could come from the results of large scale mesoscale simulations of an ensemble of the explosive consisting of the pore size distribution,

grain size distribution, binder, and other solid inclusions. These types of simulations have been performed by Baer *et al.* [79] [80]. However, much 'data mining' needs to be performed to extract the relevent 'hot-spot' information required as input to any model. In the model of Hamate *et al.* [77], rather than keeping track of distributed 'hot-spots' as in [76], an aggregated 'hot-spot' concept is used which represents the overall effects of the distributed 'hot-spots'. The model has been implemented into the CASH hydrocode [81] developed at Los Alamos National Laboratory, and is able to reproduce the effect of grain size on Pop-Plot data in RDX-based explosives [77].

1.6   Hydrocodes

To enable the modelling of practical shock initiation problems to be performed, any developed reactive burn or shock initiation model must be incorporated into so-called hydrodynamics codes, usually shortened to hydrocodes. Hydrocodes are large computer programs used to simulate shock hydrodynamics problems [82]. They differ from Computational Fluid Dynamics (CFD) codes in that they must be applicable to solid materials as well as to liquids and gases. Hydrocodes solve the equations governing unsteady material dynamic motion in terms of the conservation of mass, momentum, and energy. In order to obtain a complete solution, in addition to appropriate initial and boundary conditions, it is necessary to define a further relation between the flow variables. This can be found from a material model which relates stress to deformation and internal energy (or temperature). In most cases, the stress may be separated into a uniform hydrostatic pressure and a stress deviator associated with the resistance of the material to shear distortion. Then, the relation between the hydrostatic pressure, the local density (or specific volume) and local specific internal energy (or temperature) is known as the equation of state. Constitutive strength models are used to represent the material resistance to shear distortion. Various forms of equation of state and material strength models are usually included in hydrocodes.

Hydrocode programs use a discretised mesh in one, two, and three dimensions, to model the materials being evaluated. Spatial discretisation can be performed in a Lagrangian, Eulerian, or Arbitrary Lagrangian Eulerian (ALE) setting. To obtain a numerical solution of the governing flow equations, finite difference, finite element, or finite volume techniques are commonly used [83]. In general, as the dimensional degrees of freedom required by the problem increase, so do the computational resources needed to run the problem.

The two main types of hydrocode in common use today are Lagrangian and Eulerian [84]. Lagrangian codes solve the governing flow equations assuming a Lagrangian frame of reference, where the computational mesh moves with the material flow. Eulerian codes solve the governing equations in the Eulerian frame of

reference, the mesh remaining fixed and the material flowing through it. Both methods have strengths and weaknesses and neither is suitable for all applications. In the Lagrangian approach, material interfaces and features of the flow, such as shocks, are well defined. The major disadvantage of Lagrangian codes is that if excessive material movement occurs, the numerical mesh may become highly distorted leading to an inaccurate and inefficient solution. Further, this may lead to a termination of the calculation. In contrast, Eulerian codes can cope with severe distortion since material moves through the mesh, however material interfaces and features of the flow are not tracked as accurately as in a Lagrangian code.

An ALE hydrocode can be considered as an attempt to always run with the optimum mesh, exploiting the advantages of both the Lagrangian and Eulerian methods by using the most appropriate description for different parts of a problem. Although ALE schemes have been in existence for many years [85], most of the methods have ignored the complexities of material interfaces. These methods can be regarded as Simple ALE or SALE schemes as they impose the restriction that the interfaces must remain Lagrangian. This approach may not be adequate for all applications, and recent work has attempted to address some of the deficiencies of the traditional ALE methods [86].

Adaptive mesh refinement (AMR) is a technique allowing the level of mesh resolution to vary significantly across the computational domain and to dynamically adjust to the evolving solution by placing meshes in regions of interest, for example, where the solution is changing rapidly [87]. The aim is to focus high resolution only where it is needed and, thus, obtain a level of accuracy comparable with existing (non-AMR) hydrocodes but with less demand on computational resources. This can be applied to Lagrangian, Eulerian, or even ALE codes. Reactive burn modelling is ideally suited to AMR hydrocodes. Accurate resolution of the reaction zone in a block of shock initiated explosive requires many zones/mm. When it is considered that, for many practical problems of interest, the dimensions of the explosive region can be many centimetres then calculations of this type can be very challenging on non-AMR codes; having to mesh the entire computational domain with uniformly fine zones is inefficient and the computational costs could be impractical.

The type of hydrocode to use for practical problems will usually be chosen on a problem by problem basis. Thus, where possible, any reactive burn model should be implemented in a range of different types of hydrocodes. In developing new models, consideration should also be given to the ease with which the model(s) can be implemented into the different types of codes. For example, model implementation in Lagrangian and Eulerian codes will be more straightforward than in ALE codes.

1.7 Thesis Outline

This thesis describes a number of aspects of the mathematical and numerical modelling of explosive shock initiation. In Chapter 2, the widely popular, continuum-based, pressure-dependent Lee-Tarver reactive burn model is considered. For evaluation purposes, the model is implemented and validated in a one-dimensional hydrocode. A critique of the model is given, including discussions regarding the predictive capability and limitations of the model. The main deficiency of pressure-dependent models is that they contain no mechanism to predict the phenomenon of shock desensitisation. Consideration is given as to how to model the effects of shock desensitisation within the confines of the Lee-Tarver model, and a simple but physically realistic desensitisation model is developed and described. The model is then applied to available experimental data to examine its suitability.

Chapter 3 concentrates on a number of aspects of the continuum-based CREST reactive burn model. For completeness, the background to CREST and an overview of the model is given. The implementation of the model in a one-dimensional, and a number of two-dimensional hydrocodes is then described in detail, and the various implementations validated. During the hydrocode implementation and use of CREST, it was found that the move to an entropy-dependent reaction rate introduces a number of computational problems not associated with pressure-based models. These problems are described, and where possible solutions to the problems found or identified. The predictive capability of the CREST model is then more rigorously examined by application of the model to detonation propagation data.

The application of a least squares solution approach for determining run-distances and run-times to detonation, using a method devised at Los Alamos National Laboratory (LANL) for fitting shock trajectory data, is described in Chapter 4. The least squares solution method is validated against run to detonation distances quoted by LANL for sustained single shocks into an HMX-based explosive. The method is then applied to shock time of arrival data from hydrocode calculations using the CREST model to see how well, or otherwise, CREST fits experimentally derived Pop-Plot data.

Explicit modelling of the formation and initiation of 'hot-spots' is described in Chapter 5, where the mechanism for 'hot-spot' formation is elastic-viscoplastic pore collapse. The chapter is essentially split into two parts. The first part details direct numerical simulation work performed to support the development of a simplified 'hot-spot' initiation model. In the second part, a simple 'hot-spot' initiation model is developed and described. Results from the direct numerical simulations and simple model are presented, and the results obtained are discussed in terms of whether they are consistent with observations, and commonly held ideas, regarding the shock initiation of heterogeneous solid explosives.

The conclusions are given in Chapter 6, along with a discussion of future work.
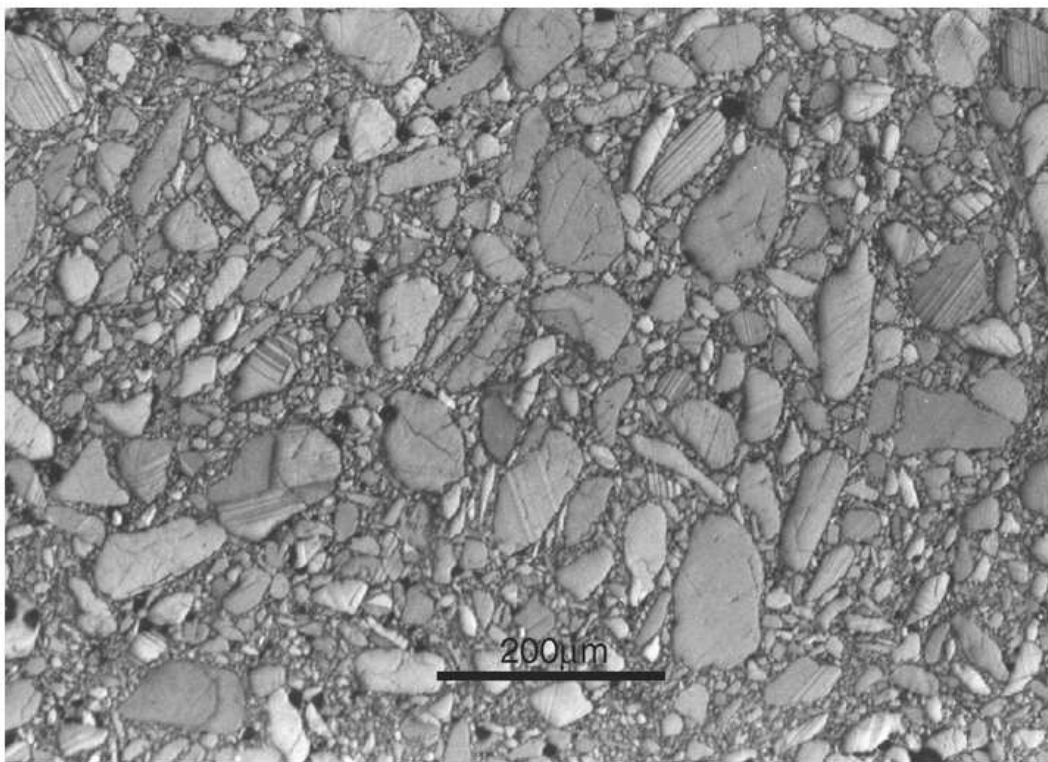
Figure 1.1: Microstructure of a heterogeneous solid explosive.
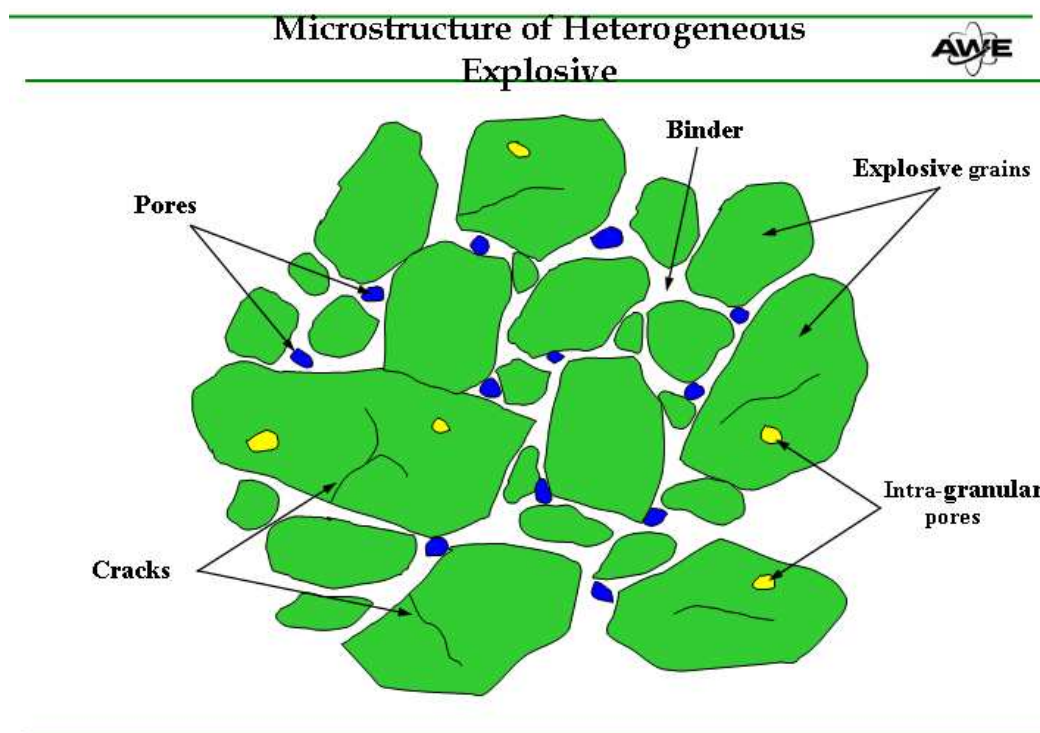
Figure 1.2: Illustration of the microstructure of a heterogeneous solid explosive.
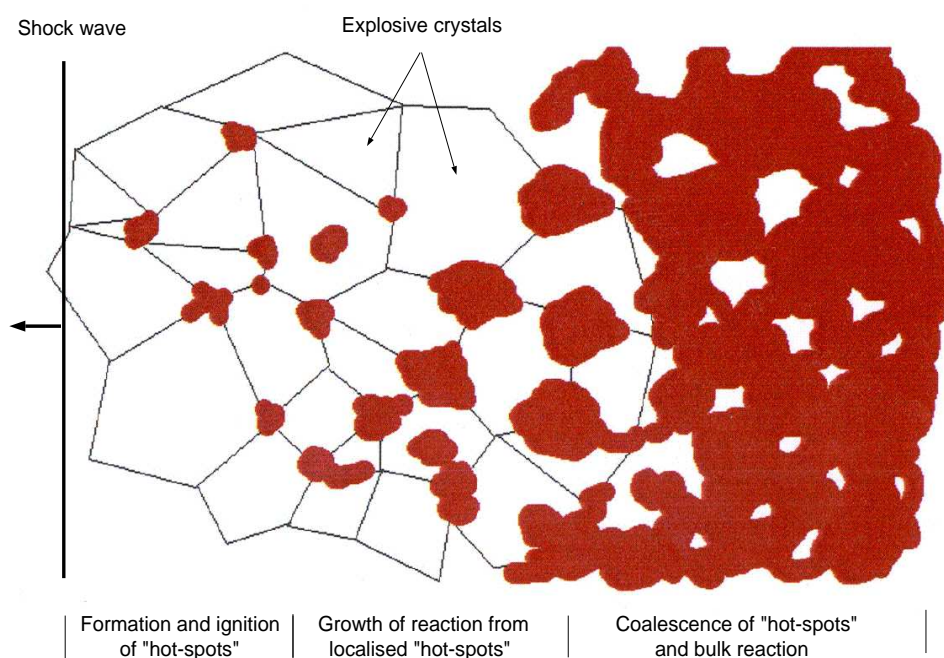
Figure 1.3: Illustration of 'hot-spot' formation and growth of reaction in a heterogeneous solid explosive (the darkened areas represent material that has burned).

PROJECTILE   TARGET

Particle Velocity
Gauges

Lexan Projectile   Impactor   Explosive
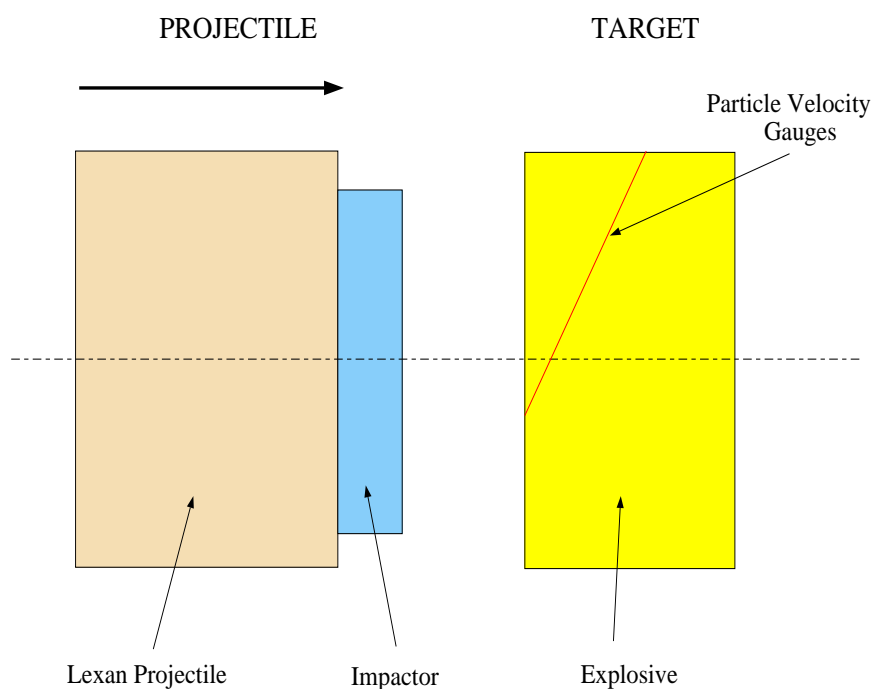
Figure 1.4: Experimental configuration for gas-gun shots.

PBX9501 Gas-Gun Shot 1133
5.2 GPa Sustained Shock Input
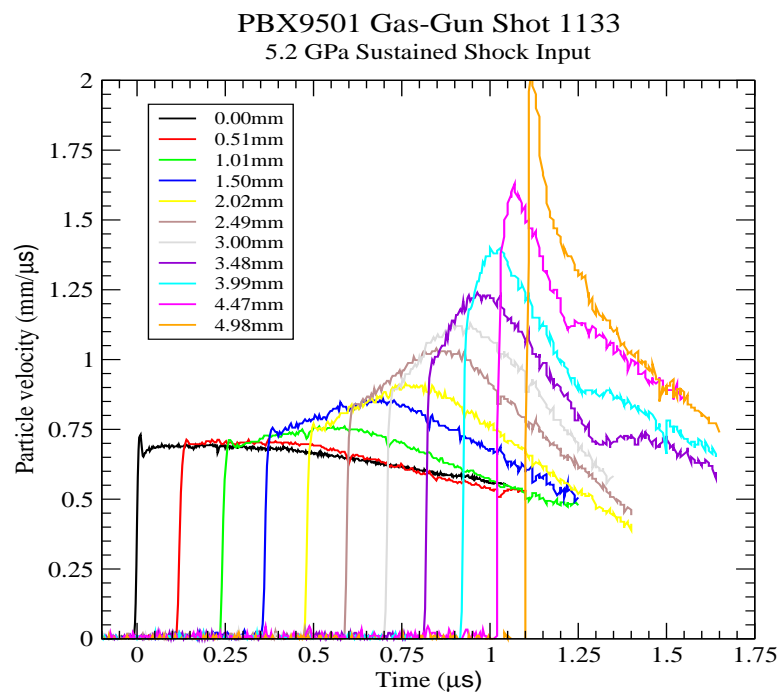
Figure 1.5: Particle velocity gauge data for PBX9501 gas-gun shot 1133.

Chapter 2

Pressure-Dependent Lee-Tarver Reactive Burn Model

2.1 Introduction

The continuum-based Lee-Tarver model for shock initiation of heterogeneous solid explosives was first described in 1980 [49]. The model was developed on the basis, backed by considerable experimental evidence, that one can clearly distinguish two distinct phases during shock initiation, (i) an ignition phase where 'hot-spots' are created due to shock compression, and the subsequent decomposition of the explosive in these localised heated regions, and (ii) a growth phase where the build-up of reaction occurs as the reaction grows outwards from the formed 'hot-spot' sites to consume the bulk of the material. Indeed, the model divides the reaction rate into an ignition term and one or more growth terms, and hence is also known as the Ignition and Growth model.

The ignition and growth concept in the Lee-Tarver model is represented by a reaction rate equation whose terms are algebraic relationships in terms of density and pressure. These terms model the 'hot-spot' and grain burning contributions of shock initiation implicity. Many of the fitting constants in the reaction rate equation have physical meaning, for example related to viscoplastic 'hot-spot' heating during pore collapse, the outward burning of spherical 'hot-spots', and the inward burning of explosive grains. However, the ignition term relates to single shock input, and the growth terms are purely functions of pressure, which has disadvantages that are discussed below.

At the time, the Lee-Tarver model provided a much improved capability for modelling shock initiation problems of interest. Today, the Lee-Tarver model is the most popular reactive burn model for use in hydrocode calculations of shock initiation, as any review of conference papers in the field will testify. The model is widely used because; (i) it is readily available, and hence has been embedded in

24

many hydrocodes, and (ii) it has been applied to a relatively large number of explosives. Initially, the Lee-Tarver model was successful at reproducing Pop-Plot data for single sustained shocks. The Pop-Plot [31], named after one of its originators, represents the run distance to detonation in an explosive as a function of the input shock pressure. However, as time has progressed the limitations of the model have become apparent as new data, making use of advances in diagnostic techniques, has become available, and also as the range of phenomena to which the model has been applied has increased.

The main disadvantage of utilising a pressure-dependent reaction rate in any model is that it has no mechanism to describe complex shock behaviour, for example double shock compression of an explosive. Experimentally, it is well known that the reaction rate behind a second shock travelling through preshocked material is less than that behind a single shock of the same pressure *e.g.* [39] [51]. This phenomenon is commonly referred to as 'shock desensitisation'. It is important to considerations of safety, as many accident scenarios for explosives confined by inert materials involve double or multiple shock compressions of the explosive, and hence needs to be represented in any model. For any reaction rate based on the local pressure, *e.g.* Lee-Tarver, it is necessary to have an additional desensitisation model to account for the double shock observations, otherwise the reaction rate behind the second shock will be too strong, and detonation will occur much earlier.

In this chapter, the theory of the popular Lee-Tarver model is described. The model has been implemented in PERUSE [88], a one-dimensional Lagrangian hydrocode which is used as a test-bed for developing, testing, and comparing different reactive burn models. Results of calculations to validate the implementation of the model are presented. A critique of the Lee-Tarver model is then given, including discussions of the predictive capability and limitations of the model. To illustrate one of the major deficiencies of pressure-dependent reactive burn models, the standard Lee-Tarver model is applied to double shock explosive experiments in which the phenomenon of shock desensitisation has been observed. Consideration is then given as to how to model the effects of shock desensitisation within the confines of the Lee-Tarver model, and a simple but physically realistic desensitisation model is developed and described. This is then applied to a number of double experiments on the HMX-based explosive EDC37 to further examine its suitability to model double shock situations. Finally, the conclusions are given.

2.2   Description of the Basic Model

2.2.1   Preamble

The Lee-Tarver Ignition and Growth model [49] consists of two basic elements: (i) an EOS model for the reacting material, and (ii) a reaction rate model to govern the rate of explosive decomposition. In the model, the reacting material is assumed to be a mixture consisting of two components, unreacted solid explosive and gaseous reaction products, where the unreacted material and reaction products are assumed to be in pressure and temperature equilibrium as the explosive is consumed. Separate Gruneisen-like equations of state in the Jones-Wilkins-Lee (JWL) form [89] are used to describe the unreacted and gaseous phases, and ideal mixing in which the volumes and energies of the components are additive is used.

The reaction rate model is based on an ignition and growth of reaction concept for modelling heterogeneous solid explosives as they transition from unreacted explosive to gaseous reaction products. The rate equation contains a number of terms, which are simple functions of local thermodynamic variables in terms of density and pressure, to phenomenologically represent the ignition and growth processes observed experimentally during the shock initiation of heterogeneous solid explosives.

The various components of the Lee-Tarver model are described below where, in the model equations, the subscripts s and g refer to the unreacted solid explosive and gaseous reaction products respectively.

2.2.2   Equations of State

Separate temperature-dependent JWL equations of state are used for both the unreacted explosive and the reaction products. For the unreacted explosive the pressure is defined by,

$$P_s = R_1 \, exp\left(-\frac{R_5}{\eta_s}\right) + R_2 \, exp\left(-\frac{R_6}{\eta_s}\right) + R_3\eta_s T \quad (R_3 = \omega_s C_{V_s}) \qquad (2.1)$$

and the energy given by,

$$\varepsilon_s = \frac{R_1}{R_5} \, exp\left(-\frac{R_5}{\eta_s}\right) + \frac{R_2}{R_6} \, exp\left(-\frac{R_6}{\eta_s}\right) + C_{V_s} T \qquad (2.2)$$

where η_s is the relative density of the unreacted explosive $\left(= \frac{\rho_s}{\rho_0}\right)$, ρ_s is the density of the solid phase material, ρ_0 is the initial density, C_{V_s} is the specific heat capacity of the unreacted explosive, T is the average temperature of the mixture, and R_1, R_2, R_3, R_5, R_6, and ω_s are constants. R_2 is usually negative, allowing the solid to undergo tension. This equation of state is fitted to available experimental Hugoniot

data, and $P = 0$ when $\eta_s = 1$ at the initial temperature (generally $298K$). Tarver [49] states that this form has some advantages over forms based on a linear shock velocity-particle velocity fit to Hugoniot data. The JWL equation of state can accommodate the measured bulk sound velocity and the experimentally observed curvature of shock velocity-particle velocity relationship at low shock pressures, while still approaching the linear shock velocity-particle velocity data at higher shock pressures.

For the gaseous reaction products, the pressure is defined by,

$$P_g = A\,exp\left(-\frac{XP_1}{\eta_g}\right) + B\,exp\left(-\frac{XP_2}{\eta_g}\right) + G\eta_g T \quad (G = \omega_g C_{V_g}) \qquad (2.3)$$

and the energy given by,

$$\varepsilon_g = \frac{A}{XP_1}\,exp\left(-\frac{XP_1}{\eta_g}\right) + \frac{B}{XP_2}\,exp\left(-\frac{XP_2}{\eta_g}\right) + C_{V_g}T \qquad (2.4)$$

where η_g is the relative density of the gaseous products $\left(= \frac{\rho_g}{\rho_0}\right)$, ρ_g is the density of the gaseous phase material, ρ_0 is the initial density, C_{V_g} is the specific heat capacity of the gaseous products, and A, B, XP_1, XP_2, G, and ω_g are constants. The equation of state parameters for the reaction products are derived primarily from fits to cylinder test expansion data. It is noted that the units of the energies, ε_s and ε_g, are Mb cm^3/ρ_0 g.

2.2.3 Temperature Calculation

Temperature was originally introduced to include the possibility that the reaction rate may be temperature-dependent, and to enforce the thermal equilibrium assumption for the mixture. The total internal energy of the mixture is defined by,

$$\varepsilon = (1-\lambda)\varepsilon_s + \lambda\varepsilon_g + (1-\lambda)Q \qquad (2.5)$$

where ε_s and ε_g are calculated from the unreacted and gaseous products equations of state respectively, λ is the mass fraction of explosive that has reacted, and Q is the chemical energy released from the unreacted material. As $\varepsilon = \varepsilon(\mathcal{V}, T, \lambda)$ then in incremental form,

$$d\varepsilon = \frac{D\varepsilon}{D\mathcal{V}}d\mathcal{V} + \frac{D\varepsilon}{DT}dT + \frac{D\varepsilon}{D\lambda}d\lambda \qquad (2.6)$$

Therefore, the energy equation (2.5) written in incremental form is,

$$d\varepsilon = \left[(1-\lambda) \frac{D\varepsilon_s}{D\mathcal{V}} \bigg|_{T,\lambda} + \lambda \frac{D\varepsilon_g}{D\mathcal{V}} \bigg|_{T,\lambda} \right] d\mathcal{V}$$

$$+ \left[(1-\lambda) \frac{D\varepsilon_s}{DT} \bigg|_{\mathcal{V},\lambda} + \lambda \frac{D\varepsilon_g}{DT} \bigg|_{\mathcal{V},\lambda} \right] dT$$

$$- \left[\varepsilon_s - \varepsilon_g + Q - (1-\lambda) \frac{D\varepsilon_s}{D\lambda} \bigg|_{T,\mathcal{V}} - \lambda \frac{D\varepsilon_g}{D\lambda} \bigg|_{T,\mathcal{V}} \right] d\lambda \qquad (2.7)$$

Rearranging (2.7), the increment in temperature can be written as,

$$C_V dT = d\varepsilon - Jd\mathcal{V} + Hd\lambda \qquad (2.8)$$

where

$$C_V = \frac{D\varepsilon}{DT} \bigg|_{\mathcal{V},\lambda} = (1-\lambda) \frac{D\varepsilon_s}{DT} \bigg|_{\mathcal{V},\lambda} + \lambda \frac{D\varepsilon_g}{DT} \bigg|_{\mathcal{V},\lambda}$$

$$J = \frac{D\varepsilon}{D\mathcal{V}} \bigg|_{T,\lambda} = (1-\lambda) \frac{D\varepsilon_s}{D\mathcal{V}} \bigg|_{T,\lambda} + \lambda \frac{D\varepsilon_g}{D\mathcal{V}} \bigg|_{T,\lambda}$$

$$H = -\frac{D\varepsilon}{D\lambda} \bigg|_{T,\mathcal{V}} = \varepsilon_s - \varepsilon_g + Q - (1-\lambda) \frac{D\varepsilon_s}{D\lambda} \bigg|_{T,\mathcal{V}} - \lambda \frac{D\varepsilon_g}{D\lambda} \bigg|_{T,\mathcal{V}}$$

and T is the average temperature of the mixture. Since, from the first law of thermodynamics,

$$d\varepsilon = -(P+q)d\mathcal{V} \qquad (2.9)$$

equation (2.8) can be re-written as,

$$C_V dT = -(P+J+q)d\mathcal{V} + Hd\lambda \qquad (2.10)$$

The temperature change, dT, is calculated in two steps;

- that due to the hydrodynamics dT_H at constant λ

- that due to the chemical reaction dT_B at constant $\mathcal{V}$

such that $dT = dT_H + dT_B$. The temperature change in the hydrodynamic and reaction phases are respectively given by,

$$C_V dT_H = -(P+J+q)d\mathcal{V} \qquad (2.11)$$

$$C_V dT_B = Hd\lambda \qquad (2.12)$$

Evaluating the change in temperature with respect to time gives,

$$C_V \frac{DT}{Dt} = -(P+J+q)\frac{D\mathcal{V}}{Dt} + H\frac{D\lambda}{Dt} \qquad (2.13)$$

and then,

$$C_V \frac{DT_H}{Dt} = -(P+J+q)\frac{D\mathcal{V}}{Dt} \qquad (2.14)$$

$$C_V \frac{DT_B}{Dt} = H\frac{D\lambda}{Dt} \qquad (2.15)$$

are the temperature changes with respect to time in the hydrodynamic and reaction phases respectively.

2.2.4   EOS Model for Reacting Material

The reacting material is treated as a mixture of two co-existing phases consisting of the unreacted solid explosive (reactants) and the gaseous reaction products. A simple mixture law, in terms of the mass fraction reacted λ, is used to express the relative volume of the mixture as the weighted sum of the relative volumes in the separate phases, that is,

$$\mathcal{V} = (1-\lambda)\mathcal{V}_s + \lambda\mathcal{V}_g \qquad (2.16)$$

The mass fraction of explosive that has reacted, λ, goes from 0 to 1, where $\lambda = 0$ represents no reaction (solid unreacted explosive), and $\lambda = 1$ represents complete reaction (all products). A suitable equation of state is used for each phase, and the pressures of the reactants and products are assumed to be in thermodynamic equilibrium, that is,

$$P(\mathcal{V},T,\lambda) = P_s(\mathcal{V}_s,T) = P_s(\mathcal{V}_s,T) \qquad (2.17)$$

where T is the average temperature of the mixture. The relative volumes of the reactants and products are respectively given by,

$$\mathcal{V}_s = \frac{1}{\eta_s} = \frac{\beta}{(1-\lambda)\eta} \qquad (2.18)$$

$$\mathcal{V}_g = \frac{1}{\eta_g} = \frac{(1-\beta)}{\lambda\eta} \qquad (2.19)$$

where η is the relative density, or compression, of the mixture $\left(= \frac{\rho}{\rho_0}\right)$, ρ_0 is the initial density, η_s and η_g are the relative densities of the reactants and products respectively, and β is the (real) volume fraction occupied by the reactants $\left(= \frac{\mathcal{V}_s}{\mathcal{V}}\right)$.

The volume fraction β goes from 1 down to 0, where $\beta = 1$ represents all reactants, and $\beta = 0$ represents all gaseous products.

In its inner workings, the model works in terms of the relative densities, η_s and η_g, rather than the relative volumes of the explosive in its solid and gaseous states. The pressures in the reactants and products are therefore dependent on the relative densities of the explosive in these two states, and for pressure equilibrium it is required that,

$$P_s(\eta_s, T) - P_g(\eta_g, T) = 0 \qquad (2.20)$$

Pressure equilibrium between the reactants and products is attained by adjustment of the volume fraction β, via an iterative technique, using equations (2.18), (2.19) and (2.20), and is performed at fixed λ and T. Using equations (2.18) and (2.19), (2.16) can be re-written as,

$$\frac{1}{\eta} = (1 - \lambda)\frac{1}{\eta_s} + \lambda\frac{1}{\eta_g} \qquad (2.21)$$

Adjustment of β facilitates changes in both η_s and η_g, however from (2.21) the compression of the mixture, η, remains constant.

Newton's iterative method is used to attain pressure equilibrium between the reactants and products in equation (2.20). If the method does not converge within a given number of iterations, then the slower Bisection method is used. Several derivatives of the equation of state of the mixture are needed, both for evaluation of C_V, J, and H, and for sound speed calculations. All these derivatives are evaluated at pressure equilibrium.

2.2.5 Reaction Rate Model

The reaction rate model is the most important aspect of any reactive burn model since this controls the rate at which the explosive releases its stored chemical energy. The rate equations in the Lee-Tarver model are based on considerable experimental evidence that the ignition of the explosive occurs in localised 'hot-spots', and that the build-up of reaction occurs as the reaction grows outwards from these localised ignited sites. Two different pressure-dependent forms for the reaction rate have been described [52] [53]. These are generically known as the two-term reaction rate model, and the three-term reaction rate model respectively. In both cases, the ignition and build-up sensitivities to shock are separated out.

The original version of Lee-Tarver used a two-term reaction rate equation [52], consisting of an ignition term and a single growth of reaction term,

$$\frac{d\lambda}{dt} = I(1 - \lambda)^b(\eta_s - 1 - a)^x + G_1(1 - \lambda)^c\lambda^d P^y \qquad (2.22)$$

$$\underbrace{\qquad\qquad\qquad}_{\text{ignition}} \qquad \underbrace{\qquad\qquad}_{\text{growth}}$$

where λ is the mass fraction reacted, η_s is the relative density of the shocked unreacted explosive, P is the local pressure, and I, a, b, x, G_1, c, d, and y are constants. The first term (ignition) approximates the formation of 'hot-spots' created during shock compression and the subsequent ignition of these localised heated regions, while the second term (growth) describes the subsequent growth of reaction from the ignited 'hot-spots' as the rest of the explosive is consumed.

The three-term reaction rate model consists of an ignition term and two growth terms [53], and is given by,

$$\frac{d\lambda}{dt} = I(1-\lambda)^b(\eta_s - 1 - a)^x + G_1(1-\lambda)^c\lambda^d P^y + G_2(1-\lambda)^e\lambda^g P^z \qquad (2.23)$$

$$\text{ignition} \qquad\qquad \text{growth} \qquad\qquad \text{completion}$$

where λ, η_s, and P are as defined above, and I, a, b, x, G_1, c, d, y, G_2, e, g, and z are constants. Again, the first term (ignition) represents the formation of 'hot-spots' and their subsequent ignition. The first growth term models the relatively slow growth of reaction in inward and/or outward burning of the isolated 'hot-spots', while the second growth term (completion) represents the rapid completion of the reaction as the reacting 'hot-spots' begin to coalesce. This reaction rate model was shown to be more effective at simulating shock initiation data involving high pressure, short duration shocks [53].

The reaction rate constants are empirically fitted to experimental shock initiation data. In both forms of the reaction rate model, parameter a is a critical compression that is used to inhibit ignition, and hence reaction, until a certain degree of compression has been reached. The threshold condition, $\eta_s \geq 1 + a$, must be satisfied for ignition to occur. Examination of the model parameters for a variety of explosives shows that most of the exponents remain fixed in value for the majority of heterogeneous explosives, these being related to the geometry of 'hot-spots' (spherical voids). The parameters that tend to change between explosives are I and x which control the amount of ignition as a function of shock strength and duration, and G_1, y, G_2, and z which control the rate of growth of reaction.

Constraints on the values of λ are also added to the reaction rate computations so that the various terms in the reaction rate equations can be turned on, or turned off, at various values of λ. For the two-term model (2.22), the ignition rate is set equal to zero when $\lambda \geq \lambda_{igmax}$, and the growth rate set equal to zero when $\lambda \geq \lambda_{G1max}$, whereas for the three-term model (2.23), the constraints on the ignition and growth rates are as per the two-term model, and the completion rate is set equal to zero when $\lambda \leq \lambda_{G2min}$. These allow the relative contributions of the ignition and growth term(s) to be adjusted when fitting to experimental data.

2.3   Implementation in PERUSE

2.3.1   Preamble

The Lee-Tarver Ignition and Growth model has been implemented into the one-dimensional, finite difference, multi-material Lagrangian hydrocode PERUSE [88]. This is a relatively simple research code which is used as a test-bed for developing, testing, and comparing different reactive burn models. In PERUSE, the solution of the governing fluid flow equations is advanced forward in time using an explicit two-step (predictor-corrector) numerical scheme. The predictor-corrector method operates by running for half a timestep with first-order accuracy to calculate a half timestep pressure (the predictor step), and then using this to advance the equations for a full timestep with second-order accuracy (the corrector step). The overall scheme is second order accurate in time and space [90].

2.3.2   Solution Scheme

The steps in the solution method employed for the Lee-Tarver model to advance the solution from t^n to t^{n+1} over a timestep $\Delta t^{n+\frac{1}{2}}$ are described below, where it is assumed that the state of the explosive is that of a reacting mixture. In addition, it assumes that the two-term reaction rate model (2.22) is being used. In the following difference equations the tilde symbol indicates intermediate values during a predictor or corrector step, and the superscript n represents the temporal index. For reasons of clarity, the spatial index has been omitted.

- Predictor Step   (forward Euler half timestep)

  The purpose of this stage is to compute values for the Lee-Tarver variables at the half timestep $(n+\frac{1}{2})$, and proceeds as follows, where $\mathcal{V}^{n+\frac{1}{2}}$, $E^{n+\frac{1}{2}}$, and q^n have been computed by the hydrocode.

  1. Update pressure due to the hydrodynamics (performed at fixed λ).

  Temperature :

  $$\tilde{T}^{n+\frac{1}{2}} = T^n - (P^n + J^n + q^n)\left(\frac{\mathcal{V}^{n+\frac{1}{2}} - \mathcal{V}^n}{C_V{}^n}\right) \qquad (2.24)$$

  Mixture model :

  Initial guess $\tilde{\beta}^{n+\frac{1}{2}}$ is given by,

  $$\tilde{\beta}^{n+\frac{1}{2}} = \frac{(1-\lambda^n)\eta_g{}^n}{(1-\lambda^n)\eta_g{}^n + \lambda^n\eta_s{}^n} \qquad (2.25)$$

Calculate,

$$\tilde{\eta}_s^{n+\frac{1}{2}} = (1 - \lambda^n) \frac{\eta^{n+\frac{1}{2}}}{\tilde{\beta}^{n+\frac{1}{2}}}$$

$$\tilde{P}_s^{n+\frac{1}{2}} = P_s\left(\tilde{\eta}_s^{n+\frac{1}{2}}, \tilde{T}^{n+\frac{1}{2}}\right)$$

$$\tilde{\eta}_g^{n+\frac{1}{2}} = \frac{\lambda^n \eta^{n+\frac{1}{2}}}{\left(1 - \tilde{\beta}^{n+\frac{1}{2}}\right)}$$

$$\tilde{P}_g^{n+\frac{1}{2}} = P_g\left(\tilde{\eta}_g^{n+\frac{1}{2}}, \tilde{T}^{n+\frac{1}{2}}\right)$$

and iterate on $\tilde{\beta}^{n+\frac{1}{2}}$ until $\left|\tilde{P}_s^{n+\frac{1}{2}} - \tilde{P}_g^{n+\frac{1}{2}}\right| < 10^{-6}$.

2. Calculate the explosive burn.

$$\dot{\lambda}^n = I(1 - \lambda^n)^b \left(\tilde{\eta}_s^{n+\frac{1}{2}} - 1 - a\right)^x + G_1 (1 - \lambda^n)^c (\lambda^n)^d \left(\tilde{P}^{n+\frac{1}{2}}\right)^y$$

$$\lambda^{n+\frac{1}{2}} = \lambda^n + \frac{\Delta t^{n+\frac{1}{2}}}{2} \dot{\lambda}^n$$

3. Update pressure due to the explosive burn (this is performed at fixed λ).

Temperature :

$$T^{n+\frac{1}{2}} = \tilde{T}^{n+\frac{1}{2}} + \left(\lambda^{n+\frac{1}{2}} - \lambda^n\right) \frac{\tilde{H}^{n+\frac{1}{2}}}{\tilde{C}_V^{n+\frac{1}{2}}} \tag{2.26}$$

Mixture model :

Initial guess $\beta^{n+\frac{1}{2}}$ is given by,

$$\beta^{n+\frac{1}{2}} = \frac{\left(1 - \lambda^{n+\frac{1}{2}}\right) \tilde{\eta}_g^{n+\frac{1}{2}}}{\left(1 - \lambda^{n+\frac{1}{2}}\right) \tilde{\eta}_g^{n+\frac{1}{2}} + \lambda^{n+\frac{1}{2}} \tilde{\eta}_s^{n+\frac{1}{2}}} \tag{2.27}$$

Calculate,

$$\eta_s^{n+\frac{1}{2}} = \left(1 - \lambda^{n+\frac{1}{2}}\right) \frac{\eta^{n+\frac{1}{2}}}{\beta^{n+\frac{1}{2}}}$$

$$P_s^{n+\frac{1}{2}} = P_s\left(\eta_s^{n+\frac{1}{2}}, T^{n+\frac{1}{2}}\right)$$

$$\eta_g^{n+\frac{1}{2}} = \frac{\lambda^{n+\frac{1}{2}} \eta^{n+\frac{1}{2}}}{\left(1 - \beta^{n+\frac{1}{2}}\right)}$$

$$P_g^{n+\frac{1}{2}} = P_g\left(\eta_g^{n+\frac{1}{2}}, T^{n+\frac{1}{2}}\right)$$

and iterate on $\beta^{n+\frac{1}{2}}$ until $\left|P_s^{n+\frac{1}{2}} - P_g^{n+\frac{1}{2}}\right| < 10^{-6}$.

- Corrector Step

  The CREST variables are now updated to the time level $n + 1$ as follows, where $\mathcal{V}^{n+1}$, E^{n+1}, and q^n have been computed by the hydrocode.

  1. Update pressure due to the hydrodynamics (this is performed at fixed λ).

     Temperature :

     $$\tilde{T}^{n+1} = T^n - \left(P^{n+\frac{1}{2}} + J^{n+\frac{1}{2}} + q^{n+\frac{1}{2}}\right)\left(\frac{\mathcal{V}^{n+1} - \mathcal{V}^n}{C_V^{n+\frac{1}{2}}}\right) \qquad (2.28)$$

     Mixture model :

     Initial guess $\tilde{\beta}^{n+1}$ is given by,

     $$\tilde{\beta}^{n+1} = \frac{\left(1 - \lambda^{n+\frac{1}{2}}\right)\eta_g^{n+\frac{1}{2}}}{\left(1 - \lambda^{n+\frac{1}{2}}\right)\eta_g^{n+\frac{1}{2}} + \lambda^{n+\frac{1}{2}}\eta_s^{n+\frac{1}{2}}} \qquad (2.29)$$

Calculate,

$$\tilde{\eta}_s^{n+1} = \left(1 - \lambda^{n+\frac{1}{2}}\right) \frac{\eta^{n+1}}{\tilde{\beta}^{n+1}}$$

$$\tilde{P}_s^{n+1} = P_s\left(\tilde{\eta}_s^{n+1}, \tilde{T}^{n+1}\right)$$

$$\tilde{\eta}_g^{n+1} = \frac{\lambda^{n+\frac{1}{2}} \eta^{n+1}}{\left(1 - \tilde{\beta}^{n+1}\right)}$$

$$\tilde{P}_g^{n+1} = P_g\left(\tilde{\eta}_g^{n+1}, \tilde{T}^{n+1}\right)$$

and iterate on $\tilde{\beta}^{n+1}$ until $\left|\tilde{P}_s^{n+1} - \tilde{P}_g^{n+1}\right| < 10^{-6}$.

2. Calculate the explosive burn.

$$\dot{\lambda}^{n+\frac{1}{2}} = I\left(1 - \lambda^{n+\frac{1}{2}}\right)^b \left(\tilde{\eta}_s^{n+1} - 1 - a\right)^x + G_1\left(1 - \lambda^{n+\frac{1}{2}}\right)^c \left(\lambda^{n+\frac{1}{2}}\right)^d \left(\tilde{P}^{n+1}\right)^y$$

$$\lambda^{n+1} = \lambda^n + \Delta t^{n+\frac{1}{2}} \dot{\lambda}^{n+\frac{1}{2}}$$

3. Update pressure due to the explosive burn (this is performed at fixed λ).

Temperature :

$$T^{n+1} = \tilde{T}^{n+1} + \left(\lambda^{n+1} - \lambda^n\right) \frac{\tilde{H}^{n+1}}{\tilde{C}_V^{n+1}} \tag{2.30}$$

Mixture model :

Initial guess β^{n+1} is given by,

$$\beta^{n+\frac{1}{2}} = \frac{\left(1 - \lambda^{n+1}\right) \tilde{\eta}_g^{n+1}}{\left(1 - \lambda^{n+1}\right) \tilde{\eta}_g^{n+1} + \lambda^{n+1} \tilde{\eta}_s^{n+1}} \tag{2.31}$$

Calculate,

$$\eta_s^{n+1} = \left(1 - \lambda^{n+1}\right)\frac{\eta^{n+1}}{\beta^{n+1}}$$

$$P_s^{n+1} = P_s\left(\eta_s^{n+1}, T^{n+1}\right)$$

$$\eta_g^{n+1} = \frac{\lambda^{n+1}\,\eta^{n+1}}{(1 - \beta^{n+1})}$$

$$P_g^{n+1} = P_g\left(\eta_g^{n+1}, T^{n+1}\right)$$

and iterate on β^{n+1} until $\left|P_s^{n+1} - P_g^{n+1}\right| < 10^{-6}$.

2.3.3 Validation

To validate the implementation of the Lee-Tarver model in PERUSE, a simple one-dimensional test problem was run that had previously been successfully modelled on the widely available DYNA2D hydrocode [69]. The problem is that of a sustained pressure pulse of 0.025 Mbars into a slab of the HMX-based explosive PBX9404 that is 35mm in length, see Figure 2.1. The sustained pressure pulse is introduced from one side of the computational mesh via a pressure boundary condition in PERUSE. The model developed by Tarver for PBX9404 [53] was used, which is based on the three-term reaction rate equation (2.23). The Lee-Tarver model parameters for PBX9404 are given in Table 2.1. The calculations were performed using a mesh density of 16 zones/mm, a zoning at which the calculations are mesh converged.

The calculated pressure profiles from PERUSE at a series of distances (1, 2, 5, 8, 10, 15, 20, and 25mm) along the charge length from the input face of the applied pressure are shown in Figure 2.2. The corresponding calculated profiles from DYNA2D are shown in Figure 2.3. The pressure profiles from PERUSE are in excellent agreement with the DYNA2D results, thus validating the implementation of the model in PERUSE. In the calculation, the transition to detonation occurs shortly after 15mm of run into the explosive. Once detonation is attained, the calculated detonation wave propagates at the correct steady state velocity of 8.8mm/μs.

It is observed that there are significant numerical oscillations behind the shock front in the early stages of the build-up to detonation in the DYNA2D calcualtion. However, no such numerical noise is present in the PERUSE results. This is probably due to the different forms of artificial viscosity, q, used in the two calculations. PERUSE utilises a scalar monotonic q form [91], whereas in the DYNA2D calculation the so-called 'bulk q' is used [92]. Bulk q is not a particularly accurate form of artificial viscosity, and is known to suffer from post-shock oscilallations [93].

Table 2.1: Lee-Tarver parameters for PBX9404 and EDC37.

Parameter	PBX9404 Three-term Model [53]	PBX9404 Two-term Model [52]	EDC37 Three-Term Model [63]	Units
ρ_0	1.842	1.842	1.842	g/cm^3
ρ_{0s}	1.842	1.842	1.842	g/cm^3
Reaction products equation of state				
A	8.524	8.524	8.524	Mb
B	0.1802	0.1802	0.1802	Mb
G	3.8×10^{-6}	3.8×10^{-6}	3.8×10^{-6}	
XP_1	4.60	4.60	4.60	
XP_2	1.30	1.30	1.30	
C_{V_g}	1.0×10^{-5}	1.0×10^{-5}	1.0×10^{-5}	Mb/ K
ω_g	0.38	0.38	0.38	
Q	0.102	0.102	0.102	Mb
Unreacted equation of state				
R_1	9522.0	9522.0	69.69	Mb
R_2	-0.05944	-0.05944	-1.727	Mb
R_3	2.4656×10^{-5}	2.4656×10^{-5}	2.148789×10^{-5}	
R_5	14.1	14.1	7.8	
R_6	1.41	1.41	3.9	
C_{V_s}	2.7813×10^{-5}	2.7813×10^{-5}	2.505×10^{-5}	Mb/ K
ω_s	0.8867	0.8867	0.8578	
T_0	298.0	298.0	298.0	K
Reaction rate parameters				
I	7.43×10^{11}	44.0	3.0×10^{10}	μs^{-1}
b	0.667	0.222	0.667	
a	0.0	0.0	0.0	
x	20.0	4.0	20.0	
G_1	3.1	850.0	90.0	$Mb^{-y}\mu s^{-1}$
c	0.667	0.222	0.667	
d	0.111	0.667	0.333	
y	1.0	2.0	2.0	
G_2	400.0	0.0	200.0	$Mb^{-z}\mu s^{-1}$
e	0.333	0.0	0.333	
g	1.0	0.0	1.0	
z	2.0	0.0	2.0	
λ_{igmax}	0.3	1.0	0.3	
λ_{G1max}	0.5	1.0	0.5	
λ_{G2min}	0.0	0.0	0.0	

2.4   Critique of the Lee-Tarver Model

At the time of the development of the Lee-Tarver model, data on shock initiation of explosives came mainly from Wedge Test experiments [3] [30]. In a Wedge Test, an explosive sample is subjected to a sustained shock of a prescribed pressure, and at some distance into the sample the shock wave will transition to a detonation wave. The variation of shock velocity with distance travelled down the explosive charge is recorded, from which the run distance to detonation can be determined. For a given explosive these tests are performed at various input pressures, and the derived data is presented in the form of so-called Pop Plots. The Pop Plot [31] expresses the relationship between the input shock pressure and the run distance to detonation as measured from the input boundary. The reaction rate parameters in the Lee-Tarver model were traditionally calibrated to Pop Plot data, and the model has been successful in fitting run to detonation data for a number of explosives.

Wedge Test experiments give the run-distance and run-time to detonation for a given input shock, however they give no information on the reaction history behind the shock wave before detonation is attained. The most important advance in diagnostic techniques in the last 20 years or so has been the introduction of multiple in-material gauges, initially measuring pressure and more recently particle velocity histories behind shock waves in explosives. In particular, the electromagnetic particle velocity gauge of Vorthman [35] has been used in many recent gas-gun studies to provide high quality data on the initiation and growth of reaction inside shocked explosives [36] [37] [38]. This type of data provides a more rigorous test of reactive burn models for shock initiation than simple Pop-Plot data. Although some aspects of explosive shock initiation can be adequately described by pressure-dependent reaction rates, *e.g.* the Pop Plot, such reaction rates have proved problematic in trying to accurately match in-material particle velocity histories behind a range of sustained shock inputs from gas-gun experiments. To illustrate the problem, an example is given below in terms of data obtained on the HMX-based explosive EDC37.

Wedge Test data and in-material gauge data has been aquired on EDC37 explosive. Initial data on the single shock response of EDC37 was obtained from Wedge Test experiments carried out by Rabie and Harry [30]. These experiments yielded run distance to detonation data for a range of sustained input shock pressures. More recently, detailed information on the reaction inside shocked, decomposing EDC37 explosive has been provided by gas-gun experiments fired at Los Alamos National Laboratory using embedded particle velocity gauges [38]. Based on the data obtained, Winter *et al.* [63] developed a Lee-Tarver model for EDC37 explosive.

Taken from [63], the calculated Pop-Plot for EDC37 is compared with experiment in Figure 2.4. It is seen that the Lee-Tarver model for EDC37 explosive gives very good agreement with the experimental run distance to detonation data. Also taken from [63], the experimental particle velocity histories from EDC37 gas-gun

Shot 1160, in which a single sustained shock of 35.2 kbars is input into the EDC37 sample, are compared with the corresponding Lee-Tarver calculated histories in Figure 2.5. The first experimental gauge trace is at the interface, with the other gauges at depths of 6.07, 7.96, and 9.93mm respectively into the explosive from the input boundary. Figure 2.5 illustrates the differences in shape between the experimental and calculated particle velocity profiles. The gauges in the body of the explosive show that the experimental reaction histories are 'convex'-like, whereas the calculated particle velocity histories are 'concave'-like. Although the calculation fails to accurately represent the shape of the reactive hump behind the shock at the gauge locations, it does however obtain a good match to the shock time of arrival at the same positions.

Overall, the interesting property of the calculations is that the Lee-Tarver model for EDC37 reproduces the Pop-plot (run distance to detonation) more or less correctly, but it does not reproduce the shape of the particle velocity profiles. In the calculation of EDC37 Shot 1160, it is observed that the reaction behind the shock is initially under predicted, but then there is rapid growth of reaction up to the peak in particle velocity. These two calculational effects appear to cancel each other out such that the shock velocity is correctly modelled. In other words, it appears to be a case of two wrongs making a right!

The calculated particle velocity profiles are more informative characteristics of the model quality than simple Pop-Plot data. The Lee-Tarver model fit to the particle velocity data from this single experiment (Shot 1160) could be improved, however, the difficulty comes in modelling the profiles from a range of single shock experiments at different input pressures with the same parameter set. Many attempts have been made to optimise the Lee-Tarver reaction rate parameters to fit EDC37 particle velocity histories over a range of applied shock pressures. Trying to find a (unique) set of parameters that would fit run distance data, arrival times, and particle velocity histories for a range of experiments has not proved possible. In particular, it has proved difficult to accurately represent the shape of the reactive hump behind the shock at the gauge positions. These observations are typical of Lee-Tarver calculated profiles obtained from simulations of embedded gauge experiments. The difficulty in accurately representing the shape of the data obtained from the embedded gauges probably lies in the mathematical form chosen for the reaction rate equation(s) in the model.

From a review of the literature, the Lee-Tarver model has been 'successful' at reproducing a range of explosive data including embedded gauge experiments, run distance to detonation data, detonation velocity as a function of diameter including failure diameter, and corner turning data. However, reaction rate parameters have been adjusted widely in an attempt to fit an ever increasing range of data covering different phenomena, and hence have tended to lose their physical meaning. Thus, it appears that there are now no guidelines as to the range of values that the parameters can take. Additionally, there are examples of different sets of parameters

for a given explosive being used to model different phenomena. For example, a Lee-Tarver model was developed for TATB-based explosive PBX9502 based on the shock initiation embedded gauge experiments of Gustavsen *et al.* [55]. More recently, modelling of detonation wave propagation data and 'dead zones' from corner turning experiments on PBX9502 has been described [56]. The Lee-Tarver parameter set used for modelling detonation propagation in PBX9502 explosive is different to that described for modelling the shock initiation of PBX9502. Therefore, it would appear that the predictive capability of the model is low, and its ability to predict experiments and/or phenomena outside its range of validity is questionable.

The main deficiency of the Lee-Tarver model, or any pressure-dependent model, is that there is no mechanism to predict explosive behaviour under double or multiple shock compression. Experimental studies by several researchers have shown that, where a weak precursor wave, or preshock, compresses an explosive before being followed by a stronger second shock, then the reaction behind the second shock is weaker than that for a single shock alone at the same pressure in uncompressed material [39] [40] [51] [94]. This effect has been termed 'shock desensitisation', and needs to be represented in any reactive burn model. Since the growth terms in Lee-Tarver reaction rate are dependent on the local pressure, then the model will predict an increase in reaction rate in such situations, which is at odds with experimental observations. To enable the Lee-Tarver model to be used to predict desensitisation effects, a simple but physically realistic model for shock desensitisation has been developed within the confines of the Ignition and Growth model, and is described in the next section.

2.5   Shock Desensitisation

2.5.1   Preamble

Over many years numerous researchers have observed significant differences in reaction rates between singly and multiply shocked explosives [39] [40] [51] [94]. Specifically, reaction rates are slower behind shocks propagating through preshocked, but not detonated explosive, in comparison to the same shock propagating through uncompressed material. This type of behaviour has been termed 'shock desensitisation', and is important to considerations of safety of explosives, as many accident scenarios for explosives confined by inert materials may involve double or multiple shock compressions of the explosive.

Any reaction rate model based on the local pressure, *e.g.* Lee-Tarver, will predict an increase in reaction rate in a double shock situation where a weak preshock is followed by a stronger second shock, and will produce results that are very different to experimental observations. Therefore, for pressure-dependent models it is necessary to have an additional desensitisation model to account for the double shock

observations. It is noted that with a reaction rate taken to be a function of local temperature, it is probable that no additional desensitisation mechanism would be required, since the temperature behind doubly shocked material is less than behind a single shock to the same final pressure.

Below, the important experimental evidence is reviewed, and then consideration given as to how to model the phenomenon of shock desensitisation within the confines of the pressure-dependent Lee-Tarver model. A simple but physically realistic desensitisation model is then developed and described. The model is then applied to double shock data on the HMX-based explosive EDC37 to further assess the suitability of the model in double shock situations.

2.5.2 Experimental Evidence

Campbell *et al.* [3] first established the phenomenon of shock desensitisation. They observed that a 3.9 GPa shock in a plastic bonded HMX-based explosive rendered it less sensitive to initiation by a following 10 GPa shock, in comparison to initiation by a single 10 GPa shock. The explanation given was that compression by the weak first shock suppressed the initial porosity, such that the preshocked material reacted to the subsequent shock more like a homogeneous material.

Setchell [94] examined the effects of precursor waves on the shock initiation of the HMX-based explosive PBX9404. In Setchell's experiments, initiating shocks of 5.0 GPa were preceded by either a 3.2 GPa sustained shock lasting $0.37\mu s$, or a ramp wave having a rise time of $0.6\mu s$. The build-up to detonation was inhibited while the preshock persisted, with the ramp wave having a greater desensitising effect than the sustained precursor. In both cases the run distance to detonation was extended by an amount that depended on the duration of the precursor wave.

Campbell and Travis [51] studied the shock desensitisation of the HMX-based explosive PBX9404. In their experiments, a detonation wave was run into a preshocked region of the explosive. For a preshock in the range 1.0 to 2.4 GPa, the detonation reaction was weakened and eventually quenched. By observing the extinction of the detonation wave, an inverse relationship was obtained between the time required for desensitisation, τ, and the preshock pressure, P, namely: $P^{2.2}\tau = 1140$. The desensitisation time, τ, is interpreted as the time required to eliminate the potential 'hot-spot' sites in the material.

More recently, Mulford *et al.* [39] investigated the initiation behaviour of a number of HMX-based explosives subjected to weak precursor shock waves. In their experiments a composite impactor was accelerated onto an explosive target using a gas-gun. This generated successive shocks, a weak preshock followed by a higher pressure second shock, travelling in the same direction through the explosive sample, where the second shock eventually catches up and overtakes the preshock. In experiments on PBX9404, a sustained precursor shock of 2.3 GPa was followed $0.65\mu s$ later by an initiating shock 5.6 GPa. It was observed that the precursor wave,

while it persisted, desensitised the explosive to the following higher pressure shock wave, resulting in an extension of the run distance to detonation. The transition to detonation occured at a distance, after the two shocks had coalesced into a single wave, very similar to that expected from the Pop-Plot for PBX9404 at the pressure of the main shock alone. Modest growth of reaction was observed behind the second shock as it travelled through the preshocked region. This may indicate that the precursor wave reduced, but did not eliminate, the volume of potential 'hot-spots' available to the second shock. It was noted that according to the Campbell and Travis criterion [51], the precursor shock is too short to completely desensitise the explosive; $P^{2.2}\tau = 644 < 1140$.

The double shock response of the HMX-based explosive EDC37 has also been investigated [38]. In gas-gun experiments very similar to those performed by Mulford *et al.* [39], planar sequential shocks were input into EDC37 samples. A higher pressure second shock travelled through preshocked material to catch and overtake the first shock in the situations where, (i) there was little or no observable reaction in the first shock, and (ii) there was significant reaction behind the first shock before it was overtaken by the main shock. In the first set of experiments, where there was little or no reaction in the first shock, it was observed that the second shock did not contribute to the build-up of detonation until after wave coalescence, and the run to detonation was extended by an amount for which the preshock persisted. These results are consistent with the findings of Mulford *et al.* [39]. In a separate set of experiments, the effect of significant reaction behind the first shock was investigated. It was found that, in this case, reaction before wave coalescence appears to contribute to the final build-up to detonation; the run distance to detonation from wave coalescence was found to be shorter than that expected from the Pop-Plot at the pressure of the main shock alone.

With insensitive high explosives, there is an additional phenomena of 'dead pressing' which was observed by Tarver *et al.* [40] whilst studying the effect of reflected shocks on previously shocked samples of the TATB-based explosive LX-17. Steel flyers were used to impact thin discs of LX-17 which were backed by high impedence materials to produce reflected shocks of varying magnitude in the preshocked explosive. 'Dead pressing' was observed when an initial shock of 6.8 GPa was reflected from a copper disc producing a 14.0 GPa shock propagating back through the preshocked material. At this pressure it was expected run to detonation would occur within the sample thickness. However, the embedded gauges recorded no reaction due to the reflected shock. The initial shock pressure is just below the initiation threshold for LX-17, and it was postulated that this shock removed the internal porosity such that the reflected shock found no ignition sites and just propagted as an inert shock. To model this behaviour using the Ignition and Growth model, Tarver [40] added a condition to the ignition term in the reaction rate equation (2.23) to prevent any reaction from occuring if a critical range of shock compressions (or pressures) was applied to the explosive.

In experiments on the TATB-based explosive PBX9502, Dick [95] imposed preshocks of 2.3 and 5.0 GPa respectively on pieces of detonating explosive. In both instances, the detonation failed to propagate in the preshocked explosive. The preshock pressures are below the initiation threshold for PBX9502, suggesting 'dead pressing' by mechanically compressing out the potential 'hot-spot' sites (*e.g.* pores).

In summary, the interpretation of the above experimental studies and observations is that the preshock removes the available 'hot-spot' sites, such that a subsequent stronger shock is then travelling through material deprived of reaction sites. Pure mechanical compression of pores is one plausible mechanism for 'hot-spot' removal, while 'hot-spot' initiation and subsequent low level reaction during the preshock is another suggested mechanism. The shape, magnitude, and duration of the precursor wave can all affect the extent of residual sensitivity.

The general concensus is that desensitisation due to preshocking will occur except when, (i) the time interval between the two shocks is short, and (ii) there is a following rarefaction wave. Desensitisation is a time dependent process, and a short time interval between the preshock and main shock will not permit the desensitisation process to take place, resulting in nearly normal detonation. In the case where the explosive is allowed to release following preshocking, enhanced sensitisation could occur due to the porosity recovering, or as a result of damage, which could lead to an increase in porosity.

2.5.3   Simple Model for Shock Desensitisation

The main disadvantage of pressure-dependent reaction rate models is that they contain no mechanism to predict the effects of so-called shock desensitisation, and hence a bolt-on desensitisation model is required. Here, a simple but physically realistic model for shock desensitisation is developed within the confines of the Lee-Tarver model. It is based on the modelling of the precursor shock experiments performed by Mulford *et al.* [39], where the phenomenon of shock desensitisation was observed.

Mulford *et al.* [39] investigated the initiation behaviour of the HMX-based explosives PBX9404 and PBX9501 subjected to precursor shock waves. In their experiments, a composite impactor was accelerated onto the explosive specimens using a gas-gun. The impactor consisted of a low impedence thin layer (Perspex), mounted on the front surface of a higher impedence backing material (Vistal). When the projectile impacts the explosive sample, one shock wave is driven into the explosive and another is driven back into the Perspex. The wave in the Perspex then reflects from the higher impedence Vistal eventually delivering a second, higher pressure shock, to the explosive sample. This second shock initially travels through the preshocked region but eventually catches up and overtakes the precursor wave. The experimental set-up and distance-time diagram showing the shock trajectories is shown in Figure 2.6. Embedded particle velocity gauges provided data on

the time evolution of the reaction in the explosive, and the experiments were one-dimensional over the region and time of interest.

In experiments on PBX9404, a sustained precursor shock of 23 kbars was followed 0.65μs later by a stronger second shock of 56 kbars. The experimental particle velocity gauge results are reproduced in Figure 2.7. The first gauge trace is at the projectile/explosive interface, with the second particle velocity trace at a depth of 1.0mm into the explosive. All subsequent gauges are at approximately 0.5mm intervals with the final trace at a depth of 10.0mm into the explosive. For the shock conditions of interest, the whole build-up process cannot be monitored in a single experiment. Instead two experiments were fired, one with the gauge package forward monitoring the early build-up, and another monitoring the late build-up with the gauge package aft. Figure 2.7 shows the combined data obtained from the two nominally identical double shock experiments on PBX9404. The generation of energy in the shocked material behind the shock front is indicated by an increase in particle velocity above that in the shock front. The results contain a wealth of data, and the observations that may be made are described below.

The amplitude of the preshock was insufficient to cause prompt initiation since there is little or no observable reaction in the first shock before it gets overtaken. The higher pressure second shock travels faster than the precursor wave, and the two waves coalesced after approximately 1.0μs from input of the second shock. Only modest growth of reaction was observed behind the second shock as it travelled through the preshocked region. After catch-up, the second shock rapidly grows to detonation. Detonation occurs after 9.4mm of run from impact of the first shock, or after 8.7mm after the second shock enters the explosive. The Pop-Plot for PBX9404 predicts a run of 3.5mm at the pressure of the main shock (56 kbars) alone. Measured from the location of wave coalescence, which is marked on the figure, the run is 3.8mm. The run distance over which the second shock grows to detonation after catch-up is therefore very similar to the run distance which would be expected for a single shock at the same pressure. Thus, the run distance to detonation is extended by an amount for which the preshock persists.

Initially, with the aim of highlighting the inadequacy of the standard Lee-Tarver model to predict explosive response to double shock inputs, a calculation of the Mulford precursor shock experiments on PBX9404 was performed using PERUSE. The set-up consisted of a stationary 30mm thick PBX9404 explosive target impacted by a projectile consisting of a 1.4mm thick Perspex front layer, backed by 30mm of Vistal. The target and projectile were initially in contact, with the projectile given the measured velocity of 0.931mm/μs. The two-term reaction rate model developed by Tarver for PBX9404 [52] was used, and the model parameters are given in Table 2.1. The Vistal layer of the impactor was modelled by a Linear Gruneisen EOS which has the form,

$$P = P_H(V) + \frac{\Gamma(V)}{V}(E - E_H(V)) \tag{2.32}$$

where P is the pressure, V is the specific volume, E is the specific internal energy, and P_H and E_H are the Hugoniot pressure and energy corresponding to the shock velocity (U_s)-particle velocity (U_p) relationship,

$$U_s = C_0 + sU_p \qquad (2.33)$$

and the Gruneisen gamma is given by,

$$\Gamma(V) = \Gamma_0 + \Gamma_1 \frac{V}{V_0} \qquad (2.34)$$

In the above equations C_0, s, Γ_0, and Γ_1 are material specific constants. The EOS and strength constants for Vistal are taken from [96] and are given in Table 2.2, where Y is the yield strength and μ is the shear modulus, and both are assumed constant. Another Linear Gruneisen EOS was used to model the response of the Perspex layer of the dual material impactor, and the EOS constants for Perpex [97] are also given in Table 2.2.

Table 2.2: EOS parameters for Vistal and Perspex.

Vistal [96]		Perspex [97]	
ρ_0 (g/cm^3)	3.969	ρ_0 (g/cm^3)	1.186
ρ_{0s} (g/cm^3)	3.969	ρ_{0s} (g/cm^3)	1.186
C_0 (cm/μs)	0.814	C_0 (cm/μs)	0.2598
s	1.28	s	1.516
Γ_0	0.0	Γ_0	0.0
Γ_1	2.3	Γ_1	0.97
Y (Mb)	0.058		
μ (Mb)	1.555		

The PERUSE calculation was performed using a mesh density of 16 zones/mm in the PBX9404 region. Lee-Tarver model results are mesh converged at this mesh density. Appropriate meshing was also defined for the impactor materials, and a scalar monotonic artificial viscosity was used to accurately represent the propagating shock discontinuities. Figure 2.8 shows the calculated particle velocity histories at initial positions of 0, 1, 2, 3, 4, 5, 6, 7, 8, and 9mm into the explosive charge from the side of impact. As expected, very poor agreement with experiment is obtained. Since the growth of reaction in the model is dependent on the local pressure, then the calculation predicts rapid growth of reaction behind the second shock as it travels through the preshocked region.

Consideration has been given as to how to model the phenomenon of shock desensitisation within the confines of the existing Lee-Tarver model. The interpretation of the accumulated experimental evidence on shock desensitisation is that

the preshock compresses and/or initiates the available 'hot-spot' sites, such that any subsequent shock is then travelling through material deprived of such reaction sites. Since the formation of 'hot-spots' in an explosive is a highly irreversible process and can happen only once then, to a first approximation, the formation and subsequent growth of reaction from 'hot-spots' is dependent on the shock pressure of the first wave passing through the explosive. To predict the effects of shock desensitisation within the confines of the Lee-Tarver model, the reaction rate is fixed at the pressure of the first shock seen at any given point in the explosive, P_{shk}, such that the passage of subsequent stronger shocks cannot result in any increase in the reaction rate. The quantity,

$$\bar{P} = min\,(P, P_{shk}) \tag{2.35}$$

replaces the local pressure, P, in the reaction rate equations (2.22) and (2.23). The value of P_{shk} is found as follows. In hydrocode calculations, the value of the artificial viscosity is only non-zero through an arriving shock front. When a propagating shock wave arrives at a given computational cell, the artificial viscosity in that cell becomes non-zero. It then subsequently rises and falls with the passage of the shock, eventually dropping back to zero which occurs at approximately the top of the rise time of the shock. When this happens, the shock pressure in the cell, P_{shk}, is captured.

The PERUSE calculation of the Mulford *et al.* [39] precursor shock experiments on PBX9404 was repeated using the described simple model to predict desensitisation effects within the confines of the Lee-Tarver model. The Lee-Tarver model constants for PBX9404 were unchanged. The computed particle velocity profiles utilising the desensitisation model are shown in Figure 2.9. Qualitatively the calculation reproduces the main features of the experiment; the precursor shock, while it persists, inhibits the build up to detonation of the main shock, and the run to detonation beginning approximately at the end of the preshocked region. From impact of the precursor wave, detonation occurs after approximately 9.5mm of run. This is in good agreement with the experimentally observed run distance of 9.4mm from impact of the first shock. In addition, the position and timing of shock coalescence is well modelled. From this point, the calculated run distance to detonation is approximately 4.0mm, in good agreement with the experimentally deduced value of 3.8mm.

However, the calculated time to detonation from the point where the two shocks coalesce is shorter than experiment. In addition, the small amount of observed growth in the second shock before catch-up is not modelled correctly probably due to the code freezing the reaction rate in the material at the level of the first shock. Although it is unlikely that this deficiency is significant in this particular experiment, it could become important if the second shock was stronger or if the time difference between the shocks was greater. In reality it appears that the preshock puts a brake on the growth of reaction, but does not render the explosive completely

incapable of sustaining a build-up process as assumed by the simple desensitisation model.

The described desensitisation model is a very simple way of attempting to simulate shock desensitisation within the framework of the Lee-Tarver model. The validity of this treatment needs to be investigated in the context of other multiple shock situations, and for other explosives of interest. Another HMX-based explosive on which double shock data has recently been obtained is EDC37, and the experiments and their modelling is described in the next section.

2.5.4   Modelling EDC37 Double Shock Experiments

A number of gas-gun experiments have recently been performed at Los Alamos National Laboratory to study the double shock response of the HMX-based explosive EDC37 [38]. These experiments, in which a weak preshock was followed by a stronger main shock, were very similar to the precursor shock experiments performed by Mulford *et al.* [39], and which showed an extended run to detonation in preshocked material. The experimental configuration for the EDC37 double shock experiments was the same as that shown in Figure 2.6, except that the composite impactor consisted of Kel-F mounted on the front surface of z-cut Sapphire in order to generate the required sequential shocks. Kel-F was used instead of Perspex for generation of the weaker first shock as this material has a better impedence match to EDC37 than Perspex. In the experiments, the growth of reaction in the shocked explosive samples was monitored by embedded particle velocity gauges.

The EDC37 double shock experiments and the results obtained are summarised in Table 2.3. Experiments have been performed at different input conditions; the magnitude of the input shocks is determined by the velocity of the impactor, and the time delay between the two shocks is set by the thickness of the Kel-F layer. In order to monitor the whole reaction history at each input condition, it was necessary to fire a pair of nominally identical shots, one with the gauge package monitoring the early build up, and one monitoring the late build up. The first pair of experiments (Shots 1175/76) were chosen such that there would be no observable reaction in the first shock before it is overtaken by the main shock, thus complementing Mulford's experiments on PBX9404, an explosive similar in composition to EDC37. The second pair of experiments (Shots 1194/95) were chosen such that there would be significant reaction behind the first shock before the second shock traversed the preshock region. This regime for double shock explosive had been hitherto unexplored.

The derived run distances to detonation in Table 2.3 are measured from impact of the first shock, and the value quoted in brackets is the run distance as measured from the point of shock coalescence. For Shots 1175/76 the derived run distances to detonation from impact of the first shot show reasonably good consistency between the pair of shots. The average run distance after wave coalescence in 6.35mm. This

Table 2.3: Summary of EDC37 Double Shock Experiments.

Shot No.	Impact Vel. (mm/μs)	Particle Vel. u_p (mm/μs)	Shock Vel. U_s (mm/μs)	Input Pressure (kbars)	Run Distance (mm)
1175A	0.921	0.44 ± 0.020	3.63 ± 0.10	29.4	11.96
1175B		0.77 ± 0.020	4.25 ± 0.20	62.0	(6.18)
1176A	0.925	No data	No data		12.29
1176B		0.77 ± 0.020	4.25 ± 0.20	62.0	(6.51)
1194A	1.170	No data	No data	39.3	9.43
1194B		No data	No data	85.8	(2.40)
1195A	1.165	No data	No data	39.3	8.40
1195B		No data	No data	85.8	(2.00)

is very similar to the run distance that would be expected from the Pop-Plot, see Figure 2.4, for a single shock of 62 kbars into EDC37. These results appear to indicate that the second shock does not contribute to the build up of detonation until after wave coalescence, and the run distance to detonation is extended by an amount for which the preshock persists. The observed desensitisation behaviour is thus very similar to that seen in preshocked PBX9404 and PBX9501 [39], where there was also no observable reaction seen behind the first shock in the experiments.

For Shots 1194/95, the reproducibility of the experimental data is not as good as in Shots 1175/76. For Shot 1194, detonation is attained at 9.43mm, 2.18μs from impact of the first shock. For Shot 1195, the run distance is deduced to be 8.40mm, and the run time is 2.00μs. The reasons for the differences are not known. The run distance to detonation after wave coalescence is 2.40mm for Shot 1194, and 2.00mm for Shot 1195. The expected run distance to detonation for a single shock of 86 kbars into EDC37 is approximately 4mm based on the Pop-Plot for this explosive, see Figure 2.4. Thus, reaction before wave coalescence contributes to the final build up to detonation, and the rule of thumb for lower pressure first waves, that the distance to detonation is approximately equal to the run distance at the pressure of the second shock, plus the distance to wave coalescence, does not apply if there is significant reaction in the first shock.

PERUSE calculations of the EDC37 double shock gas-gun experiments have been performed using the Lee-Tarver three-term reaction rate model for EDC37 [63] in conjunction with the simple shock desensitisation model. The Lee-Tarver EDC37 parameters are reproduced in Table 2.1. These calculations were run to test the applicability of the desensitisation model in the situation of planar sequential shocks input to the EDC37 samples, where (i) there is no observable reaction in the first shock (Shots 1175/76), and (ii) there is significant reaction in the first shock (Shots 1194/95). In the calculations, the double layered impactor was modelled using a Linear Gruneisen EOS (2.32)-(2.34) for the z-cut Sapphire backing material,

while the Kel-F front layer was modelled using a Cubic Gruneisen EOS [98] of the form,

$$P = \frac{\rho_{0s}\, C_0^2\, \xi \left[1 + \left(1 - \frac{\Gamma_0}{2}\right)\xi - \frac{A}{2}\,\xi^2\right]}{\left[1 - (s_1 - 1)\xi - s_2\,\frac{\xi^2}{\xi+1} - s_3\,\frac{\xi^3}{(\xi+1)^2}\right]^2} + (\Gamma_0 + A\xi)\,\rho_{0s}\, E \quad \xi \geq 0 \quad (2.36)$$

$$P = \rho_{0s}\left(C_0^2\,\xi + \Gamma_0\, E\right) \qquad\qquad\qquad \xi < 0 \quad (2.37)$$

where,

$$\xi = \frac{\rho}{\rho_{0s}} - 1 \qquad\qquad\qquad (2.38)$$

is the compression, and the shock velocity (U_s)-particle velocity (U_p) relationship is non-linear,

$$U_s = C_0 + s_1\, U_p + s_2\left(\frac{U_p}{U_s}\right)U_p + s_3\left(\frac{U_p}{U_s}\right)^2 U_p \qquad (2.39)$$

The EOS parameters for the impactor materials are given in Table 2.4. The parameters for z-cut Sapphire were taken from [99], while the parameters for Kel-F are due to Steinberg [98].

Table 2.4: EOS parameters for z-cut Sapphire and Kel-F.

z-cut Sapphire [99]		Kel-F [98]	
Initial Density, ρ_0 (g/cc)	3.985	Initial Density, ρ_0 (g/cc)	2.133
Solid Density, ρ_{0s} (g/cc)	3.985	Solid Density, ρ_{0s} (g/cc)	2.133
C_0 (cm/μs)	1.119	C_0 (cm/μs)	0.205
s	1.00	s_1	1.66
Γ_0	0.0	s_2	0.4064
Γ_1	2.3	s_3	-1.037
		Γ_0	0.66
		A	0.0

In the calculational set-up for EDC37 Shots 1175/76, the composite impactor consisted of a 30mm thick layer of z-cut Sapphire backing a front layer of Kel-F of thickness 1.0mm. The impactor was initially in contact with a 30mm thick EDC37 explosive target, and had an initial velocity of 0.923mm/μs. The computed particle velocity profiles for EDC37 Shots 1175/76 are compared with the experimental gauge records in Figure 2.10. The profiles correspond to gauges located at depths of 0, 2.5, 3, 4, 5, 6, 7, 8, 9, 10, and 11mm into the explosive. Again, at least qualitatively, the desensitisation model is able to reproduce the main features of

the experiment; little or no reaction in the first shock, the build-up to detonation of the second shock being inhibited by the first wave while it persists, and the run to detonation only beginning at the end of the preshocked region. However, it is noted that there are some subtle differences.

The two shock waves coalesce at approximately 5.20mm and 1.50μs compared with 5.78mm and 1.59μs respectively in the experiment. Experimentally, some reaction is observed behind the second shock as it traverses the preshocked region. However, this is not reproduced in the calculation which predicts very little or no growth of reaction in this region. After shock coalescence, normal build-up to detonation occurs. From wave coalescence, the computed run distance to detonation is 6.00mm, which is in good agreement with the value of 6.35mm deduced from experiment. It is observed, however, that the shape of the wave profiles in the build up to detonation after wave coalescence is different between experiment and calculation.

The calculational set-up for EDC37 Shots 1194/95 was the same as that described above for Shots 1175/76 except, (i) the Kel-F front layer was 1.428mm (in order to increase the time separation between the two shocks), and (ii) the velocity of the flyer was set at 1.168mm/μs. The comparison of experimental and calculated particle velocity profiles for EDC37 Shots 1194/95 is shown in Figure 2.11. Again the profiles correspond to gauges located at depths of 0, 2.5, 3, 4, 5, 6, 7, 8, 9, 10, and 11mm into the explosive. In the case of significant reaction behind the preshock, poor overall agreement is obtained between calculation and experiment. The input shocks to the explosive sample are well modelled, however poor agreement with experiment is obtained for the subsequent explosive response. The experiment shows significant reaction due to the first shock, however the calculation fails to predict any growth of reaction in or behind the first shock. As a result, the velocity of the first shock is slower than observed. The failure to model the growth of reaction due to the first shock is a direct consequence of the desensitisation model which limits the reaction growth rate at the shock pressure of the first wave seen at any given point in the explosive.

As the second shock travels through the preshocked region, a rapid increase in the calculated particle velocity at the shock front is observed, and its magnitude is much larger than seen experimentally. At first glance this seems a little odd as the desensitisation model is meant to limit the reaction rate in preshocked material, whereas an enhancement of the reaction is observed. Examination of the relative contributions of the three terms in the rate law to the overall reaction rate reveals why this is so. At the pressure of the second shock (86 kbars), the ignition term dominates the response, which, unlike the growth terms has no restrictions placed upon it in the desensitisation model. In the EDC37 three-term reaction rate model, the ignition term contributes to the overall reaction rate until the mass fraction reacted in a computational cell equals 30% (λ_{igmax}=0.3). This allows significant

reaction to occur before the ignition term is switched off, and results in wave coalescence occuring much earlier than observed. The amount of material ignited in the second shock is not modelled correctly, thus giving evidence to suggest that the contribution of the ignition term to the reaction rate should be reduced.

2.5.5 Summary

A considerable amount of experimental data has been accumulated which shows that initiation and run distance to detonation in explosives can be significantly modified by preshocking the material. For example, where a weak precursor wave, or preshock, is followed by a stronger second shock, the reaction behind the second shock is weaker than that for a single shock of the same pressure. This effect has been termed 'shock desensitisation'.

Using the standard Lee-Tarver model, simulations of experiments where shock desensitisation has been observed give poor agreement to experiment. Calculationally, the reaction rate behind the second shock is too strong and detonation occurs much earlier. This illustrates that reaction rates based on the local pressure have no mechanism for describing explosive behaviour under double shock compression, and require an additional desensitisation model to account for the double shock observations.

Consideration has been given as to how to model the effects of shock desensitisation within the confines of the pressure-based Lee-Tarver model. The development of a simple, but physically realistic model to predict desensitisation effects has been described, where the reaction rate is fixed at the pressure of the first shock seen at any given point in the explosive. This is a compromise between ensuring that the passage of any subsequent shock through preshocked material does not result in any significant increase in the reaction rate, yet ensuring that single shocks in pristine material are still able to grow to detonation more or less as given by the Pop-Plot.

Application of the desensitisation model to double shock gas-gun experiments on the HMX-based explosives PBX9404 and EDC37 has shown that, where there is little or no observable reaction in the first shock, the explosive response is well modelled. The simple desensitisation model is able to qualitatively reproduce the main experimental features; the weak precursor wave, while it persists, inhibiting the build-up to detonation of the main shock, and the run to detonation beginning approximately at the end of the preshocked region.

Applying the model outside its fitting regime, where there is significant reaction in the first shock in double shock experiments on EDC37, poor agreement with experiment is obtained. The calculation fails to correctly predict the growth of reaction due to the first shock. This is a direct consequence of the desensitisation model limiting the reaction rate at the pressure of the first shock. In addition, the agreement to the build-up of reaction due to the second shock is poor. This is due to the ignition term dominating the explosive response. Thus, the wider applicability

of the simple desensitisation model to simulate a range of double or multiple shock situations must be questioned.

The need to invoke a separate desensitisation model for double shocks is simply a manifestation of using a reaction rate model that is dependent on the local pressure. With a reaction rate dependent mainly on temperature, for example, it is quite possible that no additional mechanism is required to account for the double shock observations since the second shock develops a lower temperature than it would be behind a single shock of the same pressure. Expressed another way, the fact that, experimentally, the reaction rate behind a second shock is less than that behind a single shock of the same pressure demonstrates that the reaction rate is not largely dependent on pressure.

2.6   Conclusions

For evaluation purposes, the widely used, continuum-based, Lee-Tarver reactive burn model has been implemented and validated in the one-dimensional Lagrangian hydrocode PERUSE. The reaction rate law in the Lee-Tarver model is based substantially on the local pressure. Although some aspects of explosive shock initiation can be adequately described by a pressure-dependent reaction rate, *e.g.* Pop Plot data for sustained single shocks, such reaction rates cannot account for explosive behaviour under double shock compression.

For a reaction rate based on pressure-dependence, it is necessary to postulate an additional desensitisation model to account for double shock observations. A simple desensitisation model, developed within the confines of the Lee-Tarver model, has been applied to double shock data with mixed results. The fact that, experimentally, the reaction rate behind a second shock is less than that behind a single shock of the same pressure demonstrates that the reaction rate is not solely dependent on pressure. It follows that reaction rate models such as Lee-Tarver are based on a false premise.

To account for double shock observations without requiring to invoke a separate desensitisation model, a different form of reaction rate is needed. For example, with a reaction rate dependent mainly on temperature, it is quite possible that no additional mechanism is required since a higher pressure second shock develops a lower temperature than it would be behind a single shock of the same pressure.

Discussed in the following chapter, a new approach to shock initiation modelling that utilises a reaction rate based on entropy rather than pressure, also allows double shock experiments to be modelled without recourse to a separate desensitisation model. However, the move from a pressure-dependent reaction rate to an entropy-dependent reaction rate introduces additional numerical complexities, and these are described in detail in the next chapter.
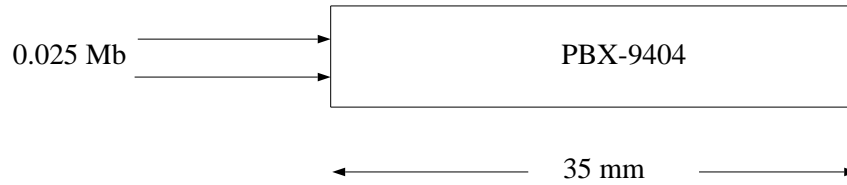
Figure 2.1: Definition of simple one-dimensional test problem.
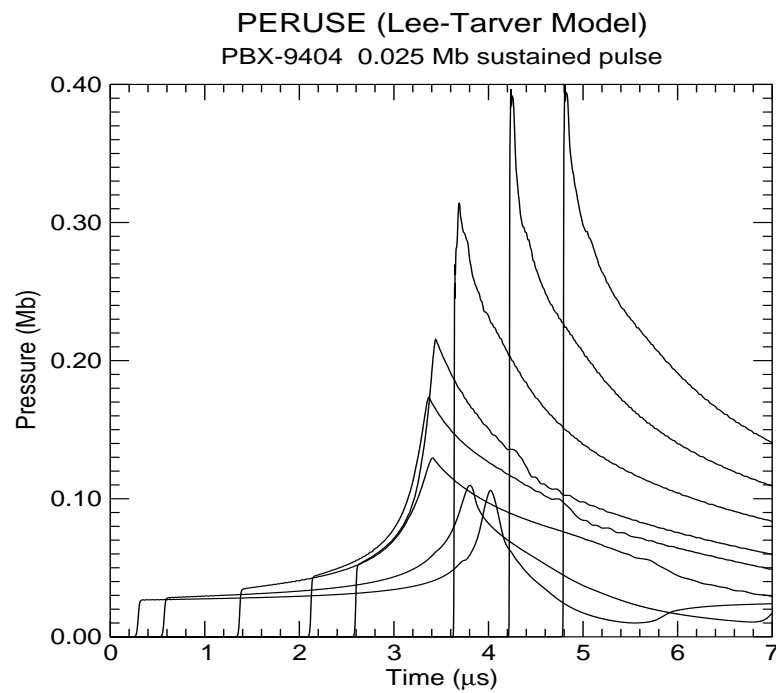
Figure 2.2: Calculated pressure profiles from PERUSE for a 0.025 Mb sustained pressure pulse into PBX-9404.
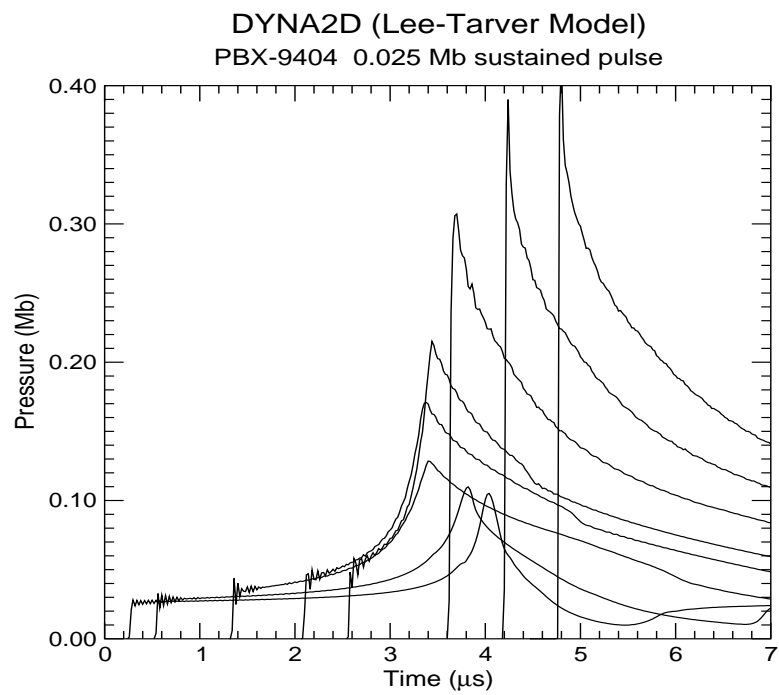
Figure 2.3: Calculated pressure profiles from DYNA2D for a 0.025 Mb sustained pressure pulse into PBX-9404.
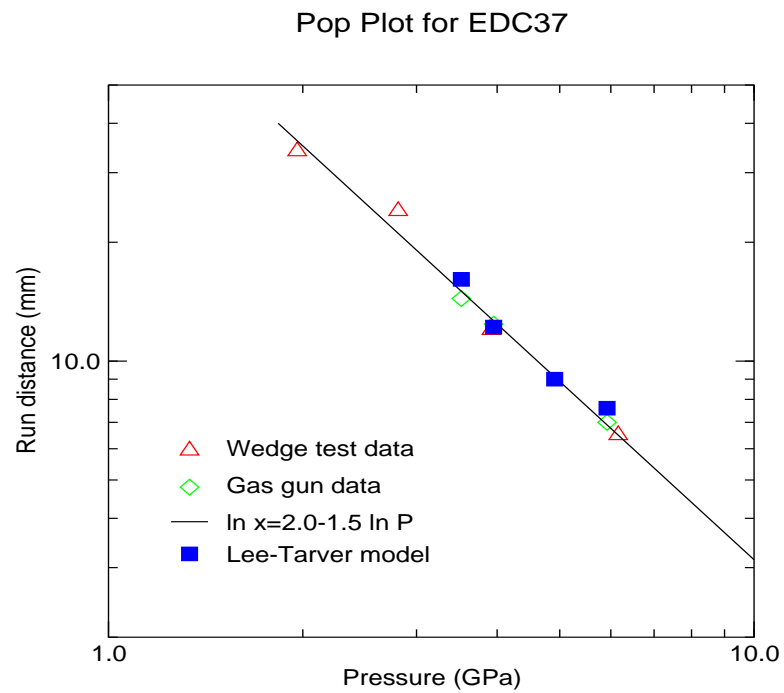
Pop Plot for EDC37

Figure 2.4: Pop-Plot data for EDC37 explosive.

Lee-Tarver Model
EDC37 Gas Gun shot 1160
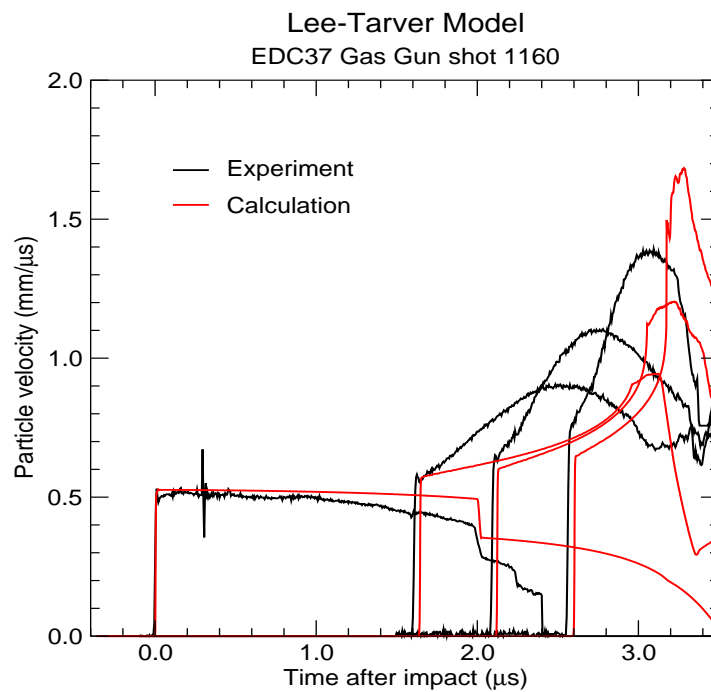
Figure 2.5: Particle velocity histories for EDC37 Gas-Gun Shot 1160.
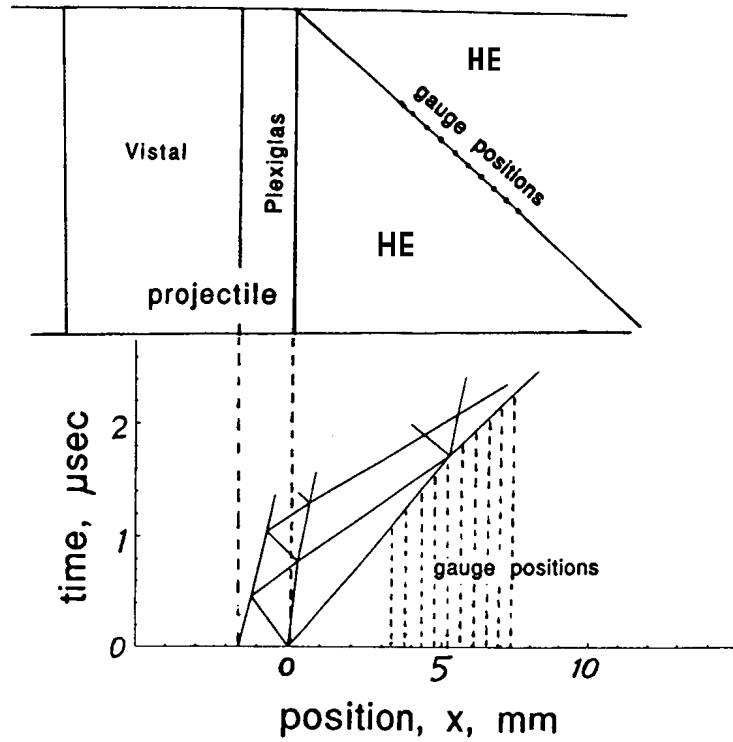
Figure 2.6: LANL precursor shock experiments; experimental arrangement and distance-time diagram showing preshock and main shock generation.
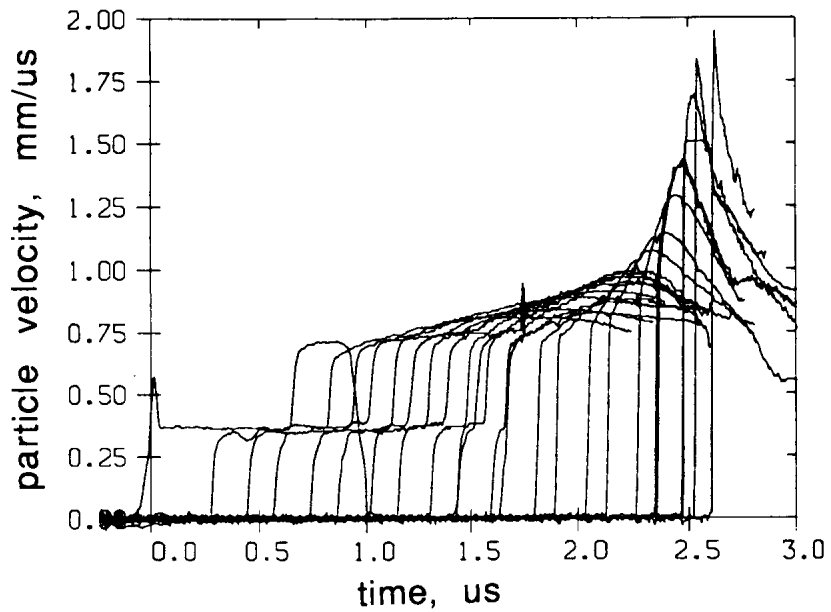
Figure 2.7: Data from LANL precursor shock experiments on PBX-9404; 23 kbar preshock followed 0.65 μs later by 56 kbar shock.
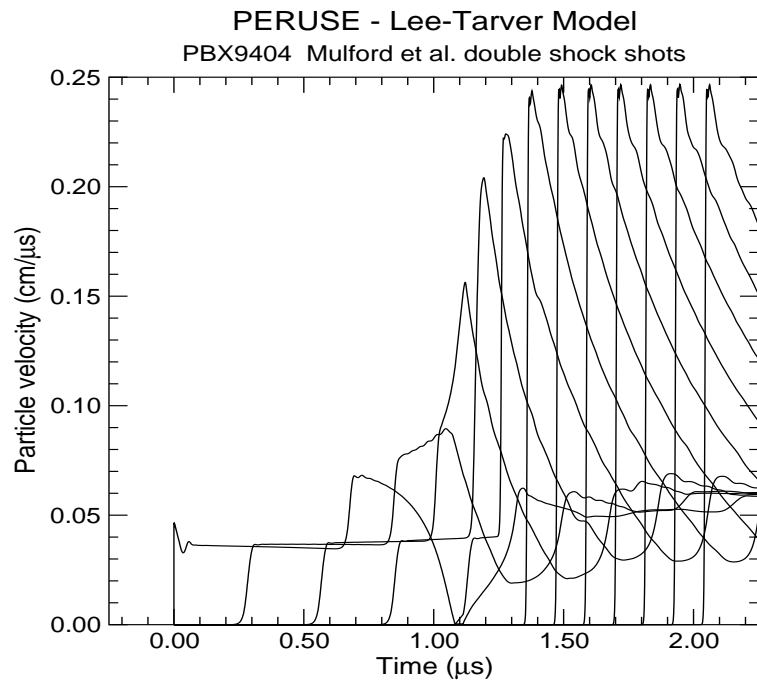
Figure 2.8: LANL precursor shock experiments; calculated particle velocity profiles in PBX9404 using the standard Lee-Tarver model.
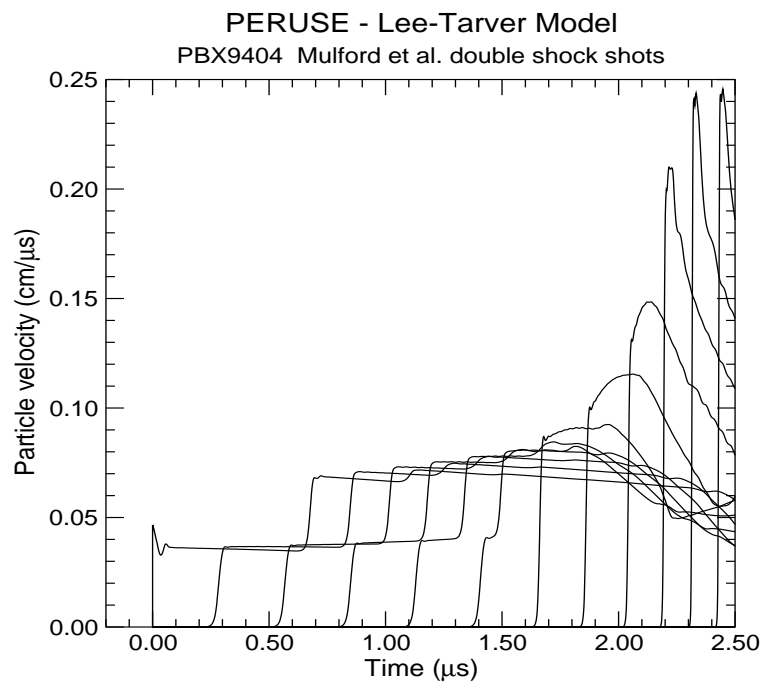
Figure 2.9: LANL precursor shock experiments; calculated particle velocity profiles in PBX-9404 using the simple desensitisation model.
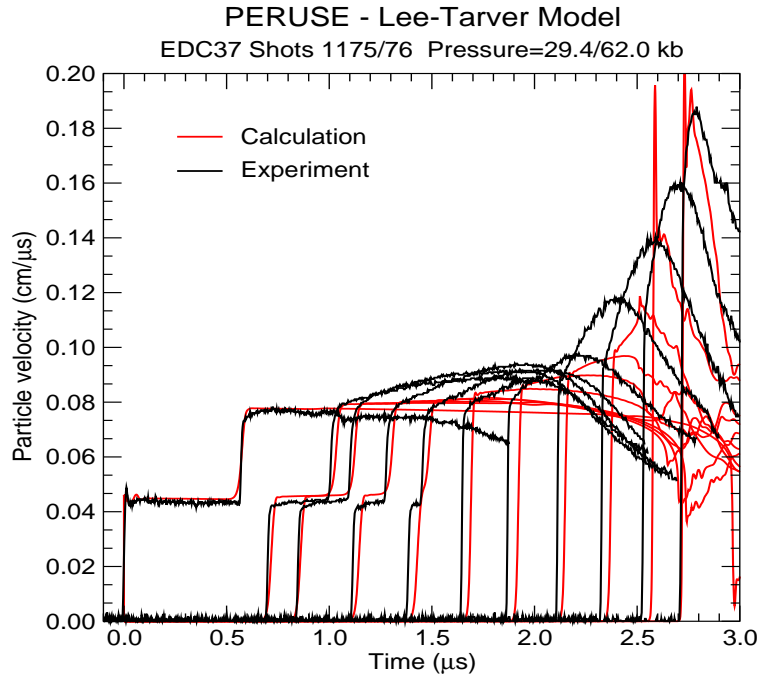
Figure 2.10: Comparison of calculated and experimental particle velocity profiles for EDC37 double shock gas-gun shots 1175/76.
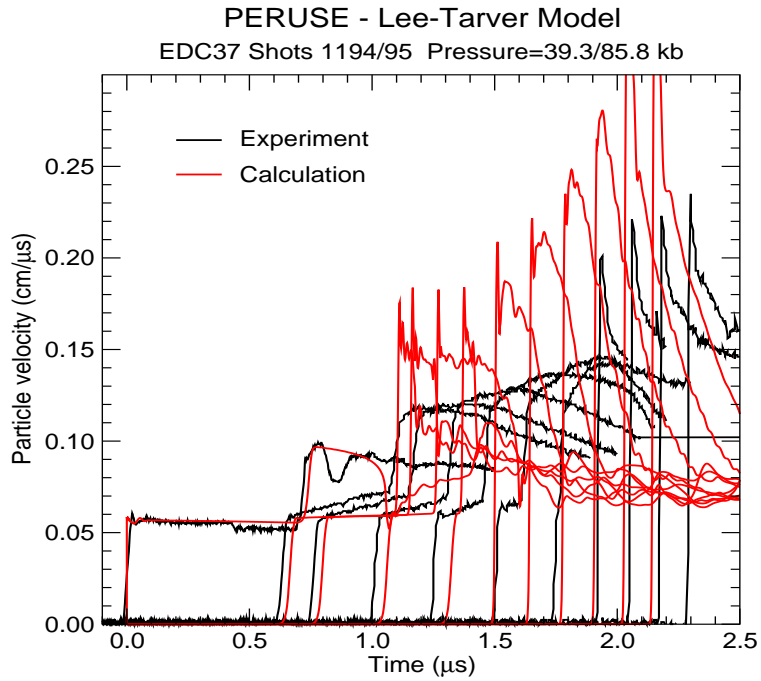
Figure 2.11: Comparison of calculated and experimental particle velocity profiles for EDC37 double shock gas-gun shots 1194/95.

Chapter 3

Entropy-Dependent CREST Reactive Burn Model

3.1   Introduction

Traditionally, reaction rates in continuum-based reactive burn models to calculate explosive shock initiation have been based on pressure and/or temperature. For example, the most widely used continuum reactive burn model in use in hydrocodes today, the Lee-Tarver model [49], uses a pressure-dependent reaction rate to describe the explosive response. The majority of these models date back to the 1970's and 1980's and, as time has progressed, (i) it has become apparent that parameters fitted to a limited set of experimental results have to be adjusted to fit different data and/or model different phenomena, and (ii) the development of new experimental techniques have permitted a far greater insight into the shock initiation process. In particular, heterogeneous explosive response to multiple shock inputs is now much better understood. This is one aspect of explosive shock initiation that cannot be predicted by pressure-based models without recourse to an additional desensitisation model (see Chapter 2). Analysis of recently acquired data from shock initiation experiments, coupled with the inability of pressure-dependent models to accurately simulate a wide range of shock initiation phenomena, has lead to the development of a new reactive burn model.

CREST [61] is a new continuum reactive burn model for simulating shock wave initiation and propagation of detonation in heterogeneous solid explosives based on the conclusions of experimental observations. The model has a completely different basis from other continuum reactive burn models in that its reaction rate is independent of local flow variables behind the shock such as pressure and temperature. The foundation for CREST, based on a detailed analysis of experimental data, is that reaction, at least to first order, is a function of shock strength [60]. The best measure for shock strength for use in hydrocodes is a function of entropy of the shocked,

59

non-reacted, explosive and hence the model utilises an entropy-dependent reaction rate. This form of reaction rate coupled with both an unreacted and a reaction products equation of state (EOS) allows CREST to calculate explosive behaviour. The overall objective of CREST is to accurately model as wide a range of explosive phenomena as possible with a relatively simple model, and without having to change the model parameters and/or the form of the reaction rate equation in order to simulate different phenomena for a given explosive.

This chapter commences by giving a brief summary of the theoretical and experimental background to CREST and, for completeness, gives an overview of the model itself. To enable shock initiation and detonation problems of interest to be modelled using CREST, the model has been built into a number of hydrocodes. The implementation of the model in a one-dimensional, and a number of two-dimensional, hydrocodes is then described in detail, and results of calculations are presented to validate the implementation of the model. During the hydrocode implementation and use of the CREST model, a number of computational problems, not associated with pressure-based models, were identified. These problems are described and, where possible, solutions have been sought to minimise the effect of these additional problems on CREST calculations. To provide a rigorous test of CREST's predictive capability, a CREST model for the TATB-based explosive PBX9502, fitted to in-material gauge data from one-dimensional experiments examining the shock to detonation transition, has been applied to two-dimensional explosive data from detonation experiments. The calculational detonation studies are described, and the results discussed, particularly in relation to the wider applicability of the CREST model. Finally, the conclusions are given.

3.2 Background to CREST

Before developing a new reaction rate model for heterogeneous solid explosives, it is important to understand the experimental data obtained in shock initiation experiments. At the time of the development of some of the continuum models that are widely used today, such as the Lee-Tarver model [49], the data available on the shock response of explosives came mainly from so-called Wedge Tests [3] [30]. These experiments measure the trajectory of the leading shock from which the variation of shock velocity can be determined. It was found that the shock velocity increases very slowly to begin with, but after a depth into the explosive, dependent on the initial shock strength, the shock velocity increases rapidly to full detonation velocity. These experiments give the run-distance and run-time to detonation from sustained input shocks, leading to the Pop Plot [31], where the run-distance and run-time to detonation decrease as the shock strength increases. However, Wedge Test experiments give no information on the reaction history behind the shock before detonation is attained.

More recently, the development of new experimental diagnostic techniques has helped to improve our understanding of the shock initiation behaviour of heterogeneous explosives. For example, the development and use of robust in-material gauges, such as the electromagnetic particle velocity gauge of Vorthman [35], has revealed new data on the growth of reaction inside shocked explosives. Using in-material particle velocity gauges, a wealth of valuable information on the reaction behaviour of impact initiated explosives has been obtained from one-dimensional gas-gun experiments carried out by Gustavsen *et al.* [36] [37] [38] at Los Alamos National Laboratory. Effectively, the particle velocity gauges indicate the growth of the bulk reaction along a number of different (Lagrangian) particle paths within the explosive samples.

CREST is based on the detailed analysis [60] of the in-material particle velocity gauge records obtained from the experiments carried out by Gustavsen and co-workers. Since all the experiments were one-dimensional in nature, the analysis is centred on one-dimensional shock initiation phenomena. The analysis showed a strong correlation of time to peak particle velocity with shock strength, and from the fact that particle velocity histories at the same shock strength scale independently of how the shock strength had developed. The conclusion of these observations is that, at least to first order, the reaction rate history for any explosive particle must depend on the shock strength experienced by the particle, and does not depend on the pressure or temperature developing along the particle path, as is assumed by all other reaction rate models. The best measure for shock strength for use in hydrocodes is a function of entropy of the shocked, non-reacted explosive, which remains constant behind the shock, unless a further shock is propagated into the explosive. CREST therefore utilises an entropy-dependent reaction rate to model the explosive reaction, where the function of entropy is evaluated from the solid phase internal energy (and specific volume) within the non-reactive EOS for the explosive.

The main advantage of using an entropy-dependent reaction rate is that no additional desensitisation model (as required by pressure-based models) is needed to model multiple shock situations. In double shock experiments, it has been shown that the reaction rate behind the second shock following a weak first shock is significantly less than behind a single shock at the same pressure, see for example [38]. Since the internal energy (and therefore entropy) reached in a material by a double shock up to a given pressure is less than that reached by a single shock to the same pressure, then a reaction rate based on entropy can naturally account for double shock phenomena.

In any reactive burn model, it is important that the equations of state of the different components of the reacting mixture are modelled as accurately as possible. Any errors in these EOS will naturally be folded into the parameters in the reaction rate model, which in turn could lead to inaccurate conclusions being made about the reactive behaviour of an explosive. The EOS for the unreacted explosive is especially important for shock initiation because, (i) it determines the pressure, temperature,

entropy *etc* in the initial shock state, and (ii) the explosive near the shock front is at or near its non-reactive state for the majority of the run to detonation. Heterogeneous explosives are always, by design, to a greater or lesser extent porous. Since the porosity can vary from sample to sample, and it is well known experimentally that small changes in porosity can change both the non-reactive Hugoniot and shock sensitivity of an explosive [36], then porosity should be a variable in any reactive burn model.

However, continuum reactive burn models have never included porosity as a parameter, and have always implicitly assumed that the unreacted Hugoniot has been measured at exactly the required degree of porosity (which will rarely be available). If an explosive sample has a different porosity to that at which the Hugoniot has been measured, then in the absence of Hugoniot data at the required porosity, the unreacted EOS of the material can only be guessed at. Therefore, to accurately model an explosive with differing porosities, the parameters in the unreacted EOS and/or reaction rate model usually have to be adjusted to match the data. To address this issue, CREST employs a porosity-dependent unreacted EOS in the model.

In CREST, porous non-reactive Hugoniots are evaluated from a single baseline EOS for the fully dense material using the Snowplough porosity model. Since there is no Hugoniot data for explosives at zero porosity, the unreacted EOS for the fully dense material is determined by extrapolating available (usually sparse) Hugoniot data for the porous explosive to a best estimate of the fully dense Hugoniot using a methodology devised by Lambourn [100]. This baseline EOS, when used in conjunction with an appropriate porosity model, allows the unreacted Hugoniot at any given porosity to be determined. CREST utilises the Snowplough model as this is the standard form currently used in the hydrocodes to model porous materials.

CREST needs in-material gauge results in order to calibrate the reaction model coefficients, coupled with both an unreacted and a reaction products EOS in order to calculate explosive behaviour. From the one-dimensional shock initiation studies carried out by Gustavsen *et al.*, in-material gauge data has been obtained on a number explosives, including the HMX-based explosives PBX9501 [36] and EDC37 [38], and the TATB-based explosive PBX9502 [37]. By fitting to the particle velocity gauge histories from sustained single shock gas-gun experiments, CREST parameters for two explosives EDC37 [61] and PBX9502 [62] have been developed. A model for PBX9501 explosive is under development.

Using a single parameter set, the fitted CREST model for EDC37 explosive was subsequently shown to be able to simulate a range of one-dimensional shock initiation data involving sustained, thin pulse, and double shock inputs [61]. A clear advantage over pressure-dependent models is that, by utilising an entropy-dependent reaction rate, the results of double shock experiments can be predicted without recourse to a separate desensitisation model. For PBX9502 explosive, it was shown that the fitted CREST model was able to reproduce one-dimensional shock initiation data covering a range of input pressures for both sustained and thin

pulse shocks [62]. In addition, the use of the Snowplough porosity model allows CREST to predict the effects of porosity on initiation threshold data for RX-03-AU [101] (which has the same composition as PBX9502) without having to adjust the model parameters [62].

3.3 Overview of the CREST Model

3.3.1 Preamble

The CREST model [61] consists of two basic parts: (i) an EOS model for the reacting material, and (ii) a reaction rate model. The reacting material is assumed to be a mixture of two co-existing phases consisting of unreacted solid explosive and gaseous reaction products, and an EOS must be provided for each phase. The non-reactive explosive is modelled via a finite strain form of EOS [100]. This is thermodynamically complete as temperature is evaluated. To model the explosive reaction products, the universal Jones-Wilkins-Lee (JWL) form of EOS [89] is used. To yield the EOS of the reacting mixture, CREST uses the Isentropic Solid Equation (ISE) model [102], where it is assumed that the solid and gaseous phases of the reacting material are in pressure equilibrium. The unreacted solid explosive is assumed to be on an isentrope through the point on its Hugoniot to which it was shocked with the gaseous detonation products taking up the remaining volume and internal energy at pressure equilibrium. The Snowplough porosity model is used to account for porosity in determining the unreacted explosive response.

The reaction rate model controls the rate of explosive decomposition in going from unreacted explosive to gaseous reaction products. The reaction rate terms in CREST are based on detailed analysis of in-material particle velocity gauge histories from explosive gas-gun experiments which suggests that, in the early stages of the growth to detonation, the reaction rate at any given particle position depends only on the shock strength at that position [60] [103]. This indicates that the solid phase entropy, which remains constant between shocks, might be an appropriate variable representing shock strength for use in a reaction rate model.

The various components of the CREST model are described below where, in the model equations, the subscripts s and g refer to the unreacted solid explosive and gaseous reaction products respectively.

3.3.2 Equations of State

Unreacted EOS

A Mie-Gruneisen form of EOS [100] [104] is used to model the unreacted explosive, where the principal isentrope, written in finite strain form, is taken to be the reference curve. This form of EOS has the advantage that it allows the temperature

and a function of entropy of the unreacted explosive to be easily evaluated for their potential use in any temperature and/or entropy-dependent reaction rate model. The unreacted EOS is described by the following expressions,

$$P_s = P_i(V_s) + \frac{\Gamma(V_s)}{V_s}(E_s - E_i(V_s)) \tag{3.1}$$

$$P_i(V_s) = 3K_{0s} f(2f+1)^{\frac{5}{2}}\left(F + \frac{f}{2}\frac{dF}{df}\right) \tag{3.2}$$

$$E_i(V_s) = \frac{9}{2}V_{0s} K_{0s} f^2 F + Q \tag{3.3}$$

$$f = \frac{1}{2}\left[\left(\frac{V_{0s}}{V_s}\right)^{\frac{2}{3}} - 1\right] \tag{3.4}$$

$$F = exp\,[g(f)] \tag{3.5}$$

$$g(f) = g_A + g_B + g_C \tag{3.6}$$

$$g_A = A_1 f + A_2 f^2 + A_3 f^3 \tag{3.7}$$

$$+ \left[B_1(f-f_c) + B_2(f-f_c)^2 + B_3(f-f_c)^3\right]\frac{1}{2}\left[1 - \frac{2}{\pi}tan^{-1}\left(\frac{f-f_c}{\delta}\right)\right]$$

$$g_B = \frac{\delta}{2\pi}(B_1 - \delta^2 B_3)\,ln\left[\delta^2 + (f-f_c)^2\right] - \frac{B_2\delta^2}{\pi}tan^{-1}\left(\frac{f-f_c}{\delta}\right) \tag{3.8}$$

$$+ \frac{\delta}{2\pi}(f-f_c)\left[2B_2 + B_3(f-f_c)\right]$$

$$g_C = \left[B_1 f_c - B_2 f_c^2 + B_3 f_c^3\right]\frac{1}{2}\left[1 - \frac{2}{\pi}tan^{-1}\left(\frac{-f_c}{\delta}\right)\right] \tag{3.9}$$

$$- \frac{\delta}{2\pi}(B_1 - \delta^2 B_3)\,ln\left(\delta^2 + f_c^2\right) + \frac{B_2\delta^2}{\pi}tan^{-1}\left(\frac{-f_c}{\delta}\right)$$

$$+ \frac{\delta}{2\pi}f_c(2B_2 - B_3 f_c)$$

$$\Gamma(V_s) = \gamma_{00} + \Gamma_1\left(\frac{V}{V_{0s}}\right)^m exp\left[-\Gamma_2\left(\frac{V}{V_{0s}}\right)\right] \tag{3.10}$$

where P_s, V_s, and E_s are respectively the pressure, specific volume, and specific internal energy of the unreacted explosive, $P_i(V_s)$ and $E_i(V_s)$ are the pressure and

specific internal energy on the principal isentrope, Γ is the Gruneisen gamma, Q is the initial specific internal energy of the non-reacted explosive, f is the finite strain variable used to define the compression, V_{0s} is the specific volume at solid density, K_{0s} is the isentropic bulk modulus, and A_1, A_2, A_3, B_1, B_2, B_3, f_c, δ, m, γ_{00}, Γ_1, and Γ_2 are constants.

The EOS is thermodynamically complete since it allows for the evaluation of temperature. In this instance temperatures are obtained most easily by defining specific heat at constant volume, C_{Vs}, as a function of temperature in the unreacted explosive on $V_s = V_{0s}$. With the principal isentrope as the reference curve, the other isentropes are given by,

$$E_s = E_i(V_s) + \tau(V_s)Z_s(V_s) \tag{3.11}$$

where $Z_s(S)$ is a function of entropy of the non-reacted explosive, and

$$\tau(V_s) = exp\left(-\int_{V_{0s}}^{V_s}\frac{\Gamma}{V_s}dV_s\right) \tag{3.12}$$

Given any state point (V_s, E_s), τ is easily evaluated from (3.12), and hence Z_s can be determined from (3.11). The important point to note is that Z_s remains constant on an isentrope, and the function Z_s is the specific internal energy at $V_s = V_{0s}$ on the isentrope through the current (V_s, E_s) point. Assuming a linear variation of C_{Vs} with the temperature in the unreacted explosive, T_s, (which is about the best that is available experimentally) then the temperature at the point where the isentrope through (V_s, E_s) intersects the line $V_s = V_{0s}$ is given by,

$$T_{1s} = T_{0s} + \frac{2Z_s}{C_{V_{0s}} + \sqrt{C_{V_{0s}}^2 + 2Z_s\frac{dC_{Vs}}{dT_s}}} \tag{3.13}$$

where T_{0s} is the initial or ambient temperature. The temperature at the chosen point (V_s, E_s) is then related to T_{1s} via the expression,

$$T_s(V_s, E_s) = \tau(V_s)\,T_{1s} \tag{3.14}$$

The above unreacted EOS for the explosive relates to material at solid density. Since all heterogeneous explosives of interest have some degree of porosity, the unreacted EOS is based on porous Hugoniot data which is first extrapolated back to zero porosity using a method devised by Lambourn [104]. The zero porosity Hugoniot is then converted to form the principal isentrope, written in finite strain form, which is used as the basis for a Gruneisen form of the EOS [100]. This EOS, when used in conjunction with an appropriate porosity model, allows the unreacted Hugoniot of the porous explosive to be determined. CREST currently utilises the

Snowplough porosity model to evaluate the unreacted Hugoniot of a porous explosive.

Reaction Products EOS

For hydrocode modelling applications, a universally used analytic EOS for the reaction products is the JWL form [89] which is given by,

$$P_g = A \left(1 - \frac{w}{R_1} \frac{V_{0s}}{V_g} \right) exp \left(-R_1 \frac{V_g}{V_{0s}} \right) + B \left(1 - \frac{w}{R_2} \frac{V_{0s}}{V_g} \right) exp \left(-R_2 \frac{V_g}{V_{0s}} \right) + \frac{w E_g}{V_g} \tag{3.15}$$

where P_g, V_g, and E_g are respectively the pressure, specific volume, and specific internal energy of the gaseous reaction products, V_{0s} is the specific volume at solid density, and A, B, R_1, R_2, and w are constants.

3.3.3 EOS Model for Reacting Material

In CREST, the ISE model [102] is used to determine the EOS of the reacting material between unreacted solid explosive and gaseous reaction products, with the assumption that the solid and gaseous phases are in pressure equilibrium. The unreacted solid explosive is assumed to be on an isentrope through the point on its Hugoniot to which it was shocked with the gaseous detonation products taking up the remaining volume and internal energy at pressure equilibrium.

The entropy in the unreacted solid explosive is set by the leading shock wave after which, in the absence of additional shocks, the solid phase entropy remains constant. To calculate shock discontinuities in the hydrocodes by a continuous but rapid jump [105], an artificial viscosity, q, is added to the pressure in the governing flow equations. In order that the solid component of the mixture reaches the correct entropy appropriate to the initial shock, or to the initial shock plus any other shocks that enter the region in which reaction is taking place, the artificial viscosity needs to be applied to the unreacted solid component of the mixture, as well as to the mixture itself, so that it experiences the shock transition(s).

Simple mixture laws in terms of the mass fraction reacted, λ, are used to express the specific volume and the specific internal energy of the mixture as the weighted sums respectively of the specific volumes and specific internal energies in the separate phases. The appropriate equations for the model are,

$$dE + (P+q) dV = 0 \tag{3.16}$$

$$dE_S + (P+q) dV_s = 0 \tag{3.17}$$

$$V = (1-\lambda)V_s + \lambda V_g \tag{3.18}$$

$$E = (1-\lambda)E_s + \lambda E_g \tag{3.19}$$

$$P_s = P_s(V_s, E_s) \tag{3.20}$$

$$P_g = P_g(V_g, E_g) \tag{3.21}$$

$$P = P_s = P_g \tag{3.22}$$

where P, V, and E are respectively the pressure, specific volume, and specific internal energy of the mixture, q is the artificial viscosity, and λ is the mass fraction reacted. These equations are written with the assumption that the initial specific internal energy of the unreacted explosive is Q, the detonation specific energy. 'Release' of energy is treated within the phase change from unreacted explosive to detonation products, with λ as the progress variable.

There are normally two ways of treating the origin of energy for the unreacted explosive. In the perhaps more traditional method, the solid starts off with zero specific internal energy at $P = 0$, $V = V_0$, and energy is released through the reaction zone. The conservation of energy in the explosive is then $dE + (P + q)dV = \lambda dQ$. In the alternative method, the solid explosive is assumed to have potential energy Q at $P = 0$, $V = V_0$, Q being the detonation energy per unit mass. Energy is not then released explicitly in the reaction zone, but implicitly through the transformation of the unreacted solid explosive to detonation products. For hydrocodes it is convenient to use the potential energy method, since it does not require a change to the conservation of energy equation in the integration scheme. Thus, the potential energy method is used in the CREST model.

For pressure equilibrium it is required that, $P_s - P_g = 0$. Given (V, E, λ) for any point in the mixture, there are then 4 equations (3.17), (3.18), (3.19), and (3.22) and 5 unknowns (P, V_s, E_s, V_g, and E_g). Note that equation (3.16) is the internal energy equation for the mixture which is calculated by the hydrocode rather than the model itself. To solve for the unknown parameters, an iterative technique is used where the specific volume of the unreacted material, V_s, is allowed to adjust to achieve pressure equilibrium. For numerical reasons, to iterate for pressure equilibrium between the reactants and products 'significant' amounts of both components of the mixture need to be present. A cut-off, ε, is included in the model to signify where the mixture treatment is turned on, and then turned off, in a computational cell based on the value of the mass fraction reacted, λ, in the cell. If $\lambda < \varepsilon$, then the explosive is modelled with its unreacted EOS only, whereas if $(1 - \lambda) < \varepsilon$ then the explosive is modelled with the EOS for the reaction products. For all other values of λ, the explosive is treated as a mixture based on the two EOS's. Typically, a value of $\varepsilon = 10^{-4}$ is used in numerical simulations using CREST.

Newton iteration is used to to attain pressure equilibrium between the solid and gaseous phases in equation (3.22). If convergence is not attained within a given number of iterations, then the much slower Bisection method is used. This should be full-proof, and to date has not caused any problems, however alternative iterative methods could be easily implemented should the need arise.

3.3.4 Reaction Rate Model

To describe the explosive decomposition, the CREST reaction rate model utilises two reaction rates; (i) a fast reaction, $\dot{\lambda}_1$, which encompasses all the primary sources of reaction ('hot-spots' *etc*), and (ii) a slower reaction rate, $\dot{\lambda}_2$, associated with the bulk burn of the explosive and activated by the fast reaction. The overall reaction rate in the explosive is given by the weighted sum of these two rates, both of which are dependent on a function of entropy of the unreacted solid explosive, Z_s, which is calculated within the finite strain EOS.

The overall reaction rate, $\dot{\lambda}$, describing the explosive decomposition is given by,

$$\dot{\lambda} = m_1\,\dot{\lambda}_1 + m_2\,\dot{\lambda}_2 \tag{3.23}$$

where m_1 and m_2 are weighting factors. The forms of the individual reaction rates are given by,

$$\dot{\lambda}_1 = (1 - \lambda_1)\left[-2\,b_1\,ln(1 - \lambda_1)\right]^{\frac{1}{2}} \tag{3.24}$$

$$\dot{\lambda}_2 = (1 - \lambda_2)\,\lambda_1\left[2b_2\left(\frac{b_2\lambda_1}{b_1} - ln\,(1 - \lambda_2)\right)\right]^{\frac{1}{2}} \tag{3.25}$$

and the derivation of these equations is discussed in [61]. All λ's can range between 0 and 1 where, in particular, $\lambda = 0$ represents no reaction (unreacted solid explosive), and $\lambda = 1$ represents complete reaction (gaseous products).

Following the reasoning given in [61], the reaction rate parameters b_1 and b_2, which largely determine the time of the peak reaction rates, and m_1 and m_2, which determine the magnitude of the peak reaction rates, are functions of the entropy parameter Z_s given by the expressions,

$$b_1 = c_0\,(Z_s)^{c_1} \tag{3.26}$$

$$b_2 = c_2\,(Z_s)^{c_3} \tag{3.27}$$

$$m_1 = (1 - \lambda)\frac{c_6\,(Z_s)^{c_{12}}}{\sqrt{b_1}} \tag{3.28}$$

$$m_2 = (1 - \lambda)\left[\frac{c_8(Z_s)^{-c_9} + c_{10}(Z_s - c_{13})^{c_{11}}}{\sqrt{b_2}}\right] \tag{3.29}$$

where $c_0, c_1, c_2, c_3, c_6, c_8, c_9, c_{10}$, c_{11}, and c_{12} are constants which are fitted to particle velocity gauge data from one-dimensional, sustained shock, gas-gun experiments. An additional constant, c_{13}, is included to represent a threshold in entropy below which there is no reaction. Incorporating the depletion factor $(1 - \lambda)$ in the expressions for the weighting factors ensures that the overall reaction rate, $\dot{\lambda}$, is a smoothly varying function of time.

3.4 Implementation of CREST in Hydrocodes

3.4.1 Overview

To enable computer simulations of a range of explosive problems of interest to be performed using CREST, the model needs to be implemented into one or more hydrocodes. Hydrocodes are large computer programs that solve the equations governing unsteady material dynamic motion in terms of the conservation of mass, momentum, and energy. In order to obtain a complete solution, in addition to appropriate initial and boundary conditions, it is necessary to define a further relation between the flow variables. This can be found from a material model which relates stress to deformation and internal energy (or temperature). In most cases, the stress may be separated into a uniform hydrostatic pressure, and a stress deviator associated with the resistance of the material to shear distortion. Then, the relation between the hydrostatic pressure, the local density (or specific volume) and local specific internal energy (or temperature) is known as the equation of state. Various forms of equation of state (EOS) and material strength models are usually included in hydrocodes.

The CREST reactive burn model described above has been implemented into the one-dimensional hydrocode PERUSE [88], and the two-dimensional hydrocodes CORVUS [86], PETRA [106], and SHAMROCK [87]. The hydrocodes solve the governing flow equations which describe the conservation of mass, momentum, and internal energy of the reacting explosive mixture. The equations associated with the model, as given in Section 3.3, are solved within the EOS call, and hence the model appears to the hydrocodes just like any other EOS routine. However, to link the model to the hydrocodes required the creation of a number of extra arrays in PERUSE, CORVUS, PETRA, and SHAMROCK, to store the appropriate variables associated with the model that need to be carried from timestep to timestep.

The common features of the hydrocodes into which the CREST model has been implemented are: (i) the use of explicit time integration for temporal discretisation, (ii) use of the microsecond (μs), centimetre (cm), and gramme (g) system of units, and (iii) use of a staggered grid in the solution scheme. The grids are termed staggered since velocity and position are nodal quantities, while all other flow variables are cell centred. In some staggered grid schemes the nodal and cell centred quantities are at different time levels, but in the hydrocodes dicussed here the numerical schemes are such that at the end of a timestep all the flow variables are at the same time level.

In the following Sections, the implementation of the CREST model in PERUSE is described first, followed by its implementation in CORVUS, PETRA and SHAMROCK in turn.

3.4.2 PERUSE

Preamble

PERUSE is a one-dimensional Lagrangian, finite difference, multi-material hydrocode for the calculation of time dependent compressible flow [88]. It is used as a test-bed for the development and testing of models of explosive shock initiation behaviour. The strategy is to develop and test models within a relatively simple research code before implementing these models in the more complex two-dimensional hydrocodes.

The solution of the governing fluid flow equations is advanced forward in time using an explicit two-step (predictor-corrector) numerical scheme. The predictor-corrector method operates by running for half a timestep with first-order accuracy to calculate a half timestep pressure (the predictor step), and then using this to advance the equations for a full timestep with second-order accuracy (the corrector step). The overall scheme is second order accurate in time and space [90].

Solution Scheme

The steps in the solution method employed for the CREST model to advance the solution from t^n to t^{n+1} over a timestep $\Delta t^{n+\frac{1}{2}}$ are described below, where it is assumed that the state of the explosive is that of a reacting mixture. In the following difference equations the tilde symbol indicates intermediate values during a predictor or corrector step, and the superscript n represents the temporal index. For reasons of clarity, the spatial index has been omitted.

- Predictor Step   (forward Euler half timestep)

    The purpose of this stage is to compute values for the CREST variables at the half timestep $(n+\frac{1}{2})$, and proceeds as follows, where $V^{n+\frac{1}{2}}$, $E^{n+\frac{1}{2}}$, and q^n are given data, computed by the hydrocode.

    1. Update pressure due to the hydrodynamics. This involves solution of equations (3.11) and (3.17)-(3.21), and is performed at fixed λ.

        ISE model : Initialise $\tilde{V}_s^{n+\frac{1}{2}}$ (start with value of V_s from end of previous step). Calculate,

$$
\tilde{E}_s^{\,n+\frac{1}{2}} \;=\; E_s^{\,n} - (P^n + q^n)\left(\tilde{V}_s^{\,n+\frac{1}{2}} - V_s^{\,n}\right)
$$

$$
\tilde{Z}_s^{\,n+\frac{1}{2}} \;=\; \frac{\tilde{E}_s^{\,n+\frac{1}{2}} - \tilde{E}_i^{\,n+\frac{1}{2}}(V_s)}{\tilde{\tau}^{\,n+\frac{1}{2}}(V_s)}
$$

$$\tilde{P}_s^{\,n+\frac{1}{2}} = P_s\left(\tilde{V}_s^{\,n+\frac{1}{2}}, \tilde{E}_s^{\,n+\frac{1}{2}}\right)$$

$$\tilde{V}_g^{\,n+\frac{1}{2}} = \frac{V^{n+\frac{1}{2}} - (1-\lambda^n)\,\tilde{V}_s^{\,n+\frac{1}{2}}}{\lambda^n}$$

$$\tilde{E}_g^{\,n+\frac{1}{2}} = \frac{E^{n+\frac{1}{2}} - (1-\lambda^n)\,\tilde{E}_s^{\,n+\frac{1}{2}}}{\lambda^n}$$

$$\tilde{P}_g^{\,n+\frac{1}{2}} = P_g\left(\tilde{V}_g^{\,n+\frac{1}{2}}, \tilde{E}_g^{\,n+\frac{1}{2}}\right)$$

and iterate on $\tilde{V}_s^{\,n+\frac{1}{2}}$ until $\left|\tilde{P}_s^{\,n+\frac{1}{2}} - \tilde{P}_g^{\,n+\frac{1}{2}}\right| < 10^{-6}$ Mbars.

2. Calculate the explosive burn. Solve equations (3.23)-(3.29).

$$\tilde{b}_1^{\,n+\frac{1}{2}} = c_0\left(\tilde{Z}_s^{\,n+\frac{1}{2}}\right)^{c_1}$$

$$\tilde{b}_2^{\,n+\frac{1}{2}} = c_2\left(\tilde{Z}_s^{\,n+\frac{1}{2}}\right)^{c_3}$$

$$\tilde{m}_1^{\,n+\frac{1}{2}} = (1-\lambda^n)\frac{c_6\left(\tilde{Z}_s^{\,n+\frac{1}{2}}\right)^{c_{12}}}{\sqrt{\tilde{b}_1^{\,n+\frac{1}{2}}}}$$

$$\tilde{m}_2^{\,n+\frac{1}{2}} = (1-\lambda^n)\left[\frac{c_8\left(\tilde{Z}_s^{\,n+\frac{1}{2}}\right)^{-c_9} + c_{10}\left(\tilde{Z}_s^{\,n+\frac{1}{2}} - c_{13}\right)^{c_{11}}}{\sqrt{\tilde{b}_2^{\,n+\frac{1}{2}}}}\right]$$

$$\lambda_1^{\,n+\frac{1}{2}} = \lambda_1^{\,n} + \frac{\Delta t^{n+\frac{1}{2}}}{2}\,\dot{\lambda}_1^{\,n}$$

$$\lambda_2^{\,n+\frac{1}{2}} = \lambda_2^{\,n} + \frac{\Delta t^{n+\frac{1}{2}}}{2}\,\dot{\lambda}_2^{\,n}$$

$$\lambda^{n+\frac{1}{2}} = \lambda^n + \frac{\Delta t^{n+\frac{1}{2}}}{2}\,\dot{\lambda}^n$$

3. Update pressure due to the explosive burn. This involves solution of equations (3.11) and (3.17)-(3.21), and is performed at fixed λ.

<u>ISE model</u> : Initialise $V_s^{n+\frac{1}{2}}$ (start with value of $\tilde{V}_s^{n+\frac{1}{2}}$ from 1. above). Calculate,

$$E_s^{n+\frac{1}{2}} = E_s^n - \left[\frac{1}{2}\left(P^n + \tilde{P}^{n+\frac{1}{2}}\right) + q^n\right]\left(V_s^{n+\frac{1}{2}} - V_s^n\right)$$

$$Z_s^{n+\frac{1}{2}} = \frac{E_s^{n+\frac{1}{2}} - E_i^{n+\frac{1}{2}}(V_s)}{\tau^{n+\frac{1}{2}}(V_s)}$$

$$P_s^{n+\frac{1}{2}} = P_s\left(V_s^{n+\frac{1}{2}}, E_s^{n+\frac{1}{2}}\right)$$

$$V_g^{n+\frac{1}{2}} = \frac{V^{n+\frac{1}{2}} - \left(1 - \lambda^{n+\frac{1}{2}}\right)V_s^{n+\frac{1}{2}}}{\lambda^{n+\frac{1}{2}}}$$

$$E_g^{n+\frac{1}{2}} = \frac{E^{n+\frac{1}{2}} - \left(1 - \lambda^{n+\frac{1}{2}}\right)E_s^{n+\frac{1}{2}}}{\lambda^{n+\frac{1}{2}}}$$

$$P_g^{n+\frac{1}{2}} = P_g\left(V_g^{n+\frac{1}{2}}, E_g^{n+\frac{1}{2}}\right)$$

and iterate on $V_s^{n+\frac{1}{2}}$ until $\left|P_s^{n+\frac{1}{2}} - P_g^{n+\frac{1}{2}}\right| < 10^{-6}$ Mbars.

4. Update reaction rates ready for the corrector step. Solve equations (3.23)-(3.29).

$$b_1^{n+\frac{1}{2}} = c_0\left(Z_s^{n+\frac{1}{2}}\right)^{c_1}$$

$$b_2^{n+\frac{1}{2}} = c_2\left(Z_s^{n+\frac{1}{2}}\right)^{c_3}$$

$$m_1^{n+\frac{1}{2}} = \left(1 - \lambda^{n+\frac{1}{2}}\right)\frac{c_6\left(Z_s^{n+\frac{1}{2}}\right)^{c_{12}}}{\sqrt{b_1^{n+\frac{1}{2}}}}$$

$$m_2^{n+\frac{1}{2}} = \left(1 - \lambda^{n+\frac{1}{2}}\right)\left[\frac{c_8\left(Z_s^{n+\frac{1}{2}}\right)^{-c_9} + c_{10}\left(Z_s^{n+\frac{1}{2}} - c_{13}\right)^{c_{11}}}{\sqrt{b_2^{n+\frac{1}{2}}}}\right]$$

$$\dot{\lambda}_1^{n+\frac{1}{2}} = \left(1 - \lambda_1^{n+\frac{1}{2}}\right)\left[-2\,b_1^{n+\frac{1}{2}}\,ln\left(1 - \lambda_1^{n+\frac{1}{2}}\right)\right]^{\frac{1}{2}}$$

$$\dot{\lambda}_2^{n+\frac{1}{2}} = \left(1 - \lambda_2^{n+\frac{1}{2}}\right)\lambda_1^{n+\frac{1}{2}}\left[2b_2^{n+\frac{1}{2}}\left(\frac{b_2^{n+\frac{1}{2}}\lambda_1^{n+\frac{1}{2}}}{b_1^{n+\frac{1}{2}}} - ln\left(1 - \lambda_2^{n+\frac{1}{2}}\right)\right)\right]^{\frac{1}{2}}$$

$$\dot{\lambda}^{n+\frac{1}{2}} = m_1^{n+\frac{1}{2}}\dot{\lambda}_1^{n+\frac{1}{2}} + m_2^{n+\frac{1}{2}}\dot{\lambda}_2^{n+\frac{1}{2}}$$

- Corrector Step

  The CREST variables are now updated to the time level $n + 1$ as follows, where V^{n+1}, E^{n+1}, and q^n are given data, computed by the hydrocode.

  1. Update pressure due to the hydrodynamics. This involves solution of equations (3.11) and (3.17)-(3.21), and is performed at fixed λ.

     <u>ISE model</u> : Initialise $\tilde{V}_s^{n+1}$ (start with value of $V_s^{n+\frac{1}{2}}$ from the predictor step).

     Calculate,

$$\tilde{E}_s^{n+1} = E_s^n - \left(P^{n+\frac{1}{2}} + q^n\right)\left(\tilde{V}_s^{n+1} - V_s^n\right)$$

$$\tilde{Z}_s^{n+1} = \frac{\tilde{E}_s^{n+1} - \tilde{E}_i^{n+1}(V_s)}{\tilde{\tau}^{n+1}(V_s)}$$

$$\tilde{P}_s^{n+1} = P_s\left(\tilde{V}_s^{n+1}, \tilde{E}_s^{n+1}\right)$$

$$\tilde{V}_g^{n+1} = \frac{V^{n+1} - \left(1 - \lambda^{n+\frac{1}{2}}\right)\tilde{V}_s^{n+1}}{\lambda^{n+\frac{1}{2}}}$$

$$\tilde{E}_g^{n+1} = \frac{E^{n+1} - \left(1 - \lambda^{n+\frac{1}{2}}\right)\tilde{E}_s^{n+1}}{\lambda^{n+\frac{1}{2}}}$$

$$\tilde{P}_g^{n+1} = P_g\left(\tilde{V}_g^{n+1}, \tilde{E}_g^{n+1}\right)$$

     and iterate on $\tilde{V}_s^{n+1}$ until $\left|\tilde{P}_s^{n+1} - \tilde{P}_g^{n+1}\right| < 10^{-6}$ Mbars.

2. Calculate the explosive burn. Solve equations (3.23)-(3.29).

$$\tilde{b}_1^{n+1} = c_0 \left(\tilde{Z}_s^{n+1} \right)^{c_1}$$

$$\tilde{b}_2^{n+1} = c_2 \left(\tilde{Z}_s^{n+1} \right)^{c_3}$$

$$\tilde{m}_1^{n+1} = \left(1 - \lambda^{n+\frac{1}{2}} \right) \frac{c_6 \left(\tilde{Z}_s^{n+1} \right)^{c_{12}}}{\sqrt{\tilde{b}_1^{n+1}}}$$

$$\tilde{m}_2^{n+1} = \left(1 - \lambda^{n+\frac{1}{2}} \right) \left[\frac{c_8 \left(\tilde{Z}_s^{n+1} \right)^{-c_9} + c_{10} \left(\tilde{Z}_s^{n+1} - c_{13} \right)^{c_{11}}}{\sqrt{\tilde{b}_2^{n+1}}} \right]$$

$$\lambda_1^{n+1} = \lambda_1^{n} + \Delta t^{n+\frac{1}{2}} \dot{\lambda}_1^{n+\frac{1}{2}}$$

$$\lambda_2^{n+1} = \lambda_2^{n} + \Delta t^{n+\frac{1}{2}} \dot{\lambda}_2^{n+\frac{1}{2}}$$

$$\lambda^{n+1} = \lambda^{n} + \Delta t^{n+\frac{1}{2}} \dot{\lambda}^{n+\frac{1}{2}}$$

3. Update pressure due to the explosive burn. This involves solution of equations (3.11) and (3.17)-(3.21), and is performed at fixed λ.

   <u>ISE model</u> : Initialise V_s^{n+1} (start with value of $\tilde{V}_s^{n+1}$ from 1. above). Calculate,

$$E_s^{n+1} = E_s^{n} - \left[\frac{1}{2} \left(P^{n+\frac{1}{2}} + \tilde{P}^{n+1} \right) + q^n \right] \left(V_s^{n+1} - V_s^{n} \right)$$

$$Z_s^{n+1} = \frac{E_s^{n+1} - E_i^{n+1}(V_s)}{\tau^{n+1}(V_s)}$$

$$P_s^{n+1} = P_s \left(V_s^{n+1}, E_s^{n+1} \right)$$

$$V_g^{n+1} = \frac{V^{n+1} - \left(1 - \lambda^{n+1} \right) V_s^{n+1}}{\lambda^{n+1}}$$

$$E_g^{n+1} = \frac{E^{n+1} - \left(1 - \lambda^{n+1} \right) E_s^{n+1}}{\lambda^{n+1}}$$

$$P_g^{n+1} = P_g \left(V_g^{n+1}, E_g^{n+1} \right)$$

and iterate on V_s^{n+1} until $\left| P_s^{n+1} - P_g^{n+1} \right| < 10^{-6}$ Mbars.

4. Update reaction rates ready for the next timestep. Solve equations (3.23)-(3.29).

$$b_1{}^{n+1} = c_0 \left(Z_s{}^{n+1}\right)^{c_1}$$

$$b_2{}^{n+1} = c_2 \left(Z_s{}^{n+1}\right)^{c_3}$$

$$m_1{}^{n+1} = \left(1 - \lambda^{n+1}\right) \frac{c_6 \left(Z_s{}^{n+1}\right)^{c_{12}}}{\sqrt{b_1{}^{n+1}}}$$

$$m_2{}^{n+1} = \left(1 - \lambda^{n+1}\right) \left[\frac{c_8 \left(Z_s{}^{n+1}\right)^{-c_9} + c_{10} \left(Z_s{}^{n+1} - c_{13}\right)^{c_{11}}}{\sqrt{b_2{}^{n+1}}}\right]$$

$$\dot{\lambda}_1^{n+1} = \left(1 - \lambda_1{}^{n+1}\right) \left[-2\, b_1{}^{n+1}\, ln\left(1 - \lambda_1{}^{n+1}\right)\right]^{\frac{1}{2}}$$

$$\dot{\lambda}_2^{n+1} = \left(1 - \lambda_2{}^{n+1}\right) \lambda_1{}^{n+1} \left[2 b_2{}^{n+1} \left(\frac{b_2{}^{n+1}\lambda_1{}^{n+1}}{b_1{}^{n+1}} - ln\left(1 - \lambda_2{}^{n+1}\right)\right)\right]^{\frac{1}{2}}$$

$$\dot{\lambda}^{n+1} = m_1{}^{n+1}\, \dot{\lambda}_1^{n+1} + m_2{}^{n+1}\, \dot{\lambda}_2^{n+1}$$

3.4.3 CORVUS

The two-dimensional, finite element hydrocode CORVUS was initially a Lagrangian code but has since evolved into an Arbitrary Lagrangian Eulerian (ALE) code via the introduction of multi-material advection [86]. At the present time, the CREST model can only be used in Lagrangian mode in CORVUS as it has yet to be linked to the ALE package.

In the Lagrangian hydro phase of CORVUS, the time differencing is performed using a predictor-corrector solution method as per PERUSE. Thus, the steps required to advance the CREST model variables from t^n to t^{n+1} over a timestep $\Delta t^{n+\frac{1}{2}}$ in CORVUS are as detailed above in Section 3.4.2.

3.4.4 PETRA

Preamble

PETRA is a legacy two-dimensional Eulerian hydrocode [106]. Each hydro timestep in PETRA is composed of a Lagrangian phase followed by a remap phase. The Lagrangian phase involves advancing the values of the mesh quantites as if the mesh were free to move. However, as an Eulerian code is based on a stationary grid, the mesh quantities will be incorrectly located unless a correction procedure

is applied. This is the remap phase which corrects the mesh quantites back onto the fixed grid, and which shall be referred to as the advection phase. The Lagrangian and advection phases are dealt with separately below.

Lagrangian Phase

The Lagrangian phase of PETRA has the the same solution method as CORVUS (Lagrangian mode), the only difference being that in PETRA the predictor-corrector algorithm for the time differencing may be applied a number of times per timestep to reduce the number of advection steps performed (since the advection step is computationally more expensive). Thus, the order of the calculation in any timestep in the Lagrangian phase of PETRA is the same as that given for PERUSE in Section 3.4.2 above, except that $\Delta t^{n+\frac{1}{2}}$ is replaced by $\Delta t_l^{n+\frac{1}{2}}$ (the Lagrangian timestep) where $\Delta t_l^{n+\frac{1}{2}} = \Delta t^{n+\frac{1}{2}}/N$, and N is the number of Lagrangian steps to be performed per advection step. Thus, each predictor step has timestep $\Delta t_l^{n+\frac{1}{2}}/2$, and each corresponding corrector step has timestep $\Delta t_l^{n+\frac{1}{2}}$, and a total of $2N$ steps are required to advance the solution from t^n to t^{n+1} in the Lagrangian phase.

Advection Phase

PETRA is based on a fixed grid and so at the end of the Lagrangian phase the mesh quantities have to be mapped back to the original mesh. For CREST, the variables associated with the model need be corrected back to the stationary mesh such that the pressure equilibrium assumption for the reacting mixture is maintained. In addition, the reaction rates need to be re-calculated in preparation for the start of the next timestep. The advection method employed for CREST is by no means unique. Indeed two different advection methods were tried; the more successful of the two methods, as described below, has been shown to give good results.

By default PETRA advects mass, momentum, and specific internal energy. Additionally for CREST, the following quantities are advected via the PETRA 'blackbox' advector; the mass fractions reacted λ_1, λ_2, and λ, and the solid component variables comprising the specific volume, V_s, specific internal energy, E_s, and specific entropy Z_s. In the following description, the superscript 0 indicates values obtained from the 'black-box' advector, while the superscript 1 indicates values that have been corrected to pressure equilibrium. It is assumed that λ_1, λ_2, λ, and Z_s are fixed so that *e.g.* $Z_s{}^1 = Z_s{}^0$.

The steps in the solution method employed for the advection phase are given below. Perform 'black-box' advection, then;

1. Calculate the reaction rates ready for the next timestep. Solve equations (3.23)-(3.29).

$$b_1{}^1 = c_0 \left(Z_s{}^1 \right)^{c_1}$$

$$b_2{}^1 = c_2 \left(Z_s{}^1 \right)^{c_3}$$

$$m_1{}^1 = \left(1 - \lambda^1 \right) \frac{c_6 \left(Z_s{}^1 \right)^{c_{12}}}{\sqrt{b_1{}^1}}$$

$$m_2{}^1 = \left(1 - \lambda^1 \right) \left[\frac{c_8 \left(Z_s{}^1 \right)^{-c_9} + c_{10} \left(Z_s{}^1 - c_{13} \right)^{c_{11}}}{\sqrt{b_2{}^1}} \right]$$

$$\dot{\lambda}_1^1 = \left(1 - \lambda_1{}^1 \right) \left[-2 \, b_1{}^1 \, ln \left(1 - \lambda_1{}^1 \right) \right]^{\frac{1}{2}}$$

$$\dot{\lambda}_2^1 = \left(1 - \lambda_2{}^1 \right) \lambda_1{}^1 \left[2 b_2{}^1 \left(\frac{b_2{}^1 \lambda_1{}^1}{b_1{}^1} - ln \left(1 - \lambda_2{}^1 \right) \right) \right]^{\frac{1}{2}}$$

$$\dot{\lambda}^1 = m_1{}^1 \, \dot{\lambda}_1^1 + m_2{}^1 \, \dot{\lambda}_2^1$$

2. Update pressure due to advection. This involves solution of equations (3.11) and (3.17)-(3.21), and is performed at fixed λ.

   ISE model : Initialise V_s (start with $V_s{}^0$, the value returned from the 'black-box' advector). Also use $E_s{}^0$ from advection. Calculate,

$$E_s{}^1 = E_s{}^0 - (P+q) \left(V_s{}^1 - V_s{}^0 \right) \tag{3.30}$$

$$P_s{}^1 = P_s \left(V_s{}^1, E_s{}^1 \right) \tag{3.31}$$

$$V_g{}^1 = \frac{V^1 - \left(1 - \lambda^1 \right) V_s{}^1}{\lambda^1} \tag{3.32}$$

$$E_g{}^1 = \frac{E^1 - \left(1 - \lambda^1 \right) E_s{}^1}{\lambda^1} \tag{3.33}$$

$$P_g{}^1 = P_g \left(V_g{}^1, E_g{}^1 \right) \tag{3.34}$$

   and iterate on V_s until $\left| P_s{}^1 - P_g{}^1 \right| < 10^{-6}$ Mbars.

3.4.5 SHAMROCK

Preamble

SHAMROCK is a modern two-dimensional, adaptive mesh refinement (AMR), Eulerian hydrocode that essentially combines the PETRA Lagrange/remap fluid scheme with a block-patching refinement methodology [87]. AMR is a technique allowing the level of resolution to vary significantly across the computational domain and to dynamically adjust to the evolving solution by placing meshes in regions of interest, for example, where the solution is changing rapidly. The aim is to focus high resolution zoning only where it is needed and, thus, obtain a level of accuracy comparable with existing (non-AMR) hydrocodes but with less demand on computational resources.

With PETRA, having to mesh the entire computational domain with uniformly fine zones can be inefficient and the computational costs can become impractical. For example, accurate resolution of the reaction zone in a block of shock initiated explosive requires many zones/mm. When it is considered that, for many practical problems of interest, the dimensions of the explosive region can be many centimetres, it becomes obvious why calculations of this type can be so challenging on PETRA. Thus, reactive burn modelling is ideally suited to an AMR code and, in particular, for modelling large scale two-dimensional reactive burn problems, SHAMROCK will be preferred to PETRA.

As stated above, SHAMROCK uses essentially the same hydro scheme as the legacy code PETRA to advance the solution through time, *ie* the variables are first advanced in time using a Lagrangian step, and then the grid is mapped back to the stationary Eulerian mesh by advecting the cell quantities across cell boundaries to account for the mesh movement. The only difference between the two Eulerian codes in this respect is that SHAMROCK only allows one Lagrangian step to be performed per advection step. Thus, the order of the calculation in any timestep in the Lagrangian phase of SHAMROCK is the same as that given in Section 3.4.2, and the remap or advection phase is as given in Section 3.4.4.

The AMR procedure in SHAMROCK uses a domain wide coarse mesh as a starting point. Using various criteria, cells of interest are flagged for refinement. From this list of flagged cells, a set of mesh patches is created that covers these cells, and is finer by a factor two in each direction. The data from the coarse mesh is then transferred to the new mesh using a second order, montone mapping method. This procedure is continued until either the finest level of refinement has been reached or no more flagging criteria have been met. Refined cells that no longer meet the various refinement criteria are subsequently de-refined back down, eventually, to the coarse level grid.

Refinement Criteria for CREST

A suitable refinement criteria in SHAMROCK for the reactive burn material is required in order to flag-up cells that need to be refined to ensure accurate but efficient calculations using the CREST model. One possible refinement criteria that could be used for reactive burn calculations is to keep any cell with a mass fraction reacted greater than 0 and less than 1 refined to the finest level specified. However, this criteria has been found to be unsuitable for CREST. In CREST, for low shock strengths, the total mass fraction reacted, λ, may never reach a value of 1. This would mean those cells whose mass fraction reacted never gets to a value of 1 being refined at the finest level for all time once reaction starts in a cell which is clearly inefficient. Since the reaction rate histories from CREST are 'bell-shaped', see Figure 3.1 which is taken from [61], then in most instances the reaction rate eventually falls back to zero when reaction is complete which may not necessarily coincide with the burn fraction being 1.

Rather than refine the mesh based on the total mass fraction reacted, λ, explosive cells modelled using CREST are refined based on the total reaction rate, $\dot{\lambda}$. The refinement criteria is that if $\dot{\lambda} > \dot{\lambda}_{min}$, where $\dot{\lambda}_{min}$ is a minimum specified value for the total reaction rate, then those cells where this criteria is met will be refined at the finest level specified in the user input file. The default value for $\dot{\lambda}_{min}$ is 0.0001. The user can flag cells with a reaction rate greater than the default minimum value to a specified level for a specified time. The default is the finest level for all time for any region modelled with the CREST model.

3.5 Validation

3.5.1 Initial Validation

The CREST model described in Section 3.3 was initially built into the one-dimensional Lagrangian hydrocode PERUSE [88]. This relatively simple code was used as a test-bed to examine a number of numerical aspects of the CREST model, and to develop the mathematical form for its reaction rate model. The first explosive to be considered was the conventional, HMX-based explosive EDC37. Data on the shock initiation behaviour of EDC37 explosive was obtained from gas-gun experiments fired at Los Alamos National Laboratory using their embedded particle velocity gauge technique [37]. The relevent EDC37 experiments are summarised in Table 3.1. By fitting to the particle velocity gauge data from a number of the sustained single shock experiments, a CREST reaction rate model for EDC37 explosive was developed [61]. The fitting was carried out using PERUSE, and at a mesh resolution of 50 zones/mm, a meshing density at which mesh converged results using CREST are attained (see Section 3.6.4 for more details on mesh sensitivity and the

CREST model). The derived CREST model was subsequently shown to be able to accurately reproduce the shock initiation response of EDC37 to sustained single and double shocks, and thin pulse shock inputs with one set of parameters, and without recourse to a separate desensitisation model for double shocks.

Table 3.1: Summary of EDC37 Gas Gun Experiments

Shot No.	Impact Vel. (mm/μs)	Impactor Material	Input Pressure (kbars)	Run Distance (mm)	Type
1267	0.487	Z-cut sapphire	27.6 $\pm$ 1.5	>16.0	Single shock
1160	0.608	Vistal	35.2 $\pm$ 1.6	14.4	Single shock
1122	0.682	Vistal	39.5 $\pm$ 1.7	12.4	Single shock
1120	0.809	Vistal	49.1 $\pm$ 1.9	No data	Single shock
1159	0.918	Vistal	59.2 $\pm$ 2.1	7.0	Single shock
1277	1.403	Z-cut sapphire	108.0 $\pm$ 3.0	2.8	Single shock
1175A 1175B	0.921	Kel-F backed with Sapphire	29.4 $\pm$ 1.7 62.0	11.96 (6.18)	Double shock
1176A 1176B	0.925	Kel-F backed with Sapphire	62.0	12.29 (6.51)	Double shock
1194A 1194B	1.170	Kel-F backed with Sapphire	39.3 85.8	9.43 (2.40)	Double shock
1195A 1195B	1.165	Kel-F backed with Sapphire	39.3 85.8	8.40 (2.00)	Double shock
1281/ 1282	1.220	Kel-F backed with Sapphire	41.5 / 90.6	10.00	Double shock
1279	1.321	Kel-F	44.5 $\pm$ 1.5	>12.0	Thin pulse shock
1280	1.320	Kel-F	44.5 $\pm$ 1.5	17.0	Thin pulse shock

To validate the implementation of the CREST reactive burn model in the two-dimensional hydrocodes, the majority of the EDC37 gas gun experiments listed in Table 3.1 were calculated on CORVUS, PETRA, and SHAMROCK, and the results compared to the corresponding PERUSE results. The CREST parameters used for EDC37 in the simulations were taken from [61], and are reproduced in Table 3.2. For the impactor materials, Vistal was modelled using a Linear Gruneisen EOS with a strength description [96]. A Linear Gruneisen EOS was also used to model the z-cut Sapphire [99], while Kel-F was modelled using a Cubic Gruneisen EOS [98]. For consistency with PERUSE, all the calculations used a mesh density of 50 zones/mm in the EDC37 explosive (the SHAMROCK simulation was performed using a uniform 0.02mm grid), with appropriate meshing defined for the impactor materials. A scalar monotonic artificial viscosity was used to give an accurate representation of the shock discontinuity [91].

As an example of results obtained from the simulations, consider the calculation of EDC37 Shot 1159 where a sustained single shock of $\sim$59 kbars is input into the explosive sample via a Vistal impactor. The calculational set-up consisted of a 30mm thick Vistal flyer impacting a 30mm thick stationary EDC37 target, see

Table 3.2: CREST parameters for EDC37 [61] and PBX9502 [62]

Parameter	EDC37	PBX9502	Units
ρ_0	1.8445	1.889	g/cm^3
ρ_{0s}	1.8445	1.942	g/cm^3
Reaction products equation of state			
A	6.642021	4.603	Mbar
B	0.2282927	0.09544	Mbar
R_1	4.25	3.903	
R_2	1.825	1.659	
ω	0.25	0.48	
Q	0.0719557	0.0373	Mbar cm^3/g
Unreacted equation of state			
K_{0s}	0.1424525	0.09314021	Mbar
A_1	2.417494	0.246257	
A_2	2.208027	11.44221	
A_3	0.0	0.0	
B_1	0.0	16.8477	
B_2	0.0	6.534913	
B_3	0.0	0.0	
f_c	0.0	0.05	
δ	0.0	0.021322	
Γ_1	32.33557	126.4052	
Γ_2	3.596933	6.554447	
γ_{00}	0.4	0.4	
m	2.0	2.0	
T_{0s}	293.0	293.0	K
$C_{V_{0s}}$	9.17×10^{-6}	1.068×10^{-5}	Mbar cm^3/g/K
$\mathrm{d}C_{V_s}/\mathrm{d}T$	0.0	2.42×10^{-8}	Mbar cm^3/g/K^2
Reaction rate parameters			
c_0	2.0×10^8	2.0×10^7	μs^{-2}(Mbar cm^3/g)$^{-c_1}$
c_1	2.0	2.5	
c_2	2.2×10^8	8.0×10^6	μs^{-2}(Mbar cm^3/g)$^{-c_3}$
c_3	2.5	2.5	
c_6	0.0	1.8×10^{12}	μs^{-1}
c_8	1.6×10^{-4}	0.0	μs^{-1}(Mbar cm^3/g)^{c_9}
c_9	1.0	1.0	
c_{10}	4.0×10^5	3.0×10^3	μs^{-1}(Mbar cm^3/g)$^{-c_{11}}$
c_{11}	1.8	1.25	
c_{12}	0.0	5.0	
c_{13}	0.0	0.0012	Mbar cm^3/g

Figure 3.2. The two materials were assumed to be initially in contact with the mesh nodes of the flyer material being given the prescribed velocity of u=0.918 mm/μs, apart from the interface nodes which had a velocity of u/2. In the simulations, calculated profiles were obtained at a number of Lagrangian particle positions along the explosive charge length from the impact surface. The initial Lagrangian positions were at 0.0, 0.9, 1.9, 2.9, 3.9, 4.9, 5.5, 6.0, 6.5, 7.0, 8.0, 9.0, 10.0, and 11.0 mm into the EDC37 explosive charge.

As stated above, the Vistal impactor was modelled using a Linear Gruneisen EOS which has the form,

$$P = P_H(V) + \frac{\Gamma(V)}{V}(E - E_H(V)) \tag{3.35}$$

where P is the pressure, V is the specific volume, E is the specific internal energy, and P_H and E_H are the Hugoniot pressure and energy corresponding to the shock velocity (U_s)-particle velocity (U_p) relationship,

$$U_s = C_0 + sU_p \tag{3.36}$$

and the Gruneisen gamma is given by,

$$\Gamma(V) = \Gamma_0 + \Gamma_1 \frac{V}{V_0} \tag{3.37}$$

In the above equations C_0, s, Γ_0, and Γ_1 are material specific constants. The EOS and strength constants for Vistal are given in Table 3.3, where Y is the yield strength and μ is the shear modulus, and both are assumed constant.

Table 3.3: EOS parameters for Vistal, Perspex, and Kel-F.

Vistal [96]		Perspex [97]		Kel-F [98]	
ρ_0 (g/cm^3)	3.969	ρ_0 (g/cm^3)	1.186	ρ_0 (g/cm^3)	2.133
ρ_{0s} (g/cm^3)	3.969	ρ_{0s} (g/cm^3)	1.186	ρ_{0s} (g/cm^3)	2.133
C_0 (cm/μs)	0.814	C_0 (cm/μs)	0.2598	C_0 (cm/μs)	0.205
s	1.28	s	1.516	s_1	1.66
Γ_0	0.0	Γ_0	0.0	s_2	0.4064
Γ_1	2.3	Γ_1	0.97	s_3	-1.037
Y (Mb)	0.058			Γ_0	0.66
μ (Mb)	1.555			A	0.0

The calculated particle velocity profiles from CORVUS, PETRA, and SHAM-ROCK are shown in Figures 3.4-3.6 respectively, whereas the corresponding calculated profiles from the original PERUSE calculation are reproduced in Figure 3.3.

In each case, the first calculated history corresponds to the interface gauge (0.0mm), with the remaining traces at ever deeper positions into the explosive. The last calculated trace is at an initial depth of 11.0mm as measured from the impact surface. Overall, Figures 3.3-3.6 indicate that very similar results are obtained between all 4 hydrocodes.

To analyse the calculated results more closely, the computed particle velocity profiles from all 4 hydrocodes for EDC37 Shot 1159 are compared in Figure 3.7. Only a selected number of the histories are displayed for ease of viewing, and these were at initial depths of 0.0, 0.9, 2.9, 4.9, 6.0, 7.0, 9.0, and 11.0mm into the explosive. In addition, the corresponding calculated function of entropy profiles at the same positions are also compared in Figure 3.8. The function of entropy defines the reaction rate in the CREST model, and it is seen from Figure 3.8 that once the explosive material has been shocked the entropy, in this single shock case, remains constant behind the shock at each Lagrangian position for the rest of the calculation. It is observed that there are some minor differences between the calculated results from the different hydrocodes and these are explained below.

The reaction rate terms in CREST are chosen such that the reaction rate depends only on the local shock strength. Since entropy remains constant between shocks, a function of entropy of the unreacted explosive is chosen as the most appropriate variable representing shock strength for use in hydrocode calculations. For a sustained single shock into an explosive the shock grows in strength with depth. This is because the pressure increases behind the shock as energy is liberated and this information is fed forward due to the flow being supersonic with respect to the shock, therefore increasing the shock strength that then increases the reaction rate. Thus, the calculated function of entropy should increase monotonically with depth. However, it is seen in Figure 3.8 that the calculated function of entropy at the interface is over-predicted in all 4 codes since the entropy here is greater than the entropy at the next gauge position shown. Thereafter, the calculated entropy increases monotonically with depth as expected. The over-calculation in the function of entropy at the impact interface is analogous to the calculational errors described by Noh [93], and occurs as a result of a numerical start up error due to excess shock heating on shock formation. This phenomenon is known generically as 'wall heating' [107] and, in relation to CREST, is discussed in more detail in Section 3.6.2.

It is observed that, in this case, the over-calculation of entropy at the interface ('wall heating' effect) is greater in magnitude in the Lagrangian codes than the Eulerian codes, consistent with the findings of Rider [107], with CORVUS giving the largest, and PETRA the smallest, over-prediction in entropy at the interface. This trend is replicated in the calculated particle velocity histories in Figure 3.7. For example, looking at the calculated histories at depths of 6.0 and 7.0mm, it is observed that the magnitude of the peak particle velocity is greatest in the CORVUS calculation followed by, in order of decreasing magnitude, PERUSE, SHAMROCK, and PETRA. However, the observed differences are small, and it can therefore be

concluded that the different hydrocodes give consistent results.

3.5.2 SHAMROCK AMR Calculations

In the previous section, calculations using the SHAMROCK hydrocode were carried out with a uniform mesh, *i.e.* without using adaptive mesh refinement (AMR). To validate CREST in AMR calculations on SHAMROCK, a number of simulations of EDC37 gas-gun Shot 1159 were performed. Up to a maximum of 3 refinement levels were included in the calculations; the coarse level mesh and the number of refinement levels were varied as follows,

1. 0.02 mm uniform mesh (3200 x 16 cells) (no mesh refinement)

2. 0.04 mm coarse level mesh (1600 x 8 cells), with 1 level of refinement

3. 0.08 mm coarse level mesh (800 x 4 cells), with 2 levels of refinement

4. 0.16 mm coarse level mesh (400 x 2 cells), with 3 levels of refinement

The number of refinement levels was chosen such that in each calculation the mesh size at the highest refinement level remained constant. This corresponds to the mesh size in the uniform mesh case (0.02mm). Remember at each level of refinement the mesh is finer by a factor two in each direction. Using the refinement criteria for CREST as given in Section 3.4.5 with $\dot{\lambda}_{min}$=0.0001, the calculated particle velocity histories from the 4 calculations are shown in Figures 3.9-3.12 respectively. These figures indicate that very similar results are obtained between AMR calculations using CREST with different numbers of refinement levels specified.

Again, to analyse the calculated results more closely, the computed particle velocity profiles from all 4 calculations are compared in Figure 3.13, and the corresponding calculated function of entropy profiles at the same positions are compared in Figure 3.14. With different levels of refinement specified in the calculations, it can be seen that near identical results are obtained. However, some numerical noise is observed in the calculated histories as the number of refinement levels specified is increased. Looking at the calculated entropy profiles in particular, there are a number of occurances where the entropy changes from a constant value for a short time before reverting back to the correct value. These changes in entropy occur where the mesh is being de-refined back down from the highest refinement level to the coarse level grid as a result of the reaction rate falling below $\dot{\lambda}_{min}$. It is observed that the magnitude of these numerical oscillations increases with the number of mesh refinement levels used. The numerical noise is due to the mesh refinement algorithm in the hydrocode, and not a function of the CREST model. This is an area that requires further investigation to examine whether the numerical noise can be removed, or at least significantly reduced, to provide improved results when several refinement levels are specified in a calculation.

3.5.3   Summary

For the particular gas-gun experiment modelled (EDC37 Shot 1159), consistent results between all 4 hydrocodes, and between SHAMROCK calculations with different levels of mesh refinement, have been obtained. In addition, consistent results between PERUSE, CORVUS, PETRA, and SHAMROCK were also obtained for the other EDC37 gas-gun experiments listed in Table 3.1, thus validating the implementation of the CREST model in the hydrocodes. The small differences observed between the calculated results correlate with the amount of 'wall-heating' associated with the function of entropy solutions obtained from the different hydrocodes. This is discussed further in Section 3.6.2.

In adaptive mesh refinement calculations on SHAMROCK, increasing the number of refinement levels leads to increased numerical noise in CREST calculations. This occurs when the adaptive mesh is de-refined back down to the coarse level grid, and is a function of the mesh refinement algorithm in SHAMROCK. It is recommended that CREST AMR calculations on SHAMROCK are not run with a large number of refinement levels specified until further investigations are carried out to identify, and fix, the source of the observed numerical noise.

At present, CREST can only be used in Lagrangian mode in the two-dimensional ALE code CORVUS. In future, CREST will be incorporated into the ALE package in CORVUS, and the validation work carried out to date will provide a baseline against which this work can be tested.

3.6   Numerical Issues Regarding the CREST Model

3.6.1   Introduction

During the hydrocode implementation and use of the CREST reactive burn model, a number of areas of concern arose from hydrocode calculations using the model. In particular, the move to entropy-based reaction rates introduces a number of computational problems, not associated with pressure-based models, which have to be addressed. The problems are: (i) an over-prediction of internal energy/entropy/temperature at the impact interface in the modelling of explosive impact problems (*eg* gas-gun experiments), (ii) shocks in porous materials in conjunction with the Snowplough porosity model, and (iii) mesh sensitivity of an entropy-dependent model.

Although the use of entropy-based reactive burn models introduces additional numerical complexities, their ability to model a wider range of initiation phenomena when compared with pressure-based models, see [61] and [62], makes it worthwhile to identify and, where possible, attempt to solve these additional problems.

3.6.2 Modelling Gas Gun Experiments

In-material, particle velocity gauges, which are fielded in one-dimensional explosive gas-gun experiments, provide valuable insight into the reaction behaviour in impact initiated high explosives, see for example [37]. The modelling of these gas-gun experiments is required to help determine the parameters in the CREST reaction rate model by fitting to the available particle velocity gauge data. A classical problem in the modelling of such experiments is an over-prediction of internal energy, and hence, a function of entropy and temperature at the impact interface.

To illustrate this problem consider a simple, hypothetical, one-dimensional impact problem where a 30mm long Perspex projectile travelling at a velocity of u=0.931 mm/μs impacts a stationary PBX9501 explosive target also 30mm in length, see Figure 3.15. The two materials were assumed to be initially in contact with the mesh nodes of the projectile being given the prescribed velocity u, apart from the interface node which had a velocity of u/2. On impact a well defined, flat-topped, shock wave should travel into the target material, and a similar shock wave travel back into the projectile. Over the timescales considered here, the dimensions of the problem are such that the projectile and the target are affected only by the initial shock wave. For this hypothetical problem, the magnitude of the shock generated in the explosive would start the initiation process in PBX9501. However, here the PBX9501 region was treated as an inert material (no energy release). When developing reactive burn models, non-reactive calculations are performed to ensure that the explosive's unreacted behaviour is accurately modelled before considering calculations with energy release.

The simulations were carried out using the one-dimensional, multi-material hydrocode PERUSE [88], which is used as a test-bed for model development. A mesh density of 10 zones/mm was defined in both materials, and a monotonically limited artificial viscosity was used to accurately represent the propagating shock discontinuity [91]. The non-reactive calculations are mesh converged at this 0.1mm resolution. The explosive was modelled with its non-reactive EOS only from the CREST model, and was assumed to be non-porous, *i.e.* the explosive was at its solid density or theoretical maximum density (TMD). The non-reactive EOS parameters for PBX9501 [108] at TMD are given in Table 3.4. The Perspex impactor was modelled using a Linear Gruneisen EOS (3.35)-(3.37), and the EOS parameters for Perspex [97] are given in Table 3.3.

The calculated pressure and particle velocity profiles through the problem at two different times from impact are shown respectively in Figures 3.16 and 3.17. As the projectile and explosive target are initially in contact, time of impact is t=0.0 μs where the material interface is at 30mm. At t=2.0 μs and t=4.0 μs from impact, the material interface is at 30.8mm and 31.5mm respectively. The pressure-particle velocity Rankine-Hugoniot solution to this simple impact problem is shown in Figure 3.18, where both materials were described by their respective EOS's in Tables

Table 3.4: Non-reactive EOS parameters for PBX9501 at TMD [108]

Parameter	Value	Units
ρ_{0s}	1.860	g/cm^3
K_{0s}	0.1403788	Mbar
A_1	3.489228	
A_2	5.635034	
A_3	0.0	
B_1	0.0	
B_2	0.0	
B_3	0.0	
f_c	0.0	
δ	0.0	
Γ_1	89.40868	
Γ_2	4.929351	
γ_{00}	0.4	
m	2.0	
T_{0s}	293.0	K
$C_{V_{0s}}$	1.016×10^{-5}	Mbar cm^3/g/K
$\mathrm{d}C_{V_s}/\mathrm{d}T$	3.16×10^{-8}	Mbar cm^3/g/K^2

3.3 and 3.4. The condition at the interface after impact is that pressure and particle velocity must be equal in both materials. This condition is satisfied at the intersection of the Hugoniot curve for PBX9501 at a density of 1.860 g/cm^3 (TMD), and the Perspex Hugoniot through the impact velocity (u_i=0.0931 cm/μs). Comparing this solution with the calculated profiles in Figures 3.16 and 3.17, it is seen that, in the shocked region, pressure and particle velocity are both modelled correctly as continuous across the impact interface, and with the correct magnitudes. Thus, by examining the pressures and particle velocities from the calculation, all appears well with the modelling of this impact problem.

However, now consider the calculated internal energy profiles through the problem at the same times from impact (t=2.0 μs and t=4.0 μs), see Figure 3.19. For ease of illustration, the internal energy-distance plot in the unreacted explosive region only is shown in Figure 3.20. The internal energy in the shocked state is different in Perspex and unreacted PBX9501 explosive due to the different compressibilities to the two materials. Perspex has the higher internal energy due to the greater volume change in the shock. The feature to note in Figures 3.19 and 3.20 is that the internal energies immediately adjacent to the impact interface in both the Perspex and unreacted PBX9501 are over-predicted as a result of the impact. Away from the immediate vicinity of the impact interface, the internal energies in both the flyer and target materials are correctly modelled. CORVUS, PETRA, and SHAMROCK

calculations of this problem also over-calculate the internal energies either side of the impact interface. Since the entropy function and temperatures calculated in the unreacted PBX9501 explosive are both functions of the solid phase internal energy, then there is a corresponding over-prediction in these quantities adjacent to the impact surface, as shown in Figures 3.21 and 3.22 respectively. Since the pressure in the shocked state is correctly modelled then, for a $P(\rho, E)$ EOS, an over-calculation in internal energy results in a corresponding under-prediction in density.

The internal energy, function of entropy, and temperature in the non-reactive explosive material are significantly over-predicted in the first 3-4 meshes adjacent to the impact surface. Calculations with different mesh resolutions have shown that the over-predicted region is a fixed number of meshes ($\sim$3-4), and hence the length of this region will vary dependent on the mesh size used. In CREST, the reaction rate is a function of the current entropy of the unreacted explosive in a mesh. Thus, unlike models that use pressure-dependent reaction rates, CREST will over-predict the extent of reaction in the explosive immediately adjacent to the impact surface since the reaction rate will be artifically too high for the first few zones in the explosive. This could potentially have serious consequences on the rest of the modelling, and could lead to incorrect conclusions being made about the reactive behaviour of the explosive.

The over calculation in internal energy at the impact interface is analogous to the computational errors described by Noh [93], and is a result of a numerical start up error due to excess 'wall-heating' on shock formation. Artificial viscosity based hydrocodes typically spread shocks over a fixed number of meshes ($\sim$3 or 4). Upon impact, it thus takes a finite time for the shock to be formed, and during this time excessive shock heating occurs in the first few zones adjacent to the impact surface, which then propagates as an error over the time frame of the calculation. Since evaluation of temperature within hydrocodes is based on internal energy calculations, then temperature-based reactive burn models will also suffer from the same ('wall-heating') problem. To the authors knowledge, this problem has not been discussed in relation to temperature-dependent reactive burn models.

The 'wall-heating' problem has been an issue for as long as shock physics calculations have been performed. It is a very difficult and challenging problem for artificial viscosity based hydrocodes to overcome, and many studies analysing this phenomenon have been carried out, see for example [107] [109]. Suitable solutions to try to minimise the effect of this long-standing problem include, (i) an artificial heat conduction cure proposed by Noh [93], (ii) use of an adaptive mesh shock capturing technique [109], and (iii) new artificial viscosity formulations [110]. To examine whether it is necessary to apply a suitable solution method to the 'wall-heating' problem in relation to CREST, the effect of the error in the function of entropy at an impact interface has been studied in reactive (energy release) gas-gun calculations of the HMX-based explosive EDC37 [111]. To prevent an over-prediction in reaction rate occuring, the entropy function in the 'wall-heated' zones

was scaled locally to remove the 'wall-heating' effect. This involved running two calculations; it is necessary to firstly run an inert simulation to determine the 'wall-heating' effect, and then run the reactive (energy release) calculation with the entropy modified locally to remove the entropy over-prediction in the vicinity of the impact surface. Comparing energy release CREST calculations with and without entropy scaling factors, showed that the over-prediction in the entropy function at the impact surface made little difference to the calculated particle velocity histories.

To an extent, the effect of the 'wall heating' problem can be seen by examining Figures 3.7 and 3.8 which compare the hydrocode results for EDC37 Shot 1159. The over-prediction in the function of entropy at the impact interface is different between the different hydrocodes, yet the differences between the calculated particle velocity histories at the different Lagrangian positions is small. This suggests that the 'wall-heating' effect may not be problematic in modelling EDC37 explosive. However, this may not be the case for other explosives of interest, and will need to be investigated every time a CREST model for a new or different explosive is developed. Therefore, to avoid having to do this, appropriate methods will in future be applied to minimise the effect of this long standing problem in relation to CREST.

3.6.3 Snowplough Shocks

All heterogeneous solid explosives of interest contain some degree of porosity, and it is well known that this has an important influence on an explosive material's non-reactive Hugoniot, see for example [36]. Recently, a methodology for determining the EOS of unreacted explosives as a function of porosity has been developed [100]. This involves extrapolating available experimental Hugoniot data for the porous explosive to a best estimate of the fully dense Hugoniot. The EOS for the fully dense material used in conjunction with an appropriate porosity model then allows the unreacted porous Hugoniot at any porosity to be recovered.

CREST employs a porosity-dependent unreacted EOS. To take account of porosity in determining a porous explosive's non-reactive Hugoniot, CREST currently uses the Snowplough porosity model. In this model, the porous material is assumed to compact to close to its solid density at zero pressure, until its state lies on the EOS surface of the fully dense material for the rest of the calculation, see Figure 3.23. In addition, it is assumed that the sound speed is zero during the compaction process. The modelling of shocks in porous materials in conjunction with the Snowplough porosity model has been shown to be an area of concern regarding the use of the CREST model. To illustrate this, the simple impact problem described previously in Section 3.6.2 was re-run with porous PBX9501 explosive in place of the explosive at TMD. The initial density of the PBX9501 region was taken to be 1.825 g/cm^3, corresponding to an initial porosity of $\sim$2%, with the explosive material again being assumed inert, and hence modelled with its non-reactive EOS

taken from the CREST model. The EOS constants for the Perspex impactor, and unreacted PBX9501 target at TMD, were as given in Tables 2.2 and 3.4 respectively. The non-reactive EOS for the porous explosive was evaluated from the EOS at solid density using the Snowplough model.

The Rankine-Hugoniot solution to this impact problem is shown in Figure 3.18. In this case, where the Perspex projectile impacts on porous PBX9501 explosive, the solution is given by the intersection of the Hugoniot curve for PBX9501 at a density of 1.825 g/cm^3, and the Perspex Hugoniot through the impact velocity (u_i=0.0931 cm/μs). The calculated pressure-distance and particle velocity-distance profiles at t=2.0μs and t=4.0μs from impact are shown in Figures 3.24 and 3.25 respectively. Comparing the calculated profiles with the Rankine-Hugoniot solution, it is seen that the calculated values across the interface are in agreement with the Hugoniot solution. However, with the introduction of porosity into the explosive, small numerical oscillations in the pressure and particle velocity profiles are now observed behind the propagating shock wave in the initially porous explosive.

The corresponding calculated internal energy profiles through the problem at the same times from impact are shown in Figure 3.26, whereas the internal energy profiles through the explosive region only are shown in Figure 3.27. When the explosive was assumed to be at TMD, the calculated internal energy, away from the immediate vicinity of the impact interface, gave a flat-topped profile behind the shock front. With the porous explosive, the calculated internal energy oscillates about the correct value throughout that part of the explosive that has been traversed by the shock giving a 'sawtooth'-like profile. Again, as with the impact calculation where the explosive was at its TMD, the calculated internal energies immediately adjacent the impact surface in both the Perspex impactor and unreacted PBX9501 explosive target are over-predicted. However, with the introduction of porosity, the magnitude by which the internal energies are over-predicted has been reduced in comparison to the calculation where the explosive was at its TMD. As the function of entropy and temperature calculated in the non-reactive explosive are both related to the solid phase internal energy, then the observed 'sawtooth'-like behaviour behind the shock front in the explosive is repeated in the calculated profiles of these quantities, see Figures 3.28 and 3.29 respectively.

The 'sawtooth'-like behaviour seen in the computed internal energy, function of entropy, and temperature profiles in the explosive region is clearly an undesirable feature, particularly when using a reaction rate model dependent on the function of solid phase entropy in a mesh. These oscillations could give rise to numerical instabilities when considering CREST calculations with energy release. Interestingly, the numerical oscillations in the calculated entropy profiles persist throughout that part of the explosive that has been traversed by the shock, whereas the oscillations in the pressure profiles appear to be damped out at some distance behind the shock wave propagating through the explosive.

The observed numerical oscillations in the computed profiles in the explosive

region are as a result of the assumptions made in the Snowplough model, in particular that the sound speed is zero while the material is in its porous state. This assumption affects the calculation of artificial viscosity. The form of artificial viscosity, q, used in hydrocodes to represent a shock discontinuity is generally defined as a combination of linear and quadratic viscosities (*e.g.* monotonic q),

$$q = C_l \rho c \left| \Delta u \right| + C_q \rho \left(\Delta u \right)^2 \tag{3.38}$$

where ρ is density, c is sound speed, Δu is the velocity jump across a mesh, and C_l and C_q are constants. For a shock wave propagating into a porous material using the Snowplough model, the artificial viscosity is defined by only the quadratic viscosity term during compaction. The linear viscosity term is only non-zero once the porosity has been removed. From past experience of modelling inert solid materials, use of only a quadratic viscosity term results in numerical oscillations behind the shock front. The purpose of the linear term is to damp out these undesirable oscillations. It is also noted that, (i) at the point at which the initially porous material compresses up to its solid density there is a discontinuity in q, and (ii) the change in internal energy during compaction is given by dE= -q dV (since P=0), where q is given by the quadratic viscosity term only.

By the particular method that the hydrocode uses to evaluate the sound speed, examination of the squares of the sound speed (c^2) calculated from the non-reacted EOS for the explosive material in its porous state has shown that, at low porosities ($\sim$few %), a realistic sound speed is returned. At higher porosities, c^2 is non-physically negative, a state that cannot be tolerated in a hydrocode. Thus, for only slightly porous explosive materials, the calculated sound speed from the non-reactive explosive's EOS could be used in the calculation of the artificial viscosity while the material is in its porous state. In PBX9501 explosive at a density of 1.825 g/cm^3 ($\sim$2% porosity), the unreacted EOS returns realistic values for c^2 while the material is being compressed to solid density. Thus, the Snowplough model was modified by removing the assumption that the sound speed is zero during the compaction process, and using the sound speed as evaluated from the non-reactive EOS.

The inert impact calculation with porous PBX9501 was repeated using the modified Snowplough model, and the computed pressure, particle velocity, function of entropy, and temperature profiles are shown in Figures 3.30, 3.31, 3.32, and 3.33 respectively. These figures show that using a realistic sound speed in the calculation of artificial viscosity while the explosive material is in its porous state, all but removes the numerical oscillations and 'sawtooth'-like behaviour previously seen when assuming that the sound speed was zero. However, the modified Snowplough model is not suitable for highly porous explosives *e.g.* Non-Ideal explosives, since the c^2 values evaluted from the non-reactive EOS will be non-physically negative. In this case, a P-α porosity model [67] will be required. The main difference between a P-α porosity model and the Snowplough model is that a P-α model provides a realistic description of the compaction process at low stress levels which is absent

from the Snowplough model, see Figure 3.23. Thus, it allows the calculation of a realistic pressure and sound speed while the material is being compressed up to its solid density, and hence use of a P-α porosity model, in place of the Snowplough model, should help improve the modelling of shocks in porous explosives using CREST.

3.6.4 Mesh Sensitivity

In developing reactive burn models, fine zoning is usually required in hydrocode calculations to ensure adequate phenomenon resolution. An initial study of the sensitivity of CREST calculations, with energy release, to mesh density has been performed by modelling one-dimensional gas-gun experiments on the conventional, HMX-based high explosive EDC37 [37]. By fitting to embedded particle velocity gauge data from these experiments, a CREST model for EDC37 explosive was developed [61], and the model parameters are given in Table 3.2. The PERUSE hydrocode [88] was used to perform the mesh sensitivity study where the mesh resolutions used ranged from 5-100 zones/mm. For each calculation, a monotonically limited artificial viscosity was used to represent the propagating shock discontinuity [91]. Since the porosity of EDC37 is small ($\sim$0.2%), for the purposes of this study it has been treated as a fully dense material. In addition, the effect of the over-prediction in the function of entropy, due to the 'wall heating' effect, has been shown to be very small in EDC37 explosive [111].

As an example of results obtained from the mesh sensitivity study, Figure 3.34 shows the calculated particle velocity histories at a number of different gauge locations for EDC37 Shot 1159. For ease of illustration, only the results at the 2.9mm, 4.9mm, and 8.0mm gauge locations are shown which correspond roughly to the early, middle, and late stages respectively of the growth to detonation process. In the calculations reaction is allowed to proceed as the function of entropy rises with the arriving shock, *i.e.* there is reaction through the shock front. The computed CREST results show that mesh resolution has a significant effect on the calculated particle velocity histories. There is increased reaction at the 2.9mm and 4.9mm gauge locations with decreasing mesh density, which in turn results in earlier shock time of arrival at the gauge locations since the shock wave is accelerating faster. Correspondingly, there is a shortening of the computed run-distance and run-time to detonation with decreasing mesh density. Overall, the results indicate that a mesh density of 50 zones/mm is required to obtain mesh converged results.

The CREST mesh sensitivity results are to be compared with the corresponding calculations of EDC37 Shot 1159 using a pressure-dependent reactive burn model. The pressure-based Lee-Tarver model [49] is the most widely used reactive burn model for hydrocode simulations of shock initiation in heterogeneous explosives, and has been implemented in the PERUSE hydrocode (see Chapter 2). A Lee-Tarver model for EDC37 explosive was previously developed by Winter *et al.* [63]

by attempting to fit to a number of the EDC37 sustained single-shock gas-gun experiments as given in Table 3.1. The Lee-Tarver parameters for EDC37 explosive are reproduced in Table 3.5.

The calculated particle velocity profiles for EDC37 Shot 1159 at 2.9mm, 4.9mm, and 8.0mm gauge locations using the Lee-Tarver model are shown in Figure 3.35. As with the CREST simulations, reaction was allowed to proceed through the arriving shock front in each computational mesh. Using the Lee-Tarver model, there is only minimal effect on the calculated results with decreasing mesh resolution over the range of mesh densities used. It is only at the coarsest resolution tested (5 zones/mm) that the resolution used starts to have some noticeable effect on the calculated particle velocity histories. The trend is to slightly delay the growth of reaction with increasing mesh size, rather than to increase it as observed with CREST. Using Lee-Tarver, there are only small differences in the run-distances and run-times to detonation over the range of mesh densities used. The Lee-Tarver calculated results show that mesh convergence occurs at a mesh density of 10 zones/mm. Thus, it would appear that an entropy-dependent model requires a finer mesh than a pressure-dependent model in order to achieve mesh converged results.

The CREST mesh sensitivity study was repeated using two alternative approaches, termed 'q-switching', for turning on the reaction in a computational mesh, namely (i) reaction turned on when the derivative of artificial viscosity, q, with respect to time is less than zero ($\frac{dq}{dt} < 0$), which occurs approximately half way through the rise time of the arriving shock front, and (ii) the reaction was suppressed until the artificial viscosity dropped below a specified threshold (*eg* 10^{-6} Mb), such that there is no reaction throughout the rise time of the shock front. The computed results for EDC37 Shot 1159 using 'q-switching' method (i) for the onset of reaction in a mesh are shown in Figure 3.36. The calculated profiles are very similar to those in Figure 3.34, showing only a small improvement in mesh convergence properties compared to the results where reaction was allowed to proceed through the arriving shock wave.

The calculated results for EDC37 Shot 1159 using 'q-switching' method (ii) above for the onset of reaction in a computational cell are shown in Figure 3.37. Delaying the onset of reaction to start at approximately the top of the rise time of the arriving shock front, has improved the mesh convergence. There is now only a small effect on the calculated particle velocity results, and hence run-distances and run-times to detonation, with decreasing mesh resolution over the range of mesh densities used. It is only the 5 zones/mm results at late times that show any significant differences. Results are mesh converged at 10 zones/mm giving comparable mesh convergence properties to the pressure-based Lee-Tarver model. Comparing the CREST results in Figure 3.37 with the Lee-Tarver results in Figure 3.35, and ignoring the differences in the shape of the calculated profiles, there is a remarkable similarity, in terms of the mesh size effect, between the two sets of calculations.

Comparing all three approaches in CREST for turning reaction on in a cell,

Table 3.5: Lee-Tarver parameters for EDC37 [63] and PBX9502 [112]

Parameter	EDC37	PBX9502	Units
ρ_0	1.842	1.911	g/cm^3
ρ_{0s}	1.842	1.911	g/cm^3
Reaction products equation of state			
A	8.524	5.31396	Mb
B	0.1802	0.027039	Mb
G	3.8×10^{-6}	4.6×10^{-6}	
XP_1	4.60	4.1	
XP_2	1.30	1.1	
C_{V_g}	1.0×10^{-5}	1.0×10^{-5}	Mb/ K
Q	0.102	0.069	Mb
Unreacted equation of state			
R_1	69.69	70.75	Mb
R_2	-1.727	-0.0023005	Mb
R_3	2.148789×10^{-5}	2.20×10^{-5}	
R_5	7.80	8.617	
R_6	3.90	-2.1306	
C_{V_s}	2.505×10^{-5}	2.487×10^{-5}	
T_0	298.0	297.827	K
Reaction rate parameters			
I	3.0×10^{10}	1.5×10^5	μs^{-1}
b	0.667	0.667	
a	0.0	0.237	
x	20.0	7.0	
G_1	90.0	0.8	$Mb^{-y}\mu s^{-1}$
c	0.667	0.667	
d	0.333	0.111	
y	2.0	1.0	
G_2	200.0	3500.0	$Mb^{-z}\mu s^{-1}$
e	0.333	0.333	
g	1.0	1.0	
z	2.0	3.7	
λ_{igmax}	0.3	0.3	
λ_{G1max}	0.5	0.5	
λ_{G2max}	0.0	0.0	

the same results are essentially obtained at the highest mesh densities (100 and 50 zones/mm) irrespective of where the reaction is turned on in respect of the arriving shock front. However, at coarser resolutions significantly different results are obtained between the different approaches. Least variation in the calculated results with mesh size is observed where reaction is suppressed throughout the arriving shock front. It is not clear why one particular method for reaction commencement in a computational cell should be preferred over any other of the approaches tried here. However, to implement the 'q-switching' methods described above required additional modifications to be made to the hydrocode, and hence the more natural approach is to allow reaction to proceed through the arriving shock wave. The mesh sensitivity study on the HMX-based explosive EDC37 has shown that using this approach the entropy-dependent CREST model requires a finer mesh (50 zones/mm) than the pressure-based Lee-Tarver model (10 zones/mm), to achieve mesh converged results.

More recently, a CREST model for the TATB-based insensitive high explosive PBX9502 has been developed [62]. Four one-dimensional, single shock, gas-gun experiments and the one-dimensional Pop-Plot were used to determine the parameters in the CREST reaction rate model for PBX9502. The single shock gas-gun experiments that the model has been calibrated to are summarised in Table 3.6. It is well known that insensitive high explosives have much longer reaction zones than conventional high explosives; typical reaction zone widths deduced from detonation experiments are (i) ~ 0.1 mm for HMX-based explosives, and (ii) ~ 1.0 mm for TATB-based explosives. Since the standard rule of thumb is that ~ 10 meshes are needed to resolve the reaction zone in an explosive, then insensitive high explosives should be less demanding on mesh resolution than conventional high explosives.

Table 3.6: Summary of single-shock PBX9502 gas-gun experiments

Shot No.	Density (g/cm^3)	Impact Vel. (mm/μs)	Impactor Material	Input Pressure (kbars)	Run Distance (mm)
2S-70	1.889	2.349	Kel-F	106.5	11.82
2S-69	1.889	2.493	Kel-F	116.2	9.17
2S-86	1.888	2.766	Kel-F	135.5	6.01
2S-85	1.886	3.118	Kel-F	162.2	3.68

To examine the mesh resolution requirements for an insensitive high explosive, the mesh sensitivity study performed on EDC37 has been repeated on PBX9502. Hydrocode calculations of gas-gun Shot 2S-69 have been carried out on PERUSE at resolutions of 5, 10, 20, 50, and 100 zones/mm to examine the mesh convergence properties of the CREST model for PBX9502 explosive. The CREST model parameters for PBX9502 are given in Table 3.2. In the calculations the Kel-F impactor

was modelled using a Cubic Gruneisen EOS [98] of the form,

$$P = \frac{\rho_{0s}\, C_0^2\, \xi \left[1 + \left(1 - \frac{\Gamma_0}{2}\right)\xi - \frac{A}{2}\,\xi^2\right]}{\left[1 - (s_1 - 1)\xi - s_2\, \frac{\xi^2}{\xi+1} - s_3\, \frac{\xi^3}{(\xi+1)^2}\right]^2} + (\Gamma_0 + A\xi)\,\rho_{0s}\, E \quad ,\xi \geq 0 \quad (3.39)$$

$$P = \rho_{0s}\left(C_0^2\,\xi + \Gamma_0\, E\right) \qquad\qquad\qquad ,\xi < 0 \quad (3.40)$$

where,

$$\xi = \frac{\rho}{\rho_{0s}} - 1 \qquad\qquad (3.41)$$

is the compression, and the shock velocity (U_s)-particle velocity (U_p) relationship is non-linear,

$$U_s = C_0 + s_1\, U_p + s_2\left(\frac{U_p}{U_s}\right)U_p + s_3\left(\frac{U_p}{U_s}\right)^2 U_p \qquad (3.42)$$

The EOS parameters for Kel-F are from Steinberg [98] and are given in Table 3.3. Particle velocity histories were obtained from the calculations at the following Lagrangian positions in the explosive material; 0.00, 3.06, 4.18, 4.96, 5.74, 6.54, 7.34, 8.12, 8.92, 9.70, 10.50, 11.00, 12.00, and 13.00mm.

Figure 3.38 shows the calculated particle velocity results for Shot 2S-69 over the range of mesh densities used, where reaction was allowed to proceed through the arriving shock front in each computational mesh. Again, for ease of illustration, only a handful of gauge locations are plotted, namely the 4.18mm, 7.34mm, and 11.0mm gauge positions, which correspond roughly to the early, middle, and late stages respectively of the growth to detonation process. For PBX9502, moving to coarser zoning increases the numerical oscillations on the calculated particle velocity histories. The shock time of arrival, and the timing and magnitude of peak particle velocity, is relatively well matched down to $\sim$10 zones/mm, and there is very little difference in the computed run-distances and run-times to detonation. At 5 zones/mm meshing, significant oscillations appear on the computed particle velocity histories, and there is increased reaction at the 7.34mm gauge position which results in earlier shock time of arrival at the 11.0mm gauge location. As a result, the computed run-distance to detonation is slightly shorter than those computed at the other mesh resolutions used here. Over the range of mesh densities used, the calculated CREST results show that there is less sensitivity to mesh size with PBX9502 compared to EDC37. Mesh converged results are obtained at a mesh density of 20 zones/mm for PBX9502, whereas a mesh density of 50 zones/mm is required to obtain mesh converged results on EDC37 explosive.

The CREST mesh sensitivity results on PBX9502 explosive have been compared with the corresponding calculated results using the pressure-dependent Lee-Tarver model. By fitting to experimental Pop-Plot data [37], a Lee-Tarver model for

PBX9502 has been developed [112], and the model parameters are reproduced in Table 3.5. The calculated particle velocity profiles at the 4.18mm, 7.34mm, and 11.0mm gauge positions for Shot 2S-69 using the Lee-Tarver model are shown in Figure 3.39, where reaction was allowed to proceed through the arriving shock front. Over the range of mesh densities used, it is observed that there is very little or no difference between the computed profiles. It is only at mesh densities less that 5 zones/mm that significant differences are observed in the computed particle velocity histories, and hence the calculated results are converged at a mesh density of 5 zones/mm. Thus, for a different explosive, it is again observed that the entropy-dependent CREST model requires a finer mesh than the pressure-dependent Lee-Tarver model to obtain mesh converged results. Again, consistent with CREST, calculations using the Lee-Tarver model are less demanding on mesh resolution for PBX9502 in comparison to EDC37. This is due to the longer reaction zones in insensitive high explosives.

To complete the CREST mesh sensitivity study on PBX9502 explosive, calculations using the two 'q-switching' approaches for turning on reaction in a computational mesh, as described previously, were also run. Figure 3.40 shows the calculated particle velocity histories at the 4.18mm, 7.34mm, and 11.0mm gauge locations for Shot 2S-69 using 'q-switching' method (i) for the onset of reaction in a mesh. Again, as with the EDC37 results, the calculated histories are very similar to those where reaction was allowed to proceed through the arriving shock front, see Figure 3.38, thus showing little improvement in the mesh convergence properties of the model. The calculated results for PBX9502 Shot 2S-69 using 'q-switching' method (ii) are shown in Figure 3.41. It is observed that, consistent with results on EDC37 explosive, mesh convergence is improved by delaying the commencement of reaction in a mesh until after the shock has formed.

To independently address the issue of mesh convergence using an entropy-based reaction rate model, Fluid Gravity, as part of an external contract, were asked to perform calculations using their two-dimensional Eulerian hydrocode EDEN [113]. Calculations on EDC37 explosive over a range of mesh densities, where different EOS's and a different form of the entropy-dependent reaction rate were used, gave very similar results to those obtained with CREST for EDC37. Therefore, it can be concluded that the form of the reaction rate and/or the EOS's used in CREST are not the cause of the mesh convergence problems. It is not yet understood why CREST requires a finer mesh than a pressure-dependent model to achieve mesh converged results, and further work is therefore required to understand the mesh convergence properties of entropy-based models.

To overcome the more restrictive mesh size requirements of an entropy-dependent model, CREST has been implemented into the two-dimensional Eulerian adaptive mesh refinement (AMR) hydrocode SHAMROCK with an appropriate refinement criteria defined for the model. This will enable large, two-dimensional shock initiation problems of interest to be simulated at the size of mesh required by CREST to

obtain mesh converged results.

3.6.5 Discussion

The modelling of simple impact problems involving explosives is important for two reasons. Firstly, many safety problems of interest involve situations of impact initiation of high explosives and, secondly, the modelling of explosive gas-gun experiments is usually required to calibrate the reaction rate parameters in a reactive burn model. The modelling of a simple, hypothetical, one-dimensional impact problem, where a Perspex projectile impacts a stationary (inert) explosive target, has been performed to highlight two areas of concern relating to the hydrocode implementation and use of the CREST reactive burn model.

The first area of concern relates to the over-calculation of specific internal energy in both the impactor and, more importantly, the unreacted explosive target in the immediate vicinity of the impact interface. This occurs irrespective of whether or not the material to be impacted is porous. To be able to model the essential experimental phenomena in shock initiation of heterogeneous solid explosives, CREST employs a reaction rate that is a function of the current entropy of the unreacted explosive in a mesh. Since the function of entropy calculated in the non-reactive explosive is related to the specific internal energy, then CREST will over-predict the rate of energy release in the explosive in the vicinity of the impact surface. This could potentially have serious repercussions on the rest of the modelling, and could lead to incorrect conclusions being made about the initiation and reaction behaviour in impact initiated explosives. The error in internal energy at the interface in modelling impact problems is caused by excessive shock heating on shock formation. This has been termed 'wall-heating', and is an inherent problem for artificial viscosity based hydrocodes to which there is no known solution, although a number of methods have been suggested to minimise the effect of the 'wall-heating' problem.

The effect of the error in the function of entropy at an impact interface was examined in energy release calculations of EDC37 gas-gun experiments [111]. To prevent an over-prediction in reaction rate occuring, the entropy function in the 'wall-heated' zones was scaled locally to remove the 'wall-heating' effect. By comparing CREST energy release calculations, both with and without entropy scaling factors, it was shown that the over-prediction in the entropy function at the impact surface made little difference to the calculated particle velocity histories. The conclusion from this study was that the 'wall-heating' effect is not problematic in modelling EDC37 explosive, and thus allows CREST to be used to model two-dimensional geometries without the need to use complicated methods to determine and apply appropriate entropy correction factors. However, this may not be the case for other explosives of interest, and will need to be investigated every time a CREST model for a new or different explosive is developed. Therefore, to avoid having to do this, proposed suitable methods to minimise the effect of the long standing 'wall-heating'

problem will in future be tried out in relation to CREST.

The second area of concern is the modelling of shocks in porous materials in conjunction with the Snowplough porosity model. The application of the Snowplough model in CREST to accurately determine the Hugoniot of unreacted porous explosive produces undesirable numerical oscillations in the calculated profiles from the simple impact problem, in particular the calculated function of entropy of the solid phase explosive. Since this is the variable upon which the CREST reaction rate model is dependent, then this could give rise to numerical instabilities in energy release calculations. The source of these unwanted oscillations has been traced to the calculation of artificial viscosity in the porous material to represent the shock discontinuity. In the Snowplough model, the velocity of sound is zero while the material is in its porous state, and hence the artificial viscosity is defined by only a quadratic viscosity term during the compaction process. The linear viscosity term, whose purpose is to damp out post-shock oscillations, is only non-zero once the porosity has been removed.

The modelling of shocks in porous materials in conjunction with the Snowplough model can be improved by removing the assumption that the sound speed is zero while the material is being compressed to solid density. It has been shown that if a real sound speed is calculated from the unreacted EOS while the material is in its porous state, and this is then used in the calculation of the artificial viscosity, then the undesirable numerical oscillations are very significantly reduced. However, this is only applicable to low porosity materials since, for highly porous materials, the values of the square of the sound speed calculated from the unreacted EOS will be non-physically negative, a state that cannot be tolerated in a hydrocode. To overcome these problems, use of a P-α type porosity model in place of the Snowplough model is being considered for CREST. The P-α porosity model aims to provide a realistic description of the compaction process at low stress levels, and enables a realistic sound speed to be calculated while the material is being compressed up to solid density. Therefore, use of a P-α model should help improve the modelling of shocks in porous materials with CREST.

In energy release calculations using the CREST reactive burn model, a further area of concern relates to the sensitivity of the model to mesh size. This has been examined by modelling one-dimensional gas-gun experiments on two different explosives, namely the conventional HMX-based explosive EDC37, and the insensitive TATB-based explosive PBX9502. Where reaction is allowed to proceed through the arriving shock front, a mesh density of 50 zones/mm is required for EDC37 to obtain mesh converged results of the shock to detonation transition, whereas PBX9502 requires a mesh density of 20 zones/mm. The coarser mesh required by PBX9502 for mesh convergence is a reflection of the longer reaction zone of insensitive high explosives like PBX9502 compared to near ideal explosives like EDC37. Using the above approach for reaction commencement in a computational cell, comparison of the mesh convergence properties of the CREST model, and pressure-based

Lee-Tarver model, has shown that the entropy-dependent CREST model requires a finer mesh than the pressure-dependent Lee-Tarver model to obtain mesh converged results; 50 zones/mm (CREST) vs 10 zones/mm (Lee-Tarver) for EDC37, and 20 zones/mm (CREST) vs 5 zones/mm (Lee-Tarver) for PBX9502.

The mesh convergence of the CREST model is improved when 'q-switching' treatments are applied. In particular, the mesh convergence properties are greatly improved in the case where the reaction rate is effectively switched off until the shock front has passed. It is not clear why one particular method for the start of reaction in a mesh should be preferred over any of the other methods that have been tried. Since modifications are required to the hydrocodes to implement the 'q-switching' methods, then the more natural approach is to allow reaction to proceed through the arriving shock front. In this case, it is not yet understood why CREST requires a finer mesh than a pressure-dependent model to achieve mesh converged results, and the work undertaken by Fluid Gravity indicates that it is not the form of the reaction rate equation and/or the EOS's used in CREST. Therefore, further investigations are required to understand the mesh convergence issues relating to an entropy-dependent model. One possible suggestion is that the CREST method may be more mesh sensitive being an entropy-dependent model, because entropy is more sensitive to errors in shock heating introduced by the artificial viscosity than a pressure-dependent method. Since artificial viscosity is an integral part of the CREST model, further investigations could include trying other types of artificial viscosity to see if different forms show more or less sensitivity to mesh size.

The finer meshing required by CREST has led to the implementation of the model in a two-dimensional Eulerian AMR hydrocode to enable large problems of interest to be calculated at appropriate mesh resolutions. The question of mesh convergence in two-dimensional calculations also needs to be addressed. The mesh sensitivity study performed needs to be extended to see whether the findings in one-dimensional calculations are also true in two-dimensional calculations. In addition, different meshing may be required to obtain mesh converged results in modelling different phenomena *e.g.* shock to detonation transition, detonation propagation, corner turning *etc*, and this also needs to be examined.

3.7   CREST Applied to Two-Dimensional Experiments

3.7.1   Preamble

To date CREST models for the conventional high explosive EDC37 [61], and the insensitive high explosive PBX9502 [62], have been developed. The EDC37 model [61] was fitted to one-dimensional particle velocity gauge data from a number of sustained, single shock, gas-gun experiments examining the shock to detonation transition. The same model was then subsequently shown to be able to simulate

one-dimensional double shock and thin pulse shock initiation experiments. Unlike pressure-based models, the double shock data was fitted without recourse to an additional desensitisation model. Four one-dimensional, single shock, gas-gun experiments and the one-dimensional Pop-Plot were used to determine the parameters in the CREST model for PBX9502 [62]. The same model was then also able to predict a number of other sustained single shock, and thin pulse initiation experiments. In addition, by utilising a porosity-dependent unreacted EOS in CREST, the model was also able to predict the effects of porosity on RX-03-AU (which has the same composition as PBX9502) initiation threshold data. Thus, CREST is able to accurately reproduce a range of one-dimensional shock initiation data on both EDC37 and PBX9502.

At the outset of the development of the CREST model, one important objective was that CREST should be a comprehensive model, meaning that it should be capable of modelling all relevent phenomena from simple shock initiation to the propagation of full detonation and its capability to fail. To examine the wider applicability of the CREST model, and to test its predictive capability, by which it is meant can it model experiments outside its fitting regime, it needs to be applied to a representative range of both one-dimensional, and more importantly two-dimensional experimental data. One such situation is whether the model can predict detonation propagation, which by its very nature is two-dimensional, as well as the one-dimensional build-up or growth to detonation from relatively weak shock inputs.

Two-dimensional detonation propagation data on EDC37 explosive is scarce. However, the detonation propagation behaviour of Los Alamos' insensitive high explosive PBX9502 has been extensively studied [114] [115] [116]. Therefore, to provide a more rigorous test of CREST's predictive capability, the PBX9502 model is applied, unmodified, to two-dimensional detonation propagation experiments. Data on the diameter effect (detonation velocity as a function of charge diameter) including failure diameter and detonation waveshapes in PBX9502, is used to see how well, or otherwise, the PBX9502 CREST model, fitted to one-dimensional shock initiation data, can predict two-dimensional detonation propagation experiments.

3.7.2 PBX9502 Detonation Experiments

A fundamental detonation performance test is the detonation rate stick, a cylinder of unconfined explosive in which the detonation velocity is measured. For propagation along a cylinder of explosive, the detonation wave interacts with the explosive surface resulting in waves reflected into the reaction zone, which change the rate of reaction. These effects diffuse inwards along the reaction zone and the wave becomes curved. The steady state velocity decreases with the diameter of the cylinder as a result of the wave curvature. When the diameter of the explosive

reduces below a critical size the detonation wave is unable to support itself and ultimately fails to propagate. A series of rate sticks fired at different diameters gives the so-called diameter effect curve, which plots the detonation velocity as a function of inverse radius or inverse diameter. The diameter effect curve terminates at the so-called failure diameter, the size below which detonation will not steadily propagate. In addition to measuring the detonation velocity, the detonation waveshape of the wave emerging from the downstream end of the cylinder can also be measured in rate stick experiments. This collection of data has been obtained on PBX9502 explosive.

The diameter effect in PBX9502 explosive was first examined by Campbell and Engelke [114]. A later detailed study by Campbell [115] explored the combined effects of charge size (including failure diameter) and initial temperature (75°C, 24°C, and -55°C) on unconfined PBX9502 rate sticks ranging in diameter from 6 to 108mm. The results showed that the diameter effect curve and failure diameter in PBX9502 are temperature dependent. In particular, at large diameters the detonation velocity decreases as the temperature increases, due to the effect of temperature on initial density, whereas as at small diameters the detonation velocity falls in line with temperature due to a decrease in the reaction rate. At intermediate charge sizes, the detonation velocity remains approximately constant with change in temperature. Finally, the failure diameter varies inversely with the initial temperature of the explosive charge.

In a more recent study of detonation in PBX9502, Hill *et al.* [116] added a wavefront measurement to the basic rate stick experiment. Waveshape and detonation velocity data were obtained for charge diameters ranging from 8 to 50mm, and at the same temperatures as the Campbell experiments in [115]. The results were consistent with Campbell's findings showing that detonation velocities in PBX9502 vary with temperature. The measured detonation waveshapes also showed a sensitivity to temperature with, at a given charge size, the hotter waves being slightly flatter. This was attributed to (due to temperature-sensitive kinetics) PBX9502 having thinner reaction zones at elevated temperatures. Comparing the available PBX9502 rate stick data, Hill *et al.* [45] noted some variability in the detonation behaviour of the explosive between the different studies; for example, the detonation velocities measured by Hill *et al.* [116] are ∼0.5% lower than those of Campbell [115]. This was attributed to the different material lots used, and will be discussed in more detail later.

This collection of detonation data on PBX9502, the diameter effect curve, failure diameter, and detonation waveshapes, contains a significant amount of useful information about the explosive that the CREST model for PBX9502 can be tested against. At the present time the model for PBX9502 has been applied to the ambient temperature data only. It is planned to apply the model to the data at the temperature extremes in the near future.

3.7.3 Numerical Simulations

Preamble

The two-dimensional Eulerian hydrocode PETRA, incorporating the CREST model, was used to simulate the unconfined PBX9502 rate stick experiments. Here, only the ambient temperature (24°C) experimental results are considered for comparison with CREST model calculations. Rate stick calculations were carried out at charge diameters of 6, 7, 7.5, 8, 8.5, 9, 10, 12, 18, and 24mm. The basic calculational set-up is shown in Figure 3.42, where only half the geometry is modelled due to the problem being cylindrically symmetric.

The PBX9502 main charge is initiated by a booster charge of PBX9501 explosive of the same diameter as the main charge. In general, the booster had a length-to-diameter (L/D) ratio of one, whereas the PBX9502 main charge had a L/D ratio of at least seven. The detonation wave reaches a steady state after propagating about four diameters in the cylindrical charge. Programmed burn, where wave propagation is determined by a Huygens' construction assuming a constant detonation velocity, is used for the booster explosive. This is initiated via a single detonation point on the axis of symmetry, and the expanding detonation products for PBX9501 are modelled via the JWL form of EOS, and whose parameters are taken from Dobratz [117]. The CREST model is used for the PBX9502 main charge where the model parameters were as given in Table 3.2, and a starting density of 1.890 g/cm^3 was used in all calculations.

The hydrocode simulations were carried out at uniform mesh resolutions of 10 and 20 zones/mm, and a scalar monotonic artificial viscosity was used to represent the propagating shock discontinuity [91]. Lagrangian marker particles were used to record the time of arrival of the shock front at various positions. These were placed along the length of the PBX9502 main charge, on axis to help determine the velocity of the detonation front, and also across the rear face of the explosive to help determine the detonation waveshape at the end of the charge.

Failure Diameter

At ambient temperature, the measured failure diameter in PBX9502 is ∼7.5-8.0mm [5]. To examine whether CREST can correctly predict the failure diameter of PBX9502, consider simulations of the 8.5mm diameter and 6.0mm diameter rate sticks, which are respectively above and below the measured failure diameter. Figure 3.43 shows the 20 zones/mm simulation of the 8.5mm diameter rate stick. The first plot shows the initial set-up, whereas the remainder of the figure shows a sequence of pressure colour plots at different times from detonation of the booster. The first pressure colour plot is at 0.5μs, and subsequent frames are at 1μs time intervals. The pressure scale runs from 0 to 0.3 Mbars. The calculated results show that at a diameter of 8.5mm, the wave propagates as a steady detonation to the end

of the charge.

The corresponding simulation of the 6.0mm diameter rate stick at 20 zones/mm is shown in Figure 3.44. The sequence of pressure colour plots are at approximately $0.4\mu s$ intervals. In this case the calculation shows detonation failure. A detonation wave initially propagates in the PBX9502 explosive, but at later times a gradual fading of the detonation front is observed, with a corresponding lowering of the shock velocity, eventually leading to detonation failure. The function of entropy is lower at the charge edge than on axis. The increased curvature of the wave at small charge diameters leads to a lowering of the function of entropy along the wavefront as the wave propagates down the length of the charge. Since the reaction rate is dependent on entropy, there is a corresponding decrease in the reaction rate eventually leading to detonation failure at some distance down the rate stick from the input face of the PBX9502 main charge.

The 6.0mm diameter rate stick simulation is in agreement with the observations of Campbell [115] who states that "charges having diameters slightly less than the failure diameter exhibit slow fading of detonation". It would be interesting to know in this instance, whether the CREST calculation agreed with the experimental distance to fade. Unfortunately, the distance to fade had not been reported from the experiment and so this comparison cannot be made. In the CREST simulations, detonation failure occurs in unconfined PBX9502 rate sticks with a charge diameter less than 7mm, which is within $\sim$1mm of experimental observations [115].

Diameter Effect Curve

The variation of detonation velocity with charge size from the numerical simulations is compared with the ambient temperature experimental data in Figure 3.45. For each calculation the marker particle results are carefully checked to ensure that the determination of the detonation velocity is carried out where the wave is a steady detonation wave. The infinite charge diameter points are from one-dimensional hydrocode simulations on PERUSE. It is observed from Figure 3.45 that CREST gives a good match to the experimental diameter effect data at small and intermediate charge sizes. However, the model does not represent the concave upwards feature of the diameter effect curve at large charge sizes, and this is a discrepency in our current modelling capability.

For the majority of heterogeneous solid explosives, the diameter effect curve is eveywhere concave down [114]. The diameter effect curve for PBX9502, like other explosives, is concave down at small and intermediate charge sizes, but is concave up at large charge sizes [115]. At the time, the observed upturn at large charge diameters was surprising, and the reason for this feature was unknown. Today, this is now understood to be a by-product of PBX9502's reaction zone structure [45]. PBX9502 is known to have a fast reaction component followed by a long tail, which represents a slow, late time, reaction component. At small and intermediate charge

sizes, it is known that this slow reaction component has little or no effect on the wave propagation. However, at larger sizes, the shock becomes flatter and a greater fraction of this tail influences the wave propagation giving it an extra 'kick'. It is this extra 'kick' that gives the diameter effect curve its upturn at large sizes.

From Figure 3.45, it is seen that the calculated diameter effect curve is everywhere concave down, following the well known trend of other heterogeneous explosives. CREST is unable to match the detonation velocity in large charges because the additional, slow reaction component, of PBX9502's reaction zone structure is not currently taken account of in the CREST reaction rate model. To account for the upturn at large charge sizes in the diameter effect curve, a slow (late time) reaction component needs to be added to the CREST model for PBX9502 to predict this feature. In addition, it is noted that the calculated diameter effect curve extrapolates to ~ 7.6 mm/μs. This is because the JWL reaction products coefficients in the CREST model for PBX9502, which are taken from [117], have been calibrated to a cylinder test experiment with a 1-inch charge diameter. The cylinder test studies the movement of explosively driven hollow metal cylinders and the data obtained is used to determine the equation of state of the detonation products [118]. As seen from the diameter effect data, the infinite charge, or Chapman-Jouguet (CJ), detonation velocity is close to ~ 7.8 mm/μs, indicating that the standard 1-inch cylinder test is really too small to determine the JWL coefficients. Thus, the JWL coefficients in the CREST model for PBX9502 need to be re-calibrated for the 'real' CJ state.

Over most of the range of data in Figure 3.45, it is observed that there is only a very small difference in the calculated detonation velocities with mesh size. However, close to the failure diameter, mesh size does have a significant effect on the calculated results; for example, at 10 zones/mm the 7mm diameter rate stick calculation fails, whereas at 20 zones/mm steady detonation is attained for the same size of charge. The results indicate that, for modelling detonation propagation in relatively large charges, a coarser mesh is required to obtain mesh converged results compared to modelling the shock to detonation transition. However, at or very close to detonation failure, finer meshing is needed for modelling small charge sizes. This finer meshing is required to accurately resolve the interaction of the detonation wave with the explosive surface in small sizes, as this affects the curvature of the wave in the vicinity of the charge surface, which in turn ultimately determines whether the detonation wave will fail to propagate.

Detonation Waveshapes

Detonation waveshapes were extracted from the 10mm and 18mm diameter rate stick calculations. Following [116], the calculated waveshapes are given by $z(r) = D_0 \, \Delta t(r)$, where D_0 is the steady detonation velocity on axis, and Δt is the time delay as a function of the radius, r, at each of the Lagrangian marker particle positions across the end face of the PBX9502 charge relative to the time of arrival on axis.

The calculated waveshape data is compared with experiment in Figure 3.46. Very good representations of the experimental waveshapes are obtained with CREST, with the smaller diameter charge giving the better calculated fit.

3.7.4 Discussion

A significant amount of detonation data on PBX9502 explosive in terms of the diameter effect (detonation velocity as a function of charge diameter) including failure diameter, and detonation waveshapes, has been used to see if the CREST model for PBX9502, developed by fitting to one-dimensional shock initiation data, can predict two-dimensional detonation propagation experiments. This is an exercise to test the wider applicability of the CREST model, and to examine whether it can predict experiments outside its fitting regime.

For the ambient temperature detonation data, it has been shown that the model is able to predict the failure diameter of PBX9502 in unconfined ratesticks to within ~1mm of the experimental value, and accurately reproduces detonation waveshape data. At intermediate and small charge sizes, the model also gives an accurate representation of the diameter effect curve. However, detonation velocities at large charge sizes are not well modelled. Overall, the calculated results indicate that CREST is capable of predicting experiments outside its fitting regime, however further work is still required as discussed below.

A discrepency in our current modelling capability is not being able to represent the concave upwards feature of the diameter effect curve at large charge sizes. A slow reaction component, which is known to give the PBX9502 curve its upturn at large sizes, needs to be added to the current CREST model for PBX9502 to predict this feature. Following experimental observations, any slow or late time reaction component added to CREST should only be apparent in increasing the detonation velocity for large charge sizes, and should have very little or no effect on the detonation velocity at intermediate and small charge sizes. It should also not influence the shock to detonation transition. This necessary improvement to the CREST reaction rate will be incorporated in due course. In addition, the coefficients for the reaction products JWL EOS in the CREST model for PBX9502 need to be re-calibrated to reflect the 'real' infinite charge detonation velocity.

To date the modelling has only considered the ambient temperature PBX9502 detonation data. Since the experimental data shows a clear effect due to initial temperature, modelling at the hot and cold extremes using CREST will be addressed once the problem of correcting the reaction rate model to account for the upturn in the diameter effect curve at large charge sizes has been solved. To take account of temprature effects using CREST, the following approach will initially be tried. Given the initial temperature, the correct starting conditions in terms of the specific internal energy and specific volume of the explosive can be calculated from the unreacted EOS in the CREST model. Consequently, the non-reactive explosive will

have different Hugoniots at the temperature extremes to the ambient temperature Hugoniot. Thus, once shocked, the unreacted explosive will be on different isentropes through the shock state, and the calculated function of entropy, and hence reaction rate, will vary with starting temperature. Thus, CREST has the potential to take account of the effect of initial temperature on explosive performance.

In Figure 3.45, it is observed that there is some variability in the diameter effect data between the different experimental studies conducted. For example, the detonation velocities measured by Hill *et al.* [116] are ∼0.5% lower than those of Campbell [115]. In the different studies, where duplicate shots have been performed to test experimental repeatability, the agreement is very good. Thus, the differences between the datasets of Hill *et al.* and Campbell are significantly greater than differences expected as a result of test repeatability. The observed differences have been attributed to the different material lots used in the studies [45]. In Campbell's experiments [115] 'recycled' PBX9502 material was used which is mainly made up of scrap taken from machine cuttings, whereas 'virgin' material containing only unused explosive was used in Hill's experiments [116]. Recycled PBX9502 has a finer grain structure than virgin material since explosive crystals are damaged and/or broken in the machining process.

Grain or particle size is an important parameter that influences explosive performance. It is generally accepted that if you reduce the grain size but maintain the same density, the detonation velocity will increase. This is because as you decrease the grain size you introduce more particles to the mixture and in doing so increase the surface area available for decomposition. A decrease in particle size results in an increase in detonation velocity and an increase in sensitivity. Hill *et al.* [45] concluded that the finer grained PBX9502 in Campbell's experimental study behaved more ideally with respect to the propagation of an established detonation. The physical argument is that 'hot-spots' will tend to concentrate around grain boundaries. This is true for most identified 'hot-spot' mechanisms, including jetting and pore collapse. Reaction must spread from these ignition sites over a distance of order the grain diameter to consume the explosive. Thus, the smaller the grains, the faster this consumption takes place, and hence finer grained material is more sensitive.

Since CREST does not explicitly take account of the explosive material structure, it cannot account for differences in detonation behaviour due to grain size effects with one set of parameters. The best that can be done is to produce a model for PBX9502 explosive that can simulate detonation propagation within lot variation, which may be all that is required. To accurately model lot-dependent variations using CREST, different sets of reaction rate parameters would be required for different grain size distributions.

3.8 Conclusions

The newly developed entropy-dependent CREST reactive burn model has been successfully incorporated and validated in a number of hydrocodes. The model is available for use in the one-dimensional Lagrangian code PERUSE, the two-dimensional ALE code CORVUS (Lagrangian mode only), the two-dimensional Eulerian code PETRA, and the two-dimensional adaptive mesh refinement (AMR) Eulerian code SHAMROCK. This enables CREST to be used to simulate a wide range of explosive problems of interest. CREST will shortly be linked to the ALE package in CORVUS to further enhance this capability.

During the hydrocode implementation and use of the CREST reactive burn model, it was found that an entropy-based model suffers from a number of computational problems not associated with pressure-dependent models. The classical 'wall-heating' problem at an impact interface could affect the selection of parameters in CREST's reaction rate model when fitting to data from explosive gas-gun experiments. This in turn could have possible consequences on the modelling of a range of shock initiation problems, and could lead to inaccurate conclusions being made about the reactive behaviour of an explosive. However, from the explosives modelled thus far, 'wall-heating' has only a minimal effect on the calculated results from CREST. In future, appropriate methods will be applied to try to minimise the effect of this long standing problem in relation to CREST simulations.

Application of the Snowplough porosity model in CREST to determine the EOS of the non-reacted porous explosive produces undesirable numerical oscillations in the calculated function of entropy of the solid phase explosive, the variable upon which the CREST reaction rate model is dependent. This could give rise to numerical instabilities in CREST calculations. To improve the modelling of shocks in low porosity explosives, the Snowplough model was modified by removing the assumption that the sound speed is zero during the compaction process. Although this modification removes unwanted numerical oscillations from calculations, it is only applicable to low porosity materials. In future, to improve the modelling of shocks in porous materials, and to enable explosives with a large range of initial porosities to be modelled using CREST, the Snowplough model will be replaced by a P-α porosity model.

A study of the sensitivity of CREST calculations to mesh density has shown that, where reaction is allowed to proceed through the arriving shock front, an entropy-dependent model requires a finer mesh than a pressure-dependent model to obtain mesh converged results. This led to the implementation of CREST in an adaptive mesh refinement (AMR) hydrocode to enable large, two-dimensional, shock initiation and detonation propagation problems of interest to calculated at appropriate mesh resolutions. It is not yet understood why CREST requires a finer mesh than a pressure-dependent model to achieve mesh converged results, and further work is required to understand the mesh convergence properties of an entropy-dependent

model.

To test the predictive capability of CREST, the model for PBX9502 explosive, developed from fitting one-dimensional data of the shock to detonation transition, has been applied, without modification, to two-dimensional detonation propagation experiments. At ambient temperature, CREST predicts the failure diameter of PBX9502 in unconfined ratesticks to within ∼1mm of the experimental value, and accurately reproduces detonation waveshape data. At intermediate and small charge sizes, the model gives an accurate representation of the diameter effect curve. However, a slow reaction component needs to be included in the model to represent the upturn in the diameter effect curve for PBX9502 at large sizes. From the modelling performed to date, CREST appears capable of predicting experiments outside its fitting regime, giving confidence in the ability of the model to accurately simulate a wide range of shock initiation and detonation phenomena.

One of the interesting properties about PBX9502 explosive is that its detonation behaviour is a function of grain size (lot variation). If the CREST model calculations are within lot variation, then in some sense this is the ideal CREST calculation to within material repeatability. To model grain size effects accurately, a reactive burn model that explicitly takes account of the structure of the explosive material will be required. This leads researchers to consider so-called mesoscale models of explosive behaviour.
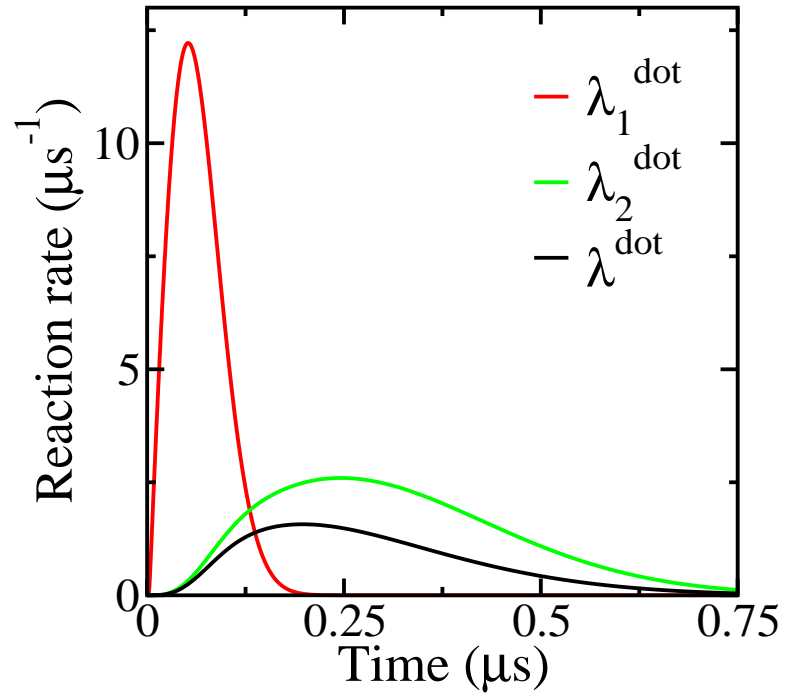
Figure 3.1: Typical CREST reaction rates (from a gauge positioned near the Vistal-EDC37 interface in a simulation of Shot 1159).
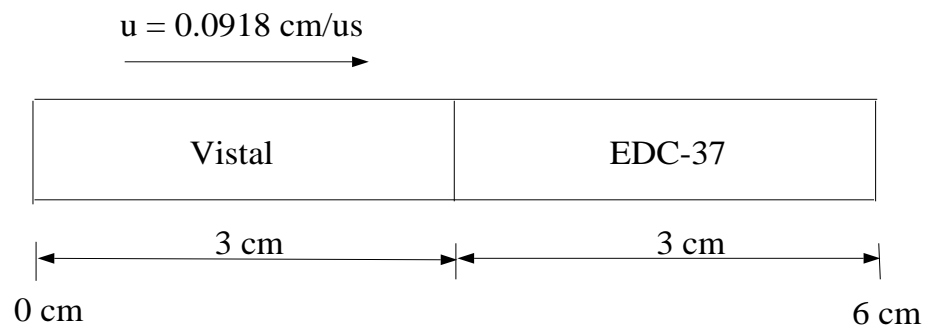
Figure 3.2: Initial calculational set-up for EDC37 Shot 1159.
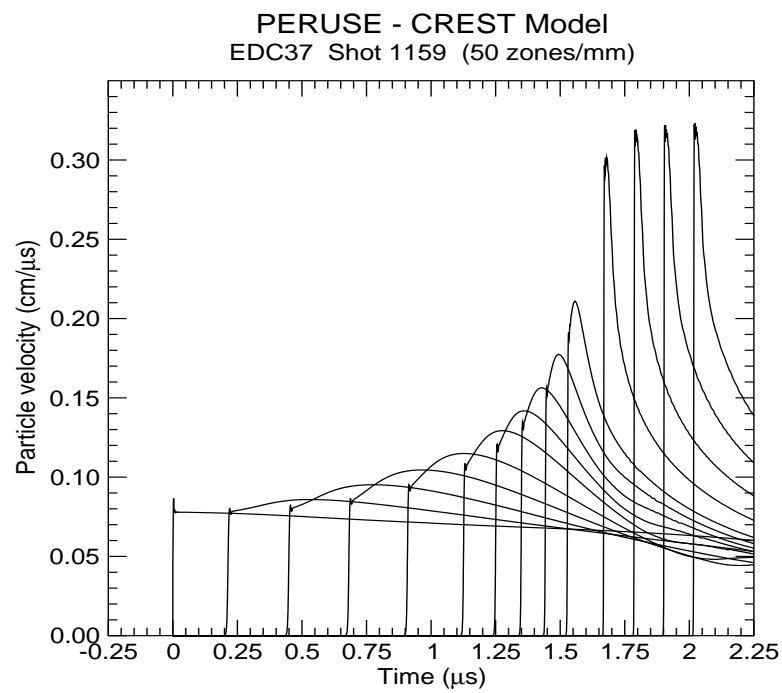
Figure 3.3: Calculated particle velocity profiles from PERUSE for Shot 1159.
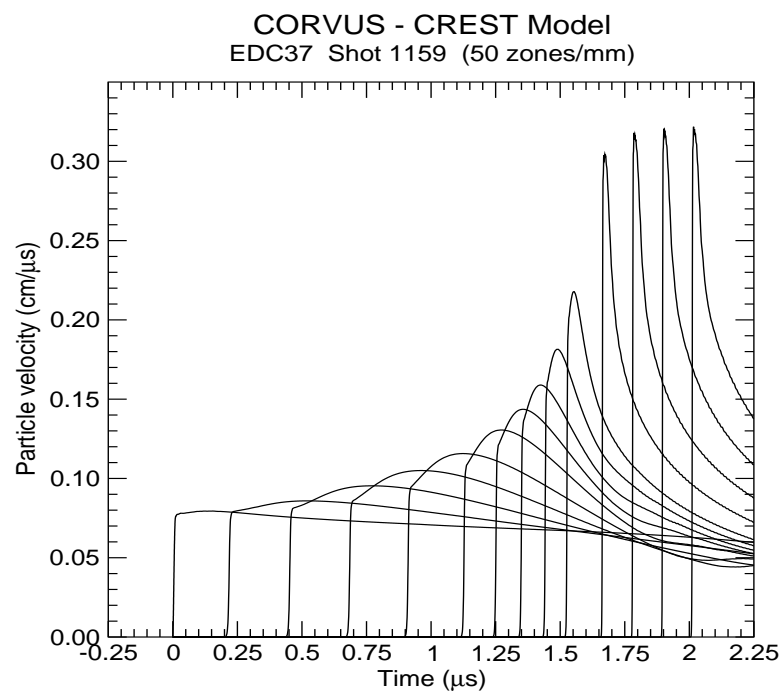
Figure 3.4: Calculated particle velocity profiles from CORVUS for Shot 1159.

PETRA - CREST Model

EDC37 Shot 1159 (50 zones/mm)
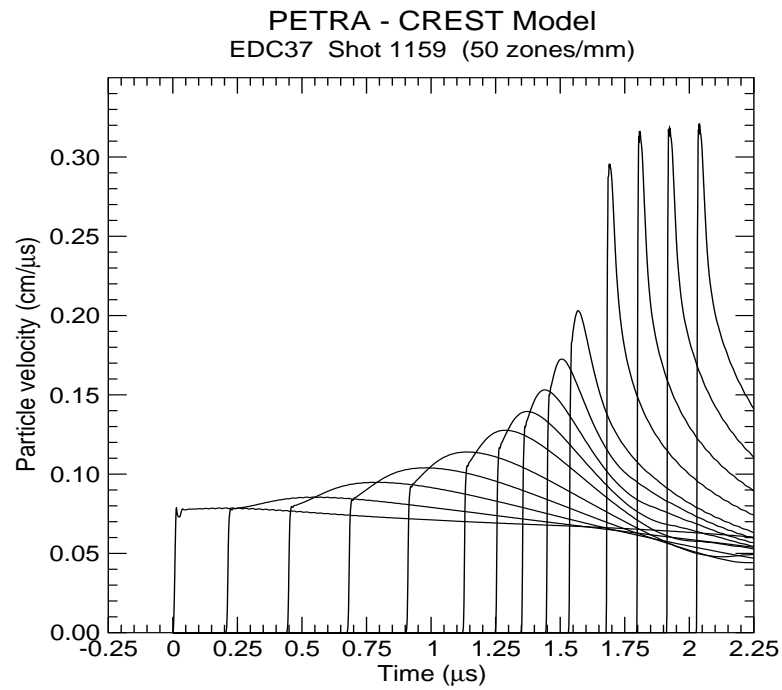
Figure 3.5: Calculated particle velocity profiles from PETRA for Shot 1159.

SHAMROCK - CREST Model

EDC37 Shot 1159 (50 zones/mm)
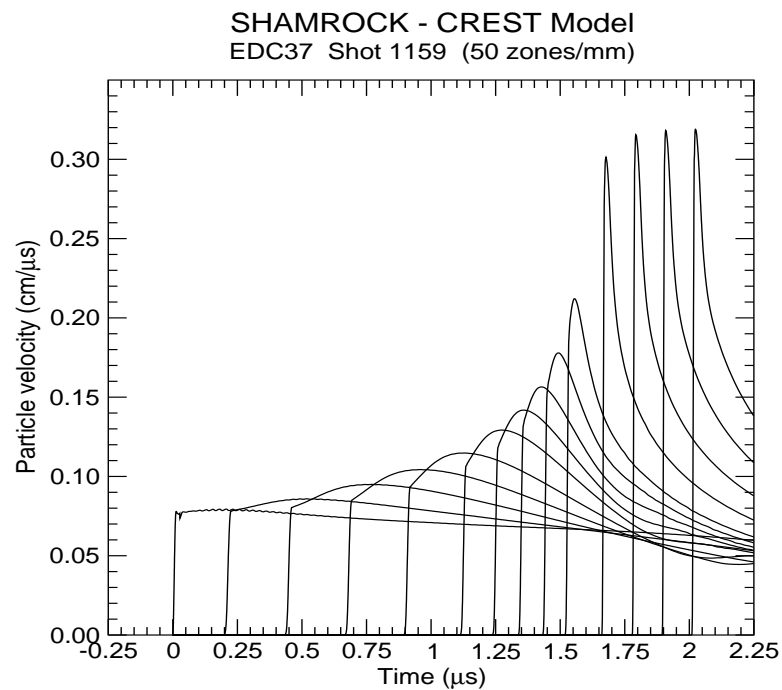
Figure 3.6: Calculated particle velocity profiles from SHAMROCK for Shot 1159.
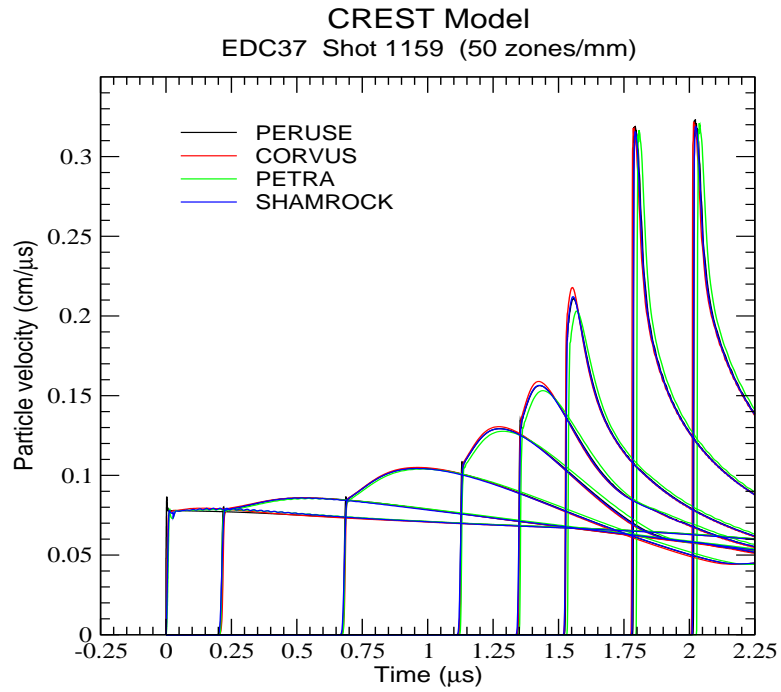
Figure 3.7: Comparison of calculated particle velocity profiles for Shot 1159.
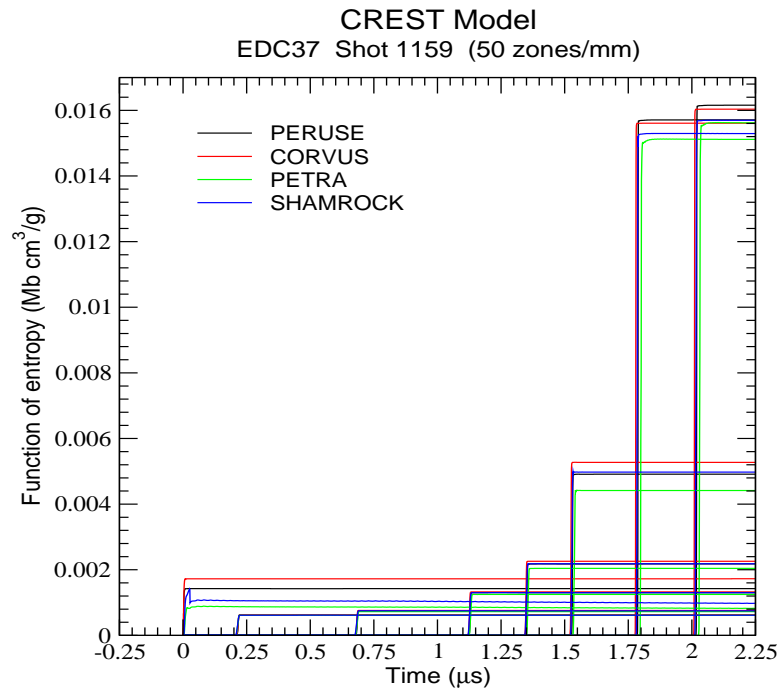
Figure 3.8: Comparison of calculated entropy function profiles for Shot 1159.
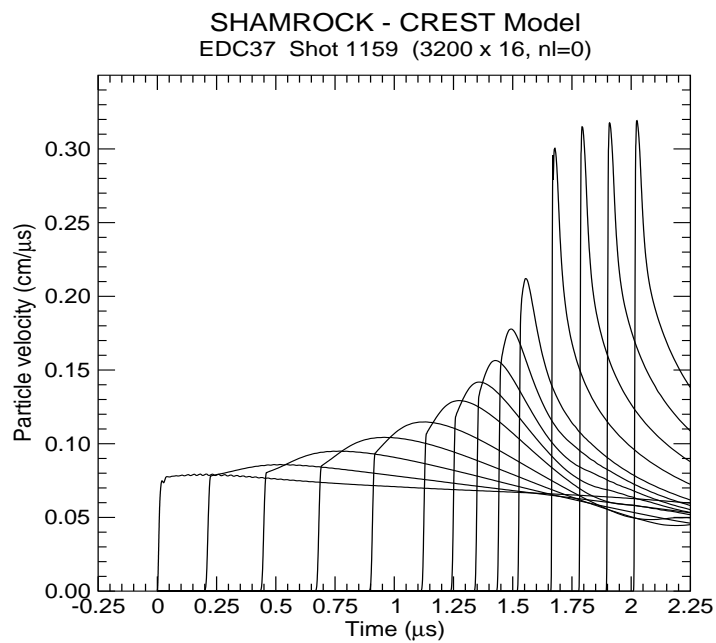
Figure 3.9: Calculated particle velocity profiles from SHAMROCK for Shot 1159; uniform 0.02mm grid.
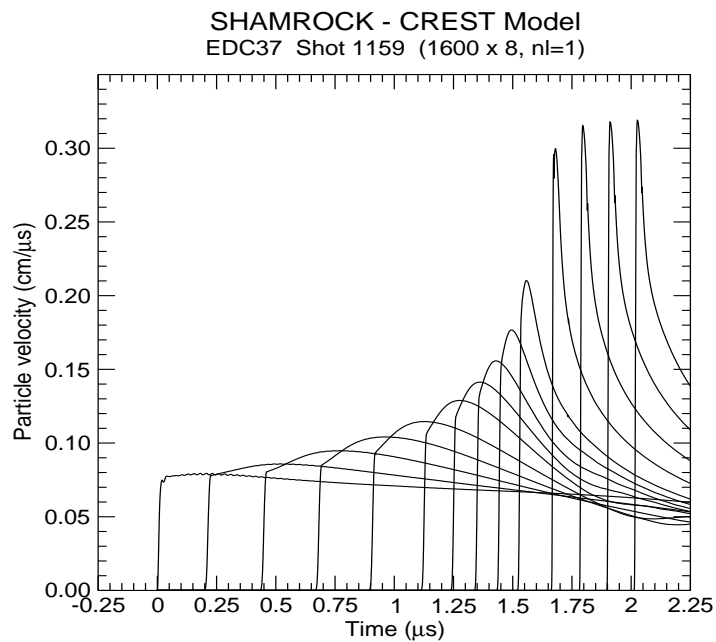
Figure 3.10: Calculated particle velocity profiles from SHAMROCK for Shot 1159; coarse 0.04mm grid and 1 level of mesh refinement.
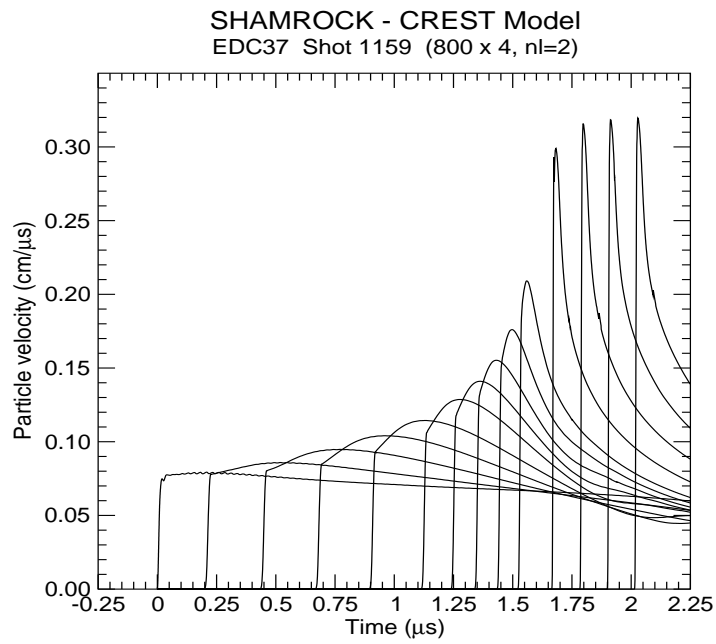
Figure 3.11: Calculated particle velocity profiles from SHAMROCK for Shot 1159; coarse 0.08mm grid and 2 levels of mesh refinement.
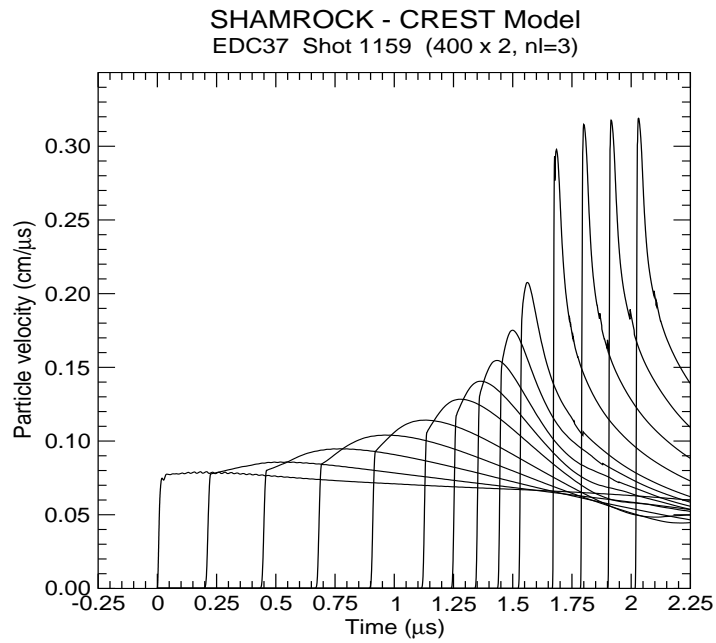
Figure 3.12: Calculated particle velocity profiles from SHAMROCK for Shot 1159; coarse 0.16mm grid and 3 levels of mesh refinement.
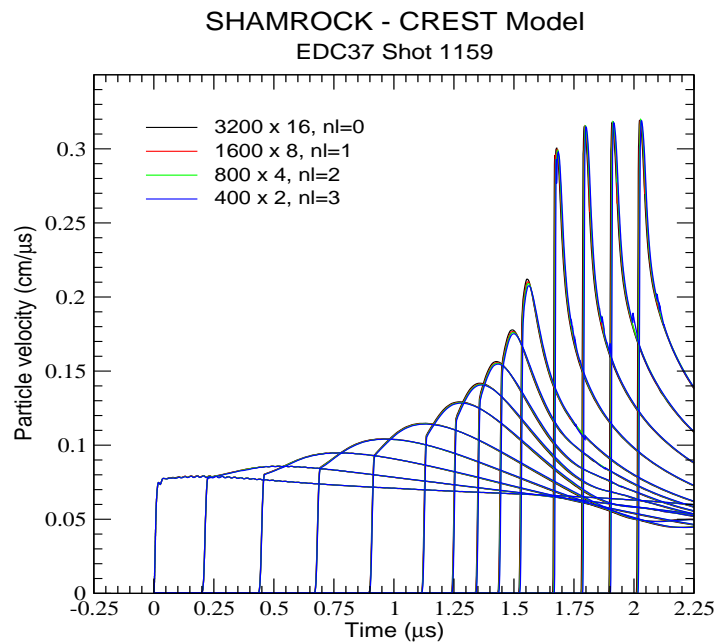
Figure 3.13: Calculated particle velocity profiles from SHAMROCK for Shot 1159; comparison of runs with different levels of mesh refinement.
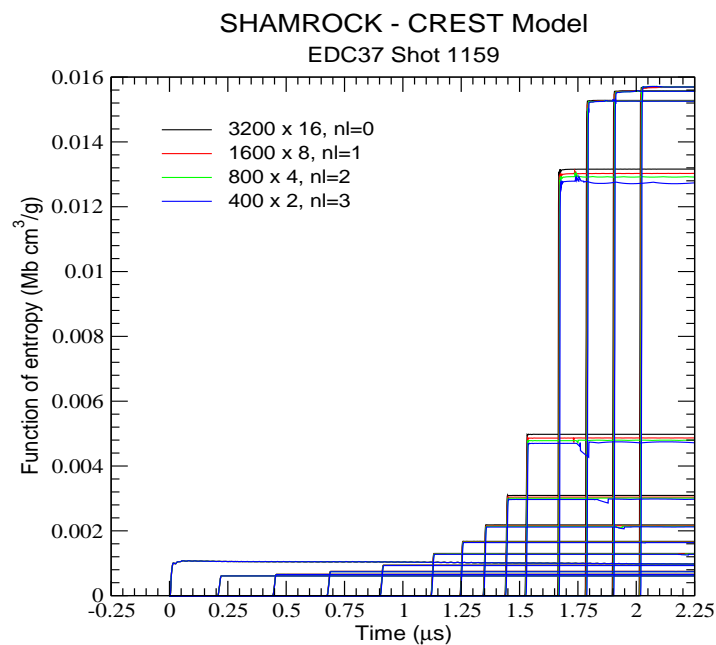
Figure 3.14: Calculated function of entropy profiles from SHAMROCK for Shot 1159; comparison of runs with different levels of mesh refinement.

u = 0.0931 cm/us
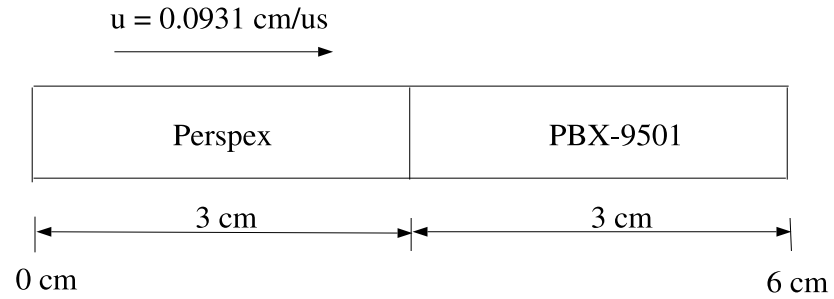
Figure 3.15: Initial geometry for simple impact problem.
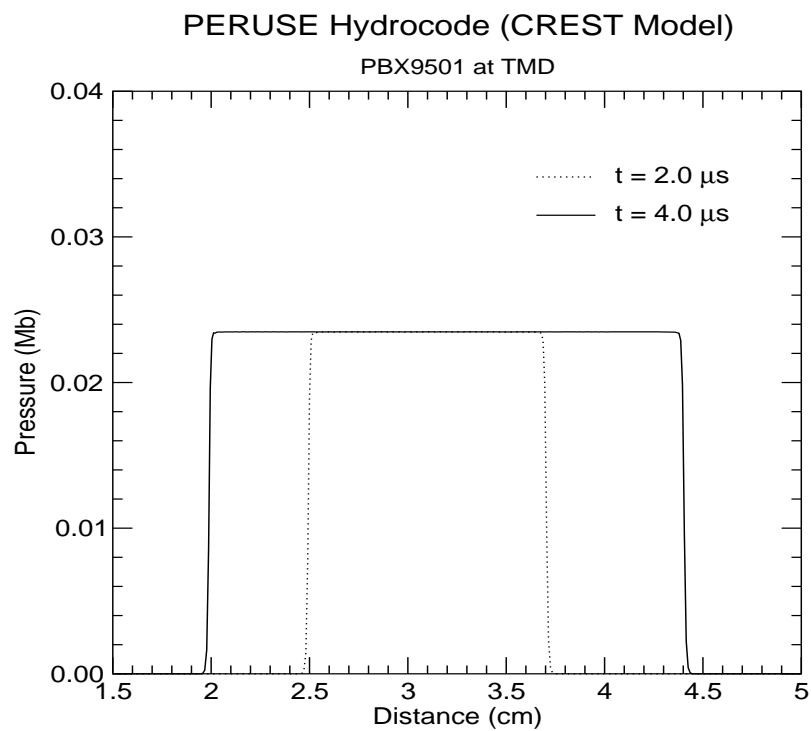
Figure 3.16: Pressure profiles for simple impact problem.
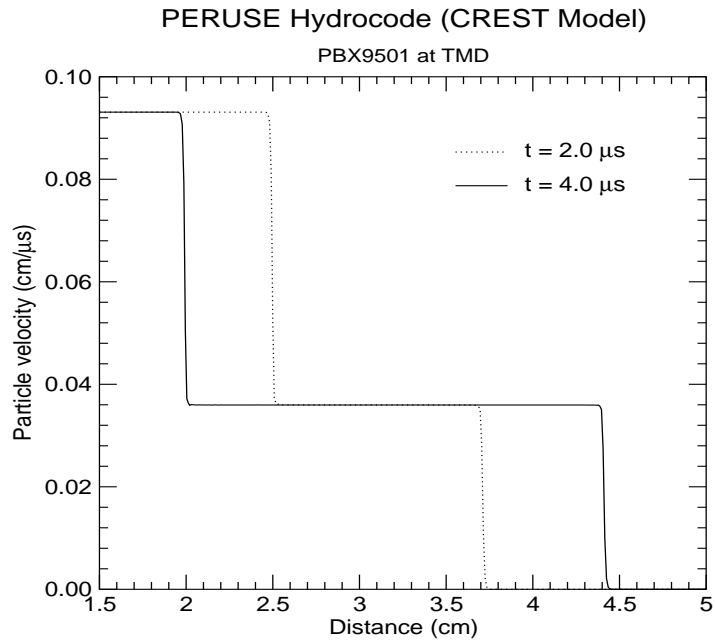
Figure 3.17: Particle velocity profiles for simple impact problem.
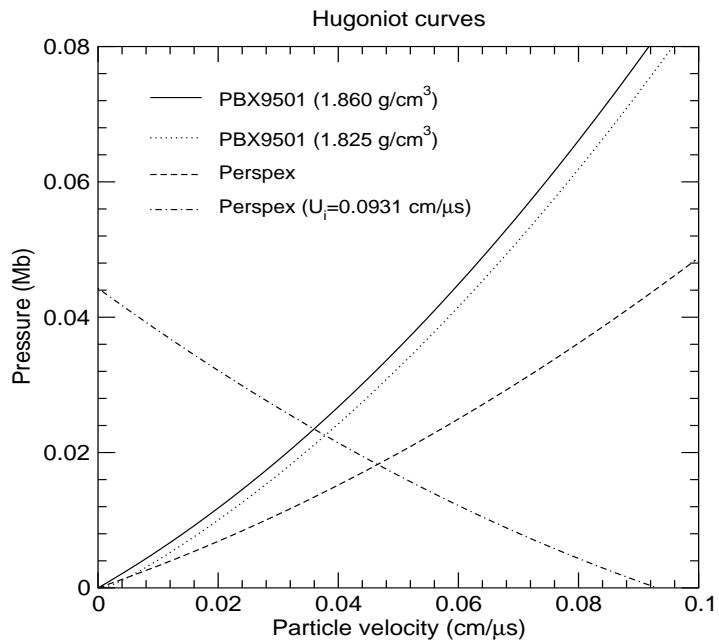
Figure 3.18: Pressure-particle velocity Hugoniot solution of simple impact problem.

PERUSE Hydrocode (CREST Model)

PBX9501 at TMD
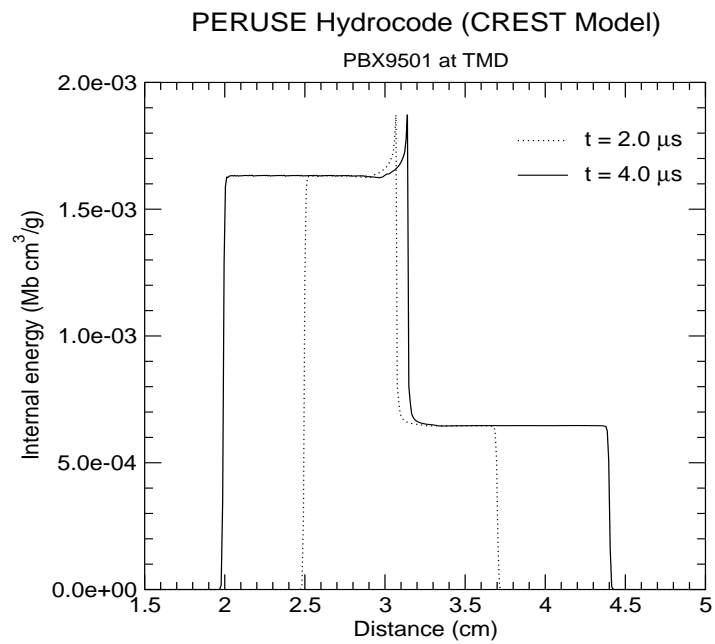
Figure 3.19: Internal energy profiles for simple impact problem.

PERUSE Hydrocode (CREST Model)

PBX9501 at TMD
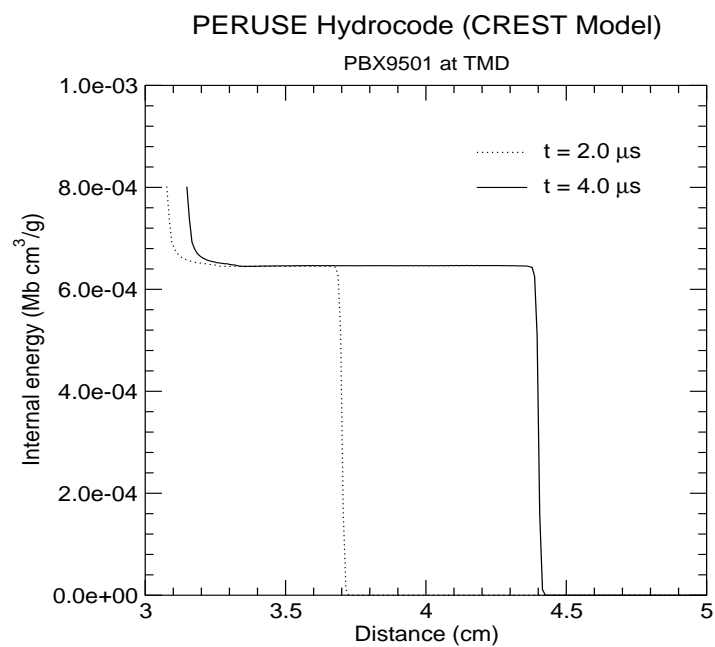
Figure 3.20: Internal energy profiles in solid PBX9501 for simple impact problem.
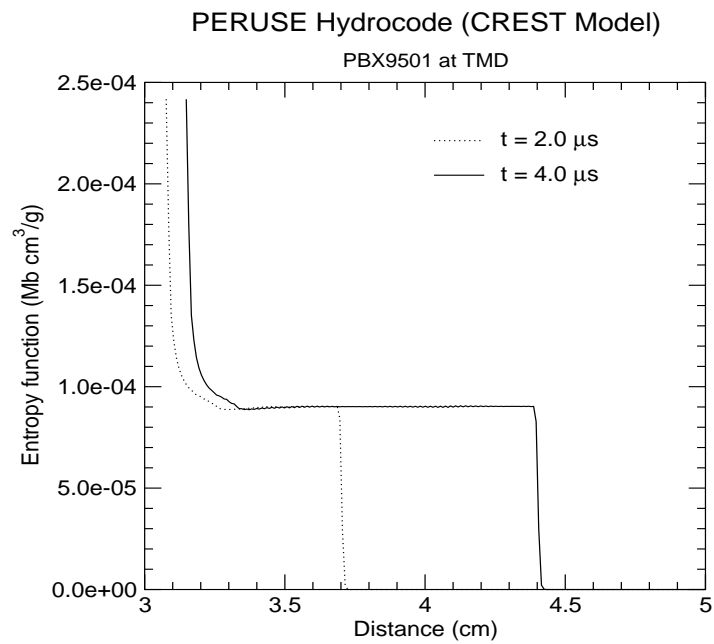
Figure 3.21: Entropy function profiles in solid PBX9501 for simple impact problem.
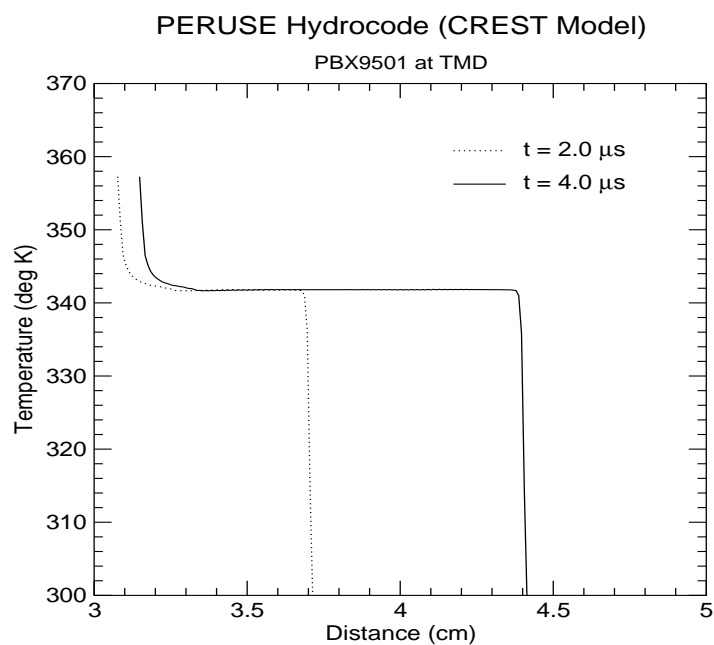
Figure 3.22: Temperature profiles in solid PBX9501 for simple impact problem.
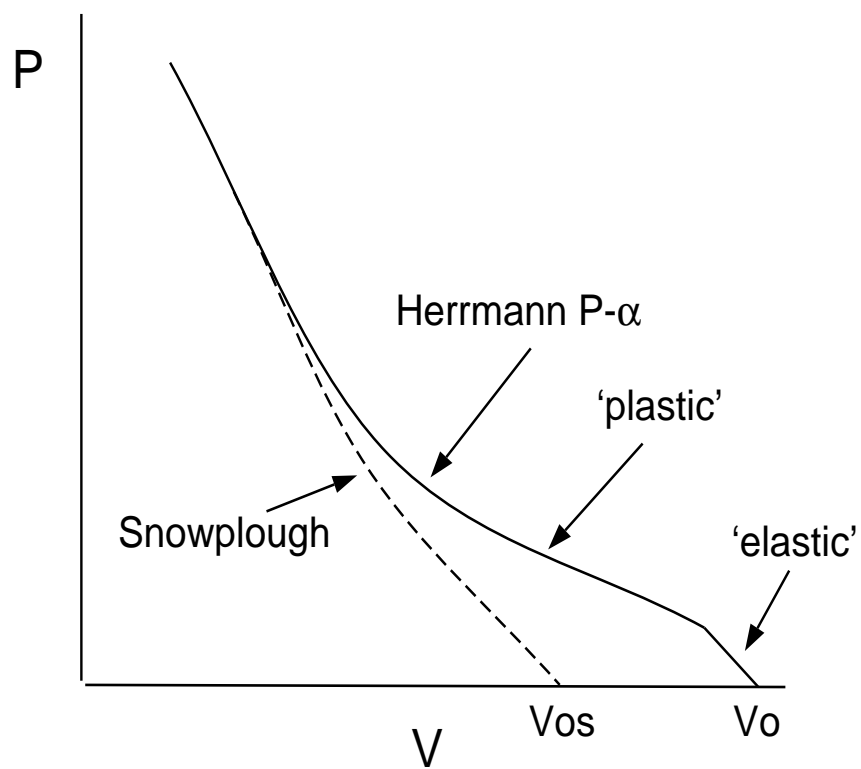
Figure 3.23: Schematic of porous Hugoniots in pressure-specific volume (P-V) space.
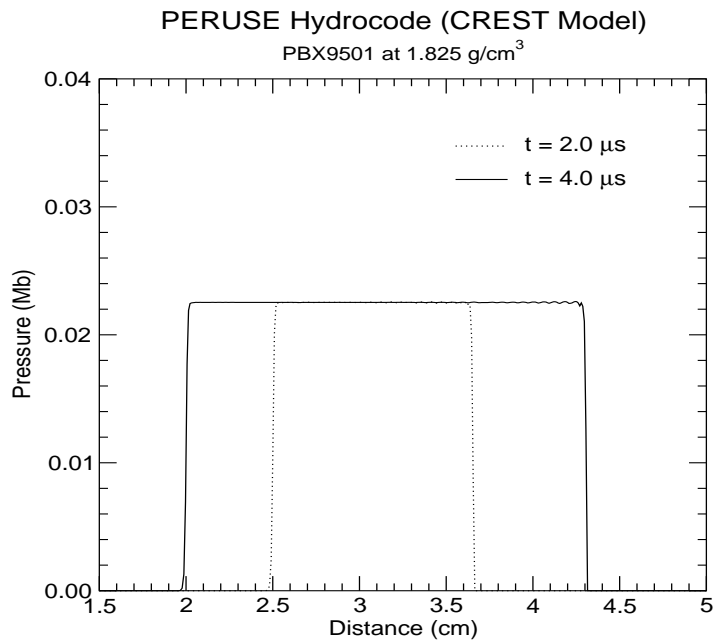
Figure 3.24: Pressure profiles for simple impact problem.
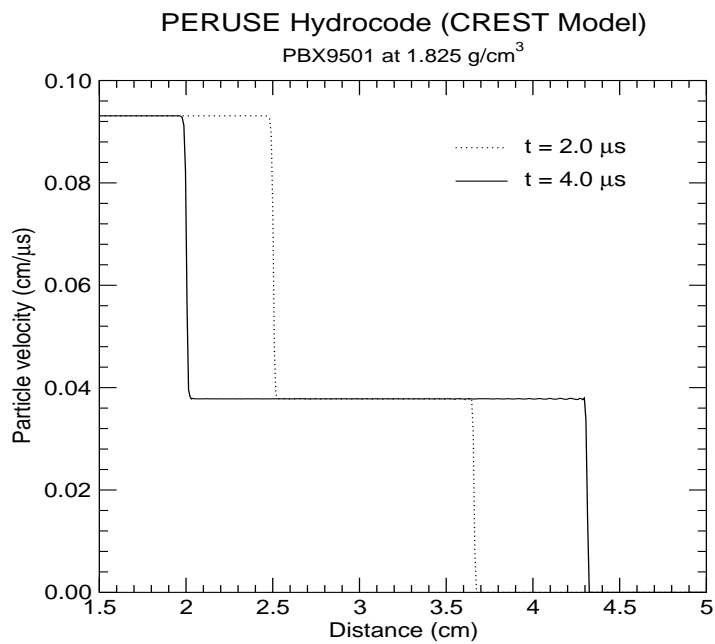
Figure 3.25: Particle velocity profiles for simple impact problem.
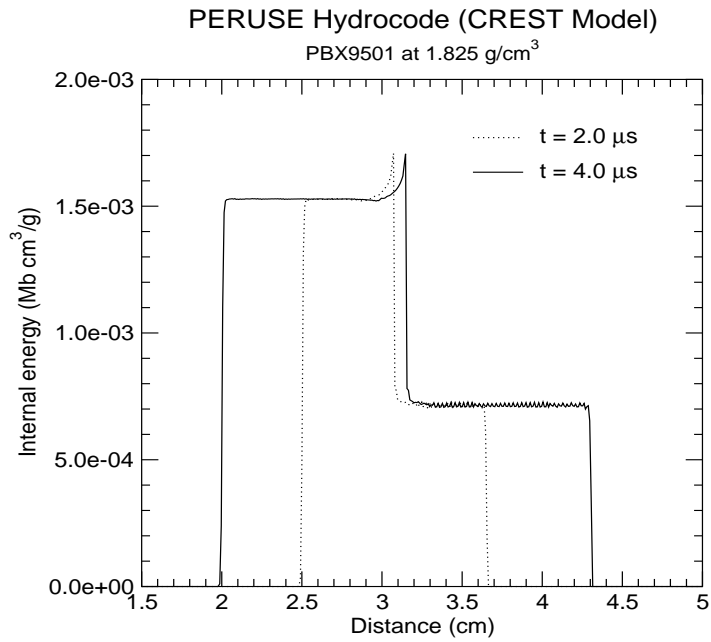
Figure 3.26: Internal energy profiles for simple impact problem.
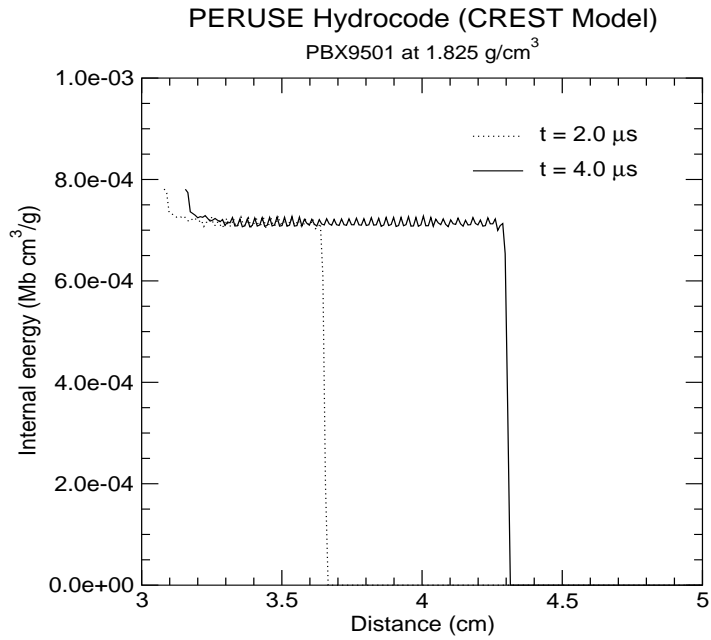
Figure 3.27: Internal energy profiles in porous PBX9501 for simple impact problem.

PERUSE Hydrocode (CREST Model)

PBX9501 at 1.825 g/cm^3
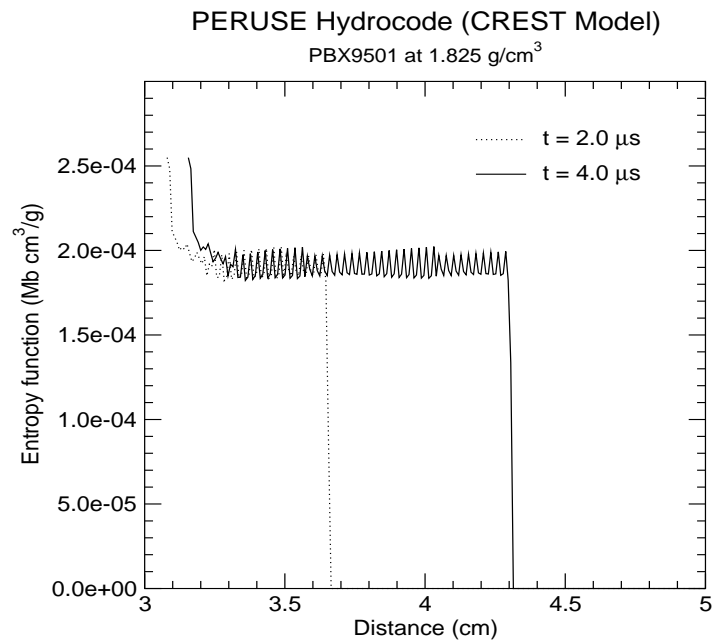
Figure 3.28: Entropy function profiles in porous PBX9501 for simple impact problem.

PERUSE Hydrocode (CREST Model)

PBX9501 at 1.825 g/cm^3
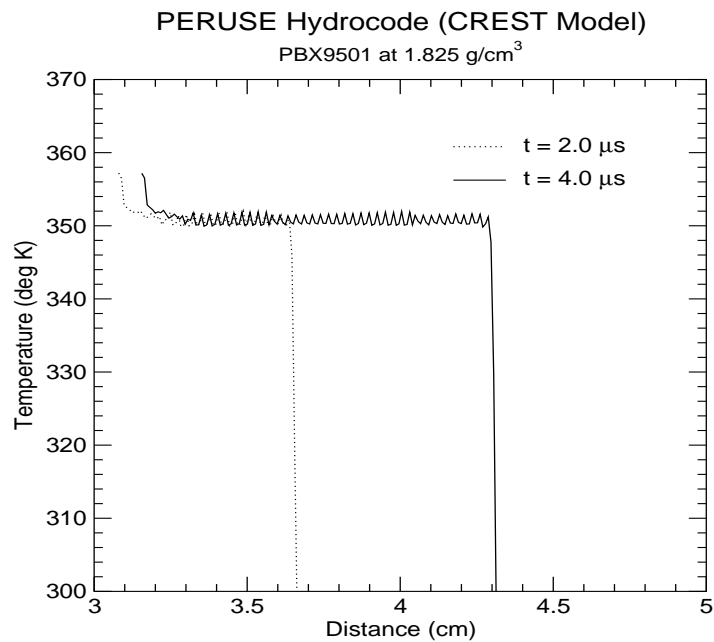
Figure 3.29: Temperature profiles in porous PBX9501 for simple impact problem.
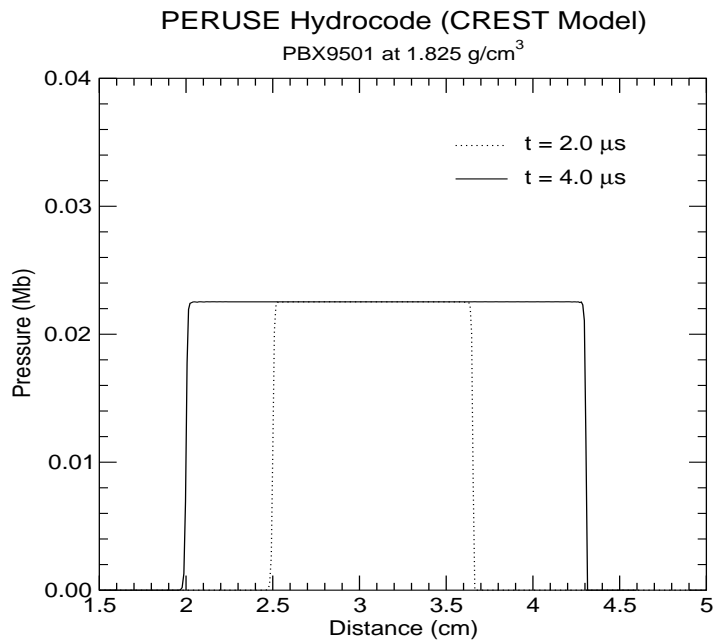
Figure 3.30: Pressure profiles for simple impact problem (using sound speed as calculated from EOS when $V_0 \geq V \geq V_{0s}$).
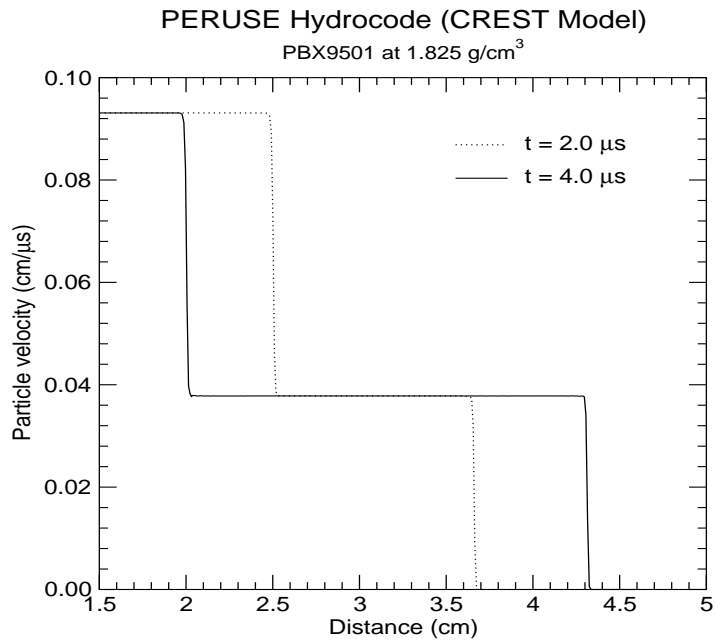
Figure 3.31: Particle velocity profiles for simple impact problem (using sound speed as calculated from EOS when $V_o \geq V \geq V_{0s}$).
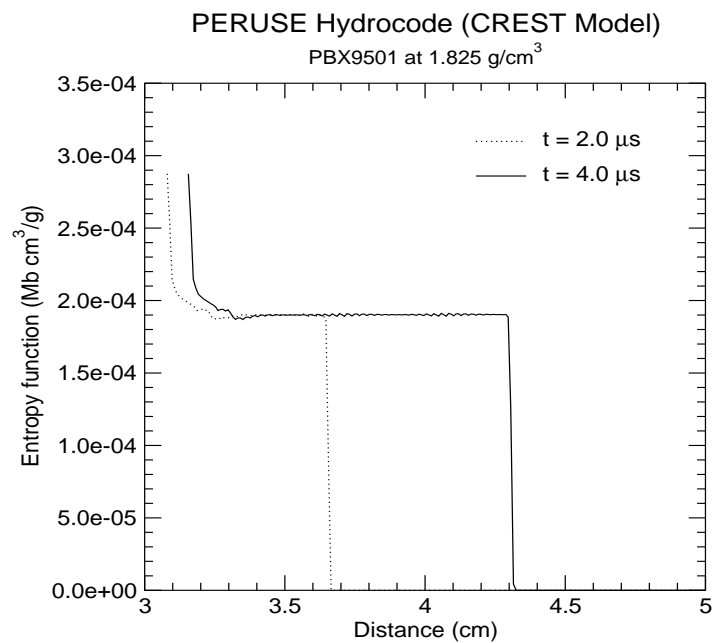
Figure 3.32: Entropy function profiles in porous PBX9501 for simple impact problem (using sound speed as calculated from EOS when $V_0 \geq V \geq V_{0s}$).
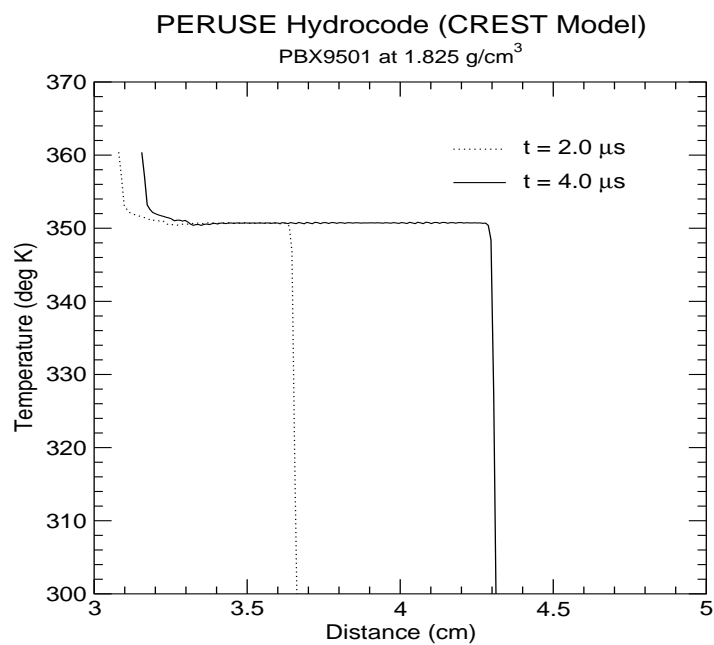
Figure 3.33: Temperature profiles in porous PBX9501 for simple impact problem (using sound speed as calculated from EOS when $V_0 \geq V \geq V_{0s}$).
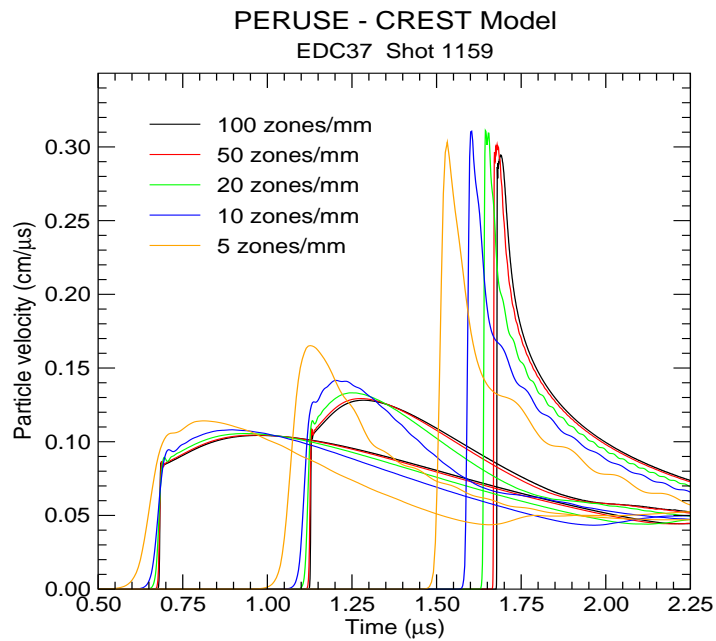
Figure 3.34: Calculated CREST profiles at 2.9, 4.9, and 8.0mm gauges for Shot 1159 (reaction through the arriving shock front).
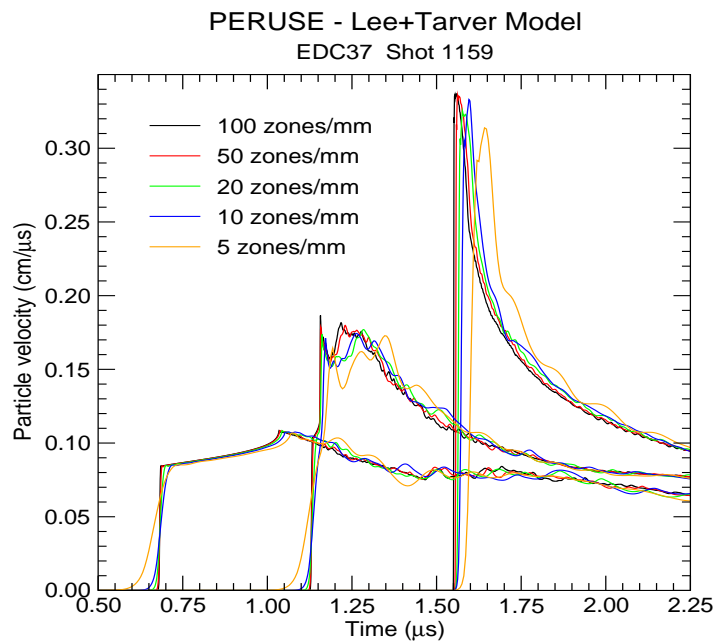
Figure 3.35: Calculated Lee-Tarver profiles at 2.9, 4.9, and 8.0mm gauges for Shot 1159 (reaction through the arriving shock front).
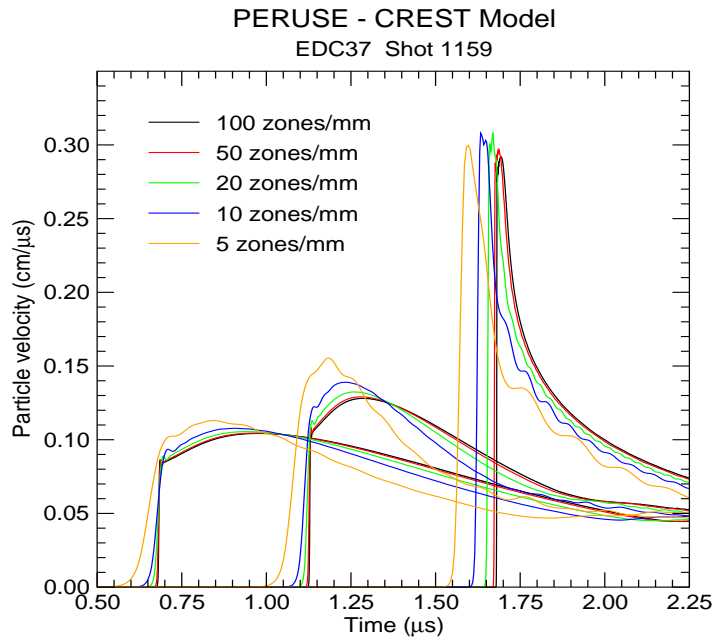
Figure 3.36: Calculated CREST profiles at 2.9, 4.9, and 8.0mm gauges for Shot 1159 using 'q-switching' method (i).
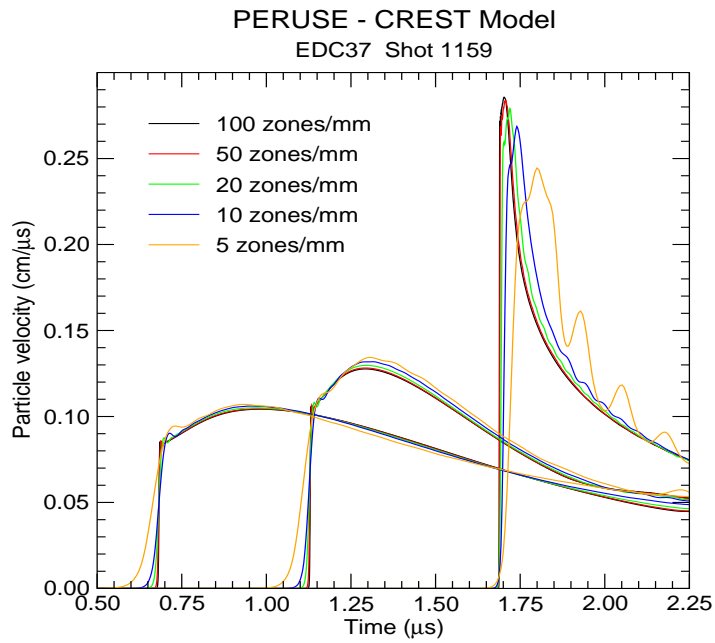
Figure 3.37: Calculated CREST profiles at 2.9, 4.9, and 8.0mm gauges for Shot 1159 using 'q-switching' method (ii).
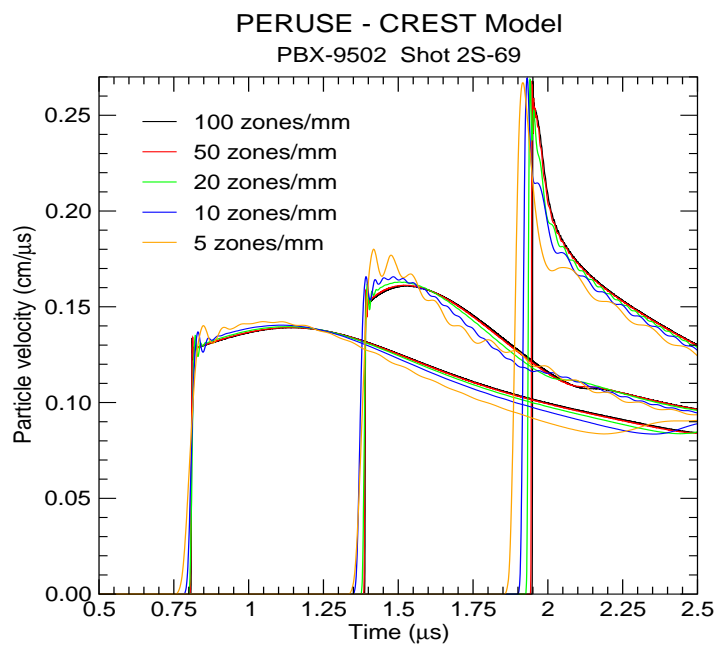
Figure 3.38: Calculated CREST profiles at 4.18, 7.34, and 11.0mm gauges for Shot 2S-69 (reaction through the arriving shock front).
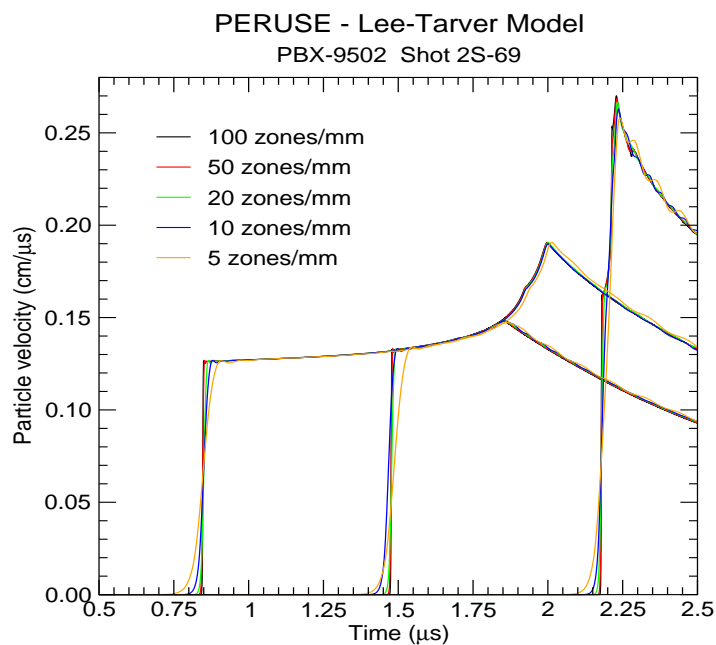
Figure 3.39: Calculated Lee-Tarver profiles at 4.18, 7.34, and 11.0mm gauges for Shot 2S-69.
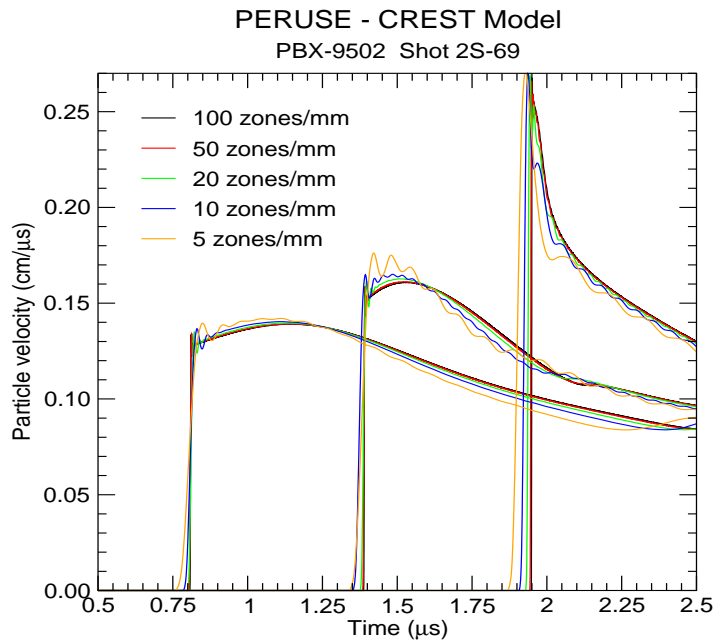
Figure 3.40: Calculated CREST profiles at 4.18, 7.34, and 11.0mm gauges for Shot 2S-69 using 'q-switching' method (i).
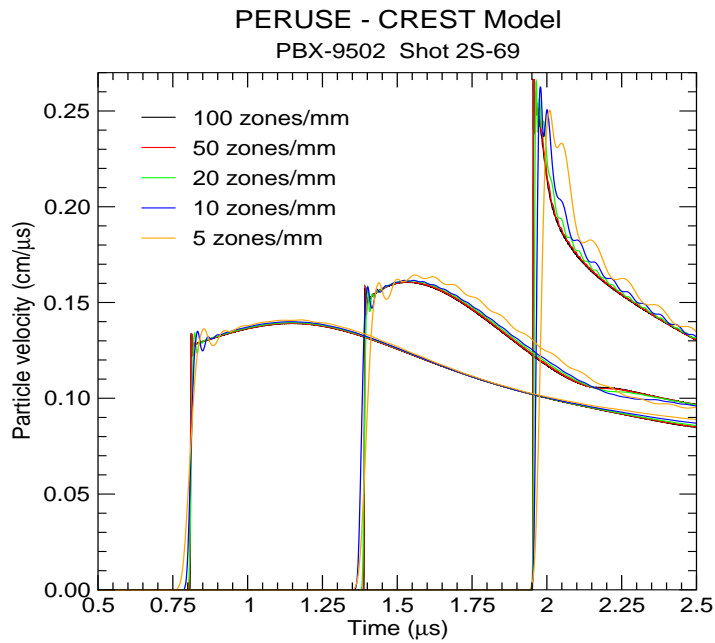
Figure 3.41: Calculated CREST profiles at 4.18, 7.34, and 11.0mm gauges for Shot 2S-69 using 'q-switching' method (ii).
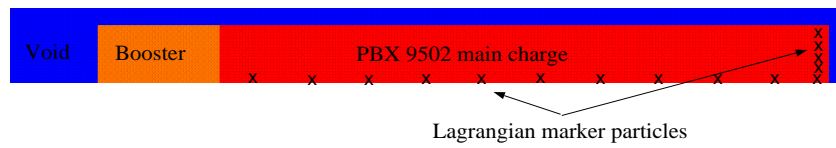
Figure 3.42: Basic set-up for PBX9502 ratestick calculations.
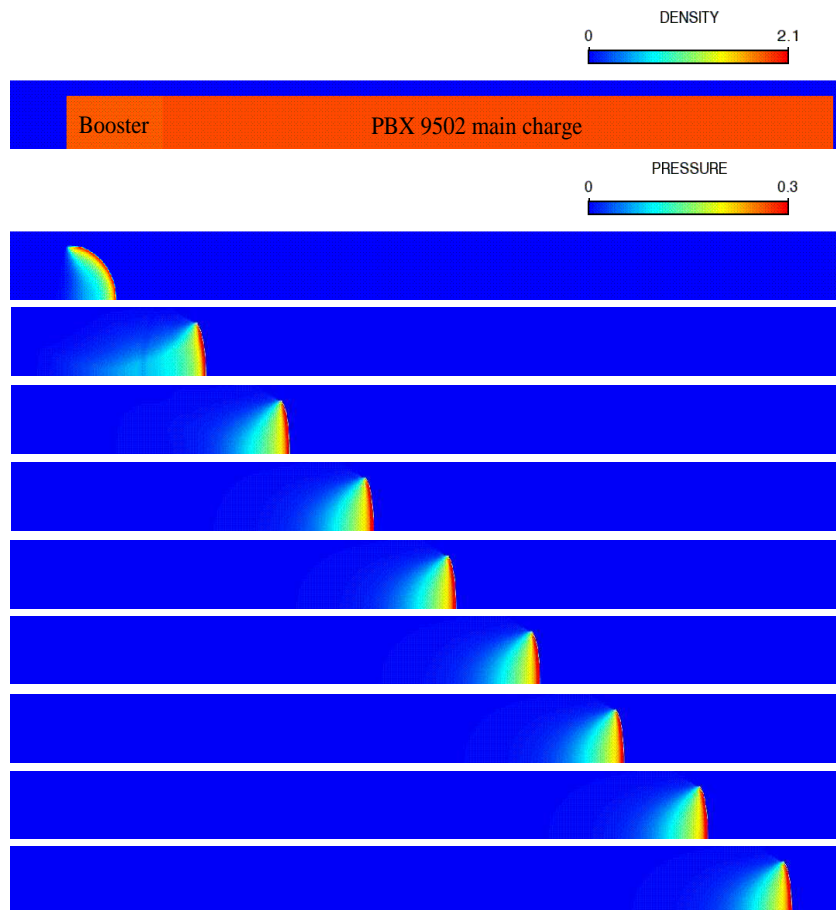
Figure 3.43: Simulation of the PBX9502 8.5mm diameter ratestick.
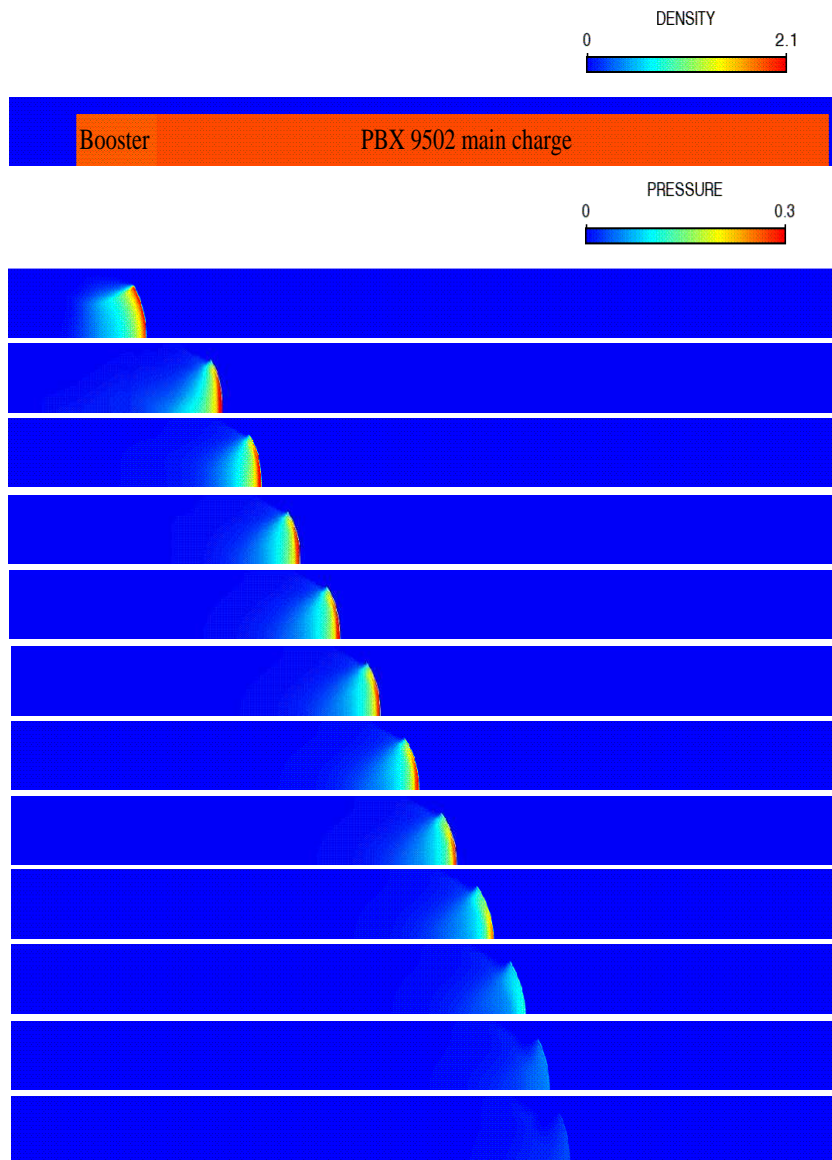
Figure 3.44: Simulation of the PBX9502 6.0mm diameter ratestick.

PBX9502 - CREST Model
D vs 1/d at Ambient Temperature
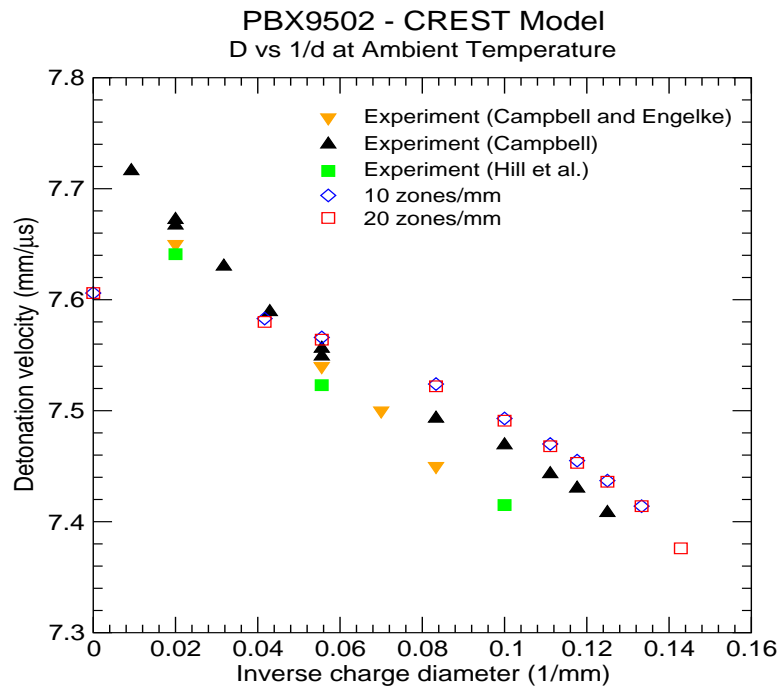
Figure 3.45: Detonation velocity as a function of charge diameter for PBX9502.

PBX9502 - CREST Model
Fits to Wavefront Data
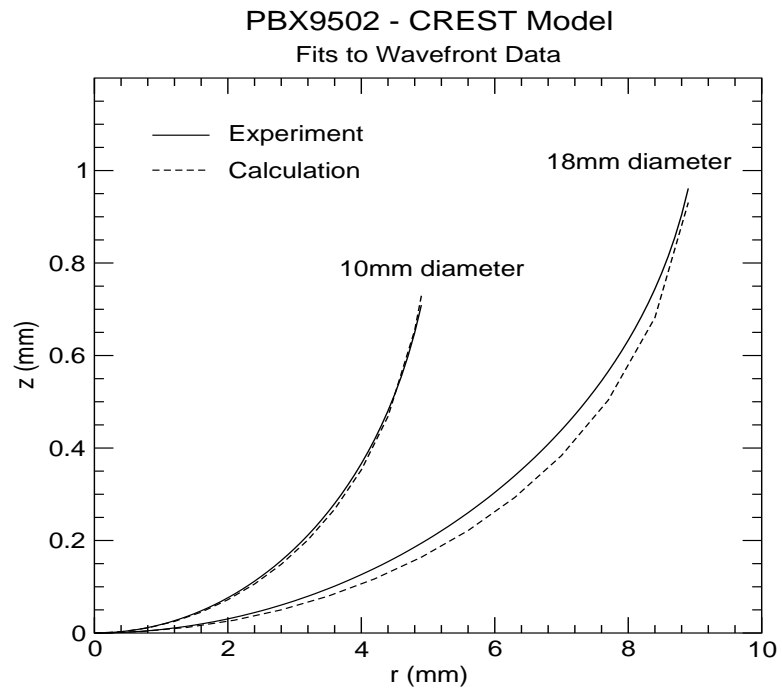
Figure 3.46: Calculated fits to PBX9502 wavefront data.

Chapter 4

Application of a Least Squares Approach for Determining Run Distances to Detonation Based on the LANL Methodology for Fitting Shock Trajectory Data

4.1   Introduction

Important measurements in explosive shock initiation are the run-distance and run-time to detonation. When shocked, an explosive does not instantly attain full detonation. Instead, the shock wave usually travels some finite distance into the explosive charge before detonation is achieved. This is termed the *run-distance*, and is defined as the distance from the input boundary to the position at which the shock wave transitions to a detonation wave. The *run-time* is defined as the time between shock input and the time at which the run-distance is reached.

Information on the shock initiation of EDC37 explosive has recently been provided by gas-gun experiments fired at Los Alamos National Laboratory (LANL) [38]. In the LANL experiments, two different types of gauge package were fielded to provide data on the shock response of the explosive; (i) particle velocity gauges to give information on the build-up of reaction behind the shock front at different locations within the explosive sample, usually before detonation occurs, and (ii) a shock tracker gauge to measure the distance-time $(x - t)$ trajectory of the shock front as it propagates through the explosive. The experimental run-distance and run-time to detonation are determined from the analysis of the shock tracker data.

An example of the data obtained from the shock tracker gauge in a gas-gun experiment is shown in Figure 4.1. This shows the shock tracker data for EDC37

gas-gun Shot 1159 in which a single sustained shock of ~59 kbars is input into the explosive sample. It is observed that the shock velocity increases very slowly to begin with as shown by the straight line slope through the first handful of data points. Thereafter, the reaction starts to build-up behind the shock front, the wave starts to accelerate, and the shock velocity increases. Close to full detonation, as indicated by the straight line through the last dozen or so data points, the shock velocity increases rapidly and the turn over to detonation occurs. The wave then travels at a constant speed corresponding to the detonation velocity.

From a plot such as this there are a number of ways to determine the run-distance and run-time to detonation. One can pick out the point by eye, looking to see where the wave is a detonation front travelling at constant velocity. The problem with this approach is that the transition to detonation is not very abrupt making it difficult to determine accurately where the onset of detonation occurs. Alternatively, the run-distance to detonation can be deduced from the intersection of the lines giving the initial shock velocity (initial slope) and the detonation velocity (final slope) as shown in Figure 4.1. However, this method has also been found to be unreliable [119].

A more accurate method for deducing the run-distances and run-times to detonation from shock trajectory data has been devised by Larry Hill at LANL [11]. His approach is to choose a differential equation which mimics the shock front behaviour in the $(x-t)$ plane, and which also behaves appropriately in every other plane which can be reached by integration or differentiation. Hill found that a differential equation in the shock velocity-shock acceleration plane, when integrated, could produce excellent fits to experimental shock trajectory data. From such fits the run-distances and run-times to detonation can be accurately determined.

Here, a fast and efficient solution method is developed and applied to the LANL approach for determining run-distances and run-times to detonation from explosive shock initiation experiments. The method chosen, suggested by Lambourn [120], is non-linear least squares fitting with constraints. To test and validate the constrained least squares solution method, it has been applied to the shock tracker data from EDC37 gas-gun experiments involving sustained single shock inputs, and the derived run-distances and run-times to detonation compared with the corresponding values quoted by LANL.

Shock trajectories, together with in-material particle velocity gauge records from explosive gas-gun experiments, comprise the primary information available for appraising reaction rate models in the shock to detonation regime. Any reactive burn model incorporated into a hydrocode should, at the very least, be able to reproduce (i) the experimental particle velocity gauge histories, and (ii) the experimentally derived Pop-Plot (run-distances and run-times to detonation plotted as a function of the input pressure) [31].

The newly developed CREST reaction rate model [61] is able to reproduce the particle velocity gauge records from EDC37 gas-gun experiments which show the

reaction build-up in shocked EDC37 explosive before detonation is attained. Since the LANL methodology for analysing shock trajectories can be applied equally well to calculated as well as experimental data, the method has also been applied to shock arrival data from hydrocode calculations of the EDC37 gas-gun experiments using CREST, to see how well, or otherwise, the CREST model for EDC37 explosive fits the experimental Pop-Plot.

The LANL methodology for fitting $(x - t)$ shock initiation data is described in Section 4.2. A number of solution methods to the LANL approach for determining run-distances and run-times to detonation from analysis of shock trajectory data, including the constrained least squares method, are described in Section 4.3. In order to apply the constrained least squares method to shock trajectory data, a series of FORTRAN routines have been written, and the overall program is described in Section 4.4. Section 4.5 then details the application of the chosen method to EDC37 experimental shock tracker data from gas-gun shots to test and validate the method. In Section 4.6 the method is then applied to shock time of arrival data from CREST calculations of the EDC37 gas-gun experiments to see how well, or otherwise, the CREST model for EDC37 fits shock time of arrival data and the Pop Plot. The conclusions are given in Section 4.7.

4.2   The LANL Method of Analysing Shock Trajectories

Post-shot analysis of explosive gas-gun experiments fired at LANL involves determination of the run-distance and run-time to detonation from the shock tracker data, assuming that detonation has been attained within the time frame of the experiment. The quoted run-distances and run-times are usually determined using a method derived by Larry Hill [11]. Hill found that a differential equation in the shock velocity-shock acceleration $(\dot{x} - \ddot{x})$ plane gave a good representation of the shock front trajectory from explosive gas gun experiments involving a run to detonation. The form of the differential equation suggested by Hill is,

$$\ddot{x} = \frac{\left(\frac{a}{100}\right) \dot{x}^{b+2} \left(\dot{x} - C\right)^{b+1} \left(D_{cj} - \dot{x}\right)}{\left(2\dot{x} - C\right) \left(D_{cj} - 0.99\dot{x}\right)} \tag{4.1}$$

where a controls the acceleration of the wave, b controls where turnover to detonation occurs, C is the intercept of the explosive's unreacted Hugoniot in the shock velocity-particle velocity $(U_s - U_p)$ plane, D_{cj} is the Chapman-Jouguet detonation velocity, and the dots indicate differentiation with respect to time. An example of the form of this function is shown in Figure 4.2. The differential equation (4.1) cannot be solved analytically and numerical integration techniques must be used to find $x(t)$ with the boundary conditions, (i) $\dot{x}(t = 0) = U_s$, and (ii) $x(t = 0) = x_0$, where

U_s is the initial shock velocity in the explosive, and x_0 is the intial position (nominally 0.0). U_s can either be estimated (from fitting to the first few shock tracker data points) or calculated from the unreacted Hugoniot if this is known.

The Hill function (4.1) is essentially a method for determining the run-distance, x_{run}, which is defined as the depth at which the shock velocity in the target explosive reaches 99% of the detonation velocity D_{cj}, where D_{cj} is usually obtained from the fit to the last few data points of the measured $(x-t)$ trajectory. The run-time to detonation, t_{run}, is defined as the time between impact and the time at which the run-distance to detonation is attained. The run-distance, x_{run}, and run-time, t_{run}, to detonation are evaluated from the following integrals with the given integration limits,

$$x_{run} = \int_{U_s}^{0.99D_{cj}} \frac{\dot{x}}{\ddot{x}} \, d\dot{x} \tag{4.2}$$

$$t_{run} = \int_{U_s}^{0.99D_{cj}} \frac{1}{\ddot{x}} \, d\dot{x} \tag{4.3}$$

There are essentially five free parameters in the method; a, b, C, D_{cj}, and U_s. In their analyses, LANL assume that C and D_{cj} are fixed, and initially used "machine" fits in which the Mathematica software package was used to vary the parameters a, b, and U_s over a limited range in an attempt to find the best fit according to a least squares criterion. Rather than rely on a commercial software package, a series of FORTRAN programs are written to solve the Hill differential equation (4.1) to determine run-distances and run-times to detonation.

4.3 Solution Methods to the LANL Approach for Determining Run-Distances to Detonation

4.3.1 Search Method

To solve the Hill differential equation (4.1) to determine run-distances and run-times to detonation from shock trajectory data, an initial solution method involved searching on a 2D grid to find the best solution. In this approach, suitable fixed values for C, D_{cj}, and U_s are chosen, and the parameters a and b are varied in an attempt to find the best fit to the shock trajectory data. A 2D matrix of (a,b) values is created which is then used to solve equation (4.1) to produce a matrix of $(x-t)$ fits. Further refined 2D matrices of (a,b) values centred on a number of the best fits from the initial grid are then searched until a 'best' best fit is found.

Although this solution method produces acceptable fits to the data, there are two main problems with this approach. Firstly, the solution method is numerically very

inefficient; for example, a calculation using a 100 x 50 grid of (a,b) values takes approximately 20 minutes to run on a SUN workstation. Secondly, the initial shock velocity in the explosive, U_s, is assumed fixed, thus there is no flexibility in the solution method to adjust this value within experimental uncertainty to improve the calculated fit to the data. Therefore, it was felt that an improved and more computationally efficient solution method for determining run-distances to detonation was required.

4.3.2   Standard Least Squares Method

Suppose we have a set of n data points (x_i, t_i^{expt}) from a given experiment where, in this case, n is the number of recorded measurements from the shock tracker gauge. Suppose given starting values of (a, b, U_s) we have a set of n calculated data points (x_i, t_i^{fit}). Assuming that this calculated fit can be improved upon, then the values of (a, b, U_s) need to be adjusted to give the best fit, *i.e.* to vary (a, b, U_s) to minimise the sum of squares, S_1, of the deviations of the measured values, t_i^{expt}, from the calculated values, t_i^{fit},

$$S_1 = \sum_{i=1}^{n} \left(t_i^{expt} - t_i^{fit} \right)^2 \tag{4.4}$$

The minimum is found by partially differentiating S_1 with respect to a, b, and U_s, and setting the partial derivatives to zero. As the fitting function, t_i^{fit}, is non-linear, the equations found by setting the partial derivatives of S_1 to zero are non-linear equations, and hence an iterative method is required to solve them. An alternative is to linearise the function being fitted in the neighbourhood of some initial values of (a, b, U_s) and to use least squares to find corrections $(\Delta a, \Delta b, \Delta U_s)$. To do this, the gradients of each t_i^{fit} with respect to (a, b, U_s) are found, and then t_i^{fit} is expanded by Taylor's series to first order to give,

$$t_i^{*} = t_i^{fit} + \frac{\partial t_i^{fit}}{\partial a} \Delta a + \frac{\partial t_i^{fit}}{\partial b} \Delta b + \frac{\partial t_i^{fit}}{\partial U_s} \Delta U_s \tag{4.5}$$

For least squares purposes, the sum to minimise is,

$$S_1{}^{*} = \sum_{i=1}^{n} \left(t_i^{expt} - t_i^{*} \right)^2 \tag{4.6}$$

and substituting for t_i^{*} gives,

$$S_1{}^{*} = \sum_{i=1}^{n} \left(t_i^{expt} - t_i^{fit} - \frac{\partial t_i^{fit}}{\partial a} \Delta a - \frac{\partial t_i^{fit}}{\partial b} \Delta b - \frac{\partial t_i^{fit}}{\partial U_s} \Delta U_s \right)^2 \tag{4.7}$$

The sensitivities (partial derivatives) in (4.7) can be estimated, by a finite difference approximation, from calculations with slightly different (a, b, U_s) values, thus

it is necessary to perform 4 separate calculations (original plus one each for each of the above sensitivies) before the method can be applied. By partially differentiating S_1^* with respect to $(\Delta a, \Delta b, \Delta U_s)$ and setting the resulting derivatives to zero, a system of 3 linear equations is obtained,

$$\frac{\partial S_1^*}{\partial \Delta a} = -2 \sum_{i=1}^{n} \left(t_i^{expt} - t_i^{fit} - \frac{\partial t_i^{fit}}{\partial a} \Delta a - \frac{\partial t_i^{fit}}{\partial b} \Delta b - \frac{\partial t_i^{fit}}{\partial U_s} \Delta U_s \right) \frac{\partial t_i^{fit}}{\partial a} = 0$$

$$\frac{\partial S_1^*}{\partial \Delta b} = -2 \sum_{i=1}^{n} \left(t_i^{expt} - t_i^{fit} - \frac{\partial t_i^{fit}}{\partial a} \Delta a - \frac{\partial t_i^{fit}}{\partial b} \Delta b - \frac{\partial t_i^{fit}}{\partial U_s} \Delta U_s \right) \frac{\partial t_i^{fit}}{\partial b} = 0$$

$$\frac{\partial S_1^*}{\partial \Delta U_s} = -2 \sum_{i=1}^{n} \left(t_i^{expt} - t_i^{fit} - \frac{\partial t_i^{fit}}{\partial a} \Delta a - \frac{\partial t_i^{fit}}{\partial b} \Delta b - \frac{\partial t_i^{fit}}{\partial U_s} \Delta U_s \right) \frac{\partial t_i^{fit}}{\partial U_s} = 0$$

The above equations can be subsequently re-arranged and solved for Δa, Δb, and ΔU_s. In the general case it is necessary to start again with the new values of t_i^*, re-evaluate the derivatives, and solve again for $(\Delta a, \Delta b, \Delta U_s)$. The process is repeated until Δa, Δb, and ΔU_s are simultaneously smaller than prescribed values so that a minimum in S_1^* has been reached, *ie* several iterations may be required and this will depend to some extent on how close the initial values (a, b, U_s) are to the minimum.

4.3.3 Constrained Least Squares Method

The problem with the standard least squares method above is that there are no limits on the magnitude of the changes to the parameters (a, b, U_s). In practice, it is desirable to be able to restrict the size of the parameter changes $(\Delta a, \Delta b, \Delta U_s)$ in case, (i) there are any rapid changes of gradient, or (ii) the parameters are known to lie within experimental uncertainities.

The method of least squares with constraints gets over these difficulties by adding extra terms to the sum to be minimised,

$$S_2^* = \left(\frac{\Delta a}{\alpha_1} \right)^2 + \left(\frac{\Delta b}{\alpha_2} \right)^2 + \left(\frac{\Delta U_s}{\alpha_3} \right)^2 + \sum_{i=1}^{n} \left(\frac{t_i^{expt} - t_i^*}{\beta} \right)^2 \tag{4.8}$$

where β is a limit on acceptable deviations of the experimental points from the best fit. The final term of equation (4.8) is the standard (weighted) least squares expression for minimising the sum of the residual squares. The first three terms of (4.8) are the extra terms, where the different constraints α_1, α_2, and α_3 are applied to produce respective acceptable variations in Δa, Δb, and ΔU_s separately. In order to minimise S_2^*, the values of Δa, Δb, and ΔU_s are such that,

$$\frac{\partial S_2^*}{\partial \Delta a} = \frac{\partial S_2^*}{\partial \Delta b} = \frac{\partial S_2^*}{\partial \Delta U_s} = 0 \tag{4.9}$$

After differentiating and rearranging the resulting equations, this leads to a system of 3 linear equations to be solved for Δa, Δb, and ΔU_s, namely,

$$\left[\frac{\beta^2}{\alpha_1^2} + \sum_{i=1}^{n}\left(\frac{\partial t_i^{fit}}{\partial a}\right)^2\right]\Delta a + \left[\sum_{i=1}^{n}\left(\frac{\partial t_i^{fit}}{\partial a}\right)\left(\frac{\partial t_i^{fit}}{\partial b}\right)\right]\Delta b$$

$$+ \left[\sum_{i=1}^{n}\left(\frac{\partial t_i^{fit}}{\partial a}\right)\left(\frac{\partial t_i^{fit}}{\partial U_s}\right)\right]\Delta U_s = \sum_{i=1}^{n}\left(t_i^{expt} - t_i^{fit}\right)\frac{\partial t_i^{fit}}{\partial a}$$

$$\left[\sum_{i=1}^{n}\left(\frac{\partial t_i^{fit}}{\partial a}\right)\left(\frac{\partial t_i^{fit}}{\partial b}\right)\right]\Delta a + \left[\frac{\beta^2}{\alpha_2^2} + \sum_{i=1}^{n}\left(\frac{\partial t_i^{fit}}{\partial b}\right)^2\right]\Delta b$$

$$+ \left[\sum_{i=1}^{n}\left(\frac{\partial t_i^{fit}}{\partial b}\right)\left(\frac{\partial t_i^{fit}}{\partial U_s}\right)\right]\Delta U_s = \sum_{i=1}^{n}\left(t_i^{expt} - t_i^{fit}\right)\frac{\partial t_i^{fit}}{\partial b}$$

$$\left[\sum_{i=1}^{n}\left(\frac{\partial t_i^{fit}}{\partial a}\right)\left(\frac{\partial t_i^{fit}}{\partial U_s}\right)\right]\Delta a + \left[\sum_{i=1}^{n}\left(\frac{\partial t_i^{fit}}{\partial b}\right)\left(\frac{\partial t_i^{fit}}{\partial U_s}\right)\right]\Delta b$$

$$+ \left[\frac{\beta^2}{\alpha_3^2} + \sum_{i=1}^{n}\left(\frac{\partial t_i^{fit}}{\partial U_s}\right)^2\right]\Delta U_s = \sum_{i=1}^{n}\left(t_i^{expt} - t_i^{fit}\right)\frac{\partial t_i^{fit}}{\partial U_s}$$

Each of the sensitivities (partial derivatives) in the above equations can be estimated from two calculations with slightly different values for a, b, and U_s respectively.

The above system of 3 linear equations can be simplified to a simple, single matrix equation to be solved by normal matrix inversion techniques. The matrix equation is written as,

$$\left(A + H^T H\right)\Delta \underline{p} = H^T\left(\underline{t}^{expt} - \underline{t}^{fit}\right) \tag{4.10}$$

where,

$$\underline{t}^{expt} = \begin{bmatrix} t_1^{expt} \\ t_2^{expt} \\ \vdots \\ t_n^{expt} \end{bmatrix} \quad \text{is vector of experimental times (dimensions (n x 1))}$$

$$\underline{t}^{fit} = \begin{bmatrix} t_1^{fit} \\ t_2^{fit} \\ \vdots \\ t_n^{fit} \end{bmatrix} \quad \text{is the vector of fitted times (dimensions (n x 1))}$$

$$\Delta \underline{p} \;=\; \begin{bmatrix} \Delta a \\ \Delta b \\ \Delta U_s \end{bmatrix} \quad \text{is vector of unknown changes (dimensions (3 x 1))}$$

$$H \;=\; \begin{bmatrix} \frac{\partial t_1{}^{fit}}{\partial a} & \frac{\partial t_1{}^{fit}}{\partial b} & \frac{\partial t_1{}^{fit}}{\partial U_s} \\[2mm] \frac{\partial t_2{}^{fit}}{\partial a} & \frac{\partial t_2{}^{fit}}{\partial b} & \frac{\partial t_2{}^{fit}}{\partial U_s} \\[2mm] \vdots & \vdots & \vdots \\[2mm] \frac{\partial t_n{}^{fit}}{\partial a} & \frac{\partial t_n{}^{fit}}{\partial b} & \frac{\partial t_n{}^{fit}}{\partial U_s} \end{bmatrix} \quad \text{is matrix of partial derivatives (dimensions (n x 3))}$$

$$H^T \;=\; \begin{bmatrix} \frac{\partial t_1{}^{fit}}{\partial a} & \frac{\partial t_2{}^{fit}}{\partial a} & \cdots & \frac{\partial t_n{}^{fit}}{\partial a} \\[2mm] \frac{\partial t_1{}^{fit}}{\partial b} & \frac{\partial t_2{}^{fit}}{\partial b} & \cdots & \frac{\partial t_n{}^{fit}}{\partial b} \\[2mm] \frac{\partial t_1{}^{fit}}{\partial U_s} & \frac{\partial t_2{}^{fit}}{\partial U_s} & \cdots & \frac{\partial t_n{}^{fit}}{\partial U_s} \end{bmatrix} \quad \text{is transposed matrix of derivatives (3 x n)}$$

$$A \;=\; \begin{bmatrix} \frac{\beta^2}{\alpha_1{}^2} & 0 & 0 \\[2mm] 0 & \frac{\beta^2}{\alpha_2{}^2} & 0 \\[2mm] 0 & 0 & \frac{\beta^2}{\alpha_3{}^2} \end{bmatrix} \quad \text{diagonal matrix of constraints (dimensions (3 x 3))}$$

On solving the system of equations for $\Delta \underline{p}$, the new estimates of the parameters are,

$$a^{new} \;=\; a^{old} + \Delta a \tag{4.11}$$

$$b^{new} \;=\; b^{old} + \Delta b \tag{4.12}$$

$$U_s{}^{new} \;=\; U_s{}^{old} + \Delta U_s \tag{4.13}$$

and the least squares process is then repeated (starting with the new estimates) until the changes (Δa, Δb, ΔU_s) are simultaneously smaller than prescribed convergence limits (ε_1, ε_2, ε_3) such that an acceptable fit is obtained. In other words, it is simultaneously required that $\Delta a < \varepsilon_1$, $\Delta b < \varepsilon_2$, and $\Delta U_s < \varepsilon_3$, so that a minimum in $S_2{}^*$ has been reached.

4.4   Fortran Programs for Application of the Constrained Least Squares Method to Shock Trajectory Data

4.4.1   Preamble

The use of the constrained least squares method for calculating run-distances and run-times to detonation based on the Hill method for fitting shock trajectory data has been written into a series of Fortran routines. The overall program can be applied to either experimental or calculated shock time of arrival data. A flowchart of the program is provided at Appendix A which illustrates the key steps involved. Standard symbols have been used in the flow diagram to represent, processing (rectangle), input-output (parallelogram), if-then branching (diamond) *etc*.

The least squares program uses the Fortran intrinsic procedure MATMUL to perform the matrix multiplications, and the resulting system of linear equations is solved via a direct matrix factorisation method using routines kindly supplied by Richard Smedley-Stevenson [121]. The program is very efficient in the use of computer time, with calculations typically taking several CPU seconds to complete.

4.4.2   User Input

The input required by the program is read in from a file called lsa.dat which is supplied by the user. There is a slight difference in the required input, depending upon whether the method is being applied to experimental or calculated data, and this difference is described below. Irrespective of the type of data that is being fitted, the user input file must contain, (i) initial values for (a, b, U_s), (ii) values for the constraints $(\beta, \alpha_1, \alpha_2, \alpha_3)$, (iii) the convergence limits (ε_1, ε_2, and ε_3), (iv) the value for C, (v) values for small changes in the parameters (δa, δb, δU_s) so that the sensitivities $\frac{\partial t_i^{fit}}{\partial a}$, $\frac{\partial t_i^{fit}}{\partial b}$, and $\frac{\partial t_i^{fit}}{\partial U_s}$ can be calculated, (vi) number of gauge positions, and (vii) the position and arrival time data for each gauge location. In the method a value for D_{cj}, the Chapman-Jouguet detonation velocity, is also required. For experimental data, the user specifies the value of D_{cj} directly, but for calculated data the user inputs the JWL reaction products' EOS parameters from the reactive burn model being used, and the program calculates D_{cj} from the supplied constants.

4.4.3   Specification of Constraints

The variability of the parameters a, b, and U_s from their respective initial starting values is controlled by their associated constraints α_1, α_2, and α_3 respectively. The smaller the value of the associated α, the tighter the constraint on that parameter, and hence the smaller will be the change in the parameter as a result of applying the least squares method. The shock velocity, U_s, should have a small value specified

for α_3 since this parameter is known to a reasonably high accuracy, *e.g.* from fitting to the first few experimental shock tracker data points. LANL usually quote the shock velocity within given limits, and thus the user should choose the value of α_3 appropriately to ensure that the value of U_s stays within experimental uncertainty. On the other hand relatively larger values for α_1 and α_2 can be input since the values for *a* and *b* are known with less certainty. β controls the goodness of the calculated fit to the experimental data, and can also be thought of as a measure of uncertainty in the experimental shock wave arrival times. Additionally, the constraints β, α_1, α_2, and α_3 can also be thought of as adjustable parameters to give an improved fit. In reality, however, it is the ratio of $\frac{\beta}{\alpha_i}$ that is important, and the best fit can to some extent be altered by varying these ratios appropriately. Typical values chosen for the constraints in the analyses performed were; α_1=1.0, α_2=1.0, α_3=0.1, and β=1.0.

4.4.4 Specification of Convergence Limits

Separate convergence limits ε_1, ε_2, and ε_3 are supplied for the calculated changes in the parameters Δa, Δb, and ΔU_s respectively. The program stops iterating when the changes are simultaneously within the specified limits, *ie* $\Delta a < \varepsilon_1$, $\Delta b < \varepsilon_2$, and $\Delta U_s < \varepsilon_3$, such that it is deemed that an acceptable fit to the supplied shock time of arrival data has been obtained.

The quality of the calculated fit will be dependent on the convergence limits specified. In each iteration, the root mean square (RMS) error for the fit is computed from the residuals $(t_i^{data} - t_i^{fit})$ and is printed out, where t_i^{data} can be either experimental or calculated time of arrival data. The RMS error provides a useful indicator of the goodness of the overall calculated fit at each iteration. If the program stops as a result of the convergence criteria being met, but it is noted that the calculated RMS value is still decreasing and has not yet reached a steady value, then it is likely that the calculated fit could be improved by reducing the convergence limits and re-running the program. Typical values chosen for the convergence limits in the analyses performed were; ε_1=0.0001, ε_2=0.001, and ε_3=0.001.

4.4.5 Calculation of Sensitivities

The sensitivities $\frac{\partial t_i^{fit}}{\partial a}$, $\frac{\partial t_i^{fit}}{\partial b}$, and $\frac{\partial t_i^{fit}}{\partial U_s}$ are estimated numerically by calculating the times of arrival, t_i^{fit}, with slightly different values of (a, b, U_s). The simple

one-sided finite difference approximations given below are used,

$$\frac{\partial t_i^{fit}}{\partial a} = \frac{t_i^{fit}(a+\delta a, b, U_s) - t_i^{fit}(a,b,U_s)}{\delta a} \tag{4.14}$$

$$\frac{\partial t_i^{fit}}{\partial b} = \frac{t_i^{fit}(a, b+\delta b, U_s) - t_i^{fit}(a,b,U_s)}{\delta b} \tag{4.15}$$

$$\frac{\partial t_i^{fit}}{\partial U_s} = \frac{t_i^{fit}(a, b, U_s+\delta U_s) - t_i^{fit}(a,b,U_s)}{\delta U_s} \tag{4.16}$$

and the sensitivities are re-evaluated during each iteration until an acceptable solution is found. At each iteration, 4 separate calculations need to be performed using respectively (a,b,U_s), $(a+\delta a, b, U_s)$, $(a, b+\delta b, U_s)$, and $(a, b, U_s+\delta U_s)$, so that the above sensitivities can be evaluated. For stability of the method, the two different initial starting points for each of the variables should not be too far apart, and it is recommended that users restrict changes to $\leq 5\%$ in each variable.

4.4.6 General Guidance

In general there is a degree of trial and error to obtaining acceptable fits using the constrained least squares method. The calculated fits will be dependent on a number of factors including; (i) how good the data is that you are attempting to fit to, (ii) starting values chosen for the parameters (a,b,U_s), and how close these values are to a minimum, (iii) values chosen for the constraints and convergence limits, and (iv) the computed derivatives (sensitivities). In particular, the solutions obtained are not unique; for example there can be a range of (a,b,U_s) values that can give equally good calculated fits (see Section 4.4 below), and the solution reached will depend on the chosen initial values for (a,b,U_s).

Once a solution is found, the program outputs the actual $(x-t)$ data, the calculated fit to the data, the residuals $(t_i^{data} - t_i^{fit})$, the Hill fit coefficients (a, b, U_s, C, D_{cj}), and the computed run-distance and run-time to detonation. At this stage the user should compare the calculated fit to the actual data and also plot out the residuals. Ideally, the residuals should be randomly distributed about zero, and all lie within acceptable limits. The user then has to use their judgement to answer the following questions; (i) is the fit acceptable?, and (ii) could the fit be possibly improved? If the user is not happy with the calculated fit, the input data should be 'intelligently' modified and the program re-run with the amended input.

If an acceptable solution has not been found after a specified number of iterations then the program currently stops. If this occurs, the user should modify either the initial starting values, the constraints, or the convergence limits, or a combination of the above and re-run the program. Alternatively, the user could extend the program to include a different stop condition to terminate the iterating process, *e.g.* say when the calculated RMS error is less than a specified value.

4.4.7   Description of Fortran Routines

The Fortran routines which apply the constrained least squares method to the described analysis of shock trajectory data are detailed below, and the listings of the routines are given on the attached CD-ROM.

- lsa.f - Main program. Reads in user input data, performs the matrix multiplications, and outputs results.

- calc_fit.f - Calculates the Hill function fit and computes the run-distance and run-time to detonation.

- linsolve.f - Solves a system of linear equations.

- velocities.f - Calculates the detonation velocity, D_{cj}, from the supplied reaction products JWL EOS.

The above suite of programs have been used in the analyses described in Sections 4.5 and 4.6 below.

4.4.8   Ancillary Programs

There are also a number of ancillary programs that are also particularly useful in relation to applying the constrained least squares method to shock trajectory data. The listings of these routines are also on the attached CD-ROM.

arrivaltimes.f

This program calculates arrival times for the shock front at given positions (*e.g.* gauge locations) from experimental or simulated Lagrangian particle velocity histories. The program is particularly useful for extracting shock wave arrival times from calculated data since this information is not readily available from hydrocode runs. At each given position, the time of arrival of the propagating shock wave is taken to occur when the output first reaches a critical value of the particle velocity. This (constant) value is input by the user, and linear interpolation is used to calculate the correct time of arrival from the supplied, discrete, particle velocity data. Note that the critical value input by the user will be dependent on the units used; particle velocity in a hydrocode is in cm/μs, whereas experimental particle velocity data from LANL is usually in mm/μs.

The critical value usually chosen as input to the program is half the particle velocity through the initial shock wave entering the explosive. However, since the particle velocity in the propagting shock increases with depth into the explosive, ideally the critical value should vary with shock strength. The program will be modified in future to calculate shock arrival times at given positions at values of

particle velocity that depend on the shock strength. The arrivaltimes.f program was used to extract shock wave arrival times from the CREST calculations described in Section 4.6.

contour.f

This program can be used to indicate where local minima occur for given (a, b) values, assuming a fixed value of U_s, and hence determine suitable starting values for the parameters (a, b, U_s) in the application of the constrained least squares solution method to fitting shock trajectory data. The program is essentially a version of the search method (described in Section 4.3.1) to solve the Hill differential equation (4.1) to determine run-distances and run-times to detonation. Suitable fixed values for U_s, C, and D_{cj} are chosen, and the parameters (a, b) are varied within given limits in an attempt to find suitable values that produce acceptable fits to shock time of arrival data by integrating equation (4.1). The RMS error for each calculated fit is computed from the residuals to give a measure of the goodness of the fit corresponding to each (a, b) pair.

To visualise the data, an IDL script was written that produces a surface plot of the inverse of the RMS error over the range of (a, b) values used. A maximum in the inverse of the RMS error gives a mimimum in the calculated fit. An example surface plot is shown in Figure 4.3 corresponding to fitting the shock tracker data from EDC37 gas-gun Shot 1159 using a 200 x 200 grid of (a, b) values. It is observed that there is a 'ridge' of suitable (a, b) values over the ranges shown that will produce equally good calculated fits since the RMS errors are very similar. This plot thus gives an indication of resonable starting values of (a, b) to use that will be close to a local minimum.

4.5   Application of the Least Squares Method to Experimental Shock Trajectory Data

To test and validate the application of the constrained least squares solution method for determining run-distances and run-times to detonation, it has been applied to the shock tracker data obtained from EDC37 sustained single shock gas-gun experiments [38]. These experiments are summarised in Table 4.1. Out of the total of 6 single sustained shock experiments fired, the run to detonation has been deduced from 4 of the experimental shots. In one experiment (Shot 1120) the shock tracker gauge failed, while in Shot 1267, run to detonation occured beyond the end of the gauge package. Note that the run-distances to detonation given in Table 4.1 are those quoted by LANL.

Using the constrained least squares solution method, the calculated fits to the experimental shock tracker data from Shots 1160, 1122, 1159, and 1277 are shown

Table 4.1: Summary of EDC37 Sustained Single Shock Gas Gun Experiments.

Shot No.	Impact Vel. (mm/μs)	Impactor Material	Input Pressure (GPa)	Run Distance x_{run} (mm)
1267	0.487	Z-cut sapphire	2.76 ± 1.5	>16.0
1160	0.608	Vistal	3.52 ± 1.6	14.4
1122	0.682	Vistal	3.95 ± 1.7	12.3
1120	0.809	Vistal	4.91 ± 1.9	No data
1159	0.918	Vistal	5.92 ± 2.1	7.0
1277	1.403	Z-cut sapphire	10.8 ± 3.0	2.8

respectively in Figures 4.4-4.7. Shown on each of these plots is the experimental shock tracker data, the best fit to this data by integrating (4.1), and the residuals ($t_i^{expt} - t_i^{fit}$) multiplied by 10. It is observed that some of the calculated fits are better than others. For example, a very good fit has been obtained to the shock tracker data from Shot 1159 (Figure 4.6), where the majority of the residuals for the fit are typically within ± 0.005 μs, and all are within ± 0.01 μs. However, a poorer fit is obtained to the early gauge elements from Shot 1122 (Figure 4.5) where the residuals for the fit are typically ± 0.05 μs. It is seen that there is a noticeable 'kink' in the data for Shot 1122 for the early gauge elements, indicating that either the tracker data is questionable or the wave is not accelerating as smoothly as would be expected. This illustrates clearly the point that the obtained calculated fits will only be as good as the data that is being fitted! The values used as input to the least squares method are given in Table 4.2, where subscript 0 indicates initial values.

Table 4.2: Input Values to Constrained Least Squares Program.

| Parameter | Shot No. | | | | | |
	1120	1122	1159	1160	1267	1277
a_0	0.05	0.05	0.05	0.05	0.05	0.10
b_0	2.50	2.50	2.50	1.50	2.00	2.00
U_{s0}	4.00	3.84	4.19	3.75	3.56	5.00
Δa	-0.01	-0.01	-0.01	-0.01	-0.01	-0.01
Δb	-0.10	-0.10	-0.10	-0.10	-0.10	-0.10
ΔU_s	-0.10	-0.10	-0.10	-0.10	-0.10	-0.10
β	1.0	1.0	1.0	1.0	1.00	1.00
α_1	1.0	1.0	1.0	1.0	1.0	1.0
α_2	1.0	1.0	1.0	1.0	1.0	1.0
α_3	1.0	1.0	1.0	0.5	0.1	0.5
ε_1	2.0×10^{-4}	2.0×10^{-3}	1.0×10^{-4}	1.0×10^{-3}	1.0×10^{-3}	5.0×10^{-4}
ε_2	2.0×10^{-3}	2.0×10^{-3}	1.0×10^{-3}	1.0×10^{-3}	1.5×10^{-3}	1.0×10^{-3}
ε_3	1.0×10^{-3}	1.0×10^{-3}	1.0×10^{-3}	1.0×10^{-3}	1.0×10^{-3}	1.0×10^{-3}

The values for the parameters in the Hill function (4.1) that give the fits shown

in Figures 4.4-4.7 are given in Table 4.3, where C is from the measured EDC37 Hugoniot [11], and the values quoted for D_{cj} are obtained from the fits to the last few data points of the respective measured $(x - t)$ trajectories. Values of D_{cj} consistent with published data [122] are obtained for Shots 1159, 1160, and 1277. The value of D_{cj} quoted for Shot 1122 is lower than would be expected indicating that either the wave has not reached a steady detonation or again that the shock tracker data for this experiment is questionable. The remaining values required as input to the method are given in Table 4.2.

Table 4.3: Hill Function Parameters Fitted to EDC37 Shock Trajectory Data.

Shot No.	a	b	U_s (mm/μs)	C (mm/μs)	D_{cj} (mm/μs)
1160	0.055222	2.534801	3.674033	2.40	8.72
1122	0.050055	2.644321	3.692185	2.40	8.53
1159	0.034845	2.497354	4.230644	2.40	8.76
1277	0.021087	2.493027	5.000284	2.40	8.70

The run-distances and run-times to detonation derived from the calculated fits to the EDC37 experimental shock tracker data are compared with those quoted by LANL in Table 4.4. The point where detonation is attained is defined to be the point where 99% of D_{cj} is reached in the fit. Good agreement is obtained between the run-distances and run-times to detonation derived from the application of the constrained least squares method to the Hill function (4.1), and the corresponding run-distances and run-times given by LANL. It is noted that LANL quote an accuracy in their fitting process of 0.4 mm in run distance and 0.1 μs in run time. Thus the majority of values derived from this work are within the accuracies quoted by LANL. The largest discrepency occurs for Shot 1277 which has the shortest run-distance. This discrepency is probably due to the fact that, unlike the remaining shots, there are only a handful of gauge points to fit to before the turnover to detonation occurs, thus leading to a larger margin for error in the calculated run-distance and run-time.

Table 4.4: Run Distance Analysis of EDC37 Single Shock Gas Gun Experiments.

Shot No.	LANL Quoted Values		This Work	
	Run Distance x_{run} (mm)	Run Time t_{run} (μs)	Run Distance x_{run} (mm)	Run Time t_{run} (μs)
1160	14.4	3.47	14.4	3.52
1122	12.3	2.95	12.2	2.99
1159	7.0	1.45	7.0	1.46
1277	2.8	0.51	3.2	0.56

Note that although run-distances and run-times to detonation were quoted by

LANL, the fitting parameters in the Hill function (4.1) were not supplied.

4.6 Application of the Least Squares Method to Calculated Shock Trajectory Data

The application of the constrained least squares method to fitting experimental shock trajectory data based on the Hill method was successfully validated above, and can thus be applied with confidence to data from hydrocode simulations to determine run-distances and run-times to detonation from calculated results. The entropy-dependent CREST reactive burn model [61] is able to reproduce the particle velocity gauge records from EDC37 gas-gun experiments which show the reaction build-up in the shocked explosive, usually before detonation is attained. Here, the constrained least squares method is applied to shock trajectory data from hydrocode calculations of the EDC37 gas-gun experiments using CREST, to enable run-distances and run-times to detonation deduced from CREST calculations to be compared with experiment.

Calculations of the EDC37 gas-gun experiments detailed in Table 4.1 were carried out using PERUSE [88], the one-dimensional Lagrangian hydrocode which is used as a test-bed for reactive burn model development. A meshing of 50 zones/mm was used in the calculations, a resolution at which the CREST model for EDC37 is mesh converged. The CREST model parameters for EDC37 explosive were as given in [61]. Calculated arrival times for the propagating shock wave at given positions in the explosive were deduced from the calculated particle velocity histories using the arrivaltimes.f program described in Section 4.4.8, where the critical value of the particle velocity was taken to be 0.02 cm/μs.

The Hill function fits to the calculated arrival times for the EDC37 gas-gun shots are shown in Figures 4.8-4.13, where each plot shows the calculated shock arrival data, the best fit to this data by numerically integrating (4.1), and the residuals ($t_i^{calc} - t_i^{fit}$) multiplied by 10. It is observed that a good fit is obtained to all 6 shots. The majority of the residuals for the fits are within ± 0.01 μs, with the largest discrepency in arrival time being approximately 0.03 μs for Shot 1267. The values used as input to the least squares method are as given in Table 4.2, and the Hill function (4.1) parameters fitted to the EDC37 calculated shock wave arrival data are given in Table 4.5. The quoted values for C and D_{cj} are from the respective unreacted EOS and reaction products EOS in the EDC37 CREST model.

The calculated run-distances and run-times to detonation deduced from the fits are compared with the experimentally deduced values in Table 4.6. Run-distance data is usually presented in the form of a Pop-Plot [31], named after one of its originators, which expresses the relationship between the input shock pressure and the run-distance (or run-time) to detonation, usually on logarithmic scales. The calculated Pop-Plot for EDC37 is compared with experiment in Figure 2.4. In addition

Table 4.5: Hill Function Parameters Fitted to EDC37 Calculated Shock Arrival Data.

Shot No.	a	b	U_s (mm/μs)	C (mm/μs)	D_{cj} (mm/μs)
1267	0.705792	1.737367	3.491805	2.779045	8.811656
1160	0.756806	1.550453	3.644656	2.779045	8.811656
1122	0.639189	1.579896	3.754207	2.779045	8.811656
1120	0.101327	2.366737	4.016714	2.779045	8.811656
1159	0.066028	2.487148	4.192159	2.779045	8.811656
1277	0.126551	2.003240	5.001590	2.779045	8.811656

to the gas-gun data, the plot also shows EDC37 run-distance data obtained from earlier explosively driven wedge test experiments carried out by Rabie and Harry [30]. The straight line relationship is the best fit to all the experimental data. It is observed in Figure 2.4 that a good fit is obtained to the experimental Pop-Plot at high and intermediate input shock pressures, however the CREST calculations start to tail off at the low pressure end with the model giving a shorter run-distance to detonation compared to experiment. This indicates that the CREST model for EDC37 explosive is too reactive at low shock pressures (<3.5 GPa).

Table 4.6: EDC37 Gas-Gun Run Distance Analysis.

Shot No.	Experiment			Calculation		
	Pressure (GPa)	Run Distance x_{run} (mm)	Run Time t_{run} (μs)	Pressure (GPa)	Run Distance x_{run} (mm)	Run Time t_{run} (μs)
1267	2.76	> 16.0	> 4.00	2.78	16.8	4.29
1160	3.52	14.4	3.52	3.61	14.3	3.42
1122	3.95	12.2	2.99	4.16	12.7	2.94
1120	4.91	No data	No data	5.15	9.4	2.11
1159	5.92	7.0	1.46	6.06	7.4	1.58
1277	10.8	3.2	0.56	10.8	3.1	0.54

For completeness, the calculated Hill function fits to the experimental and simulated shock time of arrival data for Shots 1160, 1122, 1159, and 1277 are compared respectively in Figures 4.15-4.18. For each shot it is seen that the CREST calculations give a good match to the experimental shock trajectories. The acceleration of the shock wave is well matched to the experimental data over the majority of the run to detonation, with some differences seen in the late stages of acceleration before the turnover to detonation occurs.

4.7 Conclusions

The described constrained least squares method has been applied to shock time of arrival data from explosive gas-gun experiments to provide a fast and efficient solution method for determining run-distances and run-times to detonation using a technique devised by Larry Hill at LANL for fitting shock trajectory data. Good matches to the experimental shock tracker data from sustained single shock EDC37 gas-gun shots have been obtained, and the derived run-distances and run-times to detonation are in very close agreement with the corresponding values quoted by LANL, thus validating the application of the method.

The method was then subsequently applied to shock time of arrival data from hydrocode calculations of the EDC37 gas-gun experiments using the CREST reactive burn model. Overall, the CREST model for EDC37 explosive gives good agreement with the experimental shock trajectory data and run-distance to detonation data, however the fit to the EDC37 Pop-Plot starts to diverge at low pressures, indicating that the EDC37 CREST model needs to be improved in the low pressure region.
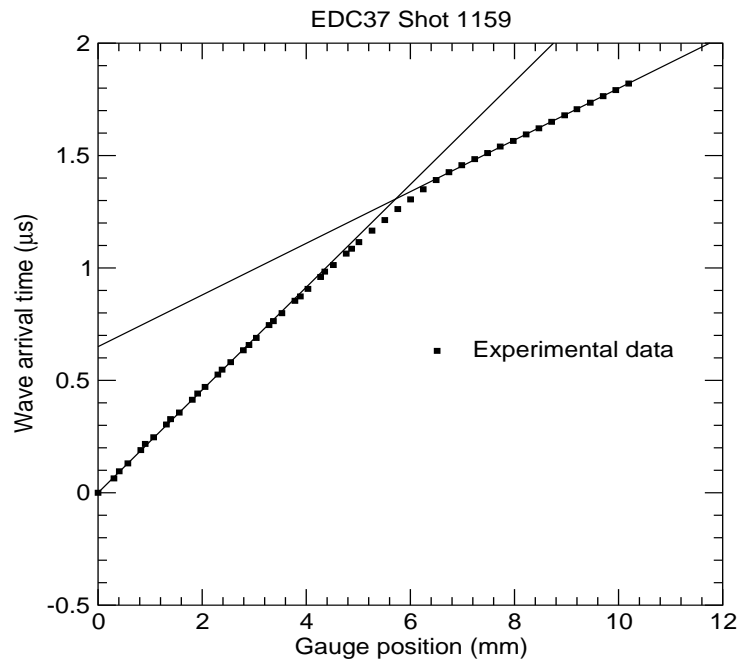
Figure 4.1: Position-time (x-t) plot for EDC37 Shot 1159 obtained from shock arrival at shock tracker gauge elements.
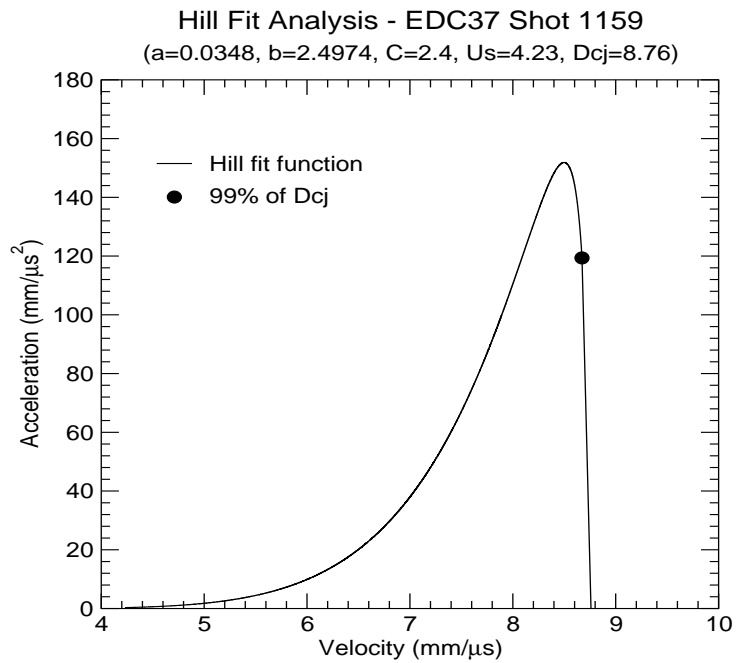
Figure 4.2: Plot of the acceleration-shock velocity function for EDC37 Shot 1159.
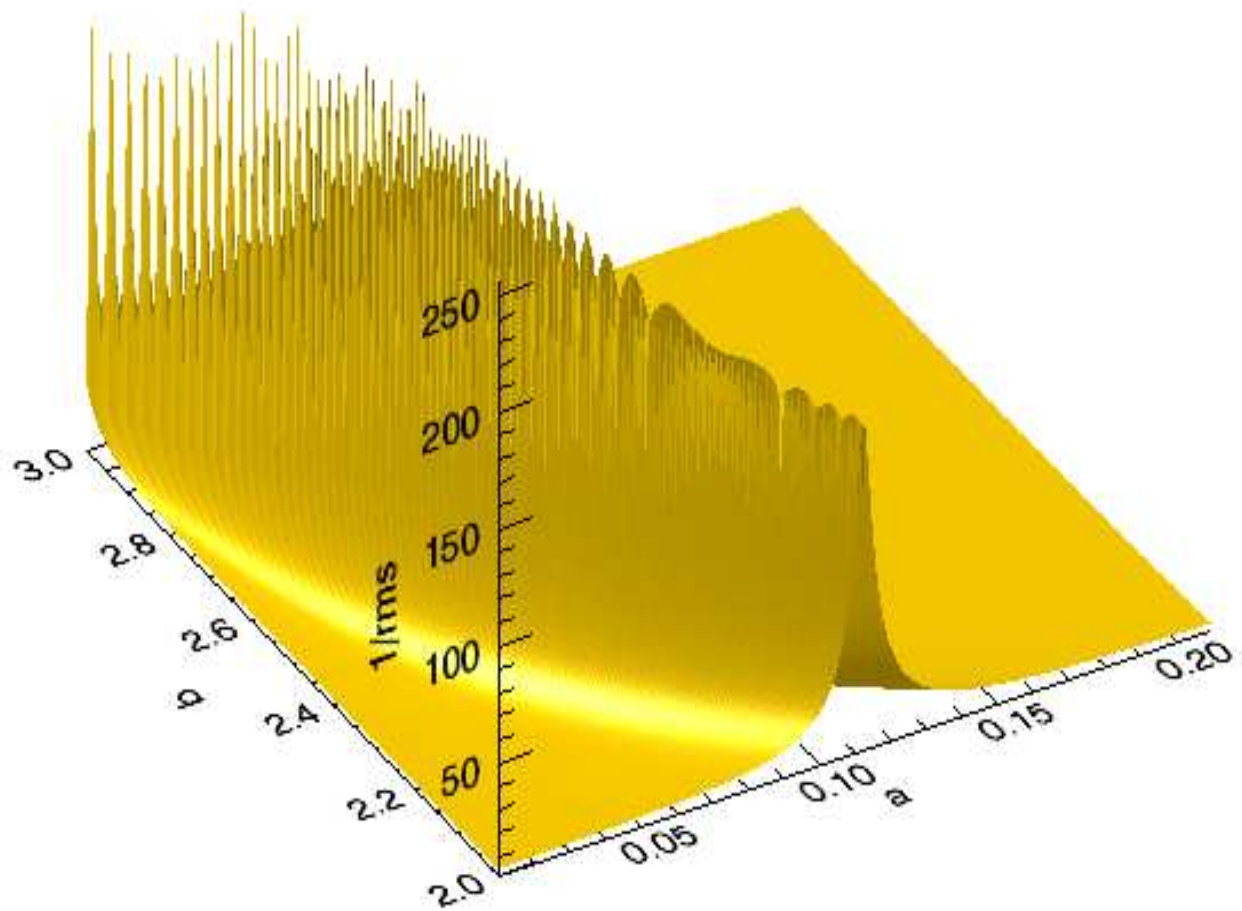
Figure 4.3: Surface plot for EDC37 Shot 1159.
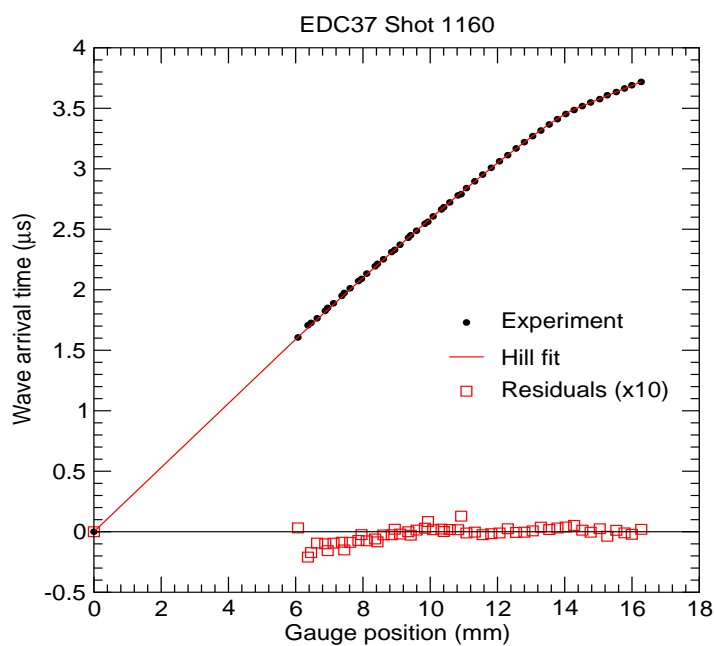
Figure 4.4: Calculated fit to experimental shock tracker data from EDC37 gas-gun Shot 1160.
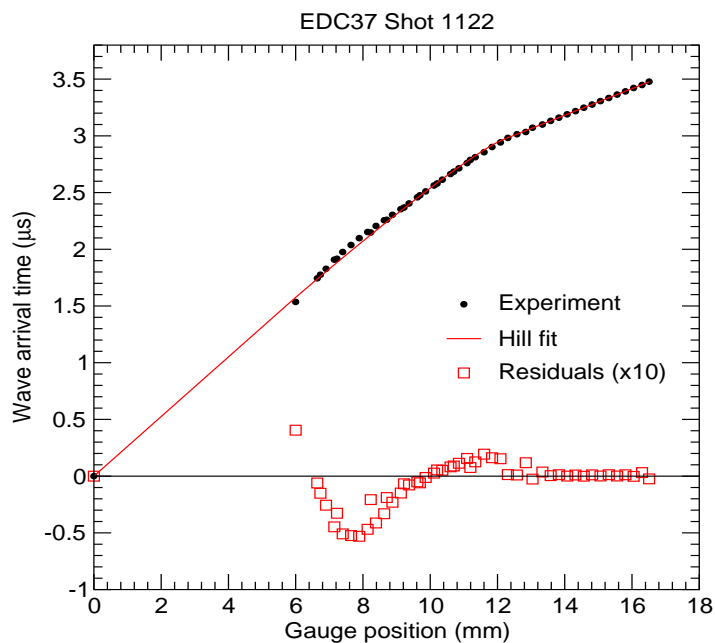
Figure 4.5: Calculated fit to experimental shock tracker data from EDC37 gas-gun Shot 1122.
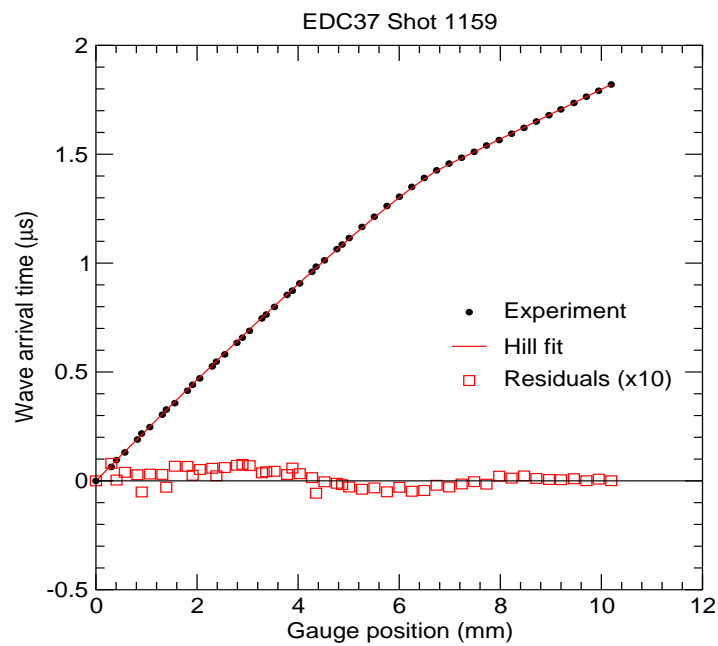
Figure 4.6: Calculated fit to experimental shock tracker data from EDC37 gas-gun Shot 1159.
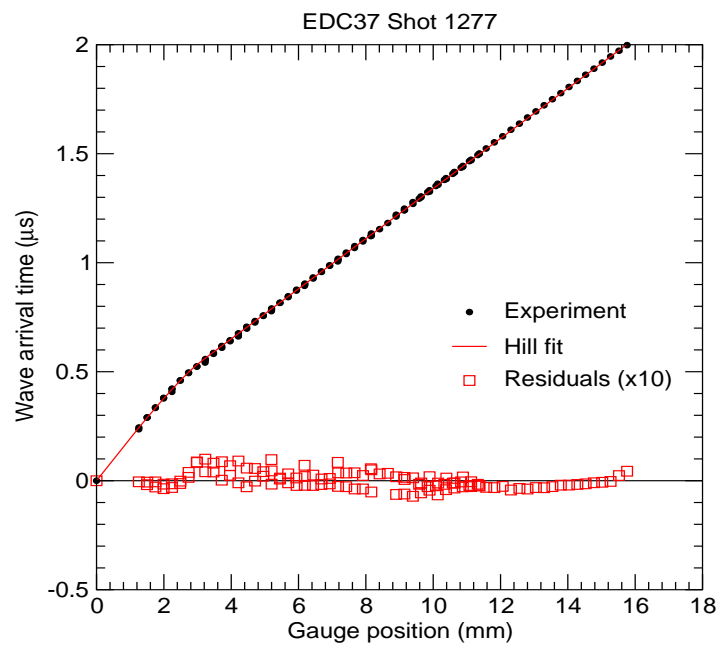
Figure 4.7: Calculated fit to experimental shock tracker data from EDC37 gas-gun Shot 1277.
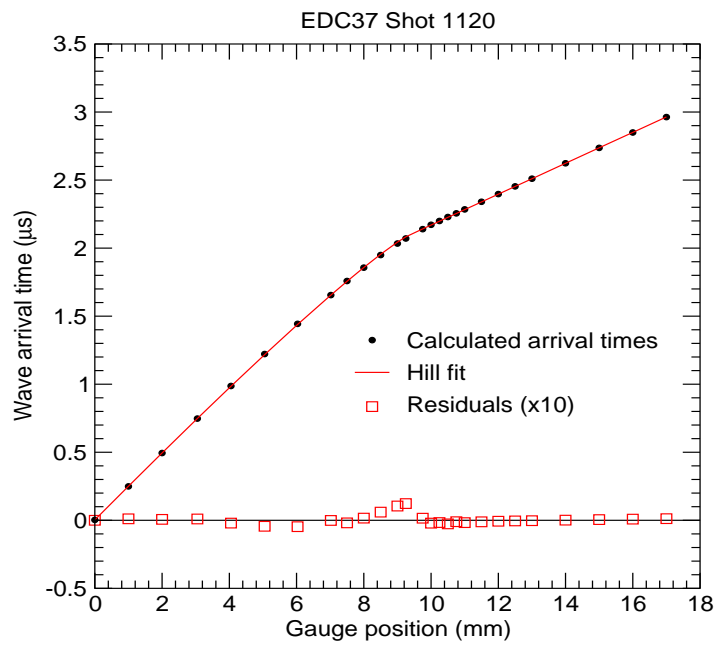
Figure 4.8: Calculated fit to CREST time of arrival data for EDC37 gas-gun Shot 1120.
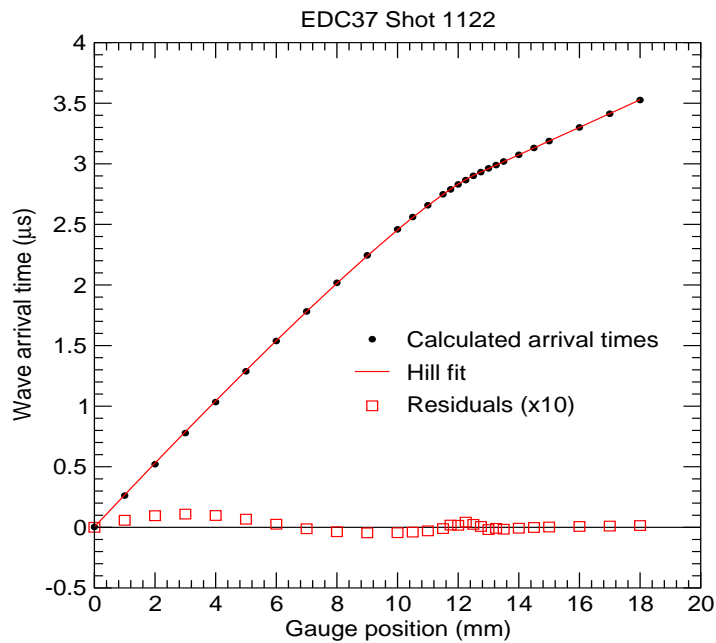
Figure 4.9: Calculated fit to CREST time of arrival data for EDC37 gas-gun Shot 1122.
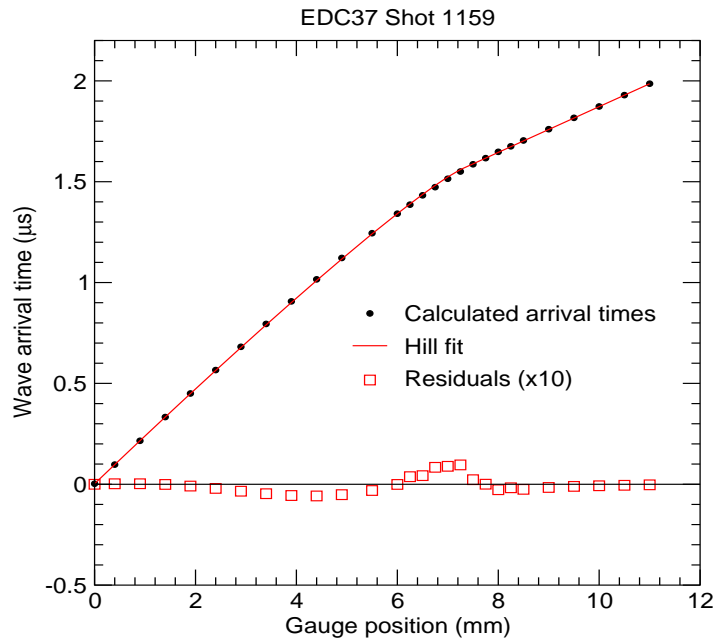
Figure 4.10: Calculated fit to CREST time of arrival data for EDC37 gas-gun Shot 1159.
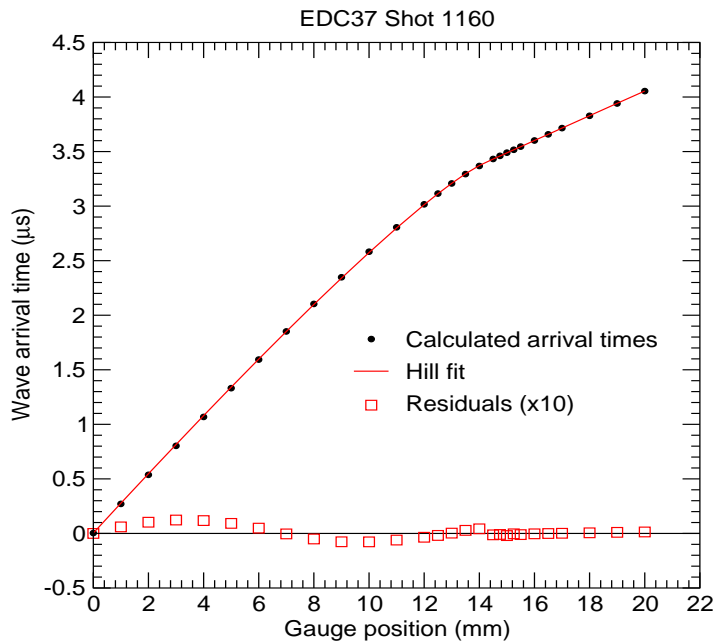
Figure 4.11: Calculated fit to CREST time of arrival data for EDC37 gas-gun Shot 1160.
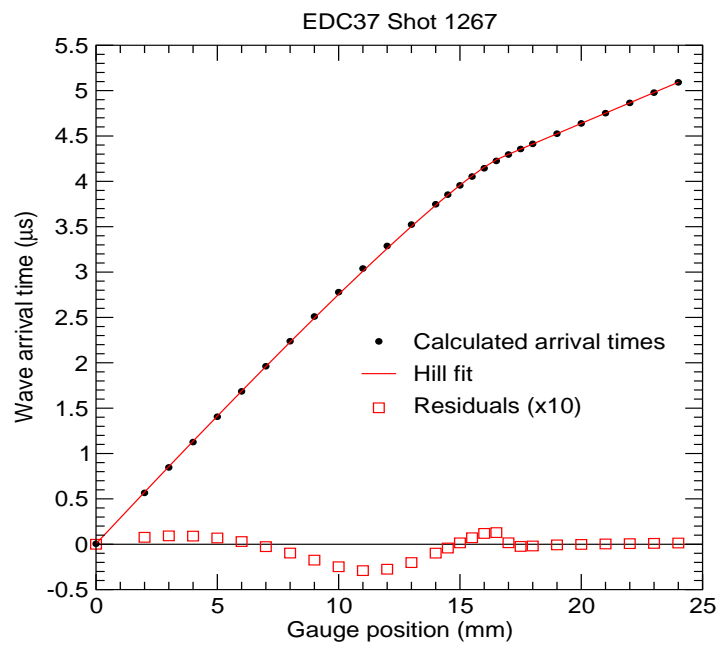
Figure 4.12: Calculated fit to CREST time of arrival data for EDC37 gas-gun Shot 1267.
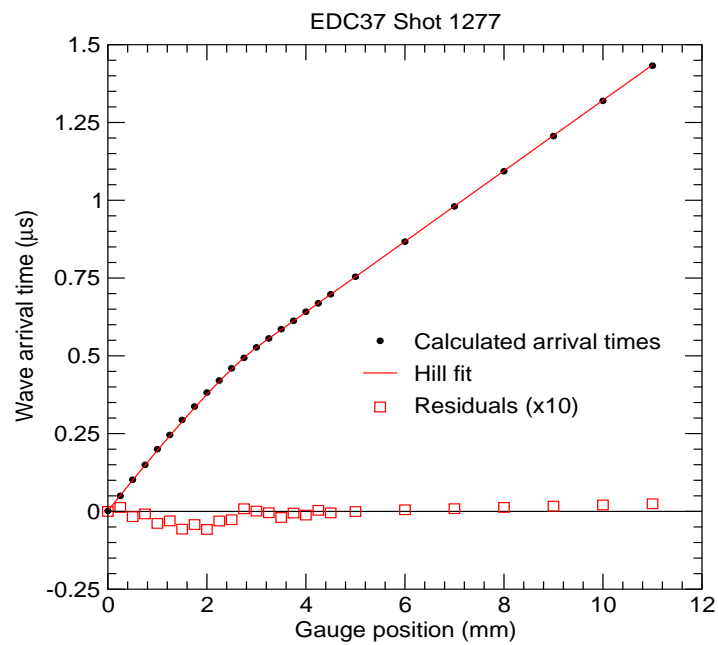
Figure 4.13: Calculated fit to CREST time of arrival data for EDC37 gas-gun Shot 1277.
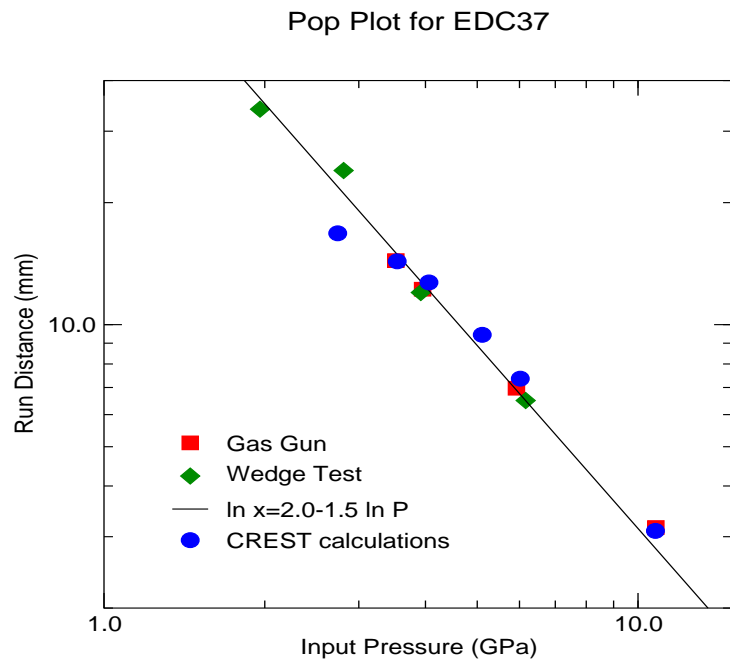
Figure 4.14: Pop Plot Data for EDC37.
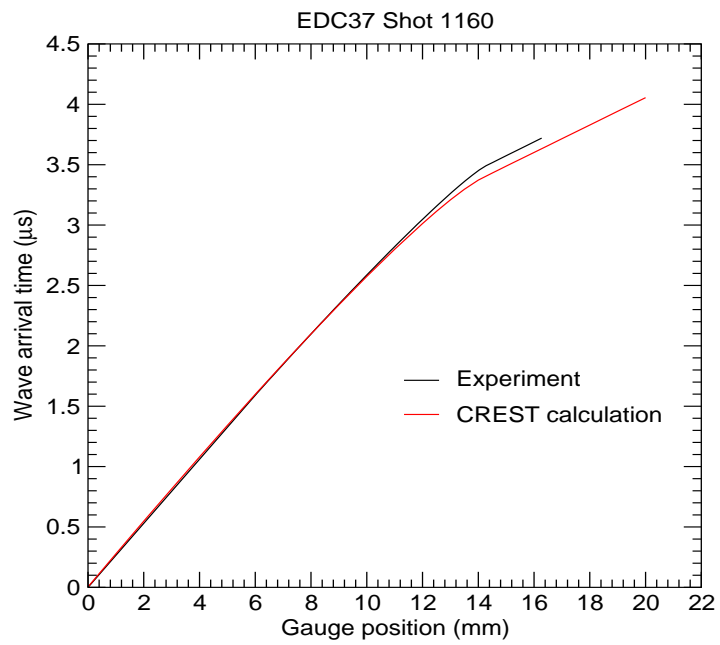
Figure 4.15: Calculated fits to shock time of arrival data for EDC37 gas-gun Shot 1160.
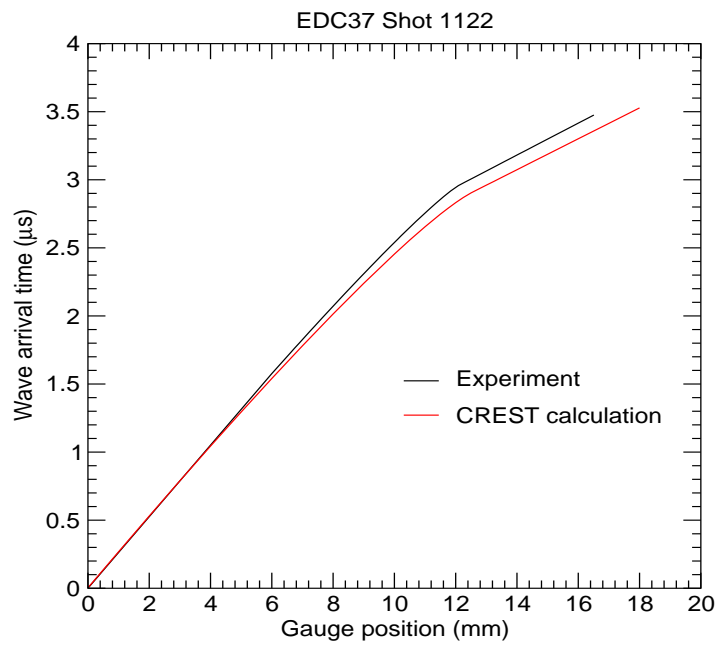
Figure 4.16: Calculated fits to shock time of arrival data for EDC37 gas-gun Shot 1122.
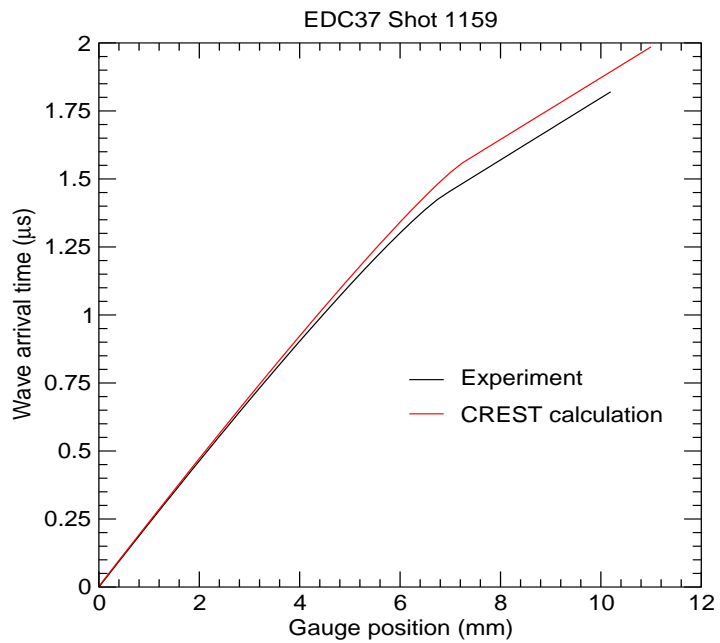
Figure 4.17: Calculated fits to shock time of arrival data for EDC37 gas-gun Shot 1159.
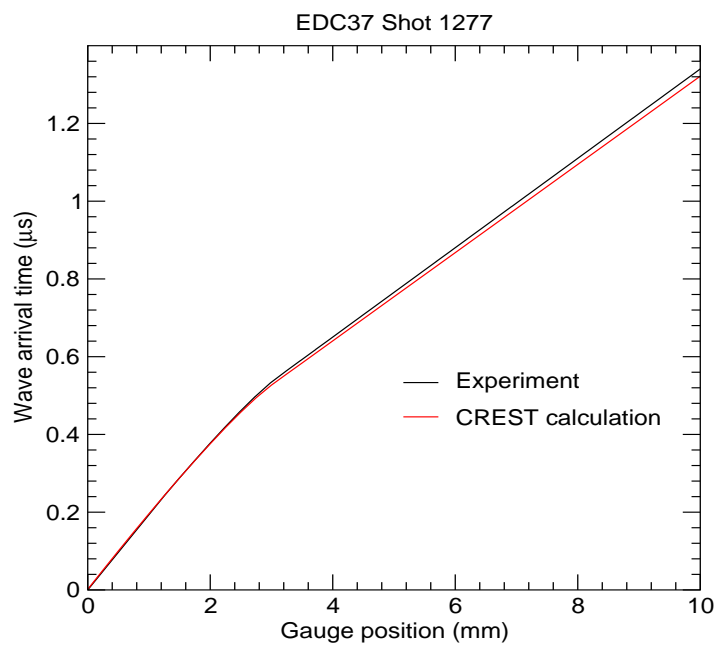
EDC37 Shot 1277

Figure 4.18: Calculated fits to shock time of arrival data for EDC37 gas-gun Shot 1277.

Chapter 5

Explicit 'Hot-Spot' Modelling

5.1 Introduction

Shock initiation of heterogeneous solid explosives is a complex problem involving a number of mechanical, thermal, and chemical processes. The key to initiation in such explosives is the generation of 'hot-spots' at material discontinuities (crystal/binder boundaries, pores, crystal defects *etc*) which act as concentration points for energy density and locally trigger the thermal reaction in the explosive [4]. During shock compression, a distribution of 'hot-spot' sizes and temperatures is created that is dependent on the initial conditions of the explosive such as initial pore size distribution, explosive particle size distribution, and binder distribution. These 'hot-spots' can then grow to consume neighbouring explosive particles or fail to grow as thermal conduction lowers their temperature before reaction can be completed. The initial conditions of the explosive are important since it is well known experimentally that the explosive morphology (initial pore size distribution, grain size distribution, crystal orientation *etc*) can affect the explosive response [45] [48].

Continuum-based reactive burn models, such as the pressure-based Lee-Tarver model [49] and the entropy-dependent CREST model [61], do not explicitly take account of the fundamental processes involved in shock initiation of heterogeneous solid explosives. For example, no attempt is made to model 'hot-spot' formation in an explosive as a result of shock compression. Instead, such models give a generalised description of the underlying physical and chemical processes involved. Their reaction rate equations are mathematical expressions that approximate 'hot-spot' formation and ignition, and subsequent growth of reaction behaviour, and the rate constants are empirically fitted to experimental data. Although the CREST reactive burn model [61] [62] is giving promising results in simulating a range of explosive phenomena with a single set of parameters, it is unable to account for the effect of particle or grain size, pore size, and binder distribution on the explosive response. These models will only be capable of reproducing the effects of changes in the initial conditions of the explosive by varying some of the constants in the model

until an improved fit with experimental data is obtained. Thus, without advances in the modelling, the effects of pore and grain size distribution, crystal orientation *etc* on an explosive's response can only be demonstrated by a battery of experiments. This approach is very costly.

Recent advances in computational capabilities now offer the chance to develop more sophisticated models of explosive initiation, and over the past decade or so, researchers have begun to consider and develop so-called physics-based or mesoscale models of explosive behaviour. Such models attempt to take account of the morphology of an explosive in terms of the initial particle or grain size, pore size, and binder distribution, and therefore have the potential to account for such initial condition differences. However, to develop such a model that can be used in hydrocode calculations to simulate real problems of interest is a large undertaking. The difficulties are obvious; at least two scales of behaviour have to be simulated, (i) microscopic 'hot-spots' (*e.g.* 0.1-10 μm), and (ii) macroscopic bulk response (*e.g.* 0.1-10 mm). In addition, detailed knowledge of the material properties of the constituent parts is required, the chemistry is far from straightforward, and there are many potential sources of 'hot-spots' as discussed by Field *et al.* [5].

Physics-based or mesoscale models of explosive shock initiation that have been developed for use in hydrocode calculations essentially fall into two categories; (i) statistical 'hot-spot' models, and (ii) 'hot-spot' models based on a particular mechanism, *e.g.* pore collapse. The former class of model does not explicity model the formation of 'hot-spots' in a material, but instead utilises the output from large scale, direct numerical simulations *e.g.* [79] [80] to define the size and distribution of 'hot-spots' as the initial conditions for a hydrocode calculation. Nicholls's recent statistical 'hot-spot' model [76] is one example of this type of approach. The aim is to model the dynamics of a population of 'hot-spots' that are able to start the chemical reaction in the explosive, and so allows for the fact that 'hot-spots' may be generated as a result of a number of different mechanisms. However, very large multiprocessor computers are required to perform the direct numerical simulations, and the task of extracting the data required as input to a statistical 'hot-spot' model is far from straightforward.

The other, and to date, more popular approach to developing a mesoscale reactive burn model is to take one particular mechanism for 'hot-spot' formation in a heterogeneous solid explosive, and use its results to deduce the form of the initial stages of the release of energy. However, various 'hot-spot' mechanisms have been proposed over the years *e.g.* pore collapse, shear banding, friction, and fracture, and currently there is no universal agreement as to the mechanism(s) by which energy localisation occurs as a result of shock compression. It is possible that there may be more than one 'hot-spot' mechanism at play, and the dominant mechanism may be dependent on factors such as the type of explosive (*e.g.* plastic bonded vs rubberised), manufacturing process (*e.g.* pressed vs cast), and type and magnitude of the shock loading.

Most modelling work carried out recently in this respect has concentrated on describing 'hot-spot' formation due to the collapse of pores in the explosive material. In heterogeneous solid explosives, pores are usually present as part of the manufacturing process. The explosive crystals or grains are usually small and irregularly shaped, hence it is difficult to manufacture them to a density near theoretical maximum density. As a result, all solid explosives have some porosity. Pores are prime candidates as potential 'hot-spot' sites since experimental work has shown an increase in sensitivity with increasing porosity (decreasing density) *e.g.* [36]. This indicates that more pores leads to more 'hot-spots', and hence a more sensitive material. Other work has also shown that void content, rather than binder or binder amount, appears to be the dominating factor in shock initiation of heterogeneous solid explosives [11].

The heating of the material as a result of pore collapse can be due to several mechanisms. Mader [7] described a purely hydrodynamic mechanism in which the upstream surface of a cavity is accelerated by the shock, leading to the formation of a jet that impacts the downstream side of the cavity. Heating is produced by compression of the solid phase material as a result of the high pressure jet impact. In the work of Bowden and Yoffe [4] the role of adiabatic compression of gaseous pores as a source of ignition was emphasised. Cook *et al.* [65] described a gas pore collapse mechanism in which gaseous pores are heated to high temperatures as a result of adiabatic compression. Explicit heat transfer from the hot gas to a thin shell of the surrounding explosive then allows the explosive to be ignited. Since solid explosives are able to withstand a certain amount of distortion, and thus have strength properties, 'hot-spot' formation as a result of pore collapse due to pure hydrodynamic effects is thought to be unlikely.

Carroll and Holt [8] considered heating due to inviscid, plastic flow during pore collapse. In their analysis pore collapse occurs in three phases; an initial elastic phase, a transitional elastic-plastic phase, and a fully plastic phase. Carroll and Holt noted that the pore volume is essentially unchanged during the first two phases, and hence the analysis could be further simplified by ignoring the initial elastic, and transitional elastic-plastic phases of pore collapse. Later, Butcher *et al.* [123] incorporated viscous effects into the Carroll and Holt model. Frey [9] studied the mechanics of pore collapse in an energetic material. Of a number 'hot-spot' mechanisms including hydrodynamic solid phase compression, hydrodynamic gas phase heating, inviscid plastic work, and viscoplastic work, it was concluded that the mechanism of viscoplastic work gave the most important contribution to the heating of the materials. Therefore, currently most shock initiation models based on pore collapse use the viscoplastic heating mechanism to describe the creation and subsequent ignition of 'hot-spots'.

Khasainov *et al.* [72] were the first to build a viscoplastic pore collapse model and apply it to 'hot-spot' formation resulting from shock propagation in heterogeneous solid explosives. As per the pore collapse model of Carroll and Holt [8], it

was assumed the pore volume remained unchanged until the applied stress exceeded the plastic yield strength of the material. The 'hot-spots' model described by Belmas *et al.* [64], is similar to that of Khasainov, and both models include the effects of thermal conduction on the 'hot-spot' temperatures. The viscoplastic models of Kang *et al.* [124], Bonnett and Butler [125], and Massoni *et al.* [73] are more complex than the other viscoplastic pore collapse models since a full description of the gas phase, and the interaction between the gaseous and solid phases is included in their models.

All the viscoplastic 'hot-spot' models described above use the Carroll and Holt hollow sphere model [8], and are built on the assumption of an incompressible solid phase at the microscopic scale proposed and justified by Carroll and Holt. Again, following the observations of Carroll and Holt [8], these models also assume that pore contraction in the inital elastic, and transitional elastic-viscoplastic phases is negligible, and that porosity changes occur as a result of viscoplastic flow only in the solid material. The model of Kim [126] is the only one of this class of model that is based on elastic-viscoplastic flow during pore collapse rather than just viscoplastic flow only.

In this chapter, a start is made in the development of a physics-based reactive burn model for hetergeneous solid explosives. The ultimate aim is to develop a 'simple' model that can be incorporated in a hydrocode, and that will be able to predict the effects of changes in particle size, pore size, and binder distribution on explosive shock initiation. The first step in this process is to model the initiation or ignition phase where 'hot-spots' are created, and decomposition starts to occur in these localised heated regions, as a result of shock compression of the explosive material. The approach described here takes one particular mechanism, that of elastic-viscoplastic pore collapse, as the basis for 'hot-spot' formation.

As part of the approach, direct numerical simulations are performed to support the development of a simplified model. Direct numerical simulations of pore collapse in a heterogeneous solid explosive are very useful for: (i) gaining insight into what parameters, or combination of parameters are important in 'hot-spot' formation and subsequent ignition, (ii) identifying the important phenomena that need to be included in any simplified model, and (iii) testing the various assumptions and results of a simple 'hot-spot' model.

The one-dimensional, multi-material, Lagrangian hydrocode PERUSE [88] contains an elastic-viscoplastic constitutive model. This constitutive model can be used to examine plastic deformation around a collapsing pore as a possible 'hot-spot' mechanism. This code will be used to perform direct numerical simulations, investigating phenomena in which the viscous heating effect is expected to be significant and a likely source of ignition. The hydrocode calculations can also be used to test the assumptions and results of a simplified pore collapse model to describe explosive ignition that it is intended to incorporate or build into a hydrocode.

This chapter is essentially split into two parts. The first part details the direct numerical simulation work performed using PERUSE, where 'hot-spots' are formed as a result of elastic-viscoplastic flow in the vicinity of a collapsing pore. Results of simulations are presented showing how such obvious physical parameters as porosity and pore size, rise time of the shock, magnitude of the shock pressure, double shock loading, or material parameters can affect 'hot-spot' formation in a heterogeneous solid explosive, and to observe whether the results of the calculations are consistent with commonly held ideas about shock initiation and sensitivity of porous explosives. The second part describes a simple 'hot-spot' initiation model, based on elastic-viscoplastic pore collapse, that has been developed. The described simple model contains a number of features found in other viscoplastic 'hot-spot' models described in the literature, but with one major important difference that brings into question the validity of the simplifying assumption that pore collapse occurs by virtue of viscoplastic flow only, which is common to all these other models. Results from the simple model are compared with direct numerical simulations using PERUSE to examine how well, or otherwise, the simple 'hot-spot' model is performing. Finally, the conclusions are given and future work discussed.

5.2 Direct Numerical Simulations of Explosive 'Hot-Spot' Initiation

5.2.1 Preamble

Direct numerical simulations of physical processes that are thought to be of importance in the formation of 'hot-spots' in an explosive material (pore collapse, friction, shear *etc*) are very useful for gaining insight into whether, and under what conditions, proposed 'hot-spot' mechanisms will be important. Such simulations require sub-micron sized meshes due to the dimensions of 'hot-spots' created as a result of shock compression (0.1 - 10μm [4]). Since it is currently impractical to use such meshing in hydrocode simulations of large scale shock initiation problems of interest, the results of the direct numerical simulations, in the first instance examining the formation and subsequent reaction of a single 'hot-spot' in isolation, can be used to support the development of simpler mesoscale models of explosive behaviour.

Baer [79] [80] has performed large scale, direct numerical simulations of an ensemble of explosive grains, pores, and binder defining the mesoscale structure of an explosive, subject to shock wave loading. This type of modelling helps to provide new insights into the micro-mechanical behaviour of heterogeneous energetic materials. In particular, sources of energy localisation leading to the formation of 'hot-spots' can be identified, and the distribution of 'hot-spots' obtained can be used as input to a statistical 'hot-spot' model [76]. However, such simulations require very

large amounts of computing power.

A comparatively simpler approach is to take a particular 'hot-spot' mechanism, and model the details of the chosen mechanism and the subsequent explosive response. Pore collapse, viscoplastic effects, shear banding, adiabatic gas compression, friction, and shock reflections from internal imperfections, are all 'hot-spot' mechanisms that have been proposed as energy sources [5]. However, the relative importance of each of these mechanisms is still subject to considerable conjecture. The most popular mechanism for describing 'hot-spot' formation in a heterogeneous solid explosive is viscoplastic pore collapse. This is because: (i) it is well known experimentally that variations in porosity can affect the shock sensitivity of an explosive [36], and (ii) viscoplastic flow in the solid phase material in the vicinity of a collapsing pore has been shown to be a very efficient heating mechanism leading to 'hot-spot' ignition [9].

One important question concerns the location of the pores in an explosive material. The possibilities are: (i) the pores are in the binder, (ii) the pores are within the explosive crystals, (iii) the pores are adjacent to an explosive crystal (*e.g.* between crystal and binder), or (iv) some combination of the above. The viscoplastic pore collapse models [72]-[73] assume that pores are located at the centre of a spherical shell of the solid explosive material. This can account for (ii) and (iii) above, however these models do not consider the effect that the binder material may have on the explosive response. The elastic-viscoplastic model of Kim [127] is the only model to consider the effect of binder on the pore collapse response.

In the direct numerical simulations described in this section, the 'hot-spot' mechanism is shock induced pore collapse. In the first instance, following the approach taken elsewhere [72]-[73], it is assumed that the pores are located at the centre of a spherical shell of the solid material. The one-dimensional Lagrangian hydrocode PERUSE [88] is used to perform the simulations. PERUSE contains an elastic-viscoplastic constitutive model which is used to examine elastic-viscoplastic deformation around a collapsing pore as a 'hot-spot' mechanism. Various phenomena in which elastic-viscoplastic heating is thought to be significant and a likely source of ignition are investigated. The results of the simulations are later used to test the assumptions, and compare results from a simplified 'hot-spot' model that is intended to be incorporated in a hydrocode.

In order to be able to perform direct numerical simulations of shock induced 'hot-spot' formation in heterogeneous solid explosives, it is necessary to define the model for the explosive upon which numerical simulations will be carried out, and then to define the fundamental material properties of the explosive. The model of the explosive, and its associated equation of state (EOS) and material parameters are described in the following sections.

The usefulness of performing direct numerical simulations is illustrated by showing how the formation of 'hot-spots' can be affected by such obvious physical parameters as porosity and pore size, rise time of the shock, and magnitude of the

shock pressure, or to material properties such as viscosity. The effect of a double shock on the pore collapse response has also been investigated to look at the effect of preshocking the material before arrival of a second stronger shock. This is to examine the phenomenon of 'shock desensitisation'. In the course of this work, general trends rather than quantitative results were of interest, and to observe whether the results of the calculations are consistent with commonly held ideas about shock initiation and sensitivity of porous explosives.

5.2.2   Overview of PERUSE

PERUSE is a one-dimensional, Lagrangian, multi-material hydrocode [88]. It solves a system of partial differential equations describing time-dependent compressible flow (in Lagrangian form), and includes the modelling of material strength. Material strength effects are accounted for via a rate-dependent elastic-viscoplastic constitutive model [128]. The implementation of this strength model in PERUSE allows calculations of elastic-viscoplastic heating effects in explosive materials to be studied. Previous hydrocode modelling work has shown that elastic-viscoplastic work in the vicinity of a collapsing pore is a very efficient heating mechanism leading to the formation of 'hot-spots' in an explosive material [88]. Specific to the hydrocode modelling of 'hot-spots' performed here, the capabilities of PERUSE have subsequently been expanded to include the effects of heat conduction and an Arrhenius reaction rate law as described respectively in Sections 5.2.3 and 5.2.4.

In the elastic-viscoplastic strength model, viscosity is introduced via modification of the classical Wilkins radial return scheme [129]. The predicted stress deviators, rather than being retracted directly onto the yield surface are instead relaxed towards it, the relaxation rate being governed by the viscosity parameter, η. When the viscosity is zero, the elastic-viscoplastic model reduces to the elastic-plastic formulation of Wilkins [129]. In this model, the yield condition of Von Mises [130] is used to describe the elastic limit, and the shear modulus, yield strength and viscosity are all assumed to be constant. Here, the concept of viscosity is that of a solid viscosity which is qualitatively different from the more familiar concept of viscosity in a fluid.

The elastic-viscoplastic strength model [128] is based on the network shown in Figure 5.1. This network forms the basis of the Perzyna model [131] which is widely used in other application areas. The response of the elastic and plastic elements are as described by Wilkins [129] for rate-independent elastic-plastic flow. The rate sensitivity of response is provided by complicating the response of the plastic element to include a viscous drag. The viscous element response assumed is a generalisation of the standard textbook linear viscous fluid formulated originally by Newton (1687) and developed into the Navier-Stokes continuum form by the work of various authors including Navier and Poisson. For a more detailed description of the elastic-viscoplastic strength model, and its implementation in PERUSE, the

reader is referred to [88].

The governing flow equations that are solved in the current version of PERUSE are summarised below. This includes extending the capabilities of the code to include the effects of heat conduction and a reaction rate equation carried out for this thesis. In the following equations the parameter g defines the geometry of the system as: slab (g=1), axisymmetric (g=2), or spherical (g=3). The stress and strain quantities relating to the elastic, viscous, and plastic elements of the strength model are denoted by the superscripts e, v, and p respectively. The superscript vp qualifies quantities relating to the parallel connection of the viscous and plastic elements. Total stress and strain quantities for the overall response of the material will carry no qualifying superscripts.

Conservation of mass :

$$\frac{D\rho}{Dt} = -\rho \nabla . u \tag{5.1}$$

Equation of motion :

$$\frac{Du}{Dt} = -r^{g-1}\frac{\partial \Sigma_r}{\partial m} + (g-1)\frac{(\Sigma_\theta - \Sigma_r)}{\rho r} \tag{5.2}$$

Energy equation :

$$\frac{De}{Dt} = -(P+Q)\frac{\partial \left(r^{g-1}u\right)}{\partial m} + \frac{1}{\rho}\frac{DW^P}{Dt} + \frac{\partial}{\partial m}\left(\kappa\, r^{g-1}\frac{\partial T}{\partial r}\right) \tag{5.3}$$

Velocity :

$$\frac{Dr}{Dt} = u \tag{5.4}$$

Lagrangian mass coordinate :

$$dm = \rho\, dV = \rho\, r^{g-1}dr \tag{5.5}$$

Lagrangian derivative :

$$\frac{D}{Dt} = \frac{\partial}{\partial t} + u\frac{\partial}{\partial r} \tag{5.6}$$

Total stresses :

$$\Sigma_r = P + Q - S_1 \tag{5.7}$$

$$\Sigma_\theta = P + Q - S_2 \tag{5.8}$$

Velocity strains :

$$\dot{\varepsilon}_1 = \frac{\partial u}{\partial r} \tag{5.9}$$

$$\dot{\varepsilon}_2 = \frac{u}{r} \qquad (\dot{\varepsilon}_2 = 0 \ \text{for g=1}) \tag{5.10}$$

$$\dot{\varepsilon}_3 = \dot{\varepsilon}_2 \qquad (\dot{\varepsilon}_3 = 0 \text{ for g=1 and g=2}) \tag{5.11}$$

Stress Deviators :

$$\dot{S}_i = 2\mu\dot{e}_i, \quad \|S\| \leq \sqrt{\frac{2}{3}}Y \qquad i = 1,2,3 \tag{5.12}$$

$$\dot{S}_i + \frac{\mu}{\eta}\left(1 - \sqrt{\frac{2}{3}}\frac{Y}{\|S\|}\right)S_i = 2\mu\dot{e}_i, \quad \|S\| > \sqrt{\frac{2}{3}}Y \qquad i = 1,2,3 \tag{5.13}$$

$$\dot{e}_i = \dot{\varepsilon}_i - \frac{1}{3}\nabla.u \qquad i = 1,2,3 \tag{5.14}$$

$$\nabla.u = \dot{\varepsilon}_1 + \dot{\varepsilon}_2 + \dot{\varepsilon}_3 \tag{5.15}$$

$$\|S\| = \sqrt{S_1{}^2 + S_2{}^2 + S_3{}^2} \tag{5.16}$$

$$S_1 + S_2 + S_3 = 0 \tag{5.17}$$

Von Mises Yield Condition:

$$S_1{}^2 + S_1{}^2 + S_3{}^2 - \frac{2}{3}Y^2 \leq 0 \tag{5.18}$$

Stress/strain response :

$$\begin{aligned} S_i = S_i{}^e = S_i{}^{vp} \quad &: \quad \dot{\varepsilon}_i = \dot{\varepsilon}_i^e + \dot{\varepsilon}_i^{vp} \quad : \quad \dot{e}_i = \dot{e}_i^e + \dot{e}_i^{vp} \qquad i = 1,2,3 \\ S_i{}^{vp} = S_i{}^v + S_i{}^p \quad &: \quad \dot{\varepsilon}_i^{vp} = \dot{\varepsilon}_i^v = \dot{\varepsilon}_i^p \quad : \quad \dot{e}_i^{vp} = \dot{e}_i^v = \dot{e}_i^p \qquad i = 1,2,3 \end{aligned} \tag{5.19}$$

$$\sum_{i=1}^{3} \dot{\varepsilon}_i^p = \sum_{i=1}^{3} \dot{\varepsilon}_i^v = \sum_{i=1}^{3} \dot{\varepsilon}_i^{vp} = 0 \quad : \quad \dot{e}_i^{vp} = \dot{\varepsilon}_i^{vp} \tag{5.20}$$

$$S_i{}^v = 2\eta\,\dot{e}_i^{vp}, \quad S_i{}^p = \sqrt{\frac{2}{3}}\frac{Y}{\|S\|}S_i \qquad i = 1,2,3 \tag{5.21}$$

Total plastic work :

$$\frac{DW^P}{Dt} = \frac{DW^v}{Dt} + \frac{DW^p}{Dt} \tag{5.22}$$

$$\frac{DW^v}{Dt} = S_1{}^v\dot{e}_1^{vp} + S_2{}^v\dot{e}_2^{vp} + S_3{}^v\dot{e}_3^{vp} \tag{5.23}$$

$$\frac{DW^p}{Dt} = S_1{}^p\dot{e}_1^{vp} + S_2{}^p\dot{e}_2^{vp} + S_3{}^p\dot{e}_3^{vp} \tag{5.24}$$

Reaction rate:

$$\frac{\partial \lambda}{\partial t} = f(\rho, P, Z_s, T, \lambda) \tag{5.25}$$

Pressure equation of state:

$$P = P(\rho, e, \lambda) \tag{5.26}$$

The above system of equations is solved numerically via the method of finite differences using an explicit two-step (predictor-corrector) scheme that is second-order accurate in time and space. The numerical solution scheme was previously described in detail in [88], and the difference equations given. The scheme was vaildated against a number of well established test problems, and further details of the validation procedure can be found in [88]. The numerical solution of the new features, heat conduction and a reaction rate law, recently added to PERUSE are described respectively in Sections 5.2.3 and 5.2.4 below.

5.2.3 Heat Conduction

Heat conduction effects are deemed to be very important in shock initiation of heterogeneous solid explosives, particularly in relation to the dynamic formation of 'hot-spots'. Passage of a shock wave of sufficient strength will lead to the creation of 'hot-spots' in the explosive material. However, dependent upon factors such as shock strength and duration, and the size and temperature of the 'hot-spots' created as a result of the shock compression, the 'hot-spots' could cool before any reaction occurs. This could be due to heat loss to the surrounding cooler material, or as a result of release waves cooling the 'hot-spots'. To include the effects of heat conduction in the modelling, the capabilities of the PERUSE hydrocode have been expanded to include heat conduction as described below.

The one-dimensional heat conduction equation that describes the diffusion of heat in a medium is written in its most general form as,

$$\frac{\partial(\rho\, C_V\, T)}{\partial t} = \frac{\partial}{\partial r}\left(\kappa\, \frac{\partial T}{\partial r}\right) \tag{5.27}$$

where r is the space coordinate, ρ is the density, C_V is the specific heat at constant volume, T is the temperature, and κ is the coefficient of thermal conductivity. Following the notation in [88], rewritting (5.27) in Lagrangian form in terms of the specific internal energy, e, assuming $T = e/C_V$, gives

$$\frac{De}{Dt} = \frac{\partial}{\partial m}\left(\kappa\, r^{g-1}\frac{\partial T}{\partial r}\right) \tag{5.28}$$

where m is the Lagrangian mass coordinate, parameter g equals 1, 2, or 3 according to whether the geometry is plane, axisymmetric, or spherical, and C_V and κ are

assumed constant. Heat conduction therefore gives an additional term to the internal energy equation, see equation (5.3), and in the current implementation this is solved explicitly. Following the notation in [88], the one-dimensional heat conduction equation (5.28) is discretised as follows:

Predictor step

Add to $e_{j+\frac{1}{2}}^{n+\frac{1}{2}}$,

$$\frac{1}{2}\frac{\Delta t^{n+\frac{1}{2}}}{M_{j+\frac{1}{2}}}\left[H_{j+1}^{n}-H_{j}^{n}\right] \tag{5.29}$$

where $\Delta t^{n+\frac{1}{2}}$ is the timestep, $M_{j+\frac{1}{2}}$ is the Lagrangian cell mass, and the heat flux through a boundary cell j is given by,

$$H_{j}^{n}=A_{j}^{n}\,\kappa_{j}^{n}\left(\frac{T_{j+\frac{1}{2}}^{n}-T_{j-\frac{1}{2}}^{n}}{\frac{1}{2}\left(r_{j+1}^{n}-r_{j-1}^{n}\right)}\right) \tag{5.30}$$

where A_{j} is the cell face area, and

$$\kappa_{j}^{n}=\frac{1}{2}\left(\kappa_{j+\frac{1}{2}}^{n}+\kappa_{j-\frac{1}{2}}^{n}\right) \tag{5.31}$$

Corrector step

Add to $e_{j+\frac{1}{2}}^{n+1}$,

$$\frac{\Delta t^{n+\frac{1}{2}}}{M_{j+\frac{1}{2}}}\left[H_{j+1}^{n+\frac{1}{2}}-H_{j}^{n+\frac{1}{2}}\right] \tag{5.32}$$

where the heat flux through a boundary cell j is given by,

$$H_{j}^{n+\frac{1}{2}}=\overline{A}_{j}\,\kappa_{j}^{n+\frac{1}{2}}\left(\frac{T_{j+\frac{1}{2}}^{n+\frac{1}{2}}-T_{j-\frac{1}{2}}^{n+\frac{1}{2}}}{\frac{1}{2}\left(\overline{r}_{j+1}-\overline{r}_{j-1}\right)}\right) \tag{5.33}$$

and

$$\overline{A}_{j} \quad = \quad \frac{1}{2}\left(A_{j}^{n+1}+A_{j}^{n}\right) \tag{5.34}$$

$$\overline{r}_{j} \quad = \quad \frac{1}{2}\left(r_{j}^{n+1}+r_{j}^{n}\right) \tag{5.35}$$

$$\kappa_{j}^{n+\frac{1}{2}} \quad = \quad \frac{1}{2}\left(\kappa_{j+\frac{1}{2}}^{n+\frac{1}{2}}+\kappa_{j-\frac{1}{2}}^{n+\frac{1}{2}}\right) \tag{5.36}$$

The A_j's are the cell face areas and are computed as given in [88]. The stability timestep criterion for the explicit solution of the one-dimensional heat conduction equation given by,

$$\Delta t = \frac{1}{2} \frac{\rho \, C_V}{\kappa} \, (\Delta r)^2 \tag{5.37}$$

is taken into account when determining the overall stable timestep for each computational cycle.

5.2.4 Reaction Rate Law

Many reaction rate models have been developed by various researchers. These models usually describe the rate of increase of the reacted (or burned) mass fraction λ of the explosive material as a function of its thermodynamic state, and can be considered special cases of the general form,

$$\frac{\partial \lambda}{\partial t} = f(\rho, P, Z_s, T, \lambda) \tag{5.38}$$

where ρ, P, Z_s, and T are respectively the density, pressure, entropy function, and temperature of the material. The reaction rate laws in the Lee-Tarver Ignition and Growth model [52] [53] are examples of such models, and these depend on pressure (and density) but not temperature. However, in reality reaction rates are initially dependent on the temperature attained in the 'hot-spots'.

One of the simplest and most popular temperature-dependent reaction rate models is the first-order Arrhenius rate law [1] which has the (Lagrangian) form,

$$\frac{D\lambda}{Dt} = (1 - \lambda) \, Z \, e^{-\frac{E^*}{RT}} \tag{5.39}$$

where λ is the mass fraction reacted, Z is the frequency factor, E^* is the activation energy of the material, R is the universal gas constant, and T is the current temperature. The Arrhenius model depends on temperature only; as the temperature increases the rate of burning increases. In the numerical scheme the mass fraction reacted, λ, is a cell centred quantity, and the difference equations corresponding to the discretisation of equation (5.39) are;

$$\text{Predictor step}: \qquad \lambda_{j+\frac{1}{2}}^{n+\frac{1}{2}} = \lambda_{j+\frac{1}{2}}^{n} + \frac{1}{2}\Delta t^{n+\frac{1}{2}} \left(1 - \lambda_{j+\frac{1}{2}}^{n}\right) Z \, e^{-\frac{E^*}{R\,T_{j+\frac{1}{2}}^{n}}} \tag{5.40}$$

$$\text{Corrector step}: \qquad \lambda_{j+\frac{1}{2}}^{n+1} = \lambda_{j+\frac{1}{2}}^{n} + \Delta t^{n+\frac{1}{2}} \left(1 - \lambda_{j+\frac{1}{2}}^{n+\frac{1}{2}}\right) Z \, e^{-\frac{E^*}{R\,T_{j+\frac{1}{2}}^{n+\frac{1}{2}}}} \tag{5.41}$$

where Z, E^*, and R are assumed constant.

At the present time the reaction rate is decoupled from the hydrodynamics. In other words, for a given temperature, the reaction rate and hence mass fraction reacted will be computed, but this then does not feed back into the hydrodynamics. In reality, once the reaction starts this will further raise the temperature of the explosive material resulting in an increase in the reaction rate. Thus, the solution of the reaction rate equation is currently used to get a minimum estimate of the mass fraction of material that could be ignitied in the 'hot-spots'.

5.2.5 Explosive Model

A one-dimensional idealised spherical model for the explosive is assumed which consists of an isolated spherical pore at the centre of a spherical shell of the solid material, see Figure 5.2. This model is based on the work of Carroll and Holt [8] who showed that a simple hollow sphere model could describe the dynamic compaction behaviour of porous materials reasonably well. The initial pore radius is a_0 which is equal to the inner radius of the solid material, b_0 is the outer radius of the solid, and P_s is the time-dependent pressure applied to the external surface of the solid. The applied external stress, P_s, represents the effect of a shock wave, and the resulting pore collapse is assumed to be spherically symmetric.

Defining, α_0, the initial distention ratio as,

$$\alpha_0 = \frac{\text{total volume of the porous material}}{\text{volume of solid material}} = \frac{V_0}{V_{s0}} \tag{5.42}$$

then the relationship between α_0, and the inner radius a_0 and the outer radius b_0 of the solid material, is

$$\alpha_0 = \frac{b_0{}^3}{b_0{}^3 - a_0{}^3} \quad \text{or} \quad \left(\frac{b_0}{a_0}\right)^3 = \frac{\alpha_0}{\alpha_0 - 1} \tag{5.43}$$

and the initial porosity of the explosive, ϕ_0, is defined by,

$$\phi_0 = \left(\frac{a_0}{b_0}\right)^3 = \frac{\alpha_0 - 1}{\alpha_0} \tag{5.44}$$

The pore can be treated as a spherical void or can be gas filled. Where the pore is assumed to be gaseous, the gas phase is not modelled explicitly in the calculations. Instead the gaseous pore is modelled as a boundary condition to the solid using an ideal gas equation of state, and pressure and temperature are assumed to be uniform through the gas.

The model of the explosive is obviously a strong simplification of the actual explosive geometry. In reality, a heterogeneous solid explosive material consists of a suspension of pores inside the mixture of crystals, binder *etc*, where the size and distribution of pores are not uniform. In addition, the collapse of the pores

resulting from the passage of a shock will be non-spherical. Only an isolated pore is considered here, where a_0 represents the average pore radius in the explosive, and the outer radius b_0 represents some average measure of the distance between two pores. Pore-pore interactions are neglected. Although very simplistic, the model shown in Figure 5.2 does allow the formation of 'hot-spots' to be described in a simple and generic fashion without loss of the basic characteristics of 'hot-spots'.

5.2.6 Equation of State and Material Parameters

The well characterised HMX-based explosive PBX9404 was chosen as the material to be modelled. This is because the initiation behaviour of PBX9404 is fairly representative of solid heterogeneous explosives in general, and the majority of its material constants and parameters are to be readily found in the literature *e.g.* [31].

The solid (unreacted) explosive material was modelled using a simple polynomial EOS based on the linear shock velocity (U_s)-particle velocity (U_p) fit to unreacted shock data on PBX9404 [132]. The analytic simple polynomial EOS [129] has the form,

$$P = A_0 + A_1\,\xi + \tilde{A}_2\,\xi^2 + A_3\,\xi^3 + \left(B_0 + B_1\,\xi + B_2\,\xi^2\right)\rho_0 E \qquad (5.45)$$

$$\text{where} \quad \xi = \frac{\rho}{\rho_0} - 1, \quad \text{and} \quad \tilde{A}_2 = \begin{cases} A_2 & \xi \geq 0 \\ A_2^* & \xi < 0 \end{cases} \qquad (5.46)$$

and A_0, A_1, A_2, $A_2{}^*$, A_3, B_0, B_1, and B_2 are constants. Starting from the quoted $U_s - U_p$ relationship for PBX9404 [132], reference [133] was used to derive the constants for the simple polynomial EOS for PBX9404, and these are given in Table 5.1.

Table 5.1: EOS constants for PBX9404.

Parameter	Value
Initial Density, ρ_0 (g/cm^3)	1.84
A_0	0.0
A_1	0.11408184
A_2	0.30573933
$A_2{}^*$	-0.30573933
A_3	0.0
B_0	1.0
B_1	1.0
B_2	0.0

The assumed default material parameters for PBX9404 are given in Table 5.2, the majority of which have been taken from the literature. The values for the yield

strength, Y, shear modulus, μ, and specific heat, C_V, were taken from [52], while the coefficient of thermal conductivity, κ_s, was obtained from [117]. The Arrhenius constants, Z and E^*, for PBX9404 are due to Rogers [134], and the universal gas constant, R, is 8.3147×10^{-5} Mbcm^3/ K mole.

Table 5.2: Material parameters for PBX9404.

Material parameter	Value
Yield strength, Y (Mb)	0.002
Shear modulus, μ (Mb)	0.0454
Viscosity, η (Mb μs)	0.001
Initial temperature, T_0 (K)	300.0
Specific heat, C_V (Mb cm^3/g/K)	1.512×10^{-5}
Thermal conductivity, κ_s (Mb cm^3/cm/μs/K)	4.1667×10^{-14}
Frequency factor, Z	1.81×10^{19}
Activation energy, E^* (Mb cm^3/mole)	2.205
Pressure stress, P_s (Mb)	0.01
Initial pore radius, a_0 (μm)	10.0
Initial outer radius, b_0 (μm)	46.416
Initial porosity, ϕ_0 (%)	1.0
Rise time of shock, τ (μs)	0.1

The porosity of PBX9404 pressed to a density of 1.84 g/cm^3 is typically of the order of 1%, and the initial pore radius is assumed to be 10 μm. From (5.44) this then defines the initial outer radius of the explosive shell as 46.416 μm. The applied pressure stress, P_s, is taken to be 10 kbars, which corresponds to a relatively weak shock, and the rise time of the applied pressure or shock is $\tau = 0.1\,\mu$s, *i.e.* there is a linear correspondence between pressure and time from $t = 0\,\mu$s to $t = 0.1\,\mu$s after which the applied pressure remains constant at 10 kbars, see Figure 5.3(a). The assumed value for the material viscosity is 0.001 Mb μs, and T_0 is the initial (ambient) temperature of the solid explosive.

If the pore is assumed to be gaseous, the gas phase is modelled with an ideal gas EOS of the form,

$$P = (\gamma - 1)\,\rho\,e \tag{5.47}$$

where ρ is the density, e is the specific internal energy, and γ is a constant. Where the pore is assumed gaseous in the calculations, the initial conditions in the gas were as defined in Table 5.3. The initial density of the gas is 1.293×10^{-3} g/cm^3 corresponding to the mean density of air at the reference temperature and pressure (1 atmosphere), and it is assumed that $\gamma = 1.4$. The initial energy in the gas is then defined by (5.47), and the specfic heat can then be calculated from the initial energy and temperature. The coefficient of thermal conductivity of air was taken from [135].

Table 5.3: Initial conditions for gas-filled pore.

Parameter	Value
Initial density, ρ_{g0} (g/cm^3)	1.293×10^{-3}
Initial pressure, P_{g0} (Mb)	1.0×10^{-6}
Ratio of specific heats, γ	1.4
Initial temperature, T_{g0} (K)	298.0
Initial energy, e_{g0} (Mb cm^3/g)	1.93349×10^{-3}
Specific heat, C_V (Mb cm^3/g/K)	6.4882×10^{-6}
Thermal conductivity, κ_g (Mb cm^3/cm/μs/K)	2.3917×10^{-15}

The calculations described in the following sections should be taken as being representative of the explosive PBX9404, rather than quantitative. In all cases, the mesh sizes employed in the simulations were chosen so as to ensure good resolution of the physics of the pore collapse during the timescales of the calculations. Typically 600-2000 mesh cells were employed through the thickness of the solid material dependent on the rate of pore collapse; the faster the speed of collapse, the finer the meshing required to adequately resolve the phenomena in the vicinity of the collapsing pore.

5.2.7 'Hot-Spot' Formation Due to Elastic-Viscoplastic Heating

To illustrate the very high effectiveness of the elastic-viscoplastic mechanism of heating the solid explosive material which surrounds a collapsing pore, consider a calculation using the defined model of the explosive, and taking the EOS constants and material parameters for PBX9404 as given in Tables 5.1 and 5.2 respectively. In this example, the pore was assumed to be a void and heat conduction was not modelled. The time evolution of the pore radius is plotted in Figure 5.4, and the corresponding increase in temperature at the surface of the collapsing pore is shown in Figure 5.5. The calculated radial distribution of temperature through the thickness of the solid material at various times during the calculation is shown in Figure 5.6. Temperature profiles such as these help to show the extent of the 'hot-spot' region in the vicinity of the collapsing pore.

It is observed that significant temperature increases are calculated in a thin layer of the solid material surrounding the collapsing pore. The maximum calculated temperature occurs at the pore surface, with the temperature montonically decreasing away from this surface. The radius of this thin heated layer, or 'hot-spot', is approximately equal to the initial pore radius. Most 'hot-spot' reaction theories indicate that the size of a 'hot-spot' is very nearly the size of a particle or of a void or pore before it collapsed. Away from the 'hot-spot' region there is only a small increase in temperature above ambient. Energy dissipation due to elastic-viscoplastic

work in the vicinity of the collapsing pore is responsible for the significant heating of the solid material leading to the creation of the observed 'hot-spot'.

With heat conduction modelled, heat will be transferred from the 'hot-spot' region to cooler portions of the solid material. In addition, if the pore is gaseous then, at the same time, heat will be transferred from the gas to the surrounding solid material as it has been shown that significantly higher temperatures are calculated in the gas phase than in the solid phase [88]. A calculation was performed to illustrate the effect of including heat conduction in the modelling, where the pore was assumed to be gas-filled with initial conditions as given in Table 5.3. The solid phase was modelled as described previously using the EOS constants and material parameters as given in Tables 5.1 and 5.2 respectively. The computed results are presented in terms of the radial distribution of temperature in the solid shell at various times during the calculation, see Figure 5.7. At atmospheric pressure and with heat conduction modelled, it has been observed that the gas in this particular case has an insignificant effect on the calculated temperatures in the solid (due to the amount of energy in the gas being very small) in comparison to the situation where the pore was treated as a void. Thus, the effect of including heat conduction in this calculation can be seen by comparison with the results in Figure 5.6. It is seen that heat conduction has a significant effect on the calculated temperatures, where the re-distribution of heat in the solid phase through heat transfer to the cooler portions of the material results in a lower temperature 'hot-spot'.

Passage of a shock wave of sufficient strength will lead to the creation of 'hot-spots' in the explosive material. However, dependent upon factors such as the shock strength and the size and temperature of the 'hot-spots' created by the shock compression, the 'hot-spots' could die out due to loss of heat from these localised high temperature regions to their cooler surroundings before ignition occurs. This illustrates that heat conduction is an important phenomena in modelling 'hot-spot' initiation.

5.2.8 Material Viscosity

Most of the material parameters for a given explosive are usually fairly well known or can be found relatively easily, *e.g.* shear modulus and yield strength. One of the biggest uncertainties is in the material viscosity, η. Data on the material viscosity of solid explosives is not readily available in the literature, and it can only be estimated indirectly, for example, by calibration to experimental shock initiation data. In the elastic-viscoplastic strength model, η is currently assumed constant.

To examine the sensitivity of computations to the value chosen for the viscosity, calculations were run for different values of η in the range 1.0×10^{-5} to 5.0×10^{-3} Mb μs. In the calculations, the pore was assumed to be a void, and the effects of heat conduction were not modelled. Apart from the change in the value of η, the EOS constants and material parameters were as given in Tables 5.1 and 5.2. Figures

5.8 and 5.9 respectively show the effect on the calculated pore radius, and the pore surface temperature, to changes in the value of the viscosity. As the maximum temperature occurs at the pore surface, it is of interest to follow the temperature here. It is seen that the value of material viscosity has a significant effect on the pore collapse response and the associated calculated temperatures adjacent to the pore surface. With increasing viscosity, the calculated temperatures at the pore surface increase, but the rate of pore collapse decreases. However, at the higher values of η a point appears to be reached where increasing the viscosity does not result in any further significant increase in temperature, but merely delays the time to reach that temperature through a slower pore wall velocity.

These results show that careful consideration needs to be given to the choice of appropriate values for viscosity for any given heterogeneous solid explosive. In the constitutive model, η is assumed to be constant, and a value of 0.001 Mb μs has been used in the remainder of this work. However, further work is needed to ascertain what values of η are appropriate, and to investigate whether, and to what extent, viscosity varies with pressure, temperature, and strain.

5.2.9 Porosity and Initial Pore Size

The initial porosity of the explosive material is defined by equation (5.44), and there are two different ways of changing the initial porosity within the context of our model: (i) keep the inner radius of the shell fixed, and change the outer radius, and (ii) keep the outer radius of the shell fixed, and change the inner radius. Changing the shell inner radius changes the initial pore size.

To examine the sensitivity of 'hot-spot' formation in the explosive to changes in porosity, hydrocode calculations were run at three different initial porosities: 1%, 2%, and 5%. Both methods of changing the initial porosity, as outlined above, were examined. Keeping the initial inner radius fixed at $a_0 = 10\mu$m, the initial outer radii, b_0, corresponding to 1%, 2%, and 5% porosity are respectively 46.42 μm, 36.84 μm, and 27.14 μm. Similarly, keeping the initial outer radius fixed at $b_0 = 46.42\mu$m, the initial pore sizes, a_0, corresponding to porosities of 1%, 2%, and 5% are 10 μm, 12.5 μm, and 17.2 μm respectively. The EOS constants for the solid explosive were as given in Table 5.1 and, apart from the changes to the initial inner and outer radii, the remaining explosive parameters were as given in Table 5.2. In the calculations, the pore was assumed to be a void, and initially the effects of heat conduction were not modelled.

The computed results corresponding to the changes in initial porosity, where the initial inner radius is fixed and the initial outer radius adjusted to change the initial porosity, are shown in Figure 5.10. These plots show the time evolution of the pore radius, the temperature at the surface of the collapsing pore, and the mass fraction reacted of explosive material as a percentage of the total mass. It is seen that the initial porosity has a significant effect on the pore collapse response. Increasing the

overall porosity results in an increase in velocity of the pore wall, a higher pore surface temperature and hence a higher temperature 'hot-spot', and a faster reaction rate. Thus, the calculations show an increase in sensitivity of the explosive with increasing porosity, which is well established experimentally, see for example [136]. The results also indicate that only a small fraction of the material would be ignited or burned in the 'hot-spots'. This ties in with experimental evidence indicating that the amount of explosive contributing to the ignition process is related to the material porosity.

Using the alternative approach to changing the initial porosity by changing the initial inner radius, hence pore size, and keeping the initial outer radius fixed, no significant differences in the calculated results were observed compared with those in Figure 5.10. In other words, at a constant porosity and without heat conduction modelled, the same results are obtained irrespective of the initial pore size. However, it is generally understood that pore size is an important physical parameter affecting shock initiation and sensitivity of heterogeneous solid explosives. When heat conduction is included in the modelling, the initial pore size, assuming constant porosity, does have a significant effect on the computed results. This is illustrated by looking at the case of 5% initial porosity. The computed results with heat conduction modelled and assuming 5% porosity are shown in Figures 5.11-5.13. Figure 5.11 shows the time evolution of the pore surface temperature and mass fraction reacted, where the results without heat conduction modelled are also shown for comparison, while Figures 5.12 and 5.13 show the radial distribution of temperature through the solid explosive for initial pore sizes of 10μm and 17.2μm respectively.

With heat conduction modelled, it is now observed that, at constant porosity, the pore surface temperature is lower in the case of the smaller initial pore size, and hence a lower temperature 'hot-spot' is formed. In each case, the radius of the heated layer, or 'hot-spot', is approximately equal to the initial pore radius. Large initial pores thus lead to large 'hot-spots', and small pores to small 'hot-spots'. Heat conducts faster out of the smaller 'hot-spot' as a result of the larger temperature gradient through the heated layer in comparison to the bigger 'hot-spot'. As small 'hot-spots' cool more rapidly, it will therefore take higher pressures and higher 'hot-spot' temperatures to get a material with small sized pores to ignite before the 'hot-spots' cool. The above results are consistent with experimental observations of ignition thresholds being correlated with the size and temperature of the 'hot-spots' created by shock passage [137].

5.2.10 Rise Time of the Shock

Calculations have been performed to examine the effect of the rise time of the shock on the pore collapse response. Three different rise times for the shock were used in the calculations, namely (i) $\tau = 0.1\mu$s, (ii) $\tau = 0.5\mu$s, and (iii) $\tau = 1.0\mu$s,

after which the applied pressure, P_s, remained constant at 10 kbars. In each case, there was a linear relationship between pressure and time over the duration of the rise time. In the calculations the pore was treated as a void. Apart from the change in the rise time, the EOS constants and material parameters for the solid explosive were as given in Tables 5.1 and 5.2 respectively.

Initially calculations were run without heat conduction modelled, and the computed results are shown in Figure 5.14. As expected, the rise time of the shock has a significant effect on the pore response. The pore surface temperature decreases for increasing rise time of the shock, and hence lower temperature 'hot-spots' are obtained. The reduction in the 'hot-spot' temperatures due to the longer rise time of the shock therefore leads to slower reaction rates, and hence less material reacted. It is noted that the final (stopping) radius is the same in each calculation. This is as expected following the approach of Carroll and Holt [8], where the final radius of the pore using their simple hollow sphere model is a function of the yield strength, initial density and porosity, and final pressure.

The hydrocode calculations were then repeated but with heat conduction introduced into the modelling. Figure 5.15 shows the comparison of calculated results with and without taking account of heat transfer. Heat conduction clearly has a significant effect on the computed results, resulting in a reduction in the pore surface temperature and thus giving lower temperature 'hot-spots'. Looking ahead to the development of a simple 'hot-spot' initiation model for implementation in a hydrocode to enable realistic shock initation problems to be modelled, it is worth noting that the above results show that the physics of the pore will be very dependent on the capture (rise time) of the shock. Thus, a very accurate shock capturing method will be needed in the hydrocode in conjunction with the simple pore collapse model. To capture the shock accurately, this may require the model to be incorporated in an adaptive mesh refinement hydrocode such as SHAMROCK [87].

5.2.11   Magnitude of the Pressure

To study how the magnitude of the pressure loading can effect the pore collapse response, calculations were run at three different shock pressures, namely, (i) $P_s = 10$ kbars, (ii) $P_s = 15$ kbars, and (iii) $P_s = 20$ kbars. In each case the rise time of the shock was 0.1 μs and, thereafter, the pressure remained constant at the prescribed value. In the calculations the pore was assumed to be a void. Apart from the change in the magnitude of the pressure, the EOS constants and material parameters for the solid material were as given in Tables 5.1 and 5.2 respectively. Heat conduction effects were not modelled.

The computed results corresponding to the different pressure loadings are shown in Figure 5.16, which shows the time evolution of the pore radius, pore surface temperature, and mass fraction of explosive reacted. As expected, the pore wall collapses faster with increased pressure loading, resulting in higher pore surface

temperatures and hence higher temperature 'hot-spots', and faster reaction rates. The observed small scale oscillations seen in Figure 5.16 are due to the propagation of the elastic wave in the solid explosive, where the period of oscillation corresponds to the transit time of this wave as it travels backwards and forwards through the thickness of the solid material. At higher pressures, assuming the pore is a void, the pore may fully implode. This will not occur if the pore is gaseous. The energy of the gas phase may become significant at higher pressures, and heat transfer from the gas to the solid may be important.

5.2.12 Double Shock Loading (Preshocking)

The effects of multiple shocks on the pore collapse response and subsequent formation of 'hot-spots' can be easily examined via direct numerical simulations. Of interest is the phenomenon of 'shock desensitisation', discussed in previous chapters, where a weak first shock renders an explosive less sensitive to a following stronger shock. The pore response to a double shock process has been studied, where the double shock loading consisted of a precursor wave, or preshock, of P_1 = 10 kbars followed a given time later by a main shock of P_2 = 20 kbars. Both the precursor and main shocks had a rise time of $\tau = 0.1$ μs. The input shock profile is shown in Figure 5.3(b). Two calculations were performed using the given shock magnitudes but varying the time delay, δ, between the first and second shocks with, (i) $\delta = 0.5$ μs, and (ii) $\delta = 1.0$ μs. In the calculations the pore was assumed to be a void, and the EOS constants and material parameters for the solid material were as given in Tables 5.1 and 5.2 respectively. Heat conduction effects were not modelled.

The calculated double shock results showing the time evolution of the pore radius, the temperature at the pore surface, and the mass fraction reacted are shown in Figure 5.17, where the corresponding single shock results are also shown for comparison. It is seen that the temperature at the pore surface in a double shock process up to pressure P_2 is less than in a single shock at the pressure of the second shock alone. Thus, preshocking the explosive material results in a lower temperature 'hot-spot' in comparison to the single shock response. These observations are explained as follows. The pore starts to contract as a result of the compression due to the first shock. When the second shock is input into the material, the porosity of the explosive and pore size are both less than they were initially. A reduction in porosity makes the material less sensitive, as shown previously in Section 5.2.9, resulting in a lower temperature 'hot-spot'. Assuming a temperature-dependent reaction rate, then the reaction rate is slower behind a shock propagating through preshocked explosive, in comparison to the same shock propagating through pristine material, giving less material reacted in the 'hot-spot'.

The results obtained are qualitatively consistent with observations on the so-called desensitisation effect *e.g.* [38]. In addition, the calculated 'hot-spot' temperatures are also dependent on the time delay between the precursor and main shocks;

the longer the time delay, the lower the 'hot-spot' temperature obtained. The longer the time separation between the first and second shocks, the more the porosity and the size of the pore are reduced before the second shock enters the material. This further reduces the sensitivity of the material, resulting in a further reduction in the 'hot-spot' temperature. This indicates a time-dependent 'hot-spot' deactivation process which is consistent with the theory of Campbell and Travis [51].

5.2.13   Discussion

The mechanism by which spherical pores collapse to form 'hot-spots' in an explosive material as a result of elastic-viscoplastic flow has been examined using the one-dimensional Lagrangian hydrocode PERUSE. Overall, the results obtained from the direct numerical simulations are consistent with observations, and commonly held ideas, regarding the initiation and sensitivity of heterogeneous solid explosives subjected to weak shock waves. General trends in pore response and associated 'hot-spot' temperatures have initially been of interest rather than quantitative results.

The computed results show that 'hot-spot' temperatures increase with increasing porosity. Assuming that initiation is thermal in origin, then increasing porosity results in an increase in sensitivity. This correlates with experimental evidence that explosive sensitivity is related to porosity. For example, significant differences have been observed in Pop-plot data for a given explosive at different initial densities [36]. The data shows that lower density material is more sensitive (shorter run distance to detonation for a given input pressure), with the implication that this is because the material is more porous.

At constant porosity and with heat conduction included in the modelling, the initial pore size also has a significant effect on the calculated 'hot-spot' temperatures. It is observed that the formed 'hot-spots' as a result of pore collapse are approximately equal to the intial pore radius. Smaller 'hot-spots' are more easily cooled by heat conduction than larger ones as a result of a larger temperature gradient in the smaller 'hot-spot'. Therefore, bigger initial pores, which yield larger 'hot-spots', are more efficient at igniting the explosive. Conversley, it is more difficult to ignite an explosive with smaller pores, and higher pressures will be required in comparison to a material containing larger pores. The results are in agreement with commonly held ideas regarding the effect of pore size on explosive response, and shows the importance of including the effects of heat conduction in the modelling.

The shock sensitivity of heterogeneous solid explosives is usually discussed in terms of grain size and/or porosity, rather than pore size. This is because it is difficult to obtain data on pore sizes in a heterogeneous solid explosive. Thinking in terms of grain size rather than pore size, assuming constant porosity, a larger pore has a larger volume of solid explosive associated with it compared to a smaller pore, and hence has a larger grain size. This is a plausible argument if the pores

are located between grains, but not if the pores are in the grains. In terms of Pop-Plot behaviour, the sensitivity of heterogeneous explosives to grain size effects has shown that, at low shock pressures, fine grain material is less sensitive than coarse grain material [42] [43]. Thus, the calculations examining the effect of pore size on 'hot-spot' temperatures appear to be consistent with these observations. It is noted that the sensitivity behaviour for weak shocks is in contrast to the behaviour at higher pressures, such as at detonation, where finer grained material is more sensitive, as discussed in Chapter 3 and [42]. The hypothesis is that the difference in behaviour is related to time to ignition for 'hot-spots'; at low pressures the ignition time is long in comparison to that at high pressures where it is thought to be negligible.

In the case of double shocks, the calculated results show that subjecting the explosive to a weak first shock renders the material less sensitive to following stronger shocks. Shocking the material to a given pressure in a two shock process generates a lower temperature 'hot-spot' in comparison to where the material was shocked to the same (final) pressure by a single shock. This follows commonly held ideas regarding the phenomenon known as 'shock desensitisation' [38]; the precursor wave, or preshock, deactivates the 'hot-spots' by reducing the overall porosity (and pore size) before the arrival of the second shock. The results also indicated that the 'hot-spot' deactivation process is time-dependent since 'hot-spot' temperatures are lowered by increasing the time separation between the two shocks. These observations are consistent with the theory of Campbell and Travis [51].

To date the modelling work neglects the effect of binder on the explosive response. One possibility is that the important pores in a heterogeneous solid explosive are located in the binder material rather than next to, or inside, the explosive crystals. A layer of binder could be included between the pore and the solid explosive to examine pore collapse leading to 'hot-spot' formation in this case. This will require knowledge of the equation of state and material properties for the binder as well as the solid explosive. A further complication is whether the binder is pure or is laden with fine explosive particles [138]. As part of the manufacturing process, it is generally believed that fine crystallites mix with the binder to give what is known as 'dirty binder', and the material behaviour of pure and contaminated binder may be different.

In reality, pore collapse in a shock compressed explosive will be non-spherical. Two-dimensional direct numerical simulations of a shock wave interacting with a pore are required to test whether spherical pore collapse is a valid approximation. Additionally, the pores in an explosive may be irregularly shaped, and the geometry of the 'hot-spots' formed as a result of shock compression could also be an important factor in determining the explosive response. Thus, simulations to examine the geometry of pores on 'hot-spots' are also required. Two dimensional direct numerical simulations could also be performed to study the effect of a shock wave interacting with a matrix of pores to examine, for example, pore-pore interactions.

Since the elastic-viscoplastic constitutive model in PERUSE is also available in the two-dimensional, adaptive mesh refinement, Eulerian hydrocode SHAMROCK [87], then such calculations could be performed.

The development of a simplified 'hot-spot' initiation model based on elastic-viscoplastic pore collapse is described in the next section. The results of the direct numerical simulations will be used as a reference to test the validity of the various assumptions in a simplified 'hot-spot' model, and to check that the simple model can reproduce to a reasonable degree of accuracy the results from the PERUSE calculations.

5.3 Simple 'Hot-Spot' Initiation Model

5.3.1 Introduction

The mesh sizes used in the direct numerical simulations of 'hot-spot' initiation described above, are way beyond current computing resources for these to be utilised in macroscopic hydrocode modelling of shock initiation problems of interest. The only way forward, therefore, is to develop a simplified 'hot-spot' initiation model which can be coupled to a hydrocode, and which should be able give comparable results (*e.g.* pore radius, temperature, and mass fraction reacted) to those obtained from the direct numerical simulations. Any such model should explicitly describe the important physical, thermal, and chemical processes involved in explosive shock initiation, *e.g.* dynamics of pore collapse, heat conduction, 'hot-spot' decomposition *etc*, but still be simple enough to use in a hydrocode without unacceptably increasing the computation time.

The direct numerical simulation work showed that 'hot-spots' in heterogeneous solid explosives can be created by local elastic-viscoplastic strains in the vicinity of a collapsing spherical pore due to the passage of relatively weak shocks. The resulting increases in temperature would lead to ignition (the start of chemical decomposition) in the explosive. Based on mechanical deformation (primarily viscoplastic flow) around collapsing pores, a number of models to describe 'hot-spot' formation and subsequent ignition in heterogeneous solid explosives have been developed [72]-[73] and [126]. Since the description of the 'hot-spot' should be simple, these models utilise the Carroll and Holt [8] hollow sphere model, and all assume spherical symmetry of the pore collapse process. In addition, the models are built on the assumption of an incompressible solid phase, proposed and justified by Carroll and Holt, which leads to a great simplification of the theoretical analysis, and makes the development of a simple 'hot-spot' model tractable. Following the approach of Carroll and Holt [8], these models assume that mechanical deformation of the solid material occurs as a result of viscoplastic flow only in the vicinity of the collapsing pore. Only the model of Kim [126] is based on elastic-viscoplastic flow.

The model developed and described here is also based on the work of Carroll and Holt [8] and Butcher *et al.* [123]. It therefore contains a number features found in other micro-mechanical 'hot-spot' models described in the literature [72]-[126], and which have had some success in describing the response of porous explosives to a range of different shock loadings. However, there is one major difference. In the viscoplastic 'hot-spot' models developed elsewhere [72]-[73], heating of the solid phase material occurs as a result of viscoplastic flow only in the vicinity of a collapsing pore. This assumption is consistent with the observations of Carroll and Holt [8] who showed that volume changes in the first two phases of pore collapse (initial elastic and transitional elastic-viscoplastic) are negligible. This implicitly assumes that the whole of the spherical shell of solid material has yielded, and is undergoing viscoplastic flow. For solid explosives subjected to weak shocks it will be shown that this is an invalid assumption.

In the following sections, the construction of a simple, preliminary, 'hot-spot' initiation model based on elastic-viscoplastic pore collapse is described. Firstly, a description of the geometrical configuration used in developing the mathematical model is presented, and the assumptions made to simplify the model are given. The general form of the partial differential equations for elastic-viscoplastic pore collapse are then introduced, and the interface, boundary, and initial conditions needed to solve the system of equations are given. To make an efficient numerical solution of the governing equations possible, they are integrated to yield a set of ordinary differential equations to describe the pore response. By simplifying the modelling in this way, the aim is to eventually incorporate the simple 'hot-spot' initiation model into a hydrodynamics code without unacceptably increasing the amount of computation.

The initial model described below provides the framework for further model enhancements to be made, and which are planned. For example, in the preliminary model described below, the effects of heat conduction are ignored. However, this is an important physical process in the formation and ignition of 'hot-spots', and will therefore be included as the model is developed further. It is emphasised that the aim of the simple 'hot-spot' model is to describe the ignition phase in explosive shock initiation, *i.e.* formation of 'hot-spots' resulting from shock compression, and the subsequent decomposition of the explosive in these localised heated regions. The model, as it currently stands, is not intended to describe the subsequent growth of reaction behaviour from the 'hot-spots' as the rest of the explosive is consumed.

5.3.2 Physical Model and Assumptions

Consistent with PERUSE hydrocode calculations, and following previous 'hot-spot' modelling work [72]-[126], the explosive is represented by the one-dimensional hollow sphere pore collapse model described by Carroll and Holt [8] for compaction of inert porous materials, see Figure 5.2. This consists of an isolated spherical pore

surrounded by a spherical shell of the solid explosive material. This single pore model is used to represent the average response of a much larger sample of the explosive containing multiple, randomly distributed pores. Therefore, the initial inner radius, a_0, of the sphere represents the average pore radius in the explosive sample, and its initial outer (external) radius, b_0, is chosen such that the initial porosity and the measured overall porosity of the porous material are equal. It is noted that this explosive model does not take account of the binder nor pore-pore interactions which may both be important.

In conjunction with the physical model of the explosive detailed above, the following assumptions are made in developing a simple 'hot-spot' initiation model;

1. Pore collapse and flow of the solid material is treated as one-dimensional, spherically symmetric. This is valid when the time required for a shock wave to transit the pore is small compared to the collapse time [9].

2. The solid explosive material is assumed incompressible during its radial motion, after passage of the shock wave.

3. The solid explosive is an isotropic elastic-viscoplastic material, where the yield strength, Y, and the material viscosity, η, are constant.

4. The pore is a void, *i.e.* contains no gas.

The formulation of a preliminary 'hot-spot' initiation model, based on the explosive model and the assumptions detailed above, is now described.

5.3.3 Governing Partial Differential Equations

Application of the laws of conservation of mass, momentum, and energy, to the hollow sphere configuration shown in Figure 5.2, and under the assumptions given above, yields a system of coupled partial differential equations (PDE's) which, along with the appropriate initial and boundary conditions, describes the behaviour of the porous material under shock loading. For one-dimensional, spherically symmetric flow of an incompressible material, the form of the governing equations can thus be written as (compare with Section 5.2.2);

Conservation of mass :
$$\nabla.u = 0 \tag{5.48}$$

Equation of motion :
$$\rho \frac{Du}{Dt} = -\frac{\partial \Sigma_r}{\partial r} + \frac{2}{r}(\Sigma_\theta - \Sigma_r) \tag{5.49}$$

Energy equation :
$$\rho \, C_V \frac{DT}{Dt} = \frac{DW^P}{Dt} \tag{5.50}$$

Velocity :

$$\frac{Dr}{Dt} = u \tag{5.51}$$

Lagrangian derivative :

$$\frac{D}{Dt} = \frac{\partial}{\partial t} + u\frac{\partial}{\partial r} \tag{5.52}$$

Total stresses :

$$\Sigma_r = P - S_1 \tag{5.53}$$

$$\Sigma_\theta = P - S_2 \tag{5.54}$$

Viscoplastic dissipation,

$$\frac{DW^P}{Dt} = 12\,\eta\left(\frac{u^2}{r^2}\right) + 2\,Y\left(\frac{|u|}{r}\right) \tag{5.55}$$

The equations defining the velocity strains and stress deviators are as given in Section 5.2.2. In order to solve the set of coupled, governing partial differential equations that comprise the mathematical model, the appropriate boundary and initial conditions must be specified. The initial conditions ($t = 0$) are:

$$u = 0 \tag{5.56}$$

$$T = T_0 \tag{5.57}$$

$$a = a_0 \tag{5.58}$$

$$b = b_0 \tag{5.59}$$

The boundary conditions at the inner pore radius, $r = a$,

$$u = \dot{a} \tag{5.60}$$

The boundary conditions at the outer pore radius, $r = b$,

$$\Sigma_r = P_s \tag{5.61}$$

where the function P_s represents the stress-time profile applied to the solid shell.

5.3.4 Model Formulation

Preamble

The governing equations presented above form a general set of coupled PDE's that describe the dynamic and thermodynamic behaviour of a hollow sphere subjected to an externally applied stress-time profile. Rather than solving this system

of PDE's, it is possible to reduce the governing equations to a set of ordinary differential equations (ODE's) in order to make their numerical solution less computationally intensive. The transformation of the governing equations from PDE's to ODE's is described below, and presented here are the final form of the equations (ODE's) solved in the preliminary 'hot-spot' initiation model.

Pore Radial Motion

When the time-dependent pressure stress, P_s, is applied to the external surface of the solid shell, see Figure 5.2, this initiates the contraction of the pore. The integration of the mass and momentum equations, with the application of the proper interface and boundary conditions leads to an expression for the radial acceleration of the pore surface. The integration of the equation for the conservation of mass (5.48) with the substitution of the radial velocity interface condition (5.60) into the resulting equation, gives an expression for the velocity field in the solid shell,

$$u = \frac{\dot{a}\, a^2}{r^2} \tag{5.62}$$

which depends only on radial position, and the position and velocity of the pore interface. By substituting the above expression for velocity into the momentum equation (5.49), integrating from the inner radius, $r = a$, to the outer radius, $r = b$, and applying the boundary conditions at these radii, an expression for the acceleration of the pore interface is found,

$$-\rho \left\{ a\,\ddot{a}\left(1 - \phi^{\frac{1}{3}}\right) + \frac{1}{2}\dot{a}\left[4\dot{a}\left(1 - \phi^{\frac{1}{3}}\right) - \dot{a}\left(1 - \phi^{\frac{4}{3}}\right)\right] \right\} = P_s + P_v - P_y \tag{5.63}$$

where ϕ is the porosity, P_v is the viscous (strain-rate dependent) stress, P_y is the elastic-plastic (strain dependent) stress, and a dot above a symbol denotes a derivative with respect to time. Equation (5.63) is essentially the classic Rayleigh bubble equation [139] but extended to take account of material strength effects and finite porosity on pore radial motion. The viscous and elastic-plastic stresses, which act

together to resist the pore collapse, are given by the equations,

$$
P_v = \begin{cases}
0 & , \quad \alpha_0 \geq \alpha \geq \alpha_1 \\[2ex]
12\, a^2\, \dot{a} \int_a^c \dfrac{\eta}{r^4}\, dr & , \quad \alpha_1 \geq \alpha \geq \alpha_2 \\[2ex]
12\, a^2\, \dot{a} \int_a^b \dfrac{\eta}{r^4}\, dr & , \quad \alpha_2 \geq \alpha \geq 1
\end{cases}
$$

and

$$
P_y = \begin{cases}
\dfrac{4\mu\,(\alpha_0 - \alpha)}{3\,\alpha\,(\alpha - 1)} & , \quad \alpha_0 \geq \alpha \geq \alpha_1 \\[2ex]
\dfrac{2}{3}\, Y \left(1 - \dfrac{2\mu(\alpha_0 - \alpha)}{Y\alpha} + ln\left\{ \dfrac{2\mu(\alpha_0 - \alpha)}{Y(\alpha - 1)} \right\} \right) & , \quad \alpha_1 \geq \alpha \geq \alpha_2 \\[2ex]
\dfrac{2}{3}\, Y\, ln\left(\dfrac{\alpha}{\alpha - 1} \right) & , \quad \alpha_2 \geq \alpha \geq 1
\end{cases}
$$

where η is the material viscosity, r is radius, μ is the shear modulus, Y is the yield strength, and α is the distention ratio. The distention ratio, α, and porosity, ϕ, are respectively given by the equations,

$$
\alpha_0 = \frac{b_0{}^3}{b_0{}^3 - a_0{}^3} \qquad ; \qquad \alpha = \frac{b^3}{b^3 - a^3} \tag{5.64}
$$

$$
\phi_0 = \left(\frac{a_0}{b_0} \right)^3 = \frac{\alpha_0 - 1}{\alpha_0} \qquad ; \qquad \phi = \left(\frac{a}{b} \right)^3 = \frac{\alpha - 1}{\alpha} \tag{5.65}
$$

where the subscript 0 denotes initial conditions, and the location of the external radius, b, is found from the assumption of incompressibility of the solid material, *i.e.*

$$
b^3 - a^3 = b_0{}^3 - a_0{}^3 \tag{5.66}
$$

As a result of the applied stress, P_s, the deformation of the sphere occurs in three distinct phases: *(i)* an initial (elastic) phase where there is no yielding ($\alpha_0 \geq \alpha \geq \alpha_1$), *(ii)* a transitional elastic-viscoplastic phase where part of the shell has yielded ($\alpha_1 \geq \alpha \geq \alpha_2$), and *(iii)* a totally viscoplastic phase where the whole of the spherical shell has yielded ($\alpha_2 \geq \alpha \geq 1$). Initial yield (elastic to elastic-viscoplastic) and total yield (elastic-viscoplastic to viscoplastic) occur at distention ratios

$$
\alpha_1 = \frac{2\mu\alpha_0 + Y}{2\mu + Y} \tag{5.67}
$$

and

$$\alpha_2 = \frac{2\mu\alpha_0}{2\mu+Y} \tag{5.68}$$

respectively, and the transitions are smooth as you go from one state of stress to the next. As the shear modulus, μ, and the yield strength, Y, are assumed constant, then the values of α_1 and α_2 are the same for all applied pressure profiles, however, the transition pressures will be different for different applied pressure profiles.

The equation describing the elastic phase holds within the elastic range of the material, *i.e* until the yield limit is reached. If the applied pressure increases beyond this point, yielding begins at the pore wall and propagates outwards, and the material is described by the transitional elastic-viscoplastic phase. In this transitional phase, the time-dependent interface between elastic and viscoplastic flow, denoted c, is given by,

$$c = \sqrt[3]{\frac{2\mu B}{Y}}, \quad \text{where} \quad B = \frac{a_0^3(\alpha_0-\alpha)}{\alpha_0-1} \tag{5.69}$$

The equation describing the pore radius in this phase holds until the elastic-viscoplastic interface reaches the outer radius of the shell ($c = b$), corresponding to the entire spherical shell yielding. Thereafter, the motion is governed by the equation describing the fully viscoplastic phase.

Following the observation of Carroll and Holt [8], 'hot-spot' initiation models based on viscoplastic pore collapse that have been developed elsewhere [72]-[73] assume that the pore volume remains essentially unchanged until the applied pressure, P_s, exceeds the yield value P_y where,

$$P_y = \frac{2}{3}Y\,ln\left(\frac{\alpha}{\alpha-1}\right) \tag{5.70}$$

In other words, volume changes during the elastic and elastic-viscoplastic phases of collapse are assumed negligible, and pore collapse occurs by virtue of viscoplastic flow only in the material. This in turn assumes that, once the yield condition is satisfied, the whole of the spherical shell instantaneously yields and is flowing viscoplastically. However, results of PERUSE calculations (to be shown shortly) have shown that, for weak and moderate shock waves, the whole of the spherical shell does not yield but is instead in the transitional elastic-viscoplastic state. Therefore, our simple 'hot-spot' initiation model explicitly models all of the three possible phases of pore collapse.

Temperature Increase Resulting From Pore Collapse

As the pore contracts due to the applied pressure stress, the temperature increases in the solid shell during its radial motion as a result of mechanical deformation due to the elastic-plastic and viscous stresses generated. For any model to be useful in a hydrocode to simulate explosive shock initiation, the total averaged burn

fraction, λ, in the hollow sphere needs to be computed. In order to obtain this, we need to know how the local burn fraction varies through the solid shell as a function of radius, r, and time, t: $\lambda(r,t)$. The local burn fractions, $\lambda(r,t)$, are found from integrating a reaction rate law which in general is written as,

$$\frac{d\lambda}{dt} = f(\rho, P, Z_s, T, \lambda) \tag{5.71}$$

where ρ, P, Z_s, and T are respectively the density, pressure, function of entropy, and temperature of the material. In this work, the temperature-dependent Arrhenius reaction rate equation [1] is chosen as the reaction rate law. Therefore, to compute the local reaction rates, $\frac{d\lambda}{dt}(r,t)$, in the hollow sphere, the temperature field in the collapsing shell, $T(r,t)$, is required.

In the viscoplastic 'hot-spot' models [124]-[73], two different approaches to calculating the temperature profile through the solid shell have been adopted. In [124] an integral transformation method was used to compute the interface temperature. This simplified the problem by converting the energy equation into a single integral differential equation and eliminated the need to solve the thermal field in the entire solid shell $(a < r < b)$. However, the integral approach requires the assumption of a thermal profile in the solid shell, and both exponential and polynomial expressions have been used for this purpose. The applicability of this approach was questioned by Bonnett [125] and Massoni *et al.* [73] who instead opted to solve the energy equation in its (original) PDE form using finite difference methods. Both approaches have their advantages and disadvantages. Clearly, the latter approach is computationally more expensive than the former.

An alternative approach to those described above for calculating the temperature field has been adopted here for the simple 'hot-spot' initiation model. From the direct numerical simulations describing 'hot-spot' formation (see Section 5.2), it was shown that the size of a 'hot-spot' created in the vicinity of a collapsing pore is approximately equal to the size of the pore before it collapsed. Outside this region there is only a small increase in temperature above ambient, and this does not significantly affect the total averaged reaction rate, and hence burn fraction, through the spherical shell. These observations are used to define a domain for the 'hot-spot' $(a < r < r_{hs})$ which is a fraction of the total domain $(a < r < b)$ for the solid shell. The 'hot-spot' domain is then defined by a number of discrete (Lagrangian) points. It is convenient to use Lagrangian particles as the solid material deforms during pore collapse, and the spacing of the initial points is carefully chosen to reflect this motion. The local temperature, reaction rate, and burn fraction, are computed at each of the Lagrangian positions at each step. Therefore, for computational efficiency, it is important one should use the least number of points which still gives an accurate representation of the temperature, reaction rate, and burn fraction fields in the 'hot-spot' domain.

The ODE describing the temperature increase at the Lagrangian particle positions as a result of the mechanical deformation (viscous work and elastic-plastic work) during pore radial motion is given by,

$$\rho \, C_v \frac{dT}{dt} = 12 \, \eta \left(\frac{u^2}{r^2} \right) + 2 \, Y \left(\frac{|u|}{r} \right) \tag{5.72}$$

where T is the local temperature, t is time, C_V is the specfic heat capacity at constant volume, r is the radial (Lagrangian) position, and the velocity field in the solid shell, u, is given by equation (5.62). The position and velocity of the pore surface, a and $\dot{a}$ respectively, are found from integration of equation (5.63), and the Lagrangian radial positions in the solid material at each step are calculated from the incompressibility assumption *i.e.*

$$r^3 - a^3 \; = \; r_0{}^3 - a_0{}^3 \tag{5.73}$$

In reality, the increase in temperature due to the mechanical deformation will be followed by two other processes in the explosive 'hot-spots'; heat conduction and chemical reaction. Both of these are dependent on, and at the same time, modify the temperature distribution in the explosive. At the present time, the effects of heat conduction are not included in the preliminary 'hot-spot' model. However, heat conduction will be incorporated into the model at a later date, as this phenomena has been shown to be important in 'hot-spot' initiation from the direct numerical simulation work (see Section 5.2).

Reaction Rate and Burn Fraction

The reaction rate at the Lagrangian particle positions is calculated according to the first-order temperature-dependent Arrhenius rate law,

$$\frac{d\lambda}{dt} \; = \; (1 - \lambda) \, Z \, e^{-\frac{E^*}{RT}} \tag{5.74}$$

where λ is the local mass fraction of explosive that has reacted, Z is the frequency factor, E^* is the activation energy, R is the universal gas constant, and T is the local temperature. Equation (5.74) represents the local reaction rate in the 'hot-spot', giving a maximum at the inner radius where the temperature is the highest, a minimum at the extent the 'hot-spot' domain, and a monotonic decrease between them. Integration of (5.74) yields the burn fractions at the Lagrangian positions, $\lambda(r,t)$. Since we are interested in the total averaged burn fraction in the hollow sphere, the local burn fractions are integrated over the 'hot-spot' domain to obtain this quantity,

$$\lambda(t) = \frac{\int_a^{r_{hs}} \lambda(r,t) \, 4 \pi \, r^2 dr}{\frac{4}{3} \pi \, (b^3 - a^3)} \tag{5.75}$$

It is assumed that the reaction rate, and hence burn fraction, is zero outside the 'hot-spot' domain $(r_{hs} < r < b)$.

5.3.5   Initial Testing of the Simple 'Hot-Spot' Model

The ODE's describing the simplified 'hot-spot' initiation model (5.63), (5.72) and (5.74) are integrated numerically using a fifth-order Runge-Kutta method with adaptive stepsize control [140] to obtain respectively the time evolution of the pore radius, local temperatures, and local burn fractions. Numerical integration of the local burn fraction field to obtain the total averaged burn fraction through the spherical shell (5.75), is performed using the classical trapezoidal rule.

Sample results obtained from the described simple 'hot-spot' initiation model are now presented, and the results are compared with the corresponding direct numerical simulations (Section 5.2) to illustrate how well, or otherwise, the simple 'hot-spot' model is performing. Consistent with the PERUSE calculations, the explosive material was taken to be PBX9404 with initial density, ρ_0=1.84 g/cc, and the default material parameters were as given by Table 5.2.

Calculated results from the simple 'hot-spot' model corresponding to an applied shock pressure of $P_s = 10$ kbars, with a rise time of $\tau = 0.1$ μs, are shown in Figures 5.18-5.20. Figure 5.18 shows the time evolution of the pore radius, temperature at the surface of the collapsing pore, and the total averaged mass fraction reacted, where the results from the corresponding PERUSE hydrocode calculation are also shown for comparison. Figure 5.19 shows the time evolution of the various interfaces for this particular problem, namely the inner shell radius (a), the outer shell radius (b), and the interface between elastic and viscoplastic flow (c). The time evolution of c shows that, for this example, the whole of the solid shell does not yield, and the collapse is in the transitional elastic-viscoplastic phase. The solid shell yields initially at the pore surface, and as the collapse progresses, the viscoplastic region spreads further out. The radial distribution of temperature through the spherical explosive shell as calculated by the simple model is shown in Figure 5.20, and the corresponding PERUSE results are shown in Figure 5.21.

Overall, the calculated results from the simple model are consistent with those from the direct numerical simulation. Good agreement is obtained between the two modelling approaches in terms of the time evolution of the pore radius and the pore surface temperature. In addition, the calculated temperature profiles through the thickness of the solid explosive show good agreement between the simple 'hot-spot' model and hydrocode calculations. Consistent with the PERUSE results, the simple model gives the maximum temperature at the surface of the collapsing pore, with the temperature monotonically decreasing away from the pore surface, and the extent, or radius, of the 'hot-spot' region agrees very well with the hydrocode simulation. The agreement between the hydrocode and simple model in terms of the calculated mass fraction reacted is not as good as that obtained to the pore radius or

the 'hot-spot' temperatures. As the temperature profiles through the 'hot-spot' are in very good agreement, then this could be due to the simple trapezium integration formula (5.75) used in the simple model to integrate the local burn fraction field to obtain the total averaged burn fraction through the shell. Use of a more accurate integration technique may therefore be required. Here, it is observed that only a small fraction of the total explosive material by mass is ignited in the 'hot-spots'.

One of the key assumptions of the simple 'hot-spot' model is that the shell of solid explosive collapses incompressibly. The observed small differences between the PERUSE and simple model calculations are due to the assumption of incompressibility of the solid material in the simple 'hot-spot' model, as shown below. The incompressibility assumption gives a small reduction in the velocity of the pore wall during collapse in comparison to the hydrocode calculation, and the final (stopping) radius is slightly bigger than that predicted by the hydrocode. This small difference in the velocity of the pore results in a slightly lower temperature at the pore surface from the simple model. As the temperatures in the hydrocode are cell centred quantities then, the pore surface temperature in fact corresponds to the temperature at the cell centre of the first cell adjacent to the pore surface, *i.e.* the temperature half a cell's width away from the actual pore surface. The calculated pore surface temperature from the simple model corresponds to this position to allow a direct comparison to be made.

In the simple polynomial EOS used in the PERUSE calculation to model the repsonse of the solid explosive, the constant A_1 is the bulk modulus, K, of the material [133]. The bulk modulus is given by, $K = \rho_0 c_0{}^2$, where ρ_0 is the initial density and c_0 is the bulk sound speed. Changing A_1 changes the sound speed, which in turn changes the compressibility of the material; increasing A_1 implies increasing the sound speed which makes the material less compressible. Indeed, the bulk modulus, K, is sometimes referred to as incompressibility. Conversely, the reciprocal of K is called the compressibility. Thus, by adjusting the value of A_1 in the polynomial EOS, the hypothesis that the calculational differences are due to the incompressibility assumption in the simple model can be tested.

In the default PERUSE calculation, the maximum density of the unreacted explosive is 1.975 g/cm^3, corresponding to the explosive being compressed by $\sim$7% from its starting density of 1.84 g/cm^3. Three further calculations have been performed with different values of the constant A_1 namely 0.2, 0.4, and 1.0. At these values of A_1 in the simple polynomial EOS, the maximum calculated densities in the shell of PBX9404 are 1.928, 1.887, and 1.860 g/cm^3 respectively. The time evolution of the pore radii from the hydrocode calculations are shown in Figures 5.22 and Figure 5.23 along with the corresponding simple 'hot-spot' model calculation. It is seen that the PERUSE calculations now approach the incompressible solution of the simple model as the compressibility of the material is reduced, thus confirming that the observed differences between the hydrocode and simple 'hot-spot' model calculations is due to the incompressibility assumption in the simple

model.

The direct numerical simulations using PERUSE have shown that, for weak and moderate shocks, the solid explosive shell does not fully yield but is instead in the transitional elastic-viscoplastic phase of pore collapse. For this reason, all three phases of collapse (initial elastic, transitional elastic-viscoplastic, and fully viscoplastic) as described by Carroll and Holt [8] are included in the simple 'hot-spot' initiation model. Other 'hot-spot' initiation models [72]-[73] based on Carroll and Holt's pore collapse concept [8] assume that, following Carroll and Holt, volume changes in the first two phases of collapse are negligible, and pore collapse occurs by virtue of viscoplastic flow only when $P_s > P_y$, where P_y is given by equation (5.70). This assumes that, once the yield limit threshold is exceeded, the whole of the spherical shell of solid material is instantaneously flowing viscoplastically.

To compare and contrast the different modelling approaches, pore collapse as a result of viscoplastic flow only has been carried out for the problem described above where the spherical shell is subjected to a weak shock of $P_s = 10$ kbars which has a rise time of 0.1 μs. This required only minor modification of the simple 'hot-spot' model. The calculated results assuming elastic-viscoplastic flow and viscoplastic flow only are compared in Figure 5.24, where the corresponding PERUSE results are also shown for comparison. For this particular problem, it is observed that ignoring the initial elastic, and elastic-viscoplastic phases of collapse, results in significant differences in pore response when compared to the simple model and PERUSE results. The viscoplastic 'hot-spot' model under predicts the rate of collapse, and this results in a lower 'hot-spot' temperature. Thus, models based on pore collapse as a result of viscoplastic flow only are in error where it is shown that the shell is not fully viscoplastic. Thus, for weak and moderate shocks, the viscoplastic 'hot-spot' models [72]-[73] are built on an invalid assumption.

For the particular problem described above, good agreement was obtained between the computed results from the simple 'hot-spot' model and the corresponding results from the direct numerical simulation. To check the applicability of the 'hot-spot' model in other sample problems of interest, additional calculations have been performed using: (i) different initial porosities, (ii) different rise times for the shock wave (ii) different magnitudes for the shock pressure, and (ii) a double shock input. These problems were considered previously for the direct numerical simulation work, and hence the results from the simple model can be compared to the corresponding results from the PERUSE simulations to further examine how well the simple model is performing. Unless stated otherwise, the material parameters for the solid shell of PBX9404 were as given by Table 5.2.

The effect of initial porosity on pore response in the simple 'hot-spot' model has been examined. Calculations have been performed at three different initial porosities, 1%, 2%, and 5%. In each case the initial pore radius was fixed at 10 μm, and the initial outer radii were 46.42 μm, 36.84 μm, and 27.14 μm, which respectively correspond to porosities of 1%, 2%, and 5%. The computed results from the simple

'hot-spot' model are compared with the corresponding results from the PERUSE hydrocode simulations in Figure 5.25. For the cases studied, very good agreement is obtained between the results from the simple model and the direct numerical simulations on PERUSE. This indicates that the simple 'hot-spot' initiation model can account for the trend in porosity effects in heterogeneous solid explosives.

The pore response to the rise time of a shock has also been studied. The different rise times for the shock used in the calculations were: (i) $\tau=0.1\,\mu$s, (ii) $\tau=0.5\,\mu$s, and (iii) $\tau=1.0\,\mu$s. In each case the final sustained shock pressure was $P_s=10$ kbars, with a linear relationship between pressure and time over the duration of the rise time of the shock. Figure 5.26 shows the results comparison between the simple 'hot-spot' model and PERUSE simulations in terms of the time evolution of the pore radius and the temperature at the pore surface. Good agreement is obtained between the calculated results from the two different modelling approaches. It is noted that the physics of the pore is very dependent on the rise time of the shock. Since artificial viscosity-based hydrocodes typically spread a shock wave over $\sim$3-4 meshes, then any hydrocode into which the simple 'hot-spot' model is to be incorporated will require an accurate shock capturing method and/or fine meshing to ensure that the physics of the pore is accurately represented.

To examine the effect of the magnitude of the shock pressure on pore response, calculations were run at two other different shock pressures, namely, (i) $P_s = 15$ kbars, and (ii) $P_s = 20$ kbars. In each case the rise time of the shock was $\tau = 0.1\,\mu$s. Figure 5.27 shows the comparison of the computed results from the simple 'hot-spot' model (dashed lines) with the corresponding PERUSE results (solid lines) for each of the different shock pressures, where the results corresponding to $P_s = 10$ kbars are also shown. In terms of the pore radial motion, it is seen that the comparisons (simple model vs direct numerical simulation) at the higher pressures initially follow the same pattern as the comparison at $P_s = 10$ kbars, with the simple 'hot-spot' model predicting a slightly larger pore radius than the hydrocode during the early stages of pore collapse. Subsequently, however, differences in the calculational comparisons are seen at $P_s = 15$ and 20 kbars when compared to the comparison at $P_s = 10$ kbars, and the final radii at the higher pressures, as calculated by the simple model, are now slightly smaller, not bigger, than those predicted by the PERUSE hydrocode.

For the different input pressures, the calculated pore surface temperatures and total averaged mass fractions reacted from the simple 'hot-spot' model are in reasonable agreement with the corresponding PERUSE results. However, it would appear that the differences between model and hydrocode results increase with increasing pressure. Further investigations are required to understand the observed differences between the results from the simple model and PERUSE as shown in Figure 5.27. Since the velocity of the collapsing pore increases with increasing shock pressure, it is possible that in the direct numerical simulations even finer zoning is required to fully resolve the motion at higher pressures, particularly in the

important region in the immediate vicinity of the pore surface.

To examine the effect of preshocking an explosive, the response of the hollow sphere model to a pressure profile consisting of two shocks has been calculated using the simple 'hot-spot' model. The double shock loading consisted of an initial shock of $P_1 = 10$ kbars followed a given time later by a second shock of $P_2 = 20$ kbars, see Figure 5.3b. Both the precursor and main shocks each had a rise time of $\tau = 0.1$ μs. Two separate calculations were performed using different values for the time delay, δ, between the precursor and main shocks; (i) $\delta = 0.5$ μs, and (ii) $\delta = 1.0$ μs. Computed results from the simple 'hot-spot' model and PERUSE hydrocode simulation, corresponding to separate time delays of $\delta = 0.5$ μs and $\delta = 1.0$ μs, are compared in Figures 5.28 and 5.29 respectively, where the single shock results are also shown for comparison.

The calculated double shock results from the simple 'hot-spot' model in terms of the time evolution of the pore radius, pore surface temperature, and mass fraction reacted, are in good agreement with the results from the direct numerical simulations. These results show that the explosive response to double shocks can be accurately modelled with the simple 'hot-spot' initiation model, and it thus shows the potential to be able to account for the phenomenon of 'shock desensitisation' in heterogeneous solid explosives.

5.3.6   Implementation of the Simple 'Hot-Spot' Model in a Hydrocode

The described simple 'hot-spot' initiation model is currently being incorporated in a two-dimensional hydrocode, and the details of the implementation are sketched out below. The described elastic-viscoplastic pore collapse model is well adapted to describe the ignition phase of the explosive shock initation process, where the 'hot-spots' are created as a result of the shock compression, and the subsequent reaction occurs in these localised heated regions. In this ignition phase, as the calculated results have shown, only a small fraction of the explosive will be ignited or burned in the 'hot-spots'. Thus, there still remains the problem of modelling the subsequent growth of reaction outwards from the ignited 'hot-spots' as the rest of the material is consumed. This subsequent growth of reaction is usually termed surface burning or grain burning.

In order to provide a capability to model the whole reaction process, the reaction due to surface burning needs to be modelled in addition to the ignition phase. At present, changes are made to the implementation of the Lee-Tarver model [49], where the ignition term is replaced by a term deduced from the simple model of 'hot-spot' formation arising from the elastic-viscoplastic collapse of a spherical pore. The two growth terms in the Lee-Tarver reaction rate equation [53] are retained to represent the surface burning. Thus, the total reaction rate at any time is

expressed as a sum of two terms, each of which is calculated separately; the reaction rate during the ignition phase (as described by the simple 'hot-spot' model), and a reaction rate for surface burning (due to Lee-Tarver),

$$\frac{d\lambda}{dt} = \frac{d\lambda}{dt}_{\text{ignition}} + \frac{d\lambda}{dt}_{\text{surface burn}} \qquad (5.76)$$

where,

$$\frac{d\lambda}{dt}_{\text{surface burn}} = G_1(1-\lambda)^c\lambda^d P^y + G_2(1-\lambda)^e\lambda^g P^z \qquad (5.77)$$

where P is the local pressure, and G_1, c, d, y, G_2, e, g, and z are constants.

5.3.7 Discussion

To describe the ignition phase of shock initiation of heterogeneous solid explosives, a simple 'hot-spot' initiation model based on elastic-viscoplastic pore collapse is currently under development. The model currently contains a number of components commonly found in other mechanistic 'hot-spot' models, particularly those based on viscoplastic pore collapse. In particular, the simple 'hot-spot' model utilises the Carroll and Holt [8] hollow sphere model, and is built on the assumption of an an incompressible solid phase during pore collapse. However, there is one major important difference between the simple model and other similar models that have been developed elsewhere; the assumption that pore collapse occurs as a result of viscoplastic flow only is not followed in the simple 'hot-spot' model.

Computed results from the simple 'hot-spot' model have been compared to the corresponding results from the direct numerical simulations using PERUSE to assess how well, or otherwise, the current simple model is performing, and to test some of the assumptions in the model. Overall, for the problems studied, the simple 'hot-spot' model reproduces very well the results from the direct numerical simulations. This gives confidence in the performance of the model at the current stage of development. It has been shown that the differences between the results from the direct numerical simulations and the simple 'hot-spot' model are due to the incompressibility assumption of the solid phase material in the simple model. Overall, it appears that this has only a small effect on the calculated results since the change in density of the solid material as a result of shock compression is relatively small.

Viscoplastic 'hot-spot' models that have been developed elsewhere follow the assumption made by Carroll and Holt [8] that of the three phases of pore collapse (initial elastic, transitional elastic-viscoplastic, and fully viscoplastic), the first two phases can be neglected (due to the volume change in these phases being small compared to the final phase), and that pore collapse occurs as a result of viscoplastic flow only in the solid material. This implicity assumes that the whole of the spherical shell has yielded, and is undergoing plastic flow. For weak and moderate shock waves, the direct numerical simulation work has shown that pore collapse is

in the transitional elastic-viscoplastic phase, and the whole of the spherical shell does not yield. Therefore, in the simple 'hot-spot' model the assumption that pore collapse occurs as a result of viscoplastic flow only is not followed, and all three phases of pore collapse are included in the model.

For weak shocks, where the whole of the spherical shell does not yield, the pore response, assuming viscoplastic flow only in the solid phase material, is significantly different to that in the transitional elastic-viscoplastic phase. Where it is assumed the pore collapse is entirely viscoplastic, the model under-predicts the rate of pore collapse, which in turn gives significantly lower pore surface temperatures. Since the problem is treated as accurately as possible in the PERUSE simulations, and very good agreement is obtained between the simple model, assuming elastic-viscoplastic flow, and PERUSE results, it appears that viscoplastic 'hot-spot' models are built on a false assumption. Thus, not including the initial elastic and elastic-viscoplastic stages of the pore collapse is a shortcoming of the class of 'hot-spot' models based on viscoplastic flow only.

Additional investigations are now required to further test the range of validity of the simple 'hot-spot' model; for example, to higher applied pressures, and increased range of porosities, particularly low porosities ($\leq 1\%$). At higher pressures, it is possible that the whole of the spherical shell yields and the collapse is fully viscoplastic. Thus, the assumption made in other 'hot-spot' models that the shell collapses as a result of viscoplastic flow only, may be valid at higher pressures. However, if the shell is fully viscoplastic, this will not occur instantaneously throughout the shell once the yield limit is exceeded as assumed in the viscoplastic models. The viscoplastic region spreads out from the inner pore surface towards the outer regions of the shell, and hence there will be a time lag before the shell becomes completely viscoplastic. Thus, the models based on viscoplastic flow will be in error while this occurs, and this discrepency may be significant.

The HMX-based explosive EDC37 has a low initial porosity $\sim 0.2\%$, yet its shock initiation behaviour [38] is similar to that of another HMX-based explosive PBX9501 whose initial porosity is $\sim 1.5\%$ [36]. Investigations are required to examine whether viscous heating effects as a result of pore collapse can be significant and a likely source of ignition in such low porosity explosives. A further complicating factor is that EDC37 has an energetic binder whereas PBX9501, like most other heterogeneous solid explosives, does not. Thus, it may be necesary to include the binder material in the calculations to ensure accurate modelling of the pore collapse response.

One interesting aspect of the calculations is that the physics of the pore and associated 'hot-spot' temperatures are very dependent on the (capture) rise time of the shock. Artificial viscosity based hydrocodes typically spread shock waves over a fixed number of meshes (~ 3 or 4), and thus it takes a finite time for the arriving shock wave to be formed. When the simple 'hot-spot' model is considered for implementation in a hydrocode a very accurate shock capturing method and/or

fine meshing will probably be needed in hydrocode calculations to ensure that the physics of the pore is accurately modelled. To capture the shock accurately without placing excessive demand on computational resources, this may require the simple 'hot-spot' model to be incorporated in an adaptive mesh refinement hydrocode.

As in the direct numerical simulation work, the current simple 'hot-spot' model does not allow for the possibility that the binder material may be an important factor in the determining the explosive response. If the important pores are thought to be located in the binder, and assuming that its mechanical properties are known, a layer of this material can be included in the modelling between the pore and the solid explosive to examine 'hot-spot' formation in this case. Of particular interest, by comparison with corresponding results from direct numerical simulations, will be the effect of assuming an incompressible binder, and whether this will tend to limit the collapse and make ignition more difficult than a compressible one.

The next stage is to futher develop the simple 'hot-spot' model to include other important physical and chemical processes of interest. The temperature rise in the solid material will be followed by two other processes; heat conduction and chemical reaction. Both of these processes are dependent on and, at the same time, modify the 'hot-spot' temperatures. Thus, the first step in future work shall be to include heat conduction effects in the simple 'hot-spot' model, and to couple this to the mechanics and heating effects of pore collapse.

5.4 Conclusions

Recent advances in computational capabilities now offer the chance to develop more sophisticated models of explosive shock initiation. By explicitly considering the fundamental physical and chemical processes involved, more complex models that are able to predict the effect of changes in initial pore size distribution, explosive particle size distribution, and binder material can be built. The first stage in developing such a model is to explicitly account for the formation and ignition of 'hot-spots'.

Explicit 'hot-spot' modelling in one-dimension is a simple first step towards addressing the complex behaviour of shock initiation in heterogeneous solid explosives. The 'hot-spot' mechanism chosen in this work is elastic-viscoplastic flow around collapsing pores in an explosive material. The approach is two-fold: (i) perform direct numerical simulations to study 'hot-spot' formation and ignition in detail, and (ii) develop a simplified 'hot-spot' ignition model that can be built into a hydrocode. The former is used to aid understanding, and to also support the development of the later.

The one-dimensional, multi-material, Lagrangian hydrocode PERUSE contains an elastic-viscoplastic constitutive model. This code has been used to perform direct numerical simulations of 'hot-spot' initiation, where the formation of 'hot-spots'

occurs as a result of elastic-viscoplastic deformation due to shock induced pore collapse. This is a very efficient heating mechanism, and a likely source of ignition in shock compressed heterogeneous explosives. Overall, the results obtained from the PERUSE simulations are consistent with observations, and commonly held ideas, regarding the shock initiation and sensitivity of heterogeneous solid explosives subjected to weak shock waves. For example, calculated 'hot-spot' temperatures correlate well with porosity and pore size/grain size effects, and the mechanism by which pores collapse to form 'hot-spots' as a result of elastic-viscoplastic flow also shows the potential to describe the phenomenon of shock desensitisation.

A simple model based on elastic-viscoplastic pore collapse, that is intended for incorporation in a hydrocode to describe 'hot-spot' initiation, has been developed and described. In the simple model, all three phases of pore collapse are included; initial elastic, transitional elastic-viscoplastic, and fully viscoplastic. The results from the direct numerical simulations have been used to test the assumptions and results of the simple 'hot-spot' model. The simple model is performing well since it is able to accurately reproduce the results from the PERUSE simulations. The observed differences between the results from the two modelling approaches are due to the incompressibility assumption of the solid phase material in the simple 'hot-spot' model. At the shock pressures studied, the incompressibility assumption has only a small effect on the calculated results.

Viscoplastic 'hot-spot' models described in the literature assume that pore collapse occurs as a result of viscoplastic flow only in the solid explosive material. For weak and moderate shock waves, the direct numerical modelling work work has shown that the collapsing shell is never fully viscoplastic, and hence these models are built on an invalid assumption. Where pore collapse is in the transitional elastic-viscoplastic phase, viscoplastic pore collapse models are in error; they under-predict the rate of pore collapse, and give significantly lower 'hot-spot' temperatures.

Shock induced pore collapse is very dependent on the (capture) rise time of the shock. Artificial viscosity based hydrocodes typically spread shock waves over a fixed number of meshes ($\sim$3 or 4). When the simple 'hot-spot' model is considered for implementation in a hydrocode a very accurate shock capturing method and/or fine meshing will be needed in calculations in conjunction with the simple model. To capture shocks accurately without placing excessive demand on computational resources, the simple 'hot-spot' model may need to be incorporated in an adaptive mesh refinement hydrocode.

The explicit 'hot-spot' modelling work needs to be extended to include the effects of binder on the explosive response since the important pores in an explosive material may be located in the binder material rather than next to, or inside, the explosive crystals. This will require knowledge of the equation of state and material properties for the binder as well as the solid explosive. An added complication is whether the binder is pure or is laden with fine explosive particles, termed 'dirty binder', and the pore collapse response may be different as a result of these particles

contaminating the binder material.

In the modelling, pore collapse has been treated as one-dimensional spherically symmetric, however this may not reflect reality. Two-dimensional direct numerical simulations of shock induced pore collapse are required to test whether the assumption of spherical collapse is a valid approximation. Such detailed studies could also lead to an improved understanding of the formation and subsequent ignition of 'hot-spots' in a heterogeneous solid explosive.

The next stages of development for the simple 'hot-spot' model are to include heat conduction effects, and to couple these to the mechanics and heating effects of pore collapse. In addition, reaction schemes for solid explosives need to be developed. Subsequently coupling these to the elastic-viscoplastic pore collapse model will then allow a comprehensive study of pore collapse as an ignition source.
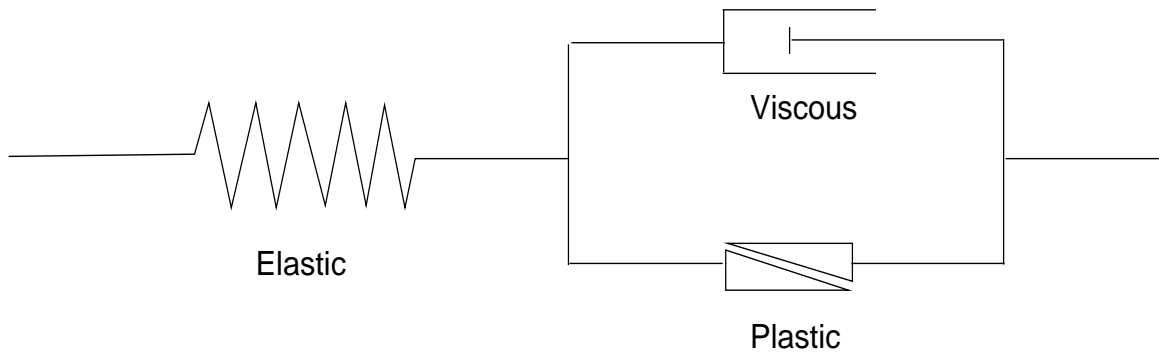
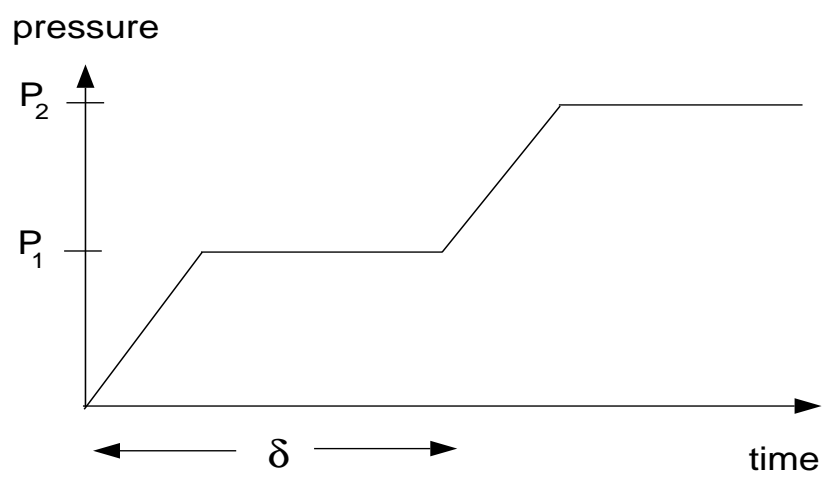Figure 5.1: Network illustrating elastic-viscoplastic response.
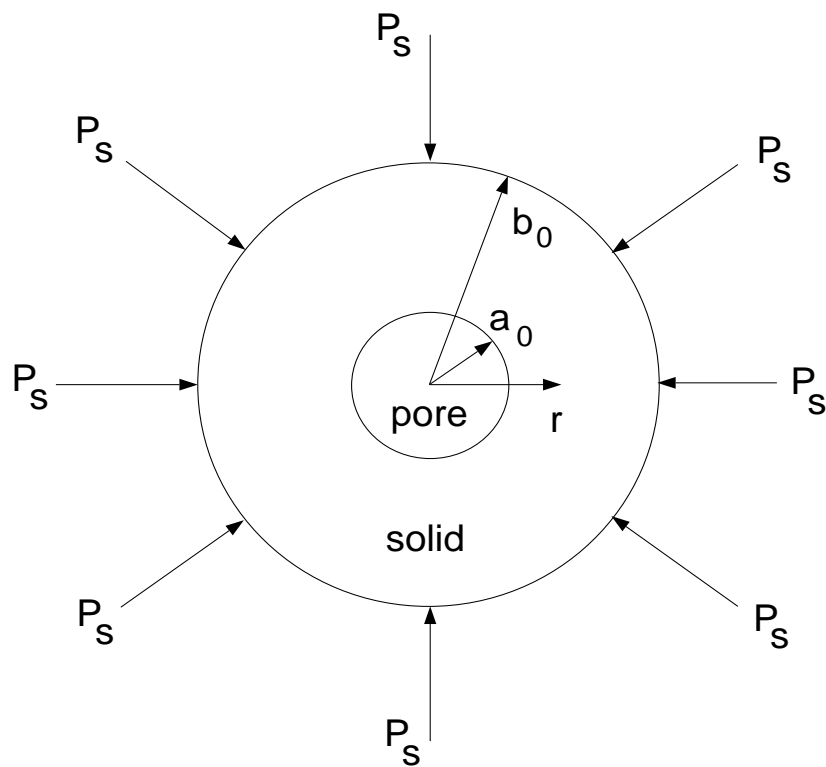
Figure 5.2: Hollow sphere configuration used to model explosive 'hot-spot' formation.
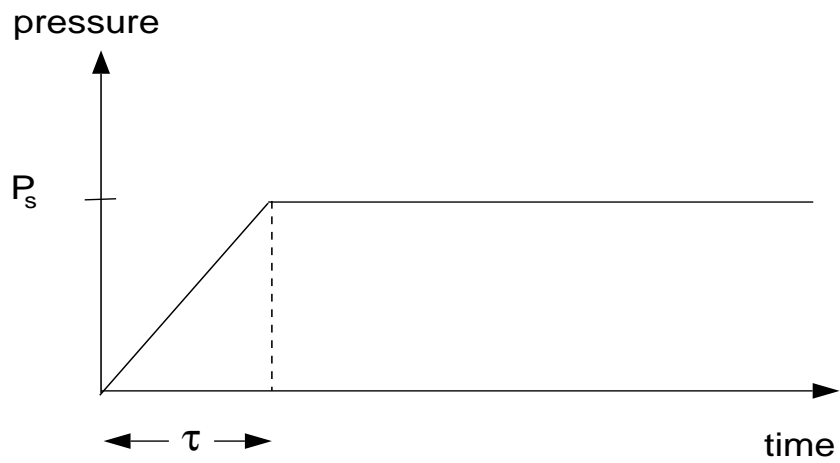
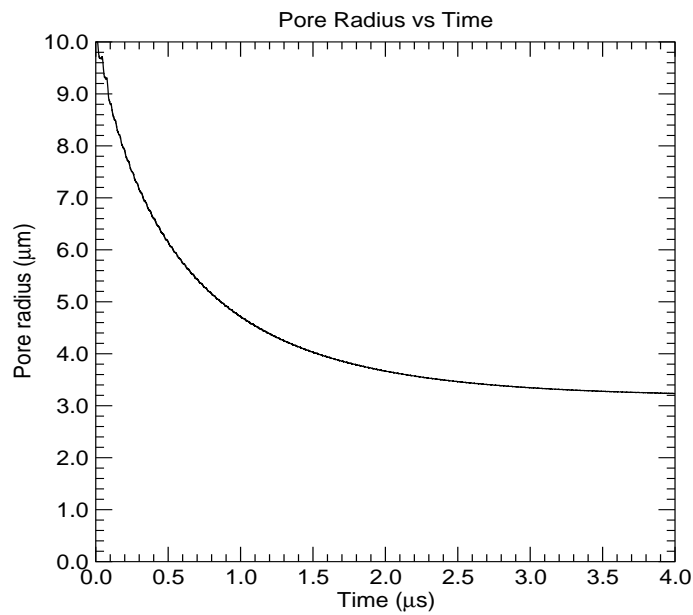Figure 5.3: Applied pressure profiles. (a) single shock, (b) double shock.

Figure 5.4: Time evolution of pore radius. a_0=10 μm, ϕ_0=1%, P_s=0.01 Mb, τ=0.1 μs, Y=0.002 Mb, μ=0.0454 Mb, and η=0.001 Mb μs.
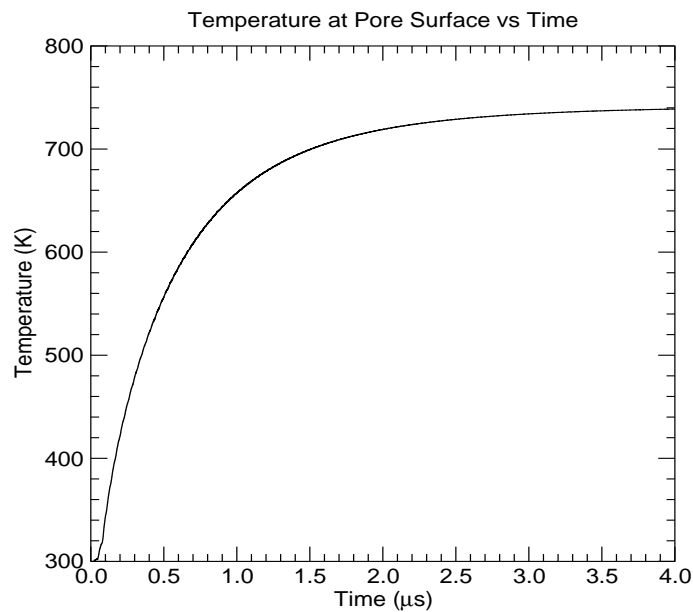
Figure 5.5: Temperature at surface of collapsing pore. a_0=10 μm, ϕ_0=1%, P_s=0.01 Mb, τ=0.1 μs, Y=0.002 Mb, μ=0.0454 Mb, and η=0.001 Mb μs.
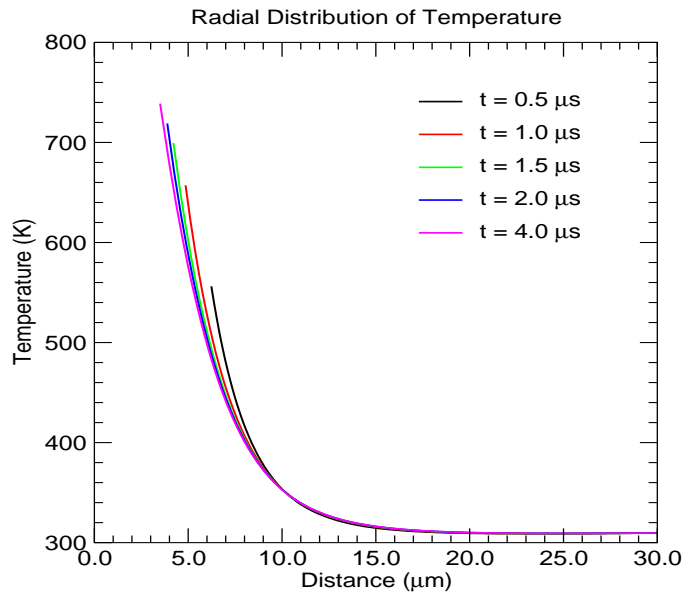
Figure 5.6: Radial distribution of temperature through the solid explosive (without heat conduction). $a_0=10\,\mu$m, $\phi_0=1\%$, $P_s=0.01$ Mb, $\tau=0.1\,\mu$s, $Y=0.002$ Mb, $\mu=0.0454$ Mb, and $\eta=0.001$ Mb μs.
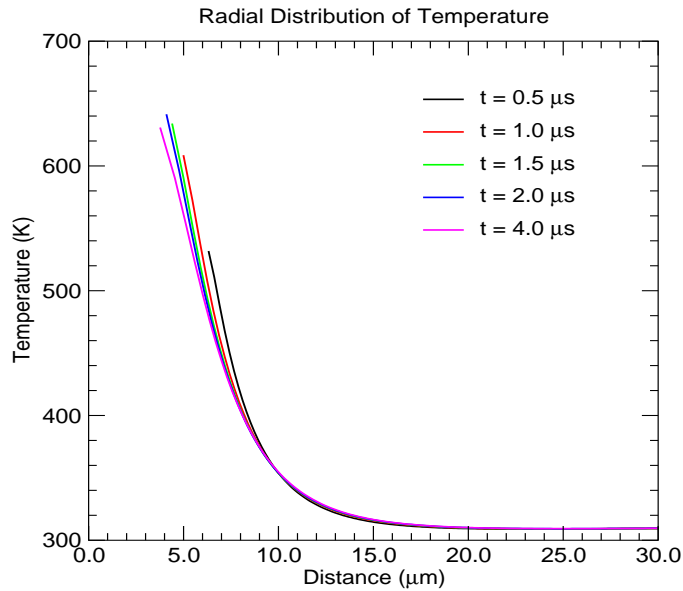

Figure 5.7: Radial distribution of temperature through the solid explosive (heat conduction modelled). $a_0=10\,\mu$m, $\phi_0=1\%$, $P_s=0.01$ Mb, $\tau=0.1\,\mu$s, $Y=0.002$ Mb, $\mu=0.0454$ Mb, $\eta=0.001$ Mb μs, and $\kappa_s=4.1667\times10^{-14}$ Mb cm^3/cm/μs/K.
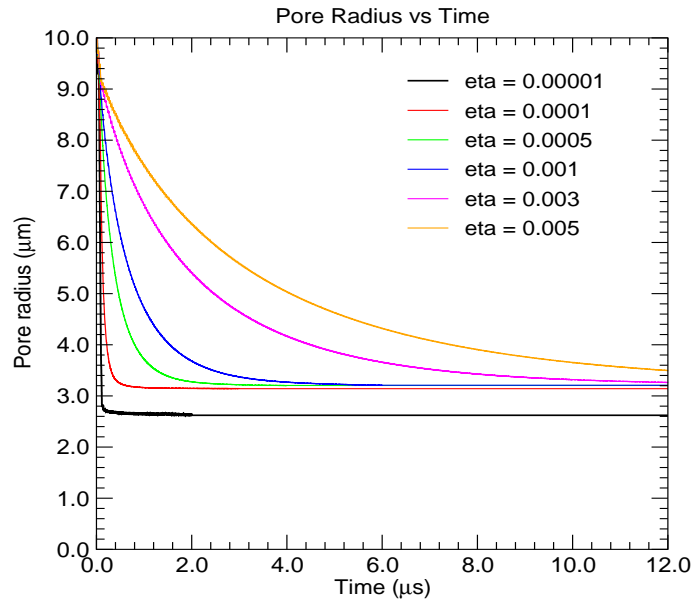
Figure 5.8: Time evolution of pore radius for different values of viscosity, η. a_0=10 μm, ϕ_0=1%, P_s=0.01 Mb, τ=0.1 μs, Y=0.002 Mb, and μ=0.0454 Mb.
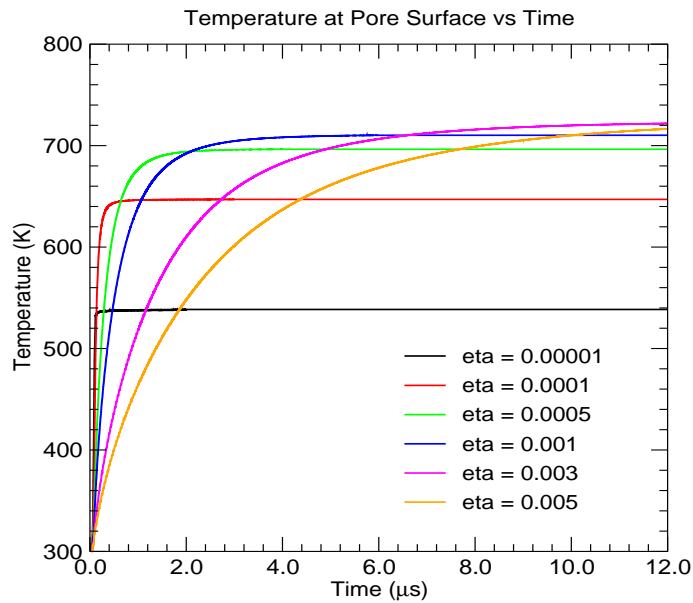

Figure 5.9: Temperature at the surface of the collapsing pore for different values of viscosity, η. a_0=10 μm, ϕ_0=1%, P_s=0.01 Mb, τ=0.1 μs, Y=0.002 Mb, and μ=0.0454 Mb.
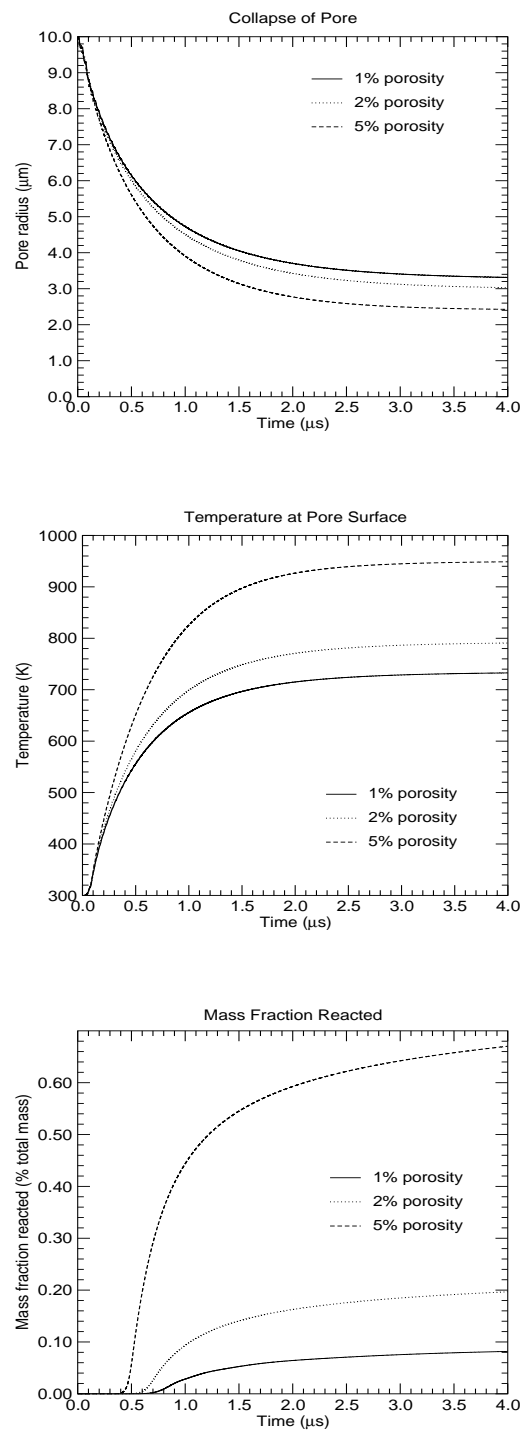
Figure 5.10: Computed results showing the effect of changes in initial porosity, ϕ_0 (without heat conduction modelled). a_0=10 μm, P_s=0.01 Mb, τ=0.1 μs, Y=0.002 Mb, μ=0.0454 Mb, and η=0.001 Mb μs.
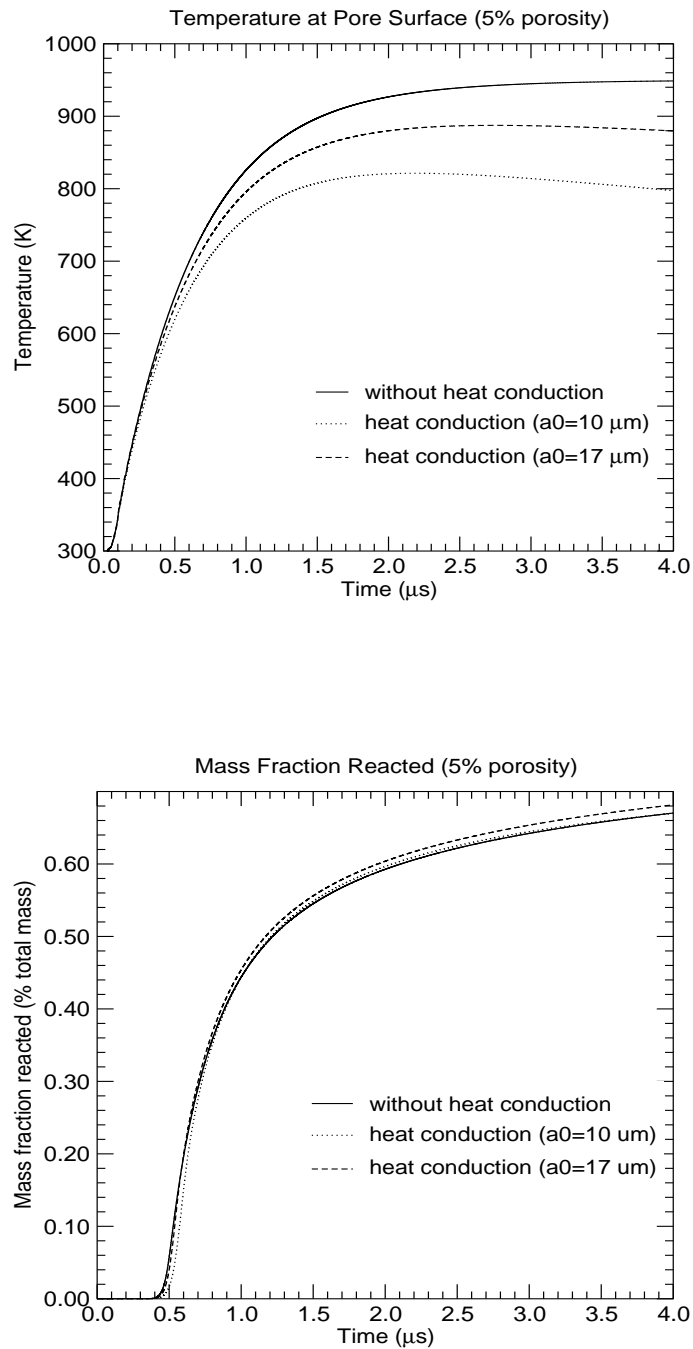
Figure 5.11: Computed results showing the effect of changes in the initial porosity (heat conduction modelled). a_0=10 μm, P_s=0.01 Mb, τ=0.1 μs, Y=0.002 Mb, μ=0.0454 Mb, η=0.001 Mb μs, and κ_s=4.1667e-14 Mbcc/cm/μs/K.

Figure 5.12: Radial distribution of temperature through the thickness of the explosive. ($\phi_0 = 5\%$, $a_0 = 10\mu m$, and $b_0 = 27.14\mu m$).
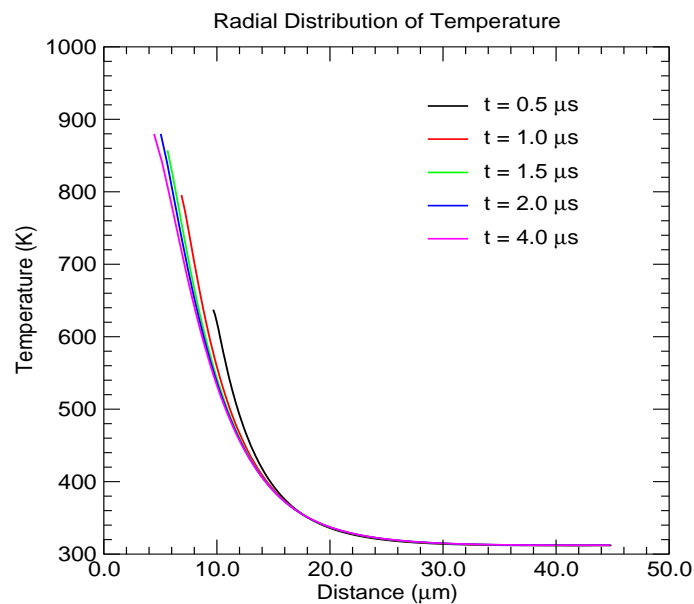
Figure 5.13: Radial distribution of temperature through the thickness of the explosive. ($\phi_0 = 5\%$, $a_0 = 17.2\mu m$, and $b_0 = 46.57\mu m$).
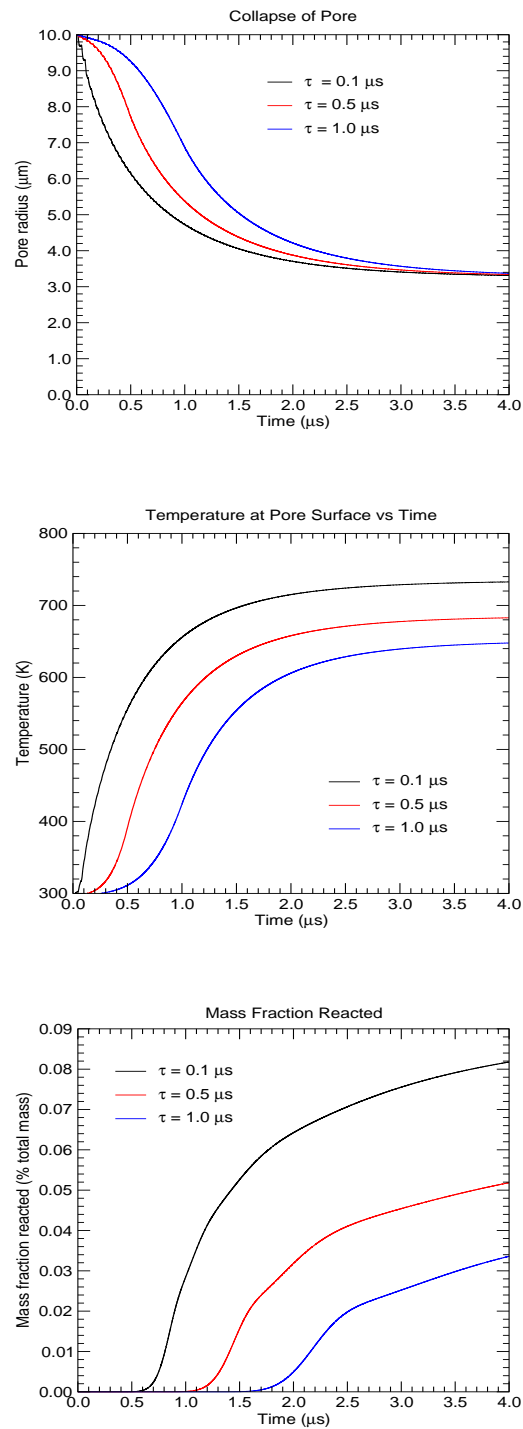
Figure 5.14: Computed results showing the effect of changing the rise time of the shock (without heat conduction modelled). a_0=10 μm, ϕ_0=1%, P_s=0.01 Mb, Y=0.002 Mb, μ=0.0454 Mb, and η=0.001 Mb μs.

Figure 5.15: Computed results showing the effect of changing the rise time of the shock with (dashed lines) and without (solid lines) heat conduction modelled. a_0=10 μm, ϕ_0=1%, P_s=0.01 Mb, Y=0.002 Mb, μ=0.0454 Mb, η=0.001 Mb μs, and κ_s=4.1667e-14 Mbcc/cm/μs/K.

Figure 5.16: Computed results showing the effect of changes in the magnitude of the pressure. a_0=10μm, ϕ_0=1%, τ=0.1μs, Y=0.002 Mb, μ=0.0454 Mb, and η=0.001 Mb μs.
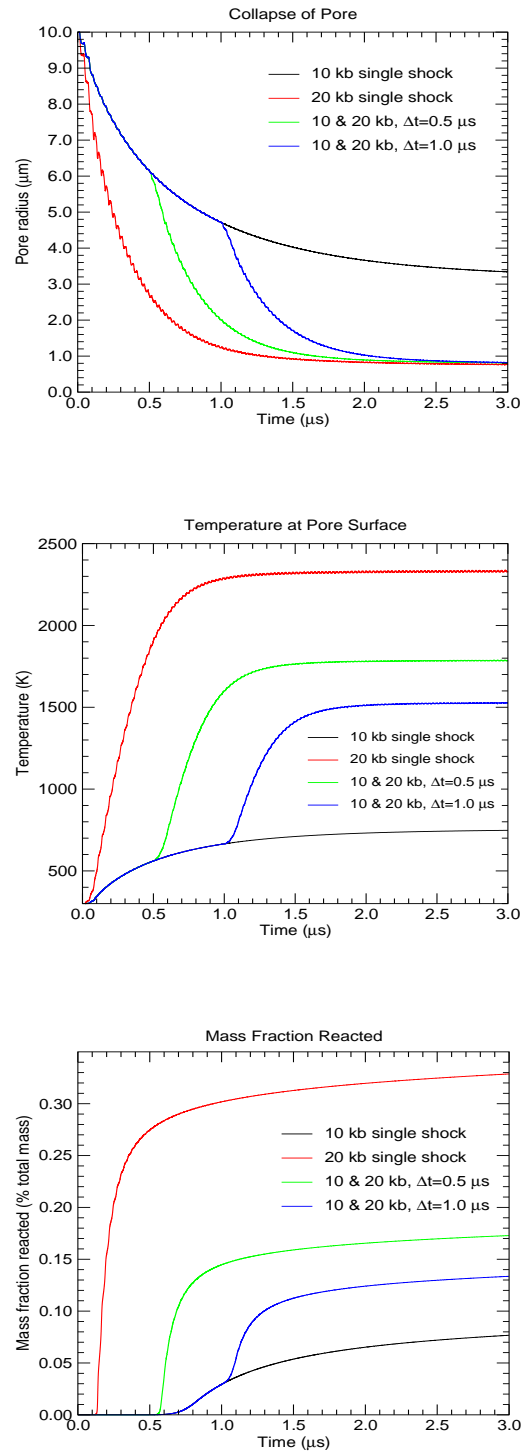
Figure 5.17: Calculated double shock results. a_0=10 μm, ϕ_0=1%, Y=0.002 Mb, μ=0.0454 Mb, and η=0.001 Mb μs.
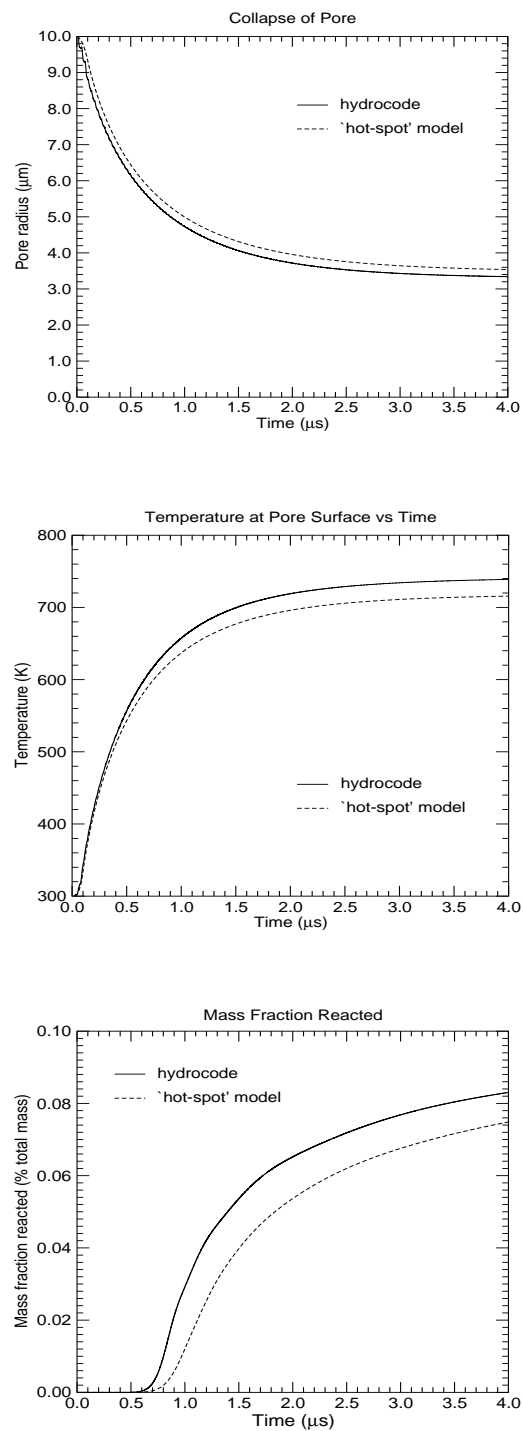
Figure 5.18: Comparison of results from simple 'hot-spot' model and PERUSE calculation. a_0=10 μm, ϕ_0=1%, P_s=0.01 Mb, τ=0.1 μs, Y=0.002 Mb, μ=0.0454 Mb, and η=0.001 Mb μs.
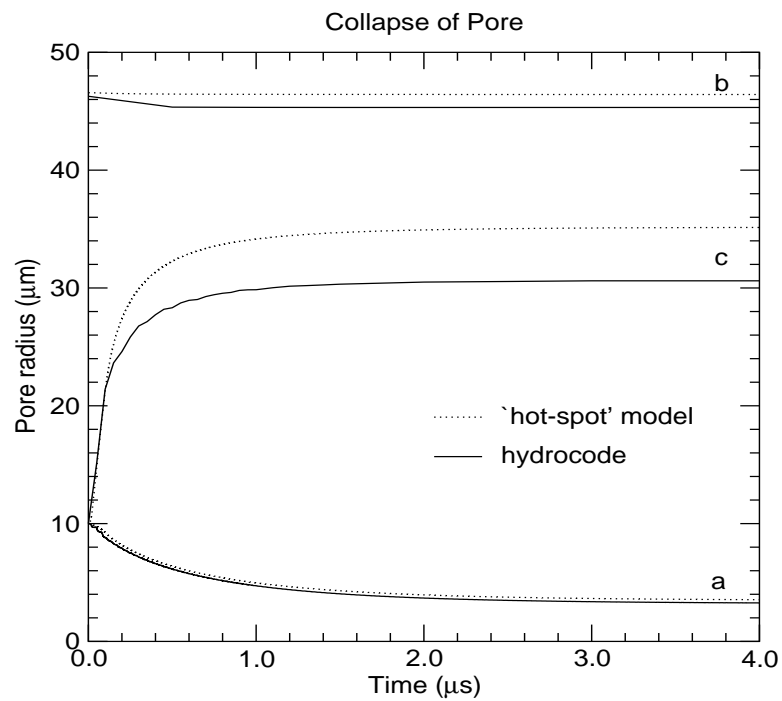
Figure 5.19: Comparison of the time evolution of the inner shell radius (a), the outer shell radius (b), and the interface between elastic and viscoplastic flow (c) from simple 'hot-spot' model and PERUSE calculation. a_0=10 μm, ϕ_0=1%, P_s=0.01 Mb, τ=0.1 μs, Y=0.002 Mb, μ=0.0454 Mb, and η=0.001 Mb μs.
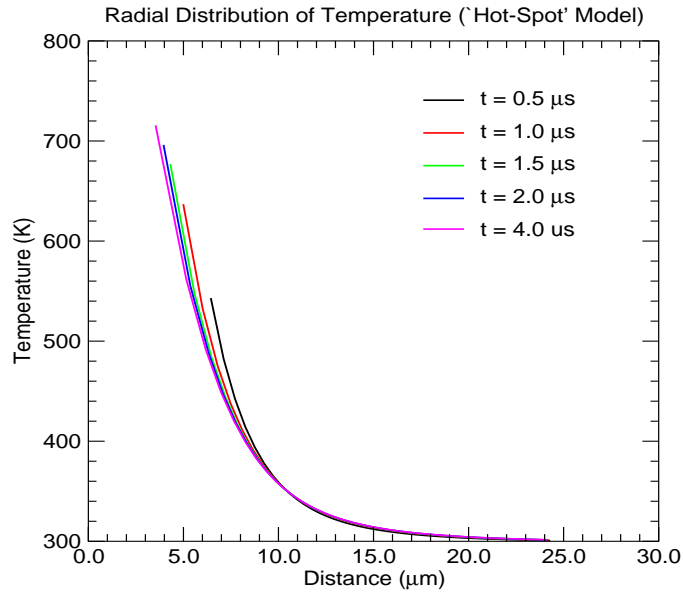
Figure 5.20: Calculated radial distribution of temperature through the solid explosive from simple 'hot-spot' model. a_0=10 μm, ϕ_0=1%, P_s=0.01 Mb, τ=0.1 μs, Y=0.002 Mb, μ=0.0454 Mb, and η=0.001 Mb μs.
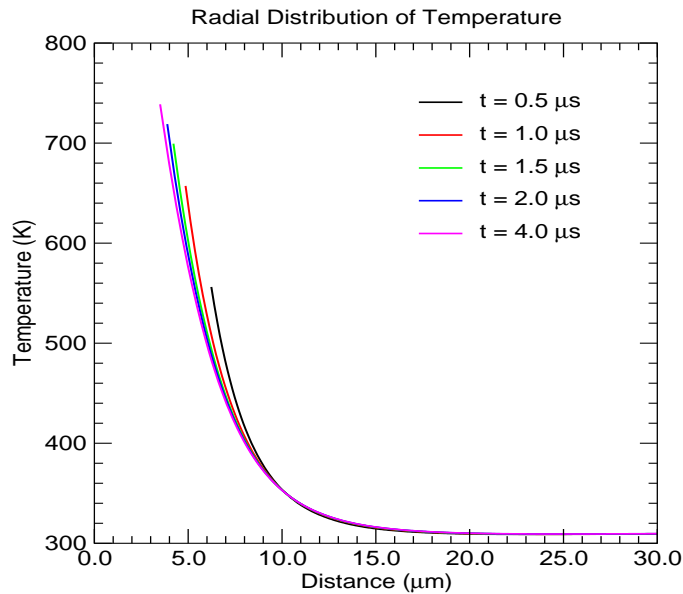
Figure 5.21: Calculated radial distribution of temperature through the solid explosive from PERUSE calculation. a_0=10 μm, ϕ_0=1%, P_s=0.01 Mb, τ=0.1 μs, Y=0.002 Mb, μ=0.0454 Mb, and η=0.001 Mb μs.
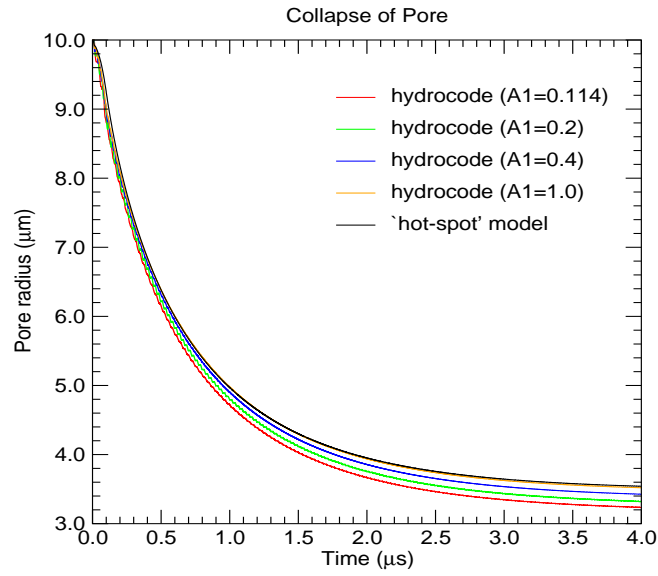
Figure 5.22: Comparison of results from simple 'hot-spot' model and PERUSE calculations. a_0=10 μm, ϕ_0=1%, P_s=0.01 Mb, τ=0.1 μs, Y=0.002 Mb, μ=0.0454 Mb, and η=0.001 Mb μs.
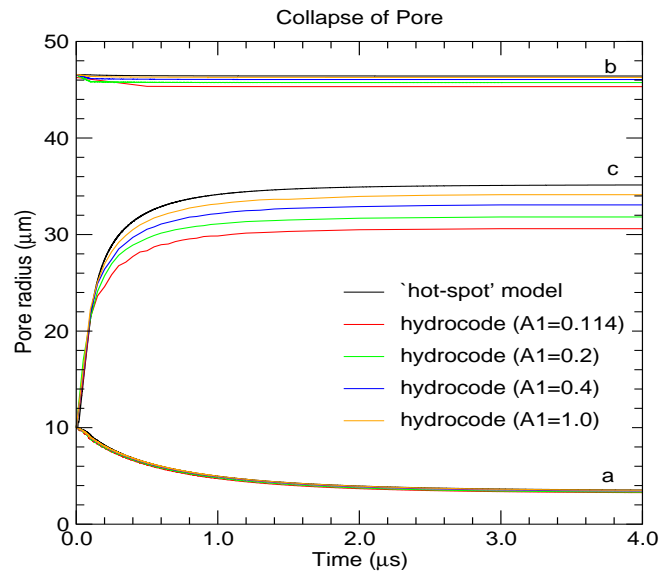
Figure 5.23: Comparison of the time evolution of the different shell radii (inner (a), outer (b), and plastic interface (c)) from simple 'hot-spot' model and PERUSE calculations. a_0=10 μm, ϕ_0=1%, P_s=0.01 Mb, τ=0.1 μs, Y=0.002 Mb, μ=0.0454 Mb, and η=0.001 Mb μs.
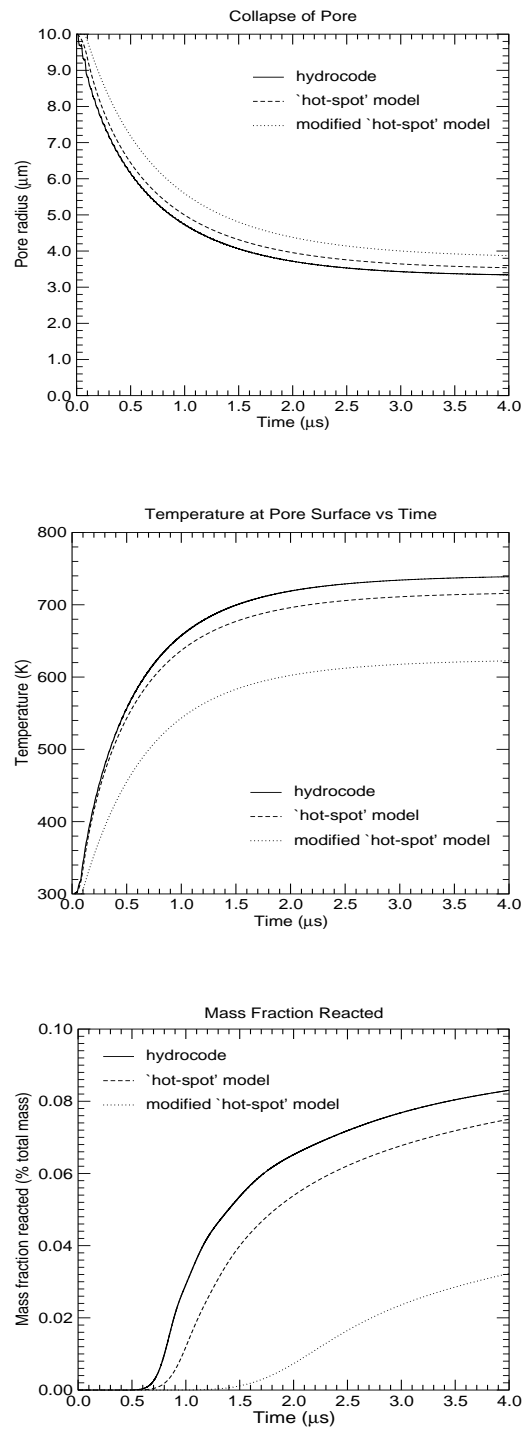
Figure 5.24: Comparison of results from simple 'hot-spot' model, modified 'hot-spot' model (viscoplastic flow only), and PERUSE calculation. a_0=10 μm, ϕ_0=1%, P_s=0.01 Mb, τ=0.1 μs, Y=0.002 Mb, μ=0.0454 Mb, and η=0.001 Mb μs.
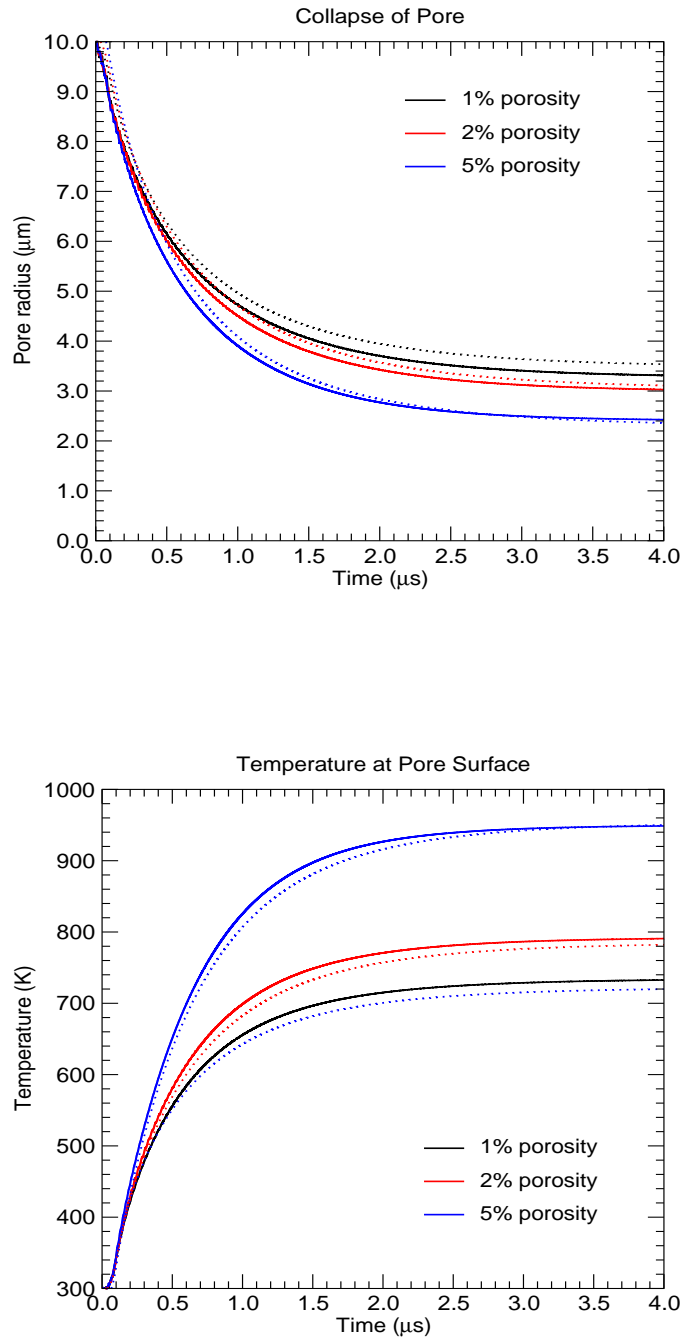
Figure 5.25: Comparison of computed results from simple 'hot-spot' model (dashed lines) and PERUSE (solid lines) showing the effect of changes in initial porosity, ϕ_0. a_0=10 μm, τ=0.1 μs, Y=0.002 Mb, μ=0.0454 Mb, and η=0.001 Mb μs.
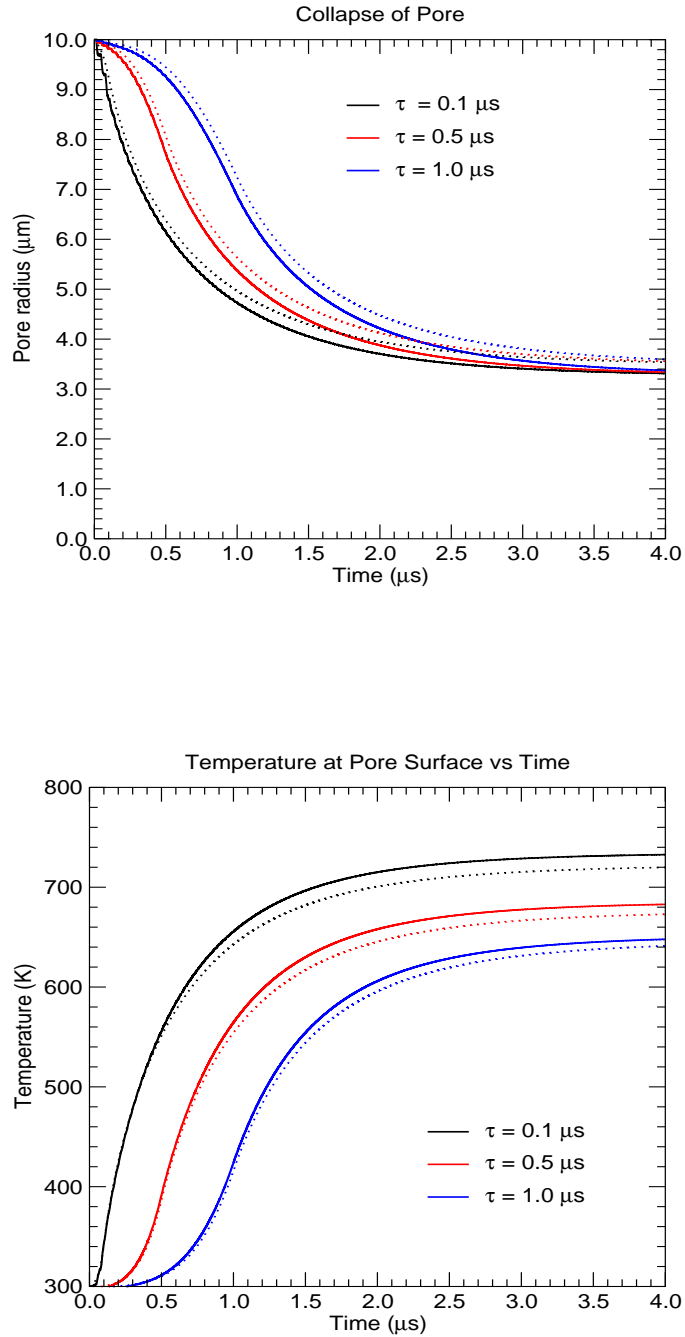
Figure 5.26: Comparison of computed results from simple 'hot-spot' model (dashed lines) and PERUSE (solid lines) showing the effect of rise time of the shock, τ. a_0=10 μm, ϕ_0=1%, Y=0.002 Mb, μ=0.0454 Mb, and η=0.001 Mb μs.
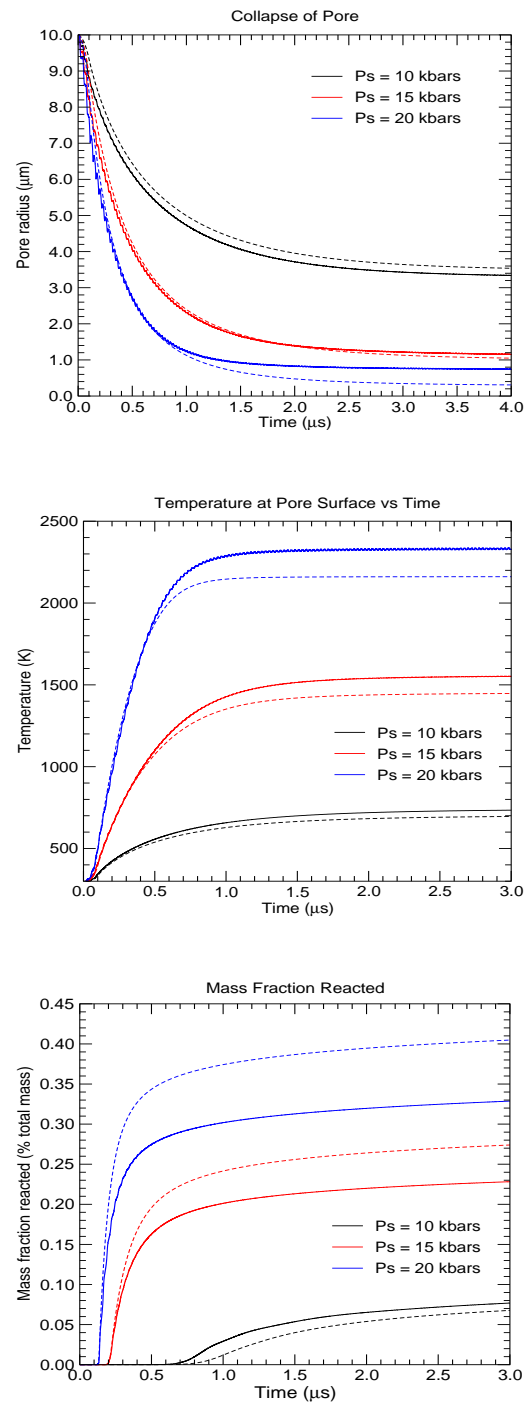
Figure 5.27: Comparison of computed results from simple 'hot-spot' model (dashed lines) and PERUSE (solid lines) showing the effect of changes in the magnitude of the pressure. a_0=10 μm, ϕ_0=1%, τ=0.1 μs, Y=0.002 Mb, μ=0.0454 Mb, and η=0.001 Mb μs.
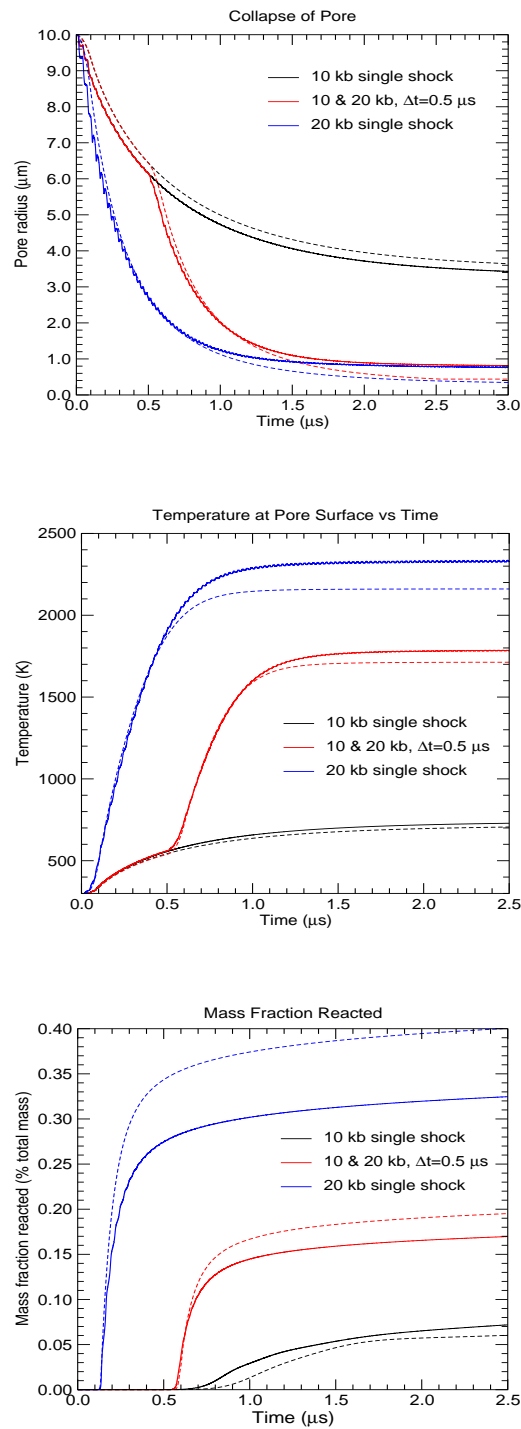
Figure 5.28: Calculated double shock results from simple 'hot-spot' model (dashed lines) and PERUSE (solid lines). $a_0=10$ μm, $\phi_0=1\%$, $\delta=0.5$ μs, $Y=0.002$ Mb, $\mu=0.0454$ Mb, and $\eta=0.001$ Mb μs.
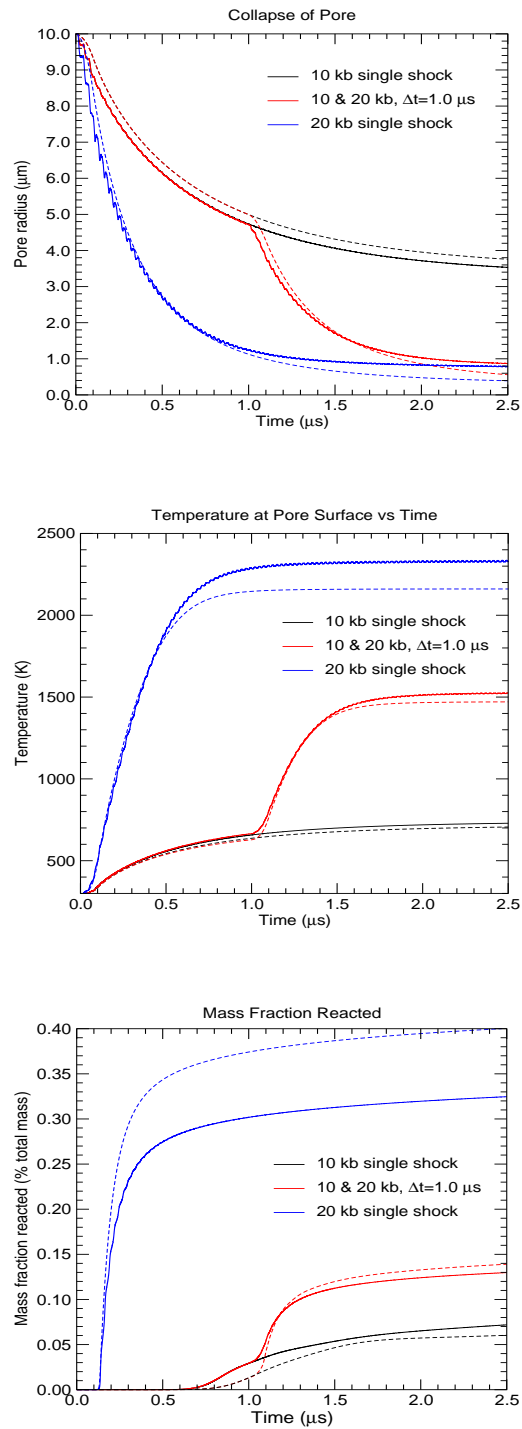
Figure 5.29: Calculated double shock results from simple 'hot-spot' model (dashed lines) and PERUSE (solid lines). a_0=10 μm, ϕ_0=1%, δ=1.0 μs, Y=0.002 Mb, μ=0.0454 Mb, and η=0.001 Mb μs.

Chapter 6

Conclusions and Future Work

Heterogeneous solid explosives are composed primarily of a mix of explosive crystals, binder material, and inter and intra-crystalline pores, where the pores and explosive crystals are usually of various sizes. It is generally accepted that the shock initiation of such explosives arises from the creation of so-called 'hot-spots', *i.e.* small regions of high temperature that are surrounded by cooler bulk material. 'Hot-spots' are created as a result of an incident shock wave interacting with material discontinuities which act as concentration points for the supplied energy and locally trigger the reaction in the explosive. 'Hot-spots' are therefore an essential ingredient in any theory on shock initiation.

For many years, continuum-based reactive burn models have been used to calculate the shock initiation behaviour of heterogeneous solid explosives. In the continuum-level models, effects occuring at the scale of the pores and explosive crystals, *e.g.* formation and ignition of 'hot-spots', are implicitly aggregated to calculate the bulk response. The next generation of shock initiation models, so-called physics-based or mesoscale models, are currently being developed to exploit advances in computing power, where the goal is to develop models that explicitly take account of the important physical and chemical processes that occur at the scale of the individual components in reactive flows. Only through the development of physics-based or mesoscale models will the effects of changes in explosive morphology (pore size distribution, crystal or grain size distribution, binder material *etc*) on explosive response be able to be predicted. However, such work is still in its infancy, and there is a long way to go before these types of models are routinely used to calculate explosive shock initiation behaviour. In this thesis, the mathematical and numerical modelling of shock initiation in heterogeneous explosives from the aspect of both continuum and mesoscale modelling has been considered.

The majority of continuum-level reactive burn models currently used in hydrocodes to model shock initiation in heterogeneous solid explosives use pressure-dependent reaction rates. For evaluation purposes the popular, pressure-dependent,

Lee-Tarver reactive burn model has been implemented and validated in a one-dimensional hydrocode. The main deficiency of the Lee-Tarver model, or any pressure-dependent model, is that there is no mechanism to predict explosive behaviour under double shock compression. In particular, pressure-based models cannot account for the phenomenon of 'shock desensitisation', where a weak precursor shock renders an explosive less sensitive to following stronger shocks. For any reaction rate based predominately on the local pressure, it is necessary to consider an additional desensitisation model to account for double shock observations.

To provide a capability to model the effects of shock desensitisation within the confines of the Lee-Tarver model, a simple but physically realistic desensitisation model has been developed. To examine its validity, the model has been applied to data, where desensitisation by preshocking has been observed, with mixed results. It is concluded that the simple desensitisation model is suitable for modelling double shock situations where there is little or no reaction in the first shock. Applying the model where there is significant reaction in the precursor wave has yielded poor agreement with experimental data. The fact that it is necessary to postulate an additional desensitisation model to account for double shock observations demonstrates that reaction rates do not depend substantially on the local pressure. It follows that pressure-dependent models are based on a false premise, and that the predictive capability of such models is low.

CREST is a new continuum reactive burn model that, by utilising entropy-, rather than pressure-, dependent reaction rates provides an improved predictive capability to model shock initiation behaviour that, importantly, removes the need for an additional desensitisation model for double shocks. The CREST model has been successfully implemented and validated in a one-dimensional, and a number of two-dimensional hydrocodes so that a wide range of explosive problems can be simulated using the model. However, during the hydrocode implementation and use of CREST, it was found that the move to entropy-based reaction rates introduces a number of computational problems not associated with pressure-based models.

The parameters in CREST's reaction rate model are fitted to particle velocity gauge data from gas-gun experiments. In the modelling of explosive impact problems such as gas-gun shots, CREST over-predicts the rate of energy release in an explosive adjacent the impact surface due to the classical 'wall-heating' error. This could affect the selection of the reaction rate parameters in the model, and has the potential to lead to inaccuarte conclusions being made about the reactive behaviour of an explosive. From the explosives that have so far been parameterised for the model, 'wall-heating' has only a very small effect on the calculated results from CREST. However, this may not be the case for other explosives of interest, and in future appropriate methods will be applied in an attempt to minimise the effect of this long standing problem in relation to CREST simulations.

A study of the sensitivity of CREST calculations to mesh density for both a HMX-based, and a TATB-based explosive, has indicated that an entropy-dependent

model requires a finer mesh than a pressure-dependent model to achieve mesh converged results. An independent study, using a different entropy-dependent reaction rate and different equations of state, came to similar conclusions. To overcome the more restrictive mesh size requirements of an entropy-dependent model, CREST has been implemented into a two-dimensional Eulerian adaptive mesh refinement hydrocode with an appropriate refinement criteria defined for the model. This will enable large problems of interest to be calculated at the size of mesh required by CREST to obtain mesh converged results. The increased mesh requirements for entropy-based models are not yet understood, and further work is required to understand the mesh convergence properties of entropy-dependent models. The mesh sensitivity study will also be extended to two-dimensional calculations to examine whether the findings in one-dimensional calculations are also true in two-dimensions.

In CREST, an explosive's initial porosity is included as a parameter in the non-reactive equation of state using the Snowplough porosity model. Application of the Snowplough model, however, produces undesirable numerical oscillations in the calculated function of entropy of the solid phase explosive, the variable upon which the CREST reaction rate model is dependent. This could give rise to numerical instabilities in CREST simulations. To improve the modelling of shocks in porous explosives, the Snowplough model was modified by removing the assumption that the sound speed is zero while the material is in its porous state. Although this modification removes unwanted numerical oscillations in entropy calculations, it is only applicable to low porosity explosives, and hence is viewed as a short-term fix. In future, to both improve the modelling of shocks in porous materials and enable a larger range of porosities to be modelled with CREST, the Snowplough model will be replaced by a P-α porosity model.

To examine the predictive capability of CREST, a model for the insensitive high explosive PBX9502, fitted to one-dimensional data of the shock to detonation transition, has been applied, without modification, to two-dimensional detonation propagation data. CREST accurately matches detonation waveshape data, predicts the failure diameter of the explosive to within $\sim$1mm of the experimental value, and over most the range of charge sizes, the diameter effect cuvre for PBX9502 is well represented. The only discrepency with the experimental detonation data is that CREST fails to predict the upturn in the diameter effect curve at large charge sizes. It is recognised that a slow reaction component needs to be added to the model to represent this feature. Once this problem has been addressed, future work will examine whether CREST can also predict the effects of temperature on PBX9502 detonation data.

Overall, the CREST model is giving promising results in modelling a range of different initiation and detonation phenomena. CREST appears capable of predicting experiments outside its fitting regime, and this gives confidence in the ability

of the model to accurately simulate a wide range of initiation and detonation phe-nomena; not only is CREST a model for the shock to detonation transition, it is also a model for detonation propagation. In future, the model will be applied to other explosive phenomena of interest, *e.g.* corner turning, detonation extinction *etc*, to examine, (i) the wider applicability of CREST, and (ii) to look for any deficiencies with the current model. Once the model has been applied to a wider range of ex-plosive phenomena, a clearer picture of the predictive capability of the model will emerge.

A constrained least squares method has been applied to shock time of arrival data to provide a fast and efficient solution method for determining run-distances and run-times to detonation using a technique devised at Los Alamos National Lab-oratory (LANL) for fitting shock trajectory data. The method can be applied equally well to experimental and calculated data. Good fits to experimental shock trajectory data from sustained single shock EDC37 gas-gun experiments have been obtained, and the derived run-distances and run-times to detonation are in very close agree-ment with corresponding values quoted by LANL, thus validating the application of the method.

The least squares method was then applied to calculated shock time of arrival data from CREST calculations of EDC37 gas-gun shots. Overall, the calculated run-distance to detonation data is in good agreement with experiment, however, the fit to the EDC37 Pop-Plot starts to diverge at low pressures, indicating that the EDC37 CREST model needs to be improved in the low pressure region. Future work will expand the capabilities of the least squares program to output shock ve-locities at each of the particle velocity gauge locations in a gas-gun experiment, as well as giving the run-distances and run-times to detonation. This data, along with the particle velocities at the shock at each gauge location, can be used to give ad-ditional Hugoniot points. This will increase the amount of non-reactive Hugoniot data available from which to develop non-reacted equations of state for explosives.

Continuum-level reactive burn models such as Lee-Tarver and CREST, do not explicitly account for phenomena occuring at the mesoscale, *e.g.* the formation and ignition of 'hot-spots'. As a result, such models are unable to account for the effect of changes in crystal or grain size, pore size, and binder distribution on the explo-sive response. To predict the effect of changes in morphology, the model constants would have to be re-calibrated to experimental data. As a simple first step towards addressing the complex phenomena occuring at the mesoscale, explicit modelling of 'hot-spot' initiation in one-dimension has been performed. Using a simple model for the explosive that consists of a pore at the centre of a spherical shell of solid ma-terial, 'hot-spots' are formed as a result of elastic-viscoplastic flow in the collapsing solid shell. Direct numerical simulations to study 'hot-spot' initiation in detail were initially performed. Following this, a simple 'hot-spot' initiation model that can be built into a hydrocode for macroscopic modelling has been developed.

Results from the simple 'hot-spot' model compare very well with corresponding

results from the direct numerical simulations. The observed differences between the two modelling approaches are due to the incompressibility assumption in the simple model. At the shock pressures studied, the incompressibility assumption has only a small effect on the calculated results. The results obtained from both approaches are consistent with observations, and commonly held ideas regarding the shock initiation and sensitivity of heterogeneous solid explosives. This gives confidence in the approach of using an elastic-viscoplastic pore collapse model to describe 'hot-spot' initiation in heterogeneous solid explosives.

Whilst developing the simple 'hot-spot' initiation model, it was found that viscoplastic 'hot-spot' models described in the literature are built on an invalid assumption. These models assume that pore collapse occurs as a result of viscoplastic flow only in the solid phase material. The direct numerical modelling work has shown that, for weak and moderate shock waves, the collapsing solid shell is never fully viscoplastic. Where pore collapse is in the transitional elastic-viscoplastic phase, viscoplastic pore collapse models under-predict the rate of pore collapse, and give significantly lower 'hot-spot' temperatures in comparison to the simple 'hot-spot' initiation model. Thus, in the shock regimes studied, the viscoplastic 'hot-spot' models are in error.

It is acknowledged that the important pores in a heterogeneous solid explosive may be located in the binder material. Thus, in future the modelling work will be extended to include the binder material. Assuming that the equation of state and constitutive properties of the binder are known, the effects on 'hot-spot' initiation of pure versus 'dirty' binders, and inert versus energetic binders, can be studied. Future work will also examine the validity of the assumption that pore collapse is spherically symmetric. To address this issue, two-dimensional direct numerical simulations of shock induced pore collapse are required. This study could also be extended to examine whether the geometry of the 'pores' is an important factor in determining the explosive response.

The explicit 'hot-spot' modelling work performed in this thesis provides a good starting point for further development of the simple 'hot-spot' initiation model. In the short term, improvements will be made to the simple model by including heat conduction effects since 'hot-spot' temperatures can be cooled by heat conduction to the surrounding bulk material. In addition, reaction schemes for solid explosives need to be developed and included so that the whole process of 'hot-spot' formation and localised heating, through to 'hot-spot' ignition can be modelled. To build a comprehensive model to describe mesoscale effects, consideration will be given longer term to developing a model for the growth of reaction as the explosive burn spreads out from 'hot-spots' to consume the bulk of the material.

Appendix A - Flowchart Showing the Key Steps in the Least Squares Program

START

Specify initial values
for a, b, U_s

Specify values for
δa, δb, δU_s
to calc sensitivities

Specify constraints
β, α_1, α_2, α_3

Specify convergence
limits on Δa, Δb, ΔU_s

Read in expt
or calc data?

expt   calc

Specify D_{cj} and C

Specify C and reaction
products EOS parameters

Calculate D_{cj} from
reaction products EOS

Specify no. of gauges

Read in (x,t) data
for each gauge location

```
                    ┌──────────────────────────────┐
                    │ Calculate arrival times for   │
                    │ standard calculation + 3      │
                    │ independently altered         │
                    │ calculations                  │
                    └──────────────────────────────┘
                                   │
                    ┌──────────────────────────────┐
                    │ Calculate Δt for standard     │
                    │ calculation, and the RMS error│
                    └──────────────────────────────┘
                                   │
                    ┌──────────────────────────────┐
                    │ Calculate sensitivities       │
                    │  ∂t/∂a, ∂t/∂b, ∂t/∂Us         │
                    └──────────────────────────────┘
                                   │
                    ┌──────────────────────────────┐
                    │ Solve least squares normal    │
                    │ equations for Δa, Δb, ΔUs     │
                    └──────────────────────────────┘
                                   │
                    ┌──────────────────────────────┐
                    │ Calculate updated a, b, Us    │
                    └──────────────────────────────┘
                                   │
```

Calculate arrival times for standard calculation + 3 independently altered calculations

Calculate Δt for standard calculation, and the RMS error

Calculate sensitivities
$$\frac{\partial t}{\partial a}, \ \frac{\partial t}{\partial b}, \ \frac{\partial t}{\partial U_s}$$

Solve least squares normal equations for Δa, Δb, ΔU_s

Calculate updated a, b, U_s

Has minimum been achieved? — yes →

Re-calculate fit for best (a, b, U_s) found from least squares method

no ↓

Too many iterations?   no →

Determine run-distance and run-time to detonation

yes ↓

STOP

Output results

STOP

Bibliography

[1] P. W. Cooper. *Explosives Engineering*. Wiley-VCH, 1996.

[2] A. W. Campbell, W. C. Davis, and J. R. Travis. Shock Initiation of Detonation in Liquid Explosives. *Physics of Fluids*, 4(4):498–510, 1961.

[3] A. W. Campbell, W. C. Davis, J. B. Ramsay and J. R. Travis. Shock Initiation of Solid Explosives. *Physics of Fluids*, 4(4):511–521, 1961.

[4] F. P. Bowden and A. D. Yoffe. *Initiation and Growth of Explosion in Liquids and Solids*. Cambridge University Press, 1952.

[5] J. E. Field, N. K. Bourne, S. J. P. Palmer, and S. M. Walley. Hot-Spot Ignition Mechanisms for Explosives and Propellants. *Phil. Trans. Soc. Lond. A*, 339:269–283, 1992.

[6] C. L. Mader. *Numerical Modelling of Explosives and Propellants (Second Edition)*. CRC Press, 1998.

[7] C. L. Mader. Initiation of Detonation by the Interaction of Shocks With Density Discontinuities. *Physics of Fluids*, 8(10):1811–1816, 1965.

[8] M. M. Carroll and A. C. Holt. Static and Dynamic Pore Collapse Relations for Ductile Porous Materials. *Journal of Applied Physics*, 43(4):1626–1636, 1972.

[9] R. B. Frey. Cavity Collapse in Energetic Materials. In *Proceedings of the 8th International Detonation Symposium*, pages 68–80, 1985.

[10] E. F. Gittings. Initiation of a Solid Explosive by a Short-Duration Shock. In *Proceedings of the 4th International Detonation Symposium*, pages 373–380, 1965.

[11] R. L. Gustavsen, S. A . Sheffield, R. R. Alcon, L. G. Hill (LANL), R. Winter, D. Salisbury, P. Taylor (AWE). Initiation of EDC37 Measured With Embedded Electromagnetic Particle Velocity Gauges. In *APS Conference on Shock Compression of Condensed Matter*, pages 879–882, 1999.

[12] G. T. Afanasev and V. K. Bobolev. Initiation of Solid Explosives by Impact. *Jerusalem Israel Program for Scientific Translations: Jerusalem*, 1971.

[13] R. E. Winter and J. E. Field. The Role of Localised Plastic Flow in the Impact Initiation of Explosives. In *Proc. Roy. Soc.*, volume A343, pages 399–413, 1975.

[14] P. M. Howe, G. Gibbons and P. E. Webber. An Experimental Investigation of the Role of Shear in Initiation of Detonation by Impact. In *Proceedings of the 8th International Detonation Symposium*, pages 294–306, 1985.

[15] J. E. Field, S. J. P. Palmer, P. H. Pope, R. Sundararajan, and G. M. Swallowe. Mechanical Properties of PBX's and Their Behaviour During Drop Weight Impact. In *Proceedings of the 8th International Detonation Symposium*, pages 635–644, 1985.

[16] J. E. Field, M. A. Parry, S. J. P Palmer, and J. M. Huntley. Deformation and Explosive Properties of HMX powders and Polymer Bonded Explosives. In *Proceedings of the 9th International Detonation Symposium*, pages 886–896, 1989.

[17] I. Plaksin, C. S. Coffey, R. Mendes, J. Ribeiro, J. Campos, and J. Direito. Formation of CRZ 3D Structure at SDT and at Shear Initiation of PBX: Effects of Front Irradiation and Reaction Localisation in HMX Crystals. In *Proceedings of the 13th International Detonation Symposium*, pages 319–330, 2006.

[18] R. B. Frey. The Initiation of Explosive Charges by Rapid Shear. In *Proceedings of the 7th International Detonation Symposium*, pages 36–42, 1981.

[19] C. S. Coffey and R. W. Armstrong. *Shock Waves and High Strain Rate Phenomena in Metals: Concepts and Applications*. Meyers, E. M. and Murr, E. L., Eds, Plenum, NY, 1981.

[20] C. S. Coffey. Phonon Generation and Energy Localization by Moving Edge Dislocations. *Phys. Rev.*, B24(12):6984, 1981.

[21] V. Krishna Mohan, V. C. Jyothi Bhasu, and J. E. Field. Role of Adiabatic Shear Bands in Initiation of Explosives by Drop-Weight Impact. In *Proceedings of the 9th International Detonation Symposium*, pages 1276–1283, 1989.

[22] M. M. Chaudhri. The Initiation of Fast Decomposition in Solid Explosives by Fracture, Plastic Flow, Friction, and Collspsing Voids. In *Proceedings of the 9th International Detonation Symposium*, pages 857–867, 1989.

[23] S. K. Chidester, L. G. Green, and C. G. Lee. A Frictional Work Predictive Method for the Initiation of Solid High Explosives From Low-Pressure Impacts. In *Proceedings of the 10th International Detonation Symposium*, pages 786–792, 1993.

[24] J. I. Copp, S. E. Napier, T. Nash, W. J. Powell, H. Skelly, A. R. Ubbelohde, and P. Woodward. The Sensitiveness of Explosives. *Philosophical Transactions of the Royal Society*, 241:198–296, 1948.

[25] G. M. Swallowe and J. E. Field. Effects of Polymers on the Drop Weight Sensitiveness of Explosives. In *Proceedings of the 7th International Detonation Symposium*, pages 24–35, 1981.

[26] G. Eden, R. A. Belcher, M. I. Andrew, and W. R. Marlow. Frozen 'Hot-Spots' in Shocked EDC35, an Insensitive High Explosive. In *Proceedings of the 9th International Detonation Symposium*, pages 1253–1259, 1989.

[27] N. K. Bourne and J. E. Field. Shock-Induced Collapse of Single Cavities in Liquids. *J. Fluid Mech.*, 244:225–240, 1992.

[28] A. M. Milne and N. K. Bourne. Experimental and Numerical Study of Temperatures in Cavity Collapse. In *Proceedings of the APS Conference on Shock Compression of Condensed Matter*, pages 914–917, 2001.

[29] N. K. Bourne. On the Collapse of Cavities. *Shock Waves*, 11:447–455, 2002.

[30] R. L. Rabie and H. H. Harry. The Characterisation of British Explosives FD16, EDC29, EDC35, and EDC37. Technical Report LA-UR-92-1928, Los Alamos National Laboratory, 1992.

[31] T. R. Gibbs and A. Popolato. *LASL Explosive Property Data*. University of California Press, 1980.

[32] F. E. Walker and R. J. Wasley. *Explosivstoffe*, 17(1):9, 1969.

[33] H. R. James. An Extension to the Critical Energy Criterion Used to Predict Shock Initiation Thresholds Lots. *Popellents, Explosives, Pyrotechnics*, 21:8–13, 1996.

[34] J. Wackerle, R. L. Rabie, M. J. Ginsberg, and A. B. Anderson. A Shock Initiation Study of PBX9404. In *Proceedings of the Symposium on High Dynamic Pressures (Comarisariat a l'Energie Atomique, Paris, France)*, page 115, 1978.

[35] J. E. Vorthman, G. Andrews, and J. Wackerle. Reaction Rates From Electromagnetic Gauge Data. In *Proceedings of the 8th International Detonation Symposium*, pages 99–110, 1985.

[36] R. L. Gustavsen, S. A. Sheffield, R. R. Alcon, and L. G. Hill. Shock Initiation of New and Aged PBX 9501 Measured With Embedded Electromagnetic Particle Velocity Gauges. Technical Report LA-13634-MS, Los Alamos National Laboratory, 1999.

[37] R. L. Gustavsen, S. A. Sheffield, and R. R.Alcon. Measurements of Shock Initiation in the Tri-Amino-Tri-Nitro-Benzene Based Explosive PBX9502: Wave Forms From Embedded Gauges and Comparison of Four Different Material Lots. *Journal of Applied Physics*, 99(114907), 2006.

[38] R. E. Winter, S. S. Sorber, D. A. Salisbury, P. Taylor, R. Gustavsen, S. Sheffield, and R. Alcon. Experimental Study of the Shock Response of an HMX-Based Explosive. *Shock Waves*, 15(2):89–101, 2006.

[39] R. N. Mulford, S. A. Sheffield, and R. A. Alcon. Initiation of Preshocked High Explosives PBX-9404, PBX-9502, PBX-9501, Monitored with In-material Magnetic Gauging. In *Proceedings of the 10th International Detonation Symposium*, pages 459–467, 1993.

[40] C. M Tarver, T. M. Cook, P. A. Urtiew, and W. C. Tao. Multiple Shock Initiation of LX-17. In *Proceedings of the 10th International Detonation Symposium*, pages 696–703, 1993.

[41] D. Stirpe, J. O. Johnson, and J. Wackerle. *Journal of Applied Physics*, 41:3884, 1970.

[42] H. Moulard, J. W. Kury, and A. Delclos. The Effect of RDX Particle Size on the Shock Sensitivity of Cast PBX Formulations. In *Proceedings of the 8th International Detonation Symposium*, pages 902–913, 1985.

[43] H. Moulard. Particular Aspect of the Explosive Particle Size Effect on Shock Sensitivity of Cast PBX Formulations. In *Proceedings of the 9th International Detonation Symposium*, pages 18–24, 1989.

[44] M. Chick, T. J. Bussell, and R. B. Frey. Some Characteristics of Bow Wave Initiation and Desensitisation. In *Proceedings of the 10th International Detonation Symposium*, pages 69–77, 1993.

[45] L. G Hill, J. B. Bdzil, W. C. Davis, and R. R Critchfield. PBX9502 Front Curvature Rate Stick Data: Repeatability and the Effects of Temperature and Material Variation. In *Proceedings of the 13th International Detonation Symposium*, pages 331–341, 2006.

[46] R. L. Gustavsen, S. A. Sheffield, and R. R. Alcon. Extended Run Distance Measurements of Shock Initiation in PBX9502. In *Proceedings of the APS*

Conference on Shock Compression of Condensed Matter, pages 915–918, 2007.

[47] P. A. Urtiew, L. M. Dickson, D. F. Aldis, and C. M. Tarver. Shock Initiation of LX-17 as a Function of its Initial Temperature. In *Proceedings of the 9th International Detonation Symposium*, pages 112–122, 1989.

[48] D. E. Hooks and K. J. Ramos. Initiation Mechanisms in Single Crystal Explosives: Dislocations, Elastic Limits, and Initiation Thresholds. In *Proceedings of the 13th International Detonation Symposium*, pages 455–464, 2006.

[49] E. L. Lee and C. M. Tarver. Phenomenological Model of Shock Initiation in Heterogeneous Explosives. *Physics of Fluids*, 23(12):2362–2372, 1980.

[50] P. K. Tang, J. N. Johnson, and C. A. Forest. Modelling Heterogeneous High Explosive Burn with an Explicit Hot-spot Process. In *Proceedings of the 8th International Detonation Symposium*, pages 488–497, 1985.

[51] A. W. Campbell and J. R. Travis. The Shock Desensitisation of PBX9404 and Composition B-3. In *Proceedings of the 8th International Detonation Symposium*, pages 1057–1067, 1985.

[52] C. M. Tarver and J. O. Hallquist. Modelling Two-Dimensional Shock Initiation and Detonation Wave Phenomena in PBX-9404 and LX-17. In *Proceedings of the 7th International Detonation Symposium*, pages 488–497, 1981.

[53] C. M. Tarver, J. O. Hallquist, and L. M. Erickson. Modelling Short Pulse Duration Shock Initiation of Solid Explosives. In *Proceedings of the 8th International Detonation Symposium*, pages 951–961, 1985.

[54] C. M. Tarver and S. K. Chidester. Ignition and Growth Modelling of Detonating TATB Cones and Arcs. In *Proceedings of the APS Conference on Shock Compression of Condensed Matter*, pages 429–432, 2007.

[55] R. L. Gustavsen, S. A. Sheffield, R. R. Alcon, J. W. Forbes, C. M. Tarver, and F. Garcia. Embedded Electromagnetic Gauge Measurements and Modelling of Shock Initiation in the TATB Based Explosives LX-17 and PBX9502. In *Proceedings of the APS Conference on Shock Compression of Condensed Matter*, pages 1019–1022, 2001.

[56] M. L. Garcia and C. M. Tarver. Three-Dimensional Ignition and Growth Reactive Flow Modelling of Prism Failure Tests on PBX9502. In *Proceedings of the 13th International Detonation Symposium*, pages 63–70, 2006.

[57] Y. Partom. A Void Collapse Model for Shock Initiation. In *Proceedings of the 7th International Detonation Symposium*, pages 506–511, 1981.

[58] Y. Partom. Hydro-Reactive Computations With a Temperature Dependent Reaction Rate. In *Proceedings of the APS Conference on Shock Compression of Condensed Matter*, pages 460–463, 2001.

[59] Y. Partom. Modelling Initiation by a Reflected Shock. In *Proceedings of the 13th International Detonation Symposium*, pages 890–894, 2006.

[60] H. R. James and B. D. Lambourn. On the Systematics of Particle Velocity Histories in the Shock to Detonation Transition Regime. *Journal of Applied Physics*, 100(084906), 2006.

[61] C. A. Handley. The CREST Reactive Burn Model. In *Proceedings of the 13th International Detonation Symposium*, pages 864–870, 2006.

[62] C. A. Handley. The CREST Reactive Burn Model. In *Proceedings of the APS Conference on Shock Compression of Condensed Matter*, pages 373–376, 2007.

[63] R. E. Winter, L. S. Markland, and S. D. Prior. Modelling Shock Initiation of HMX-Based Explosive. In *Proceedings of the APS Conference on Shock Compression of Condensed Matter*, pages 883–886, 1999.

[64] R. Belmas, J. P. Plotard, and C. Bianchi. A Physical Model of Shock to Detonation Transition in Heterogeneous Explosives. In *Proceedings of the 10th International Detonation Symposium*, pages 724–730, 1993.

[65] M. D. Cook, P. J. Haskins, and C. Stennett. Development and Implementation of an Ignition and Growth Model for Homogeneous and Heterogeneous Explosives. In *Proceedings of the 11th International Detonation Symposium*, pages 589–598, 1998.

[66] L. S. Bennett. Constitutive Modelling of Weak and Strong Shock Initiation of Porous Explosives. In *Proceedings of the 11th International Detonation Symposium*, pages 612–620, 1998.

[67] W. Herrmann. Constitutive Equation for the Dynamic Compaction of Ceramic Powders. *Journal of Applied Physics*, 40(6):2490–2499, 1969.

[68] J. P. Plotard, R. Belmas, M. Nicollet, and M. Leroy. Effect of a Preshock on the Initiation of HMX, TATB and HMX/TATB Compositions. In *Proceedings of the 10th International Detonation Symposium*, pages 507–514, 1993.

[69] R. G. Whirley and B. E. Engelmann. *DYNA2D: A Non-linear, Explicit, Two-dimensional Finite Element Code for Solid Mechanics - User Manual*. University of California Press, 1992.

[70] M. D. Cook, P. J. Haskins, C. Stennett, and A. D. Wood. Cumulative Damage Hot-Spot Model for use With Arrhenius Based Ignition and Growth Model. In *Proceedings of the 12th International Detonation Symposium*, pages 881–886, 2002.

[71] L. S. Bennett, K. Tanaka, and Y. Horie. *Shock Compression of Solids IV, Chapter 5*. Springer-Verlag, New York, 1997.

[72] B. A. Khasainov, A. A. Borisov, B. S. Ermolaev, and A. I. Korotkov. Two-Phase Visco-Plastic Model of Shock Initiation of Detonation in High Density Pressed Explosives. In *Proceedings of the 7th International Detonation Symposium*, pages 435–447, 1981.

[73] J. Massoni, R. Saurel, G. Baudin, and G. Demol. A Mechanistic Model for Shock Initiation of Solid Explosives. *Physics of Fluids*, 11(3):710–736, 1999.

[74] R. Bouma, H. J. Verbeek, B. Gruselle, and A. C Van der Steen. Application of a Viscoplastic Pore Collapse Model to the Shock Initiation Modelling of Explosives. In *Proceedings of New Models and Numerical Codes for Shock Wave Processes in Condensed Media*, pages 139–152, 1997.

[75] A. Longbottom, D. Boulton, and A. Milne. Viscoplastic Hot-Spot Ignition and Growth Model. Technical Report CR028/02, Fluid Gravity, 2002.

[76] A. L. Nicholls and C. M. Tarver. A Statistical Hot-Spot Reactive Flow Model for Shock Initiation and Detonation of Solid High Explosives. In *Proceedings of the 12th International Detonation Symposium*, pages 489–496, 2002.

[77] Y. Hamate, X. R. Lu, and Y. Horie. Development of a Reactive Burn Model: Effects of Particle Contact Distribution. In *Proceedings of the 13th International Detonation Symposium*, pages 1270–1275, 2006.

[78] A. L. Nicholls III. Users Manual for ALE3D: An Arbitray Lagrange-Eulerian 3D Code System. Technical Report UCRL-MA-152204 Rev 6, Lawrence Livermore National Laboratory, 2007.

[79] M. R. Baer, M. E. Kipp, and F. van Swol. Micromechanical Modelling of Heterogeneous Energetic Material. In *Proceedings of the 11th International Detonation Symposium*, pages 788–797, 1998.

[80] M. R. Baer and W. M. Trott. Theoretical and Experimental Mesoscale Studies of Impact Loaded Granular Explosive and Simulant Materials. In *Proceedings of the 12th International Detonation Symposium*, pages 939–950, 2002.

[81] J. Campbell and M. Shashkov. CASH-2D Version 01. Technical Report LA-CC-01-053, Los Alamos National Laboratory, 2001.

[82] C. E. Anderson. An Overview of the Theory of Hydrocodes. *Internat. J. Impact Engng.*, 5:33–59, 1987.

[83] C. Hirsch. *Numerical Computation of Internal and External Flows (Volume 1 : Fundamentals of Numerical Discretisation)*. Wiley, 1995.

[84] D. J. Benson. Computational Methods in Lagrangian and Eulerian Hydrocodes. *Comp. Meth. App. Mech. Engng.*, 99:235–394, 1992.

[85] C. W. Hirt, A. A. Ammsden, and J. L. Cook. An Arbitrary Lagrangian-Eulerian Computing Method for all Flow Speeds. *Journal of Computational Physics*, 14:227–253, 1974.

[86] A. J. Barlow. ALE in CORVUS. In *Proceedings of New Models and Numerical Codes for Shock Wave Processes in Condensed Media*, pages 581–596, 1997.

[87] B. J. Jones. The Status of SHAMROCK: A 2-Dimensional, Adaptive Mesh Refinement (AMR), Eulerian Production Code. In *Proceedings of New Models and Numerical Codes for Shock Wave Processes in Condensed Media*, pages 402–412, 1997.

[88] N. J. Whitworth. Simple One-Dimensional Model of 'Hot-Spot' Formation in Heterogeneous Solid Explosives. Master's thesis, Cranfield University, 1999.

[89] J. A. Zukas and W. P. Walters (Editors). *Explosive Effects and Applications*. Springer, 1998.

[90] J. D. Whittle. An Investigation of the Stability of Some Lagrangian Finite Difference Schemes. Technical report, AWE Internal Report (UK Unclassified), 1988.

[91] R. L. Bowers and J. R. Wilson. *Numerical Modelling in Applied Physics and Astrophysics*. Jones and Bartlett Publishers, 1991.

[92] R. D. Richtmyer and K. W. Morton. *Difference Methods for Initial-Value Problems*. Interscience (John Wiley) Publishers, 1967.

[93] W. F. Noh. Errors for Calculations of Strong Shocks Using an Artificial Viscosity and an Artificial Heat Flux. *Journal of Computational Physics*, 72:78–120, 1987.

[94] R. E. Setchell. Effects of Precursor Waves in Shock Initiation of Granular Explosives. *Combustion and Flame*, 54:171–182, 1983.

[95] C. L. Mader (Editor). *LASL Phermex Data, Volume III*. University of California Press, 1980.

[96] D. E. Munson and R. J. Lawrence. Dynamic Deformation of Polycrystalline Alumina. *Journal of Applied Physics*, 50(10):6272–6282, 1979.

[97] Prepared by Group GMX-6. Selected Hugionots. Technical Report LA-4167-MS, Los Alamos Scientific Laboratory, 1969.

[98] D. J. Steinberg. Equation of State and Strength Properties of Selected Materials. Technical Report URCL-MA-106439, Lawrence Livermore National Laboratory, 1996.

[99] L. M. Barker and R. E. Hollenbach. Shock Wave Studies of PMMA, Fused Silica, and Sapphire. *Journal of Applied Physics*, 41(10):4208–4226, 1970.

[100] B. D. Lambourn, N. J. Whitworth, C. A. Handley and H. R. James. A Finite Strain, Non-Reacted EOS For PBX9502. In *Proceedings of the APS Conference on Shock Compression of Condensed Matter*, pages 137–140, 2007.

[101] C. A. Honodel, J. R. Humphrey, R. C. Weingart, R. S. Lee, and P. Kramer. Shock Initiation of TATB Formulations. In *Proceedings of the 7th International Detonation Symposium*, pages 425–434, 1981.

[102] M. Cowperthwaite. A Constitutive Model for Calculating Chemical Energy Release Rates from the Flow Fields in Shocked Explosives. In *Proceedings of the 7th International Detonation Symposium*, pages 498–505, 1981.

[103] B. D. Lambourn. An Interpretation of Particle Velocity Histories During Growth to Detonation. In *Proceedings of the APS Conference on Shock Compression of Condensed Matter*, pages 367–370, 2003.

[104] B. D. Lambourn. An Improved EOS for Non-Reacted Explosives. In *Proceedings of the APS Conference on Shock Compression of Condensed Matter*, pages 165–168, 2005.

[105] J. von Neumann and R. D. Richtmeyer. A Method for the Numerical Calculation of Hydrodynamical Shocks. *Journal of Applied Physics*, 21:232–237, 1950.

[106] D. L. Youngs. Time-Dependent Multi-Material Flow With Large Fluid Distortion. *Numerical Methods for Fluid Dynamics, Eds. K. W. Morton and M. J. Baines (Academic Press)*, pages 273–285, 1982.

[107] W. J. Rider. Revisiting Wall Heating. *Journal of Computational Physics*, 162:395–410, 2000.

[108] B. D. Lambourn. Private communication. 2003.

[109] M. Gehmeyr, B. Cheng, and D. Mihalas. Noh's Constant Velocity Shock Problem Re-Visited. *Shock Waves*, 7(5):255–274, 1997.

[110] E. J. Caramana, M. J. Shashkov, and P. P. Whalen. Formulations of Artificial Viscosity for Multi-Dimensional Shock Wave Computations. *Journal of Computational Physics*, 144:70–97, 1998.

[111] C. A. Handley. Private communication. 2005.

[112] C. Mellor. Private communication. 2006.

[113] J. D Dunnett. Entropy Based Reactive Flow Calculations. Technical Report CR019/06, Fluid Gravity, 2006.

[114] A. W. Campbell and R. Engelke. The Diameter Effect in High-Density Heterogeneous Explosives. In *Proceedings of the 6th International Detonation Symposium*, pages 642–652, 1976.

[115] A. W. Campbell. Diameter Effect and Failure Diameter of a TATB-Based Explosive. *Propellents, Explosives, Pyrotechnics*, 9:183–187, 1984.

[116] L. G Hill, J. B. Bdzil, and T. D. Aslam. Front Curvature Rate Stick Measurements and Detonation Shock Dynamics Calibration for PBX9502 Over a Wide Temperature Range. In *Proceedings of the 11th International Detonation Symposium*, pages 1029–1037, 1998.

[117] B. M. Dobratz and P. C. Crawford. *LLNL Explosives Handbook*. Lawrence Livermore National Laboratory, 1985.

[118] W. A. Bailey, R. A. Belcher, D. K. Chilvers, and G. Eden. Explosive Equation of State Determination by the AWRE Method. In *Proceedings of the 7th International Detonation Symposium*, pages 678–685, 1981.

[119] S. D. Prior. Private communication. 2000.

[120] B. D. Lambourn. Private communication. 2005.

[121] R. Smedley-Stevenson. Private communication. 2005.

[122] S. J. White and A. M. Collyer. A WBL Consistent JWL Equation of State for the HMX-Based Explosive EDC37 From Cylinder Tests. In *Proceedings of the 3rd Khariton's Topical Scientific Readings International Conference - Extreme States of Substance: Detonation and Shock waves*, 2001.

[123] B. M. Butcher, M. M. Carroll, and A. C. Holt. Shock Wave Compaction of Porous Aluminium. *Journal of Applied Physics*, 45(9):3864–3875, 1974.

[124] J. Kang, P. B. Butler, and M. R. Baer. A Thermomechanical Analysis of Hot-Spot Formation in Condensed-Phase Energetic Materials. *Combustion and Flame*, 89:117–139, 1992.

[125] D. L. Bonnett and P. B. Butler. Hot-Spot Ignition of Condensed Phase Energetic Materials. *Journal of Propulsion and Power*, 12(4):680–690, 1996.

[126] K. Kim and C. Sohn. Modelling of Reaction Buildup Processes in Shocked Porous Explosives. In *Proceedings of the 8th International Detonation Symposium*, pages 926–933, 1985.

[127] K. Kim. Development of a Model of Reaction Rates in Shocked Multicomponent Explosives. In *Proceedings of the 9th International Detonation Symposium*, pages 593–603, 1989.

[128] I. N. Gray. Preserving Causality in Strongly Shearing Elastoplastic Flows. In *Proceedings of the APS Conference on Shock Compression of Condensed Matter*, 2001.

[129] M. L. Wilkins. Calculation of Elastic-Plastic Flow. *Methods in Computational Physics Volume 3*, pages 211–263, 1964. Academic Press.

[130] R. von Mises. *Z. Angew Math. u. Mech., 8*, pages 161–185, [English Translation: UCRL Trans. 872 (L)], 1928.

[131] P. Perzyna. The Constitutive Equations for Rate Sensitive Plastic Materials. *Quart. Appl. math.*, 20:34, 1963.

[132] S. P. Marsh. *LASL Shock Hugoniot Data*. University of California Press, 1980.

[133] L. H. Bakken and P. D. Anderson. An Equation of State Handbook (Conversion Relations Between the WONDY/TOODY and the PUFF/KO/HEMP Classes of Shock Wave Propagation Computer Codes). Technical Report SCL-DR-68-123, Sandia National Laboratories, 1969.

[134] R. N. Rogers. Thermochemistry of Explosives. *Thermochimica Acta*, 11:131–139, 1975.

[135] G. W. C. Kaye and T. H. Laby. *Tables of Physical and Chemical Constants*. Longmans, 1959.

[136] B. C. Taylor and L. H. Ervin. Separation of Ignition and Buildup to Detonation in Pressed TNT. In *Proceedings of the 6th International Detonation Symposium*, pages 3–10, 1976.

[137] R. L. Gustavsen, S. A . Sheffield, and R. R. Alcon. Low Pressure Shock Initiation of Porous HMX For Two Grain Size Distributions and Two Densities. In *APS Conference on Shock Compression of Condensed Matter*, pages 851–854, 1995.

[138] M. R. Baer and C. A. Hall. Isentropic Compression Studies of the Mesoscale Response of Energetic Composites and Constituents. In *Proceedings of the 13th International Detonation Symposium*, pages 1070–1080, 2006.

[139] M. S. Plesset and A. Prosperetti. Bubble Dynamics and Cavitation. *Ann. Rev. Fluid Mech.*, 9, 1977.

[140] W. H. Press, S. A. Teukolsky, W. T. Vetterling, and B. P. Flannery. *Numerical Recipes in Fortran 77 (Second Edition)*. Cambride University Press, 1992.